



Force measurements with the atomic force microscope: Technique, interpretation and applications

Hans-Jürgen Butt^a, Brunero Cappella^{b,*}, Michael Kappl^a

^aMax-Planck-Institute for Polymer Research, D-55128 Mainz, Germany

^bFederal Institute for Material Research and Testing, D-12205 Berlin, Germany

Accepted 1 August 2005

Abbreviations: AFM, atomic force microscope; AOT, bis(2-ethylhexyl)sulfosuccinate; BSA, bovine serum albumin; CMC, critical micellar concentration (mol/L); CSH, calcium silicate hydrate; CTAB, cetyltrimethylammonium bromide (=hexadecyltrimethylammonium bromide); DDAB, didodecyl dimethylammonium bromide; DDAPS, *N*-dodecyl-*N,N*-dimethyl-3-ammonio-1-propanesulfonate; DGDG, digalactosyldiglyceride; DLVO, Derjaguin–Landau–Verwey–Overbeek theory; DMA, dynamical mechanical analysis; DMT, Derjaguin–Müller–Toporov theory of mechanical contact; DNA, desoxyribonucleic acid; DODAB, dimethyl-dioctadecylammonium bromide; DOPC, 1,2-dioleoyl-*sn*-glycero-3-phosphocholine; DOPE, 1,2-dioleoyl-*sn*-glycero-3-phosphodylethanolamine; DOPS, 1,2-dioleoyl-*sn*-glycero-3-phospho-*l*-serine; DOTAP, 1,2-dioleoyl-3-trimethylammonium-propane chloride; DTAB, dodecyltrimethylammonium bromide; DSCG, disodium cromoglycate; DSPE, 1,2-distearoyl-*sn*-glycero-3-phosphoethanolamine; EDTA, ethylenediaminetetraacetic acid; FJC, freely jointed chain; HOPG, highly oriented pyrolytic graphite; HSA, human serum albumin; JKR, Johnson–Kendall–Roberts theory of mechanical contact; LPS, lipopolysaccharides; MD, molecular dynamics; MEMS, micro-electromechanical systems; MF, melamine formaldehyde; MGDG, monogalactosyldiacylglycerol; OMCTS, octamethylcyclotetrasiloxane, ((CH₂)₂SiO)₄; OTS, octadecyltrichlorosilane; PAA, poly(acrylic acid); PAH, poly(allyl amine hydrochloride); PBA, parallel beam approximation; PBMA, poly(*n*-butyl methacrylate), -(CH₂CC₄H₉COOCH₃)_{*n*}-; PDADMAC, poly(diallyl-dimethyl-ammonium chloride); PDMS, poly(dimethylsiloxane); PEG, polyethylene glycol; PEI, polyethyleneimine; PEO, polyethyleneoxide, -(OCH₂CH₂)_{*n*}-; PFM, pulsed force mode; PLA, polylactic acid; PMAA, poly(methacrylic acid), -(CH₂CHCOOH)_{*n*}-; PMC, polyelectrolyte microcapsules; PMMA, poly(methyl methacrylate), -(CH₂CCH₃COOCH₃)_{*n*}-; PP, poly(propylene), -(CH₂CHCH₃)_{*n*}-; PS, polystyrene, -(CH₂-CH(C₆H₅))_{*n*}-; PSD, position sensitive detector; PSS, poly(sodium styrenesulfonate); PSU, polysulfonate; PTFE, poly(tetrafluoroethylene); PVD, physical vapor deposition; PVP, poly(vinylpyridine), -(CH₂CHC₅NH₄)_{*n*}-; SAM, self-assembled monolayer; SDS, sodium dodecylsulfate; SEDS, solution-enhanced dispersion by supercritical fluids; SEM, scanning electron microscope; SFA, surface forces apparatus; SNOM, scanning near-field optical microscope; STM, scanning tunneling microscope; TEM, transmission electron microscope; TIRM, total internal reflection microscopy; TTAB, tetradecyl trimethylammonium bromide; UHV, ultra-high vacuum; WLC, wormlike chain; XPS, X-ray photoelectron spectroscopy

* Corresponding author.

E-mail address: brunero.cappella@bam.de (B. Cappella).

Nomenclature

a	contact radius (m)
a_{Hertz}	contact radius in the Hertz theory
A	area (m^2)
A_{H}	Hamaker constant (J)
A_1	area between the two contact lines above the axis $F = 0$
A_2	area between the retraction contact lines and the axis $F = 0$
b	slip length (m)
c	speed of light in vacuum (2.998×10^8 m/s), concentration (mol/L)
C	capacitance of tip and sample (F); constant of the atom–atom pair potential (J m^6)
$C_{\text{K}}, C_{\text{D}}, C_{\text{L}}$	Keesom, Debye, and London coefficients (J m^6)
d	distance between end of cantilever and PSD
D	tip–sample distance (m)
D_{jtc}	tip–sample distance at which the jump-to-contact occurs (m)
D_0	typical interatomic spacing (m)
e	unit charge (1.602×10^{-19} C)
E	Young's modulus (Pa)
$E_{\text{F}}, E_{\text{S}}$	Young's modulus of film and substrate (Pa)
$E_{\text{t}}, E_{\text{s}}$	Young's modulus of tip and sample material (Pa)
E_{tot}	reduced Young's modulus Eq. (4.4) (Pa)
f	force per unit area (Pa)
f^*	dimensionless correction factor
F	force (N)
F_{ad}	adhesion force (N)
F_{av}	average force (N)
F_{cap}	capillary force (N)
F_{el}	double-layer force (N)
F_{H}	hydrodynamic force (N)
F_{surf}	distance-dependent surface force (N)
F_0	mean rupture force (N)
h	Planck's constant (6.626×10^{-34} J s); thickness of a film on a substrate (m)
H	height of tip (m); hardness (Pa)
H_{d}	height of a deformed polyelectrolyte microcapsule (m)
I	$wt_{\text{c}}^3/12$, moment of inertia of a cantilever (m^4)
I_{PSD}	photosensor current (A)
J	relative Young's modulus, Eq. (4.12)
k_{B}	Boltzmann constant (1.381×10^{-23} J/K)
k_{c}	spring constant of cantilever (N/m)
k_{eff}	$=k_{\text{c}}k_{\text{s}}/(k_{\text{c}} + k_{\text{s}})$ effective spring constant (N/m)
k_{s}	sample stiffness (N/m)
k_0	frequency of spontaneous hole formation (Hz)
l	length of one segment in a linear polymer (m)

l_K	Kuhn length (m)
l_p	persistence length (m)
L	length of cantilever (m)
L_0	equilibrium thickness of a polymer brush (m)
m_c	mass of the cantilever (g)
m_M	ratio between the contact radius a and an annular region, where the adhesion is taken into account
m_t	mass of the tip (g)
m^*	effective mass of the cantilever (g)
n	number of carbon atoms in an alkyl chain; number of segments in a linear polymer; parameter; refractive index
n_i	refractive index
n_{av}	average number of bonds
n_∞	bulk concentration of salt in a solvent (molecules per volume)
p	permanent plastic deformation (m)
p'	intercept between the axis $F = 0$ and the tangent to the unloading curve for very high loads
P	pressure (N/m^2); probability to find the tip on top of a molecular layer; binding probability
Q	quality factor of the cantilever
r	radial distance or distance between molecules (m)
rms	root mean square roughness (m)
R	tip radius or radius of microsphere (m)
Re	Reynolds number
R_g	radius of gyration of a polymer (m)
R_m	molecular radius (m)
R_0	radius of not deformed polyelectrolyte microcapsule
s	surface stress (N/m)
S	order parameter; spreading pressure
t	time (s)
t_c	thickness of the cantilever (m)
t_s	thickness of the shell of a polyelectrolyte capsule
T	temperature (K)
u_1, u_2	dipole moment of molecules (C m)
U	potential energy between tip and sample (J)
U_A	potential energy per unit area between two planar, parallel surfaces (J/m^2)
U_c	Hooke's elastic potential of the cantilever (J)
U_{cs}	tip-sample interaction potential (J)
U_s	Hooke's elastic potential of the sample (J)
U_0	activation energy (J)
v	velocity of the tip or particle (m/s)
v_x	fluid velocity parallel to a surface (m/s)
v_0	vertical scan rate, identical to velocity of the base of the cantilever (m/s)
V	voltage (V)
V_m	molar volume of a liquid

w	width of cantilevers (m)
w_K, w_D, w_L, w_{vdW}	Keesom, Debye, London, and total van der Waals potentials between molecules
W	work of adhesion at contact per unit area (J/m^2)
W_{ad}	work of adhesion at contact (J)
x	distance in gap between two planar, parallel walls (m); relative extension of a polymer
X	horizontal coordinate originating at the base of the cantilever (m)
z	coordinate normal to a surface (m)
Z	cantilever deflection (m) at a certain horizontal coordinate
Z_c	deflection of the cantilever at its end (m)
$(Z_c)_{jtc}$	deflection of the cantilever at the jump to contact (m)
Z_i	valency of ion
Z_p	height position of the piezoelectric translator (m)
Z_0	amplitude of cantilever vibration (m)

Greek letters

α	opening angle of V-shaped cantilever; endslope of cantilever; parameter in contact theory; immersion angle
α_i	parameters describing the eigenmodes of rectangular cantilevers
α_{01}, α_{02}	electronic polarizabilities of molecules ($C^2 m^2/J$)
β, β^*	correction factor, parameter
β_1, β_2	parameters to describe plastic contact
γ	surface tension of a liquid (N/m) or surface energy
γ_D	damping coefficient (kg/s)
γ_0	surface tension of a pure liquid (N/m)
γ^{AB}	acid–base surface energy
γ^{LW}	Lifshitz–van der Waals surface energy
γ^+, γ^-	electron acceptor and electron donor components of the acid–base surface energy
Γ	surface excess (mol/m^2); grafting density ($number/m^2$)
Γ_i	imaginary part of the so-called “hydrodynamic function”
δ	indentation (m)
δ_{max}	maximal indentation (m)
Δ_{PSD}	distance the laser spot moves on the PSD (m)
ϵ, ϵ_i	dielectric constant of the medium
ϵ_0	vacuum permittivity ($8.854 \times 10^{-12} A s V^{-1} m^{-1}$)
η	viscosity (Pa s)
$\theta, \theta_a, \theta_r$	contact angle (advancing and receding)
Θ	half opening angle of a conical tip
ϑ	tilt of the cantilever with respect to the horizontal
κ	line tension (N); bending rigidity (J)
λ	Maugis parameter
λ_D	Debye length (m)
λ_H	Decay length of hydration force (m)
λ_i	wavelengths of the eigenmodes of rectangular cantilevers

λ_S	Decay length of solvation force (m)
μ	chemical potential (J/mol)
ν	Poisson's ratio
ν_e	mean absorption frequency (Hz)
ν_F, ν_S	Poisson's ratio of film and substrate (Pa)
ν_t, ν_s	Poisson's ratio of tip and sample material (Pa)
ν_0	resonance frequency of cantilever (Hz)
ν_1, ν_2	ionization frequencies (Hz)
ξ	relative deformation of a polyelectrolyte microcapsule
ρ	density (kg/m^3)
ρ_f	density of fluid surrounding the cantilever (kg/m^3)
σ	molecular diameter (m)
σ_S	surface charge density of sample in aqueous medium (C/m^2)
σ_T	surface charge density of tip in aqueous medium (C/m^2)
$\sigma_F^2 (\sigma_n^2)$	force variance, number of bonds variance
τ	inverse of vibration frequency (s)
φ	phase
ψ	electric potential (V)
ψ_P	plasticity index, Eq. (4.9)
ψ_S	electric surface potential of sample in aqueous medium (V)
ψ_T	electric surface potential of tip in aqueous medium (V)
ω	angular frequency (Hz)
ω_0	angular resonance frequency of the cantilever, $\omega_0 = 2\pi\nu_0$ (Hz)
Ω	frequency factor (number of attempts of the tip to penetrate through a layer)

Abstract

The atomic force microscope (AFM) is not only a tool to image the topography of solid surfaces at high resolution. It can also be used to measure force-versus-distance curves. Such curves, briefly called force curves, provide valuable information on local material properties such as elasticity, hardness, Hamaker constant, adhesion and surface charge densities. For this reason the measurement of force curves has become essential in different fields of research such as surface science, materials engineering, and biology.

Another application is the analysis of surface forces per se. Some of the most fundamental questions in colloid and surface science can be addressed directly with the AFM: What are the interactions between particles in a liquid? How can a dispersion be stabilized? How do surfaces in general and particles in particular adhere to each other? Particles and surfaces interactions have major implications for friction and lubrication. Force measurements on single molecules involving the rupture of single chemical bonds and the stretching of polymer chains have almost become routine. The structure and properties of confined liquids can be addressed since force measurements provide information on the energy of a confined liquid film.

After the review of Cappella [B. Cappella, G. Dietler, Surf. Sci. Rep. 34 (1999) 1–104] 6 years of intense development have occurred. In 1999, the AFM was used only by experts to do force measurements. Now, force curves are used by many AFM researchers to characterize materials and single molecules. The technique and our understanding of surface forces has reached a new level of maturity. In this review we describe the technique of AFM force measurements. Important experimental issues such as the determination of the spring constant and of

the tip radius are discussed. Current state of the art in analyzing force curves obtained under different conditions is presented. Possibilities, perspectives but also open questions and limitations are discussed.

© 2005 Elsevier B.V. All rights reserved.

Keywords: Atomic force microscope; Force curves; Surface forces

Contents

1.	Introduction	7
2.	The technique of AFM force measurements	10
2.1.	Overview.	10
2.2.	Mechanical properties of cantilevers	12
2.2.1.	General design	12
2.2.2.	Shape of the cantilever	13
2.2.3.	Dynamic properties.	14
2.2.4.	Dynamic force measurements	15
2.2.5.	Kinetic force measurements and higher vibration modes	17
2.3.	Calibration of spring constants	19
2.4.	Tip modification and characterization	23
2.4.1.	Modification	23
2.4.2.	Characterization	26
2.5.	Colloidal probes	26
2.6.	Deflection detection with an optical lever	28
3.	Analysis of force curves	30
3.1.	Conversion of force curves and the problem of zero distance.	30
3.2.	Difference between approach and retraction.	33
3.3.	Derjaguin approximation	35
3.4.	Electrostatic force.	36
4.	The contact regime	38
4.1.	Overview.	38
4.2.	Theory: Hertz, JKR, DMT and beyond	38
4.3.	Plastic deformation.	41
4.4.	Experimental results	43
5.	van der Waals forces	45
5.1.	Theory	45
5.2.	Determination of Hamaker constants, adhesion and surface energies.	49
6.	Forces in aqueous medium	54
6.1.	Electrostatic double-layer force and DLVO theory	54
6.2.	Hydration repulsion	60
6.3.	Hydrophobic attraction	61
7.	Adhesion	65
7.1.	Influence of roughness on adhesion	66
7.2.	Particle adhesion	68
7.2.1.	Adhesion of drug substances	71
7.2.2.	Interaction of membranes and particles	73
7.3.	Adhesion in MEMS and proteins	74
7.4.	Meniscus force.	75
8.	Confined liquids: solvation forces and adsorbed layers	79
8.1.	Overview.	79
8.2.	Solvation forces	80

8.3.	Lipid layers	81
8.3.1.	Theory	81
8.3.2.	Preparation of solid supported lipid bilayers	84
8.3.3.	Force curves on lipid bilayers	86
8.4.	Adsorbed surfactants.	89
8.5.	Steric forces	91
9.	Soft surfaces	95
9.1.	Particle–bubble interaction.	95
9.2.	Mechanical properties of microcapsules	101
9.2.1.	Theoretical models	101
9.2.2.	Results for hollow capsules	103
9.2.3.	Filled polyelectrolyte capsules	105
9.3.	Cells	105
9.3.1.	Elastic properties of cells	105
9.3.2.	Cell and animal adhesion	107
9.3.3.	Cell probe measurements.	109
10.	Hydrodynamic force.	110
10.1.	Introduction.	110
10.2.	Theory	111
10.3.	Experiments.	112
11.	Single molecules	114
11.1.	Molecule stretching	114
11.2.	Rupture force of specific interactions	116
12.	Imaging based on force–distance curves	119
12.1.	Force volume mode	119
12.2.	Pulsed force mode atomic force microscopy	122
13.	Conclusions and perspectives	125
	References	127

1. Introduction

The atomic force microscopy (AFM) belongs to a series of scanning probe microscopes invented in the 1980s. This series started with the scanning tunnelling microscope (STM), which allowed the imaging of surfaces of conducting and semiconducting materials [1,2]. With the STM it became possible to image single atoms on “flat” (i.e., not a tip) surfaces. In parallel the scanning near-field optical microscope (SNOM) was invented which allowed microscopy with light below the optical resolution limit [3,4]. The last one of the series is the AFM, invented by Binnig et al. [5]. The AFM with its “daughter” instruments such as the magnetic force microscope and the Kelvin probe microscope has become the most important scanning probe microscope. The AFM allowed the imaging of the topography of conducting *and* insulating surfaces, in some cases with atomic resolution.

In the AFM (Fig. 1) the sample is scanned by a tip, which is mounted to a cantilever spring. While scanning, the force between the tip and the sample is measured by monitoring the deflection of the cantilever. A topographic image of the sample is obtained by plotting the deflection of the cantilever versus its position on the sample. Alternatively, it is possible to plot the height position of the translation stage. This height is controlled by a feedback loop, which maintains a constant force between tip and sample.

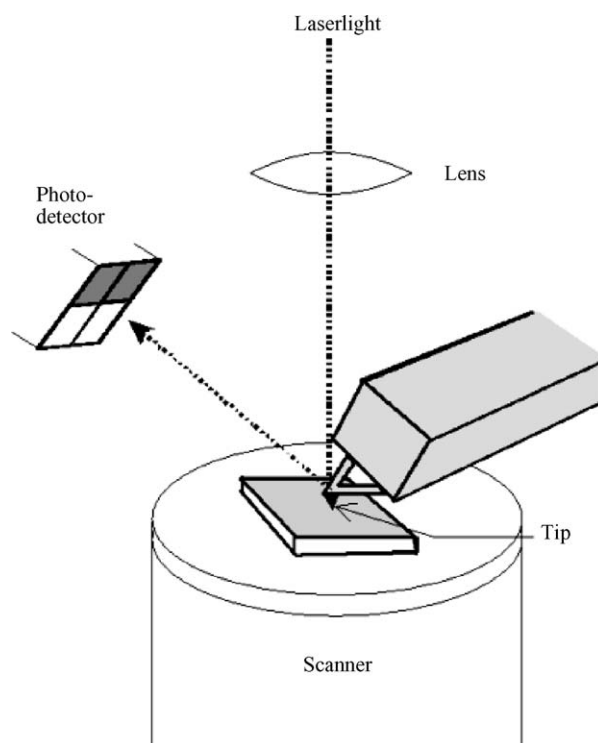


Fig. 1. Schematic of an atomic force microscope.

Image contrast arises because the force between the tip and sample is a function of both tip–sample separation and the material properties of tip and sample. To date, in most applications image contrast is obtained from the very short range repulsion, which occurs when the electron orbitals of tip and sample overlap (Born repulsion). However, further interactions between tip and sample can be used to investigate properties of the sample, the tip, or the medium in between. These measurements are usually known as “force measurements”. In an AFM force measurement the tip attached to a cantilever spring is moved towards the sample in normal direction. Vertical position of the tip and deflection of the cantilever are recorded and converted to force-versus-distance curves, briefly called “force curves”.

In the first few years force measurements with the AFM were driven by the need to reduce the total force between tip and sample in order to be able to image fragile, e.g. biological structures. Therefore it was obligatory to understand the different components of the force. In addition, microscopists tried to understand the contrast mechanism of the AFM to interpret images correctly. One prominent example was the observation of meniscus forces under ambient conditions by Weisenhorn et al. [6] in 1989. Weisenhorn et al. did not only detect meniscus forces but they also realized that imaging in liquid could significantly reduce the interaction between tip and sample in AFM imaging and thus increase the resolution.

Another important motivation was the computer industry with its demand to produce hard discs and other storage devices with high data density. This stimulated the measurement of magnetic [7–10] and electrostatic forces [11–13] and led to the development of magnetic force, electric force, and Kelvin

probe microscopy [14]. The goal was not so much to understand the force but to image the distribution of magnetization, charge, or surface potential, respectively.

The main focus of AFM force measurements today is to study surface forces *per se*. The interaction between two surfaces across a medium is one of the fundamental issues in colloid and surface science. It is not only of fundamental interest but also of direct practical relevance when it comes to dispersing solid particles in a liquid. One major step to measure surface forces quantitatively was the introduction of the colloidal probe technique [15,16]. In the colloidal probe technique a spherical particle of typically 2–20 μm diameter is attached to the end of the cantilever. Then the force between this microsphere and a flat surface is measured. Since the radius of the microsphere can easily be determined, surface forces can be measured quantitatively. For imaging, a microsphere is of course not suitable.

The AFM is not the only device to measure forces between solid surfaces. During the last decades several techniques and devices have been developed [17]. One important device is the surface forces apparatus (SFA). The SFA allows to measure directly the force law in liquids and vapors at angstrom resolution level [18,19]. The SFA contains two crossed atomically smooth mica cylinders of roughly 1 cm radius between which the interaction forces are measured. One mica cylinder is mounted to a piezoelectric translator. With this translator the distance is adjusted. The other mica surface is mounted to a spring of known and adjustable spring constant. The separation between the two surfaces is measured by use of an optical technique using multiple beam interference fringes. Knowing the position of one cylinder and the separation to the surface of the second cylinder, the deflection of the spring and the force can be calculated.

Another important, although less direct, technique for measuring forces between macromolecules or lipid bilayers is the osmotic stress method [20–22]. In the osmotic stress method a dispersion of vesicles or macromolecules is equilibrated with a reservoir solution containing water and other small solutes, which can freely exchange with the dispersion phase. The reservoir also contains a polymer which cannot diffuse into the dispersion. The polymer concentration determines the osmotic stress acting on the dispersion. The spacing between the macromolecules or vesicles is measured by X-ray diffraction. In this way one obtains pressure-versus-distance curves.

During the last 10–15 years a new technique called total internal reflection microscopy (TIRM) was developed [23]. Using TIRM the distance between a single microscopic sphere immersed in a liquid and a transparent plate can be monitored with typically 1 nm resolution. The distance is calculated from the intensity of light scattered by the sphere when illuminated by an evanescent wave through the plate. From the equilibrium distribution of distances sampled by Brownian motions the potential energy-versus-distance can be determined. TIRM complements force measurements with the AFM and the SFA because it covers a lower force range.

These techniques have allowed accurate measurement of surface and intermolecular forces and led to improved understanding in this field. However, only a limited number of systems could be investigated because of restrictions to the material properties and the complexity of the equipment. In contrast, the AFM is relatively easy to use. Since many people use the AFM for imaging it is relatively common and the technology is refined. Due to its high lateral resolution small samples can be used and material non-homogeneities can be mapped. Having small contact areas also reduces the danger of contamination and surface roughness.

In 1994 another type of AFM force measurements emerged, that of single molecule experiments. Forces to stretch single polymer molecules or to break single bonds had been measured before, but the ease and accuracy greatly stimulated the field (for a review, see Ref. [24]). The wealth of experimental results has also triggered the development of a much refined theory of bonding and bond breaking.

The aim of this review is to provide the reader with a comprehensive description of how to measure and analyze AFM force experiments. It is written for researchers who intend to use the AFM or already use it for measure forces. These can be microscopists with a background in imaging who intend to expand their possibilities by taking force curves. It also concerns colloidal and interface scientists who want to use the AFM to study interparticle and surface forces. The review highlights the contribution the AFM made to our knowledge of surface forces. We describe the technique and analysis, the advantages and scientific achievements but also the problems, limits, and pitfalls. We believe that AFM force experiments have reached such a maturity, that a comprehensive review is helpful.

2. The technique of AFM force measurements

2.1. Overview

In a force measurement the sample is moved up and down by applying a voltage to the piezoelectric translator, onto which the sample is mounted, while measuring the cantilever deflection (Fig. 2). In some AFMs the chip to which the cantilever is attached is moved by the piezoelectric translator rather than the sample. This does not change the description at all, for simplicity we assume that the sample is moved. The sample is usually a material with a planar, smooth surface. It is one of the two interacting solid surfaces. The other solid surface is usually a microfabricated tip or a microsphere. For simplicity we call this “tip”. If we explicitly refer to one of the two we mention it as “microfabricated tip” or “microsphere”.

The counterpart of the tip is the sample. The most convenient geometry is a planar surface. Problems due to sample roughness are greatly reduced in the AFM compared to other surface force techniques since the sample only needs to be smooth on a scale comparable to the radius of curvature at the end of the tip. Several materials such as mica, a silicon wafer or graphite (HOPG) are available with sufficient smoothness over the required areas. In addition, the surface of many materials can be smoothed by template stripping. Therefore the material, say a polymer, is melted on a smooth surface [25]. This can be a mica or a silicon wafer surface. After cooling and right before an experiment the surface is peeled off

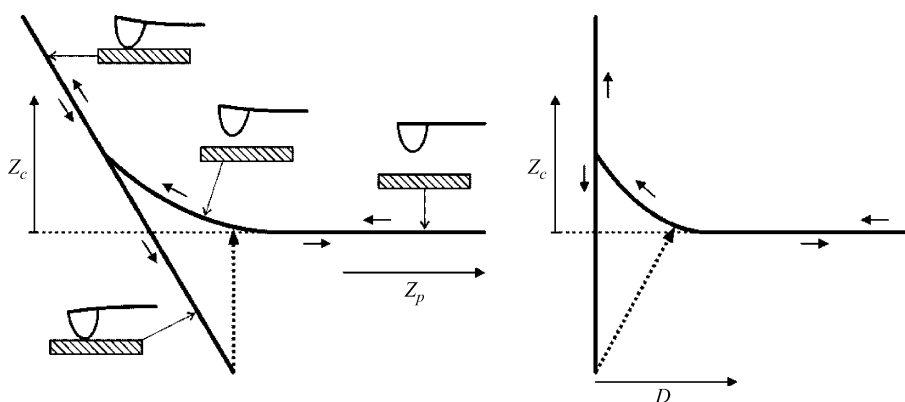


Fig. 2. Schematic of a typical cantilever deflection-vs.-piezo height (Z_c -vs.- Z_p) curve (left) and corresponding Z_c -vs.- D plot, with $D = Z_c + Z_p$.

and the freshly exposed polymer surface is used for the force measurement. The same technique can also be used for gold or other materials which can be sputtered or evaporated [26,27]. First the material is deposited onto mica or a silicon wafer. Then a steel plate is glued on top. Finally the steel plate with the deposited material is cleaved off the substrate surface. The now exposed surface of the deposited material can then be used in a force experiment.

Atomic force microscopes can be operated in air, different gases, vacuum, or liquid. Different environmental cells, in which the kind of gas and the temperature can be adjusted, are commercially available. To acquire force curves in liquid different types of liquid cells are employed. Typically liquid cells consist of a special cantilever holder and an O-ring sealing the cell.

The result of a force measurement is a measure of the cantilever deflection, Z_c , versus position of the piezo, Z_p , normal to the surface. To obtain a force-versus-distance curve, Z_c and Z_p have to be converted into force and distance. The force F is obtained by multiplying the deflection of the cantilever with its spring constant k_c : $F = k_c Z_c$. The tip-sample separation D is calculated by adding the deflection to the position: $D = Z_p + Z_c$. We call this tip-sample separation “distance”. For details see Section 3.1.

The deflection of the cantilever is usually measured using the optical lever technique [28,29]. A beam from a laser diode is focused onto the end of the cantilever and the position of the reflected beam is monitored by a position sensitive detector (PSD). Often the backside of the cantilever is covered with a thin gold layer to enhance its reflectivity. When a force is applied to the probe, the cantilever bends and the reflected light-beam moves through an angle equal to twice the change of the endslope dZ_c/dX . For a cantilever with a rectangular cross-section of width w , length L , and thickness t_c , the change of the endslope (Fig. 3) is given by

$$\frac{dZ_c}{dX} = \frac{6FL^2}{Ewt_c^3}. \quad (2.1)$$

Here, E is the Young's modulus of the cantilever material. F is the force applied to the end of the cantilever in normal direction. The signal detected with the optical lever technique is proportional to the endslope of the cantilever. The deflection of the cantilever is given by

$$Z_c = \frac{4FL^3}{Ewt_c^3} = \frac{2}{3}L \frac{dZ_c}{dX}. \quad (2.2)$$

Hence, the deflection is proportional to the signal. One should, however, keep in mind that these relations only hold under equilibrium condition. If the movement of the cantilever is significantly faster

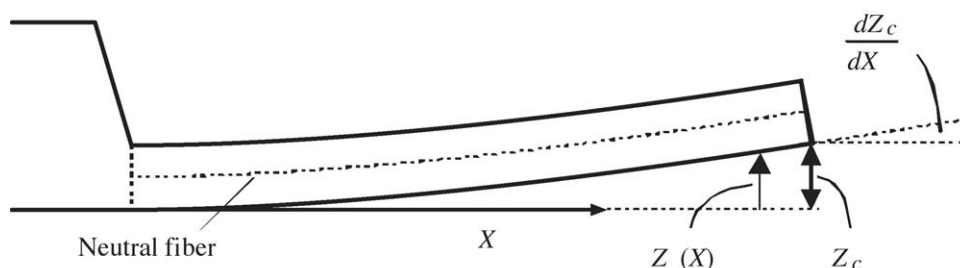


Fig. 3. Schematic side view of a cantilever with a force at its end. X is the horizontal coordinate originating at the basis of the cantilever, $Z(X)$ is the cantilever deflection at the position X , Z_c being the cantilever deflection at its end.

than allowed by its resonance frequency Eqs. (2.1) and (2.2) are not valid anymore and the signal is not necessarily proportional to the deflection.

The position of the sample is adjusted by the piezoelectric translator. Piezoelectric crystals show creep and hysteresis which affects the accuracy of the distance determination [30]. One possibility to overcome this problem is to use piezoelectric translators with integrated capacitive position sensors, which are commercially available [31]. In the same setup another deficit of commercial AFMs was overcome. Standard fluid cells of commercial AFMs are small and manually difficult to access. In addition, they consist of different materials (glass, steel, silicon, etc.) which are difficult to clean. In self-made devices the fluid cell can be made of one or few materials (like Teflon and quartz) which can be cleaned thoroughly, e.g. with hot sulfuric or nitric acid.

Usually the piezoelectric translator moves with constant velocity up and down so that its position-versus-time can be described by a triangular function. A constant approaching and retracting velocity is the most simple boundary condition when analyzing dynamic effects in a force experiment. A problem might arise for high velocities because then the cantilever might vibrate each time the direction of the movement changes. No useful deflection signal can be obtained until this vibration is damped. To be able to take force curves at higher frequency a sinusoidal voltage was applied to the piezo leading to a sinusoidal position-versus-time curve [32–34]. Typically, the frequency is 0.1–1 kHz, significantly below the resonance frequency of the cantilever and the cantilever assumes its equilibrium deflection at all times. Marti et al. [35] termed the name “pulsed force mode” for this mode of operation.

2.2. Mechanical properties of cantilevers

2.2.1. General design

The cantilever is in fact a key element of the AFM and its mechanical properties are largely responsible for its performance. Commercial cantilevers are typically made of silicon or silicon nitride. Both are covered with a native oxide layer of 1–2 nm thickness. The mechanical properties of cantilevers are characterized by the spring constant k_c and the resonance frequency ν_0 . Both can in principle be calculated from the material properties and dimensions of the cantilever. For a cantilever with constant rectangular cross-section (in the following briefly called “rectangular cantilever”) the spring constant is

$$k_c = \frac{F}{Z_c} = \frac{Ewt_c^3}{4L^3}. \quad (2.3)$$

A good cantilever should have a high sensitivity. High sensitivity in Z_c is achieved with low spring constants or low ratio t_c/L . Hence, in order to have a large deflection at small force cantilevers should be long and thin. In addition, the design of a suitable cantilever is influenced by other factors:

- External vibrations, such as vibrations of the building, the table, or noise, which are usually in the low frequency regime, are less transmitted to the cantilever, when the resonance frequency of the cantilever [36,37]

$$\nu_0 = 0.1615 \frac{t_c}{L^2} \sqrt{\frac{E}{\rho}} \quad (2.4)$$

is as high as possible ($0.1615 = (1.875)^2/2\pi\sqrt{12}$, see Eq. (2.27)). Here, ρ is the density of the cantilever material. The equation is valid for a rectangular cantilever. A high resonance frequency is

also important to be able to scan fast because the resonance frequency limits the time resolution [38,39].

- Cantilevers have different top and bottom faces. The top side is often coated with a layer of gold to increase its reflectivity. Therefore, any temperature change leads to a bending of the cantilever as in a bimetal. In addition, adsorption of substances or electrochemical reactions in liquid environment slightly changes the surface stress of the two faces. These changes in surface stress are in general not the same on the bottom and the top side. Any difference in surface stress Δs will lead to a bending of the cantilever [40,41]. For a rectangular cantilever this leads to

$$Z_c \approx \frac{4L^2 \Delta s}{Et_c^2}. \quad (2.5)$$

Practically, these changes in surface stress lead to an unpredictable drift of the cantilever deflection which disturbs force measurements. To reduce drift the ratio t_c/L should be high.

Hence, the optimal design of a cantilever is a compromise between different factors. Depending on the application the appropriate dimensions and materials are chosen. Cantilevers for AFMs are usually V-shaped to increase their lateral stiffness. They are typically $L = 100\text{--}200 \mu\text{m}$ long, each arm is about $w = 20\text{--}40 \mu\text{m}$ wide and $t_c = 0.5\text{--}1 \mu\text{m}$ thick. Typical resonance frequencies are 20–200 kHz in air [36,39,42].

All the requirements discussed above lead to the conclusion that cantilevers should be small. Only short and thin cantilevers are soft, have a high sensitivity and a high resonance frequency. Accordingly, several researchers aim to make even smaller cantilevers with higher resonance frequency [43–45]. The smallest cantilevers are $\approx 10 \mu\text{m}$ long, $0.1\text{--}0.3 \mu\text{m}$ thick and $3\text{--}5 \mu\text{m}$ wide. They are made of aluminum or silicon nitride, leading to resonance frequencies of typically 2 MHz in air. The size of cantilevers cannot be made much smaller because it becomes more and more difficult to fabricate the tips and to focus the laser beam onto such small structures [44]. Also the aperture of the lens in the incident laser beam path has to be adjusted to the cantilever size to achieve an optimal signal-to-noise ratio [46].

2.2.2. Shape of the cantilever

In this section we calculate the shape of the cantilever when a force is applied to its end in normal (vertical) direction. This is important not only to understand how the spring constant is calculated. It also is essential to see how inclination and deflection are related; please keep in mind that with the optical lever technique the inclination is measured!

The cantilever is supposed to be aligned along the horizontal x -axis (Fig. 3). When a force is applied the shape changes. For example, when a repulsive force pushes the cantilever up the material at the top face is compressed while the material at the bottom face is stretched. Somewhere in the middle the material is not deformed. This defines the so-called neutral fiber. For a rectangular cantilever made of a homogeneous material the neutral fiber is precisely in the middle. We describe the shape of the cantilever by the function $Z(X)$. In the absence of a force its shape is given by $Z(X) = 0$.

We further assume that a static force is applied, which practically means that changes of the force occur on a time scale much slower than the inverse of the resonance frequency. In a static situation the torque at all positions must be zero (otherwise it would not be static). The torque at a given position X due to the force is $F(L - X)$. The elastic response caused by compression of the cantilever at the top side and

the expansion at the bottom side is given by $EI \frac{d^2Z}{dX^2}$, where I is the moment of inertia. For a cantilever with a rectangular cross-section it is $I = wt_c^3/12$. This leads to the differential equation

$$F(L - X) = EI \frac{d^2Z}{dX^2} \Rightarrow \frac{d^2Z}{dX^2} = \frac{F}{EI} (L - X). \quad (2.6)$$

If the cross-section is constant and does not change along the cantilever (rectangular cantilever) Eq. (2.6) can be integrated twice, using the boundary conditions $Z(X = 0) = 0$ and $dZ/dX(X = 0) = 0$. The result is

$$Z = \frac{F}{2EI} \left(LX^2 - \frac{X^3}{3} \right). \quad (2.7)$$

It is interesting to note that the maximal bending of the cantilever is at its base, so at small X . At the end ($X = L$) we have a deflection

$$Z_c = Z(L) = \frac{FL^3}{3EI}. \quad (2.8)$$

Inserting $I = wt_c^3/12$ we get Eq. (2.3). The inclination at the end is

$$\frac{dZ_c}{dX} = \frac{FL^2}{2EI}. \quad (2.9)$$

Comparing the last two equations shows that the inclination is proportional to the deflection and for a rectangular cantilever we derive Eq. (2.2).

In fact, deflection and inclination are always proportional, independent of the specific geometry of the cantilever because F is not a function of X . For V-shaped cantilevers the expression is more complicated [39]. Often, however, the shape of V-shaped cantilevers can be approximated by that of a rectangular cantilever having a width of twice the width of each leg of the V-shaped cantilever; this is called the parallel beam approximation (PBA). Experiments confirmed that the shape of a cantilever with a load at its end is well described by Eq. (2.7) [47].

2.2.3. Dynamic properties

In equilibrium the shape of the cantilever is described by the equations given above. For many applications it is also important to know the dynamical properties. In this case the deflection depends on time. The most simple approach, which nevertheless leads to a realistic description of most tip movements, is to start with Newton's equation of motion:

$$m^* \frac{d^2Z_c(t)}{dt^2} + \gamma_D \frac{dZ_c(t)}{dt} + k_c Z_c(t) = F(t). \quad (2.10)$$

Here,

$$m^* = 0.2427m_c + m_t \quad (2.11)$$

is the effective cantilever mass, where $m_c = wt_c L \rho$ is the actual mass of the cantilever and m_t is the mass of the tip. The damping coefficient γ_D and the spring constant are supposed to be independent of time. Any movement is caused by the external force F in normal direction.

An important application of Eq. (2.10) is to describe periodic excitations, $F = F_0 \sin \omega t$. A periodic excitation close to the resonance frequency is the basis for non-contact (also called “dynamic”) atomic

force microscopy and for tapping mode [48–50]. To analyze the response of a cantilever to a periodic excitation we insert $F = F_0 \sin \omega t$ into Eq. (2.10). Then, in steady state, Eq. (2.10) is solved by [51]

$$Z_c(t) = Z_0 \sin(\omega t - \varphi) \quad (2.12)$$

with

$$Z_0(\omega) = \frac{F_0}{\sqrt{(k_c - m^* \omega^2)^2 + \gamma_D^2 \omega^2}} = \frac{F_0/m^*}{\sqrt{(\omega_0^2 - \omega^2)^2 + (\omega \omega_0/Q)^2}}, \quad (2.13)$$

and

$$\tan \varphi = \frac{\gamma_D \omega}{k_c - m^* \omega^2}. \quad (2.14)$$

Here, the angular resonance frequency $\omega_0 = 2\pi\nu_0 = \sqrt{k_c/m^*}$ and the quality factor $Q = \omega_0/\gamma_D$ are introduced. The amplitude Z_0 and the phase shift φ depend on the angular frequency ω . At low frequency the amplitude is given by $Z_0 = F_0/k_c$. The Z_0 increases until it reaches a maximum

$$Z_0(\omega_{\max}) = \frac{F_0 Q}{k_c \sqrt{1 - 1/4Q^2}} = \frac{F_0}{\gamma_D \sqrt{k_c m^* - (m^* \gamma_D/2)^2}} \quad (2.15)$$

at

$$\omega_{\max} = \sqrt{\frac{k_c}{m^*} - \frac{\gamma_D^2}{2m^{*2}}}. \quad (2.16)$$

Above ω_{\max} the amplitude decreases and goes to zero for $\omega \rightarrow \infty$. The phase shift is zero for low frequencies, it is $\varphi = 90^\circ$ at ω_{\max} , and it goes to 180° for $\omega \rightarrow \infty$. The quality factor describes the relative width of the resonance peak. It is equal to the resonance frequency divided by the half width of the square amplitude resonance peak. If we take the amplitude spectrum rather than the square amplitude spectrum and we denote the width of the amplitude spectrum at half height by $\Delta\omega$ (or $\Delta\nu$) then $Q = \sqrt{3}\omega_{\max}/\Delta\omega = \sqrt{3}\nu_{\max}/\Delta\nu$ for a low damped system.

Practically, in gaseous media or vacuum the resonance frequency agrees with ω_{\max} because the damping coefficient is relatively low (Fig. 4). The quality factor at normal pressure is strongly reduced as compared to vacuum. In vacuum a typical quality factor falls in the range 10^4 to 10^8 . In air this is reduced to 10–200. In liquids, however, this is different and measured values of ω_{\max} are significantly lower than ω_0 [39]. Hydrodynamic effects cause the effective mass of the cantilever to increase because the cantilever drags the surrounding liquid with it [37,52,53]. The higher the viscosity of the surrounding liquid the lower the resonance frequency of the cantilever. This effect can even be used to measure the viscosity of liquids [54].

2.2.4. Dynamic force measurements

When the tip approaches the sample and the distance becomes so small that tip and sample start to interact, the cantilever is not free anymore and the interaction has to be taken into account. It leads to a shift of the resonance frequency. For an attractive force the resonance frequency is reduced, for a repulsive force it is increased. This change of the resonance curve can be used to analyze surface forces

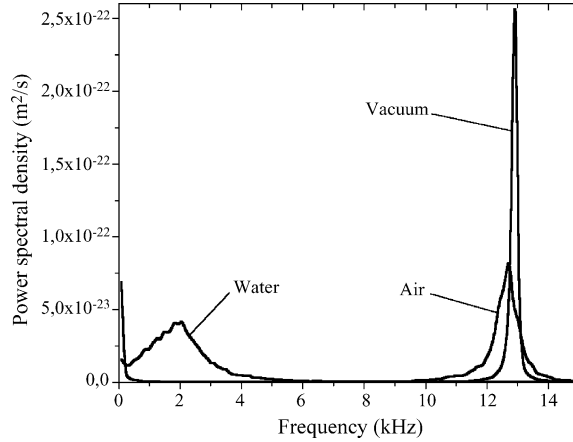


Fig. 4. Noise power spectrum for a cantilever in vacuum (0.3 mbar), air (1 bar) and in water at 22 °C. The V-shaped silicon nitride cantilever had a spring constant of 0.06 N/m (adapted from Fig. 5 of Ref. [39]).

[51]. If we knew the interaction we could in principle add this force as a term on the right side of Eq. (2.10), solve the differential equation, find the response curve and compare it to experimental results. Unfortunately, there is no unambiguous inverse process. That is, we cannot calculate force-versus-distance from a measurement of the resonance frequency-versus-distance. Either additional information or a reasonable model for the interaction is required. However, under certain assumptions and for certain approximations there are relatively direct relations between force and resonance frequency.

In a dynamic force experiment the cantilever is periodically excited by a piezoelectric transducer mounted underneath the chip. While vibrating, the distance between tip and sample is slowly ($v_0 \ll \omega Z_0$) changed, just like in a normal force experiment. Either the shift in resonance frequency is detected using a feedback system (FM, frequency modulation) [55,56] or the change in amplitude at constant excitation frequency and excitation amplitude (CE, constant excitation) is measured [57,58]. A potential advantage of dynamic force measurements is the high sensitivity. This allows to use stiffer cantilevers and thus avoid the jump-in which often prevents an accurate measurement of attractive forces (see Section 3.2).

The amplitude Z_0 can either be small or large. For small amplitudes the interaction potential does not change significantly over a distance Z_0 and the tip feels the same force independent of the specific phase. Then the resonance frequency shifts according to

$$\omega_0'^2 = \frac{k_c}{m^*} \pm \frac{1}{m^*} \left| \frac{dF}{dD} \right|, \quad (2.17)$$

where $D = Z_p + Z_c$ is the tip-sample distance.

In Eq. (2.17), the positive sign is for repulsive forces, the negative sign is valid for attractive forces. The shift is determined by the gradient of the force. Vice versa, from the measured shift of the resonance frequency the force gradient can be calculated [11].

In large amplitude dynamic AFM the jump-to-contact is avoided by using stiff cantilevers. The cantilever is vibrated at amplitudes much larger than the interatomic spacing, typically 1–100 nm. Interaction forces cause a phase shift between the excitation and the response of the cantilever. This phase shift is measured versus distance. One problem is that the theoretical analysis is not straightforward and

the method is not really used for quantitative measurements of surface forces but it is mainly used for imaging in non-contact mode [59–68].

A promising and technically simpler approach is to use thermal noise to “excite” the cantilever. For soft cantilevers thermal noise is sufficient to produce a detectable signal. To describe the effect of thermal noise quantitatively we again consider a free cantilever. Then a random force is applied at the right side of Eq. (2.10) [69] (see Ref. [70] for an introduction). This leads to a resonance curve with a shape similar to that given in Eq. (2.16) [71]. It is customary to plot the noise power spectrum rather than the amplitude. The noise power spectrum for a cantilever described by Eq. (2.10) with a random thermal force is given by

$$\left| \frac{dZ_0^2}{d\omega} \right| = \frac{k_B T}{\pi m^*} \frac{\gamma_D}{(\omega_0^2 - \omega^2)^2 + \gamma_D^2 \omega^2}. \quad (2.18)$$

This noise power spectrum changes when the probe approaches a solid surface and interaction forces set in [72–74] just as described before for resonance curves with small deflections. The shift in resonance frequency is similar to the case of a small applied amplitude. Vice versa, from an analysis of thermal noise versus distance the force and damping coefficient can be obtained [75,76]. To increase the effective temperature and thus sensitivity Koralek et al. [77] applied an additional white noise to the cantilever.

2.2.5. Kinetic force measurements and higher vibration modes

Newton’s equation of motion can also be used in a completely different way to measure forces and to circumvent the mechanical instability [78]. The time course of the snapping-in process depends on the force acting on the cantilever. The idea is to record the deflection Z_c versus time with a high time resolution ($<1 \mu\text{s}$). Knowing $Z_c(t)$, its derivative dZ_c/dt and d^2Z_c/dt^2 can be calculated, inserted into Newton’s equation of motion and the force versus time can be evaluated [79]. By plotting the force versus distance rather than time we can get a force-versus-distance curve. To distinguish it from force curves measured in equilibrium we call it “kinetic force measurement”. The advantage of the technique is that normal AFMs and standard cantilevers can be used. Only a digital oscilloscope is required to record the cantilever deflection.

The disadvantage is that in the analysis the cantilever is treated as an ideal spring with a dashpot and a point mass. In reality the cantilever is an extended body, which can have different modes of vibration. Therefore Eppell et al. [80,81] developed an improved analysis which explicitly takes the shape of the cantilever into account. A fourth-order partial differential equation, which describes the time and shape of a rectangular cantilever, has to be solved numerically.

The same equation has to be solved to calculate the frequencies and shapes of the vibration modes for a cantilever rather than for an idealized point mass (e.g. [36,82]). The angular resonance frequencies ω_i and wavelengths λ_i of the eigenmodes for a rectangular cantilever which is clamped at one end and free at the other are given by

$$\omega_i = \alpha_i^2 \frac{t_c}{L^2} \sqrt{\frac{E}{12\rho}}, \quad (2.19)$$

and

$$\lambda_i = \frac{2\pi L}{\alpha_i}. \quad (2.20)$$

Table 1
Parameters α_i for the first 10 vibration modes of a rectangular cantilever

Mode i	α_i	$\nu_i = \omega_i/2\pi$ (kHz)	λ_i (μm)
1	1.875	18.8	670.2
2	4.694	117.6	267.7
3	7.855	329.4	160.0
4	10.996	645.4	114.3
5	14.137	1066.9	88.9
6	17.279	1593.8	72.7
7	20.420	2225.9	61.5
8	23.562	2963.6	53.3
9	26.704	3806.7	47.1
10	29.845	4754.9	42.1

Resonance frequencies and wavelengths were calculated for $t_c = 0.6 \mu\text{m}$, $L = 200 \mu\text{m}$, $w = 40 \mu\text{m}$, $E = 150 \text{ GPa}$, and $\rho = 2500 \text{ kg/m}^3$ resulting in $k_c = 0.0405 \text{ N/m}$.

Values of α_i are given in Table 1 together with resonance frequencies and wavelengths for a typical rectangular cantilever for the first 10 vibration modes. For the static case ($dZ_c/dt = 0$) this fourth-order partial differential equation simplifies to an equation like Eq. (2.6).

Fig. 5 shows schematically the first four vibration modes of a rectangular cantilever. These vibration modes could indeed be observed [83]. In liquids the frequencies of all vibration modes are much lower than in gaseous medium or vacuum [53]. For V-shaped cantilevers the theoretical treatment is more complicated. Instead of analytical expression a finite element analysis or other computer aided procedures are required [84].

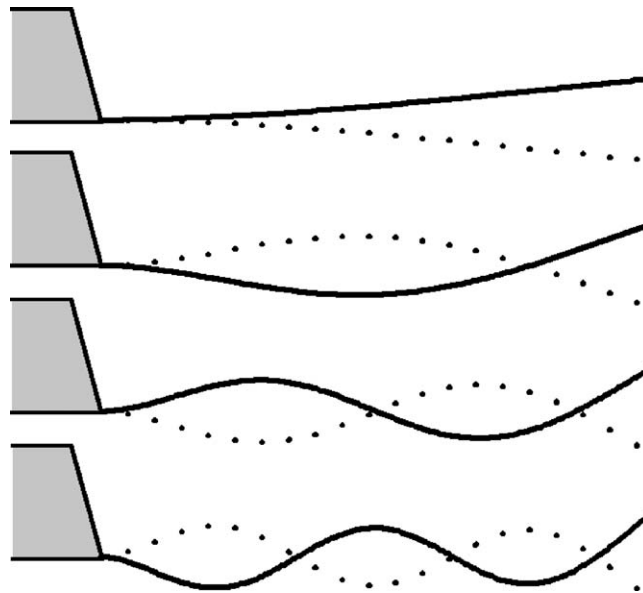


Fig. 5. First four vibration modes of rectangular cantilevers. They are scaled so that the amplitude at the end is the same.

2.3. Calibration of spring constants

As described in the previous section the spring constant can in principle be calculated from the geometry of the cantilever. The result for a rectangular cantilever was given in Eq. (2.3). For V-shaped cantilevers the spring constant can at first approximation be written in the parallel beam approximation as [38]

$$k_c = \frac{Ewt_c^3}{2L^3}. \quad (2.21)$$

This is identical to the spring constant of a rectangular beam of width $2w$ (Fig. 6). More accurate expressions have been derived [39,85]. One expression, derived by Sader [42] is often used:

$$k_c = \frac{Ewt_c^3}{2L^3} \cos \alpha \left[1 + \frac{4w^3}{t_c^3} (3 \cos \alpha - 2) \right]^{-1}. \quad (2.22)$$

Here, α is the opening angle (see Fig. 6). By comparing spring constants obtained from finite element analysis with results calculated with Eqs. (2.21) and (2.22) for typical geometries he estimated the errors to be 16% and 2%, respectively. Hazel and Tsukruk found even smaller deviations [86].

Experiments, however, showed that experimentally determined spring constants often differ significantly from calculated ones [39,87]. There are different possible reasons. First, the thickness of

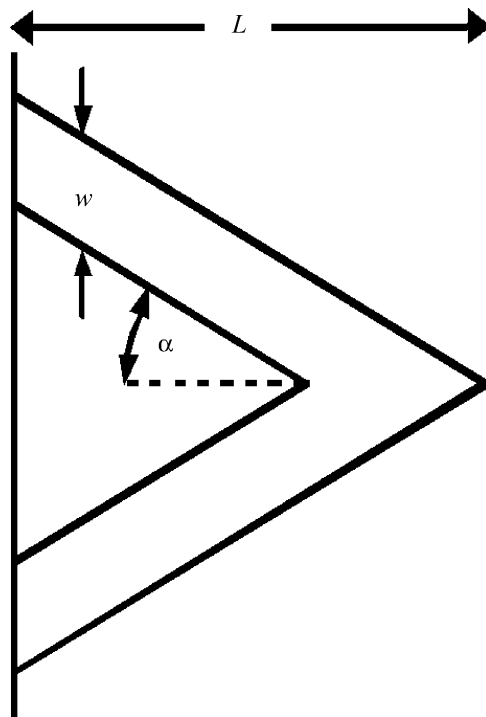


Fig. 6. Schematic top view of a V-shaped cantilever. L is the length of the cantilever, w its width, and α is the opening angle.

cantilevers is not precisely known. Cantilevers are not perfectly homogeneous and the thickness can vary. Since it enters to the third power even a slight difference in thickness leads to a significantly changed spring constant. Second, Young's modulus of a thin layer can deviate from that of the bulk material. Khan et al. [88] determined Young's modulus of 800 nm thick silicon nitride films deposited by chemical vapor deposition from the dispersion of laser-induced acoustic waves. They obtained a Young's modulus of 280 GPa (Poisson's ratio $\nu = 0.2$) rather than 146 GPa. For silicon nitride even the precise composition and, just as for silicon, the thickness of the native oxide layer is unknown. Another unknown parameter is the thickness of a gold layer evaporated onto the cantilever to increase reflectivity. It adds significantly to the mass and thus resonance frequency [86,87] and it might influence the spring constant as well. Thus, for quantitative force experiments the spring constant has to be measured. This is not a simple task. Several methods have been described but many do not appear to be simple, reliable, and precise at the same time.

A direct method is to apply a known force F to the end of the cantilever, measure the resulting deflection Z_c , and get the spring constant by $k_c = F/Z_c$. Several authors applied different kind of forces, including the gravitational force [39,89]. Maeda and Senden [90] and Notley et al. [91] apply a hydrodynamic force to the whole cantilever. Degertekin et al. [92] use acoustic radiation focused in liquid by an acoustic lense onto the cantilever. The acoustic wave causes a known force on the cantilever. Holbery et al. [93] use a commercial nanoindenter to measure spring constants of relatively stiff cantilevers. For cantilevers with spring constants above 1 N/m they report an error of less than 10%. Nanoindenters are, however, relatively expensive (similar in price as commercial AFMs) and for many force experiments the spring constant is significantly below 1 N/m. For soft cantilevers it turned out that practically it is often difficult to apply a well-defined force in the 1–10 nN range and measure the deflection accurately.

A widely used method for an absolute calibration was proposed by Cleveland et al. [94]. The idea is to attach a known mass to the end of the cantilever and measure the resulting change in resonance frequency. For a rectangular cantilever the resonance frequency can be written as

$$\nu_0 = \frac{1}{2\pi} \sqrt{\frac{k_c}{m^*}}. \quad (2.23)$$

Usually the mass of the tip can be neglected. When an extra mass M is added the resonance frequency decreases to

$$\nu'_0 = \frac{1}{2\pi} \sqrt{\frac{k_c}{m^* + M}}. \quad (2.24)$$

By measuring ν_0 and ν'_0 the spring constant can be calculated from

$$k_c = \frac{4\pi^2 M}{1/\nu'^2_0 - 1/\nu^2_0}. \quad (2.25)$$

The added mass is typically a spherical particle of gold or tungsten adhered to the end of the cantilever. The particle mass is calculated by measuring its radius by light or electron microscopy and using the bulk density of the material (19,280 kg/m³ for gold and 19,250 kg/m³ for tungsten). To adhere the particle usually no glue is necessary but the adhesion is sufficient and the method is nondestructive. Also liquid

drops deposited from a dispenser were used [95]. The liquid evaporates after few seconds which makes it a nondestructive method.

Hutter and Bechhofer [96] proposed an elegant and widely used method, which does not require the attachment of any mass and is implemented in many commercial AFMs. They suggested to measure the intensity of thermal noise. If the cantilever is modeled as a harmonic oscillator, the mean square deflection $\langle \Delta Z_c^2 \rangle$ due to thermal fluctuations is given by

$$\frac{1}{2} k_c \langle \Delta Z_c^2 \rangle = \frac{1}{2} k_B T \Rightarrow k_c = \frac{k_B T}{\langle \Delta Z_c^2 \rangle}. \quad (2.26)$$

This is obtained when integrating Eq. (2.18) over the whole frequency range and it is basically a result of the equipartition theorem. From a measurement of $\langle \Delta Z_c^2 \rangle$ one can calculate k_c .

Although at first sight this methods looks independent on the specific shape of the cantilever, it is not [82]. The reason is that the shape of the cantilever excited by thermal fluctuations is different from the shape of a cantilever with a vertical end load. As a result the relation between deflection and inclination is different. In addition, the different vibration modes have to be taken into account. Since this tends to be a bit confusing we go through the arguments one by one. For an ideal spring of spring constant k_c the mean square deflection is $\langle Z_c^2 \rangle = k_B T / k_c$. In reality we do not have an ideal spring but a rectangular cantilever. This has two consequences. First, several vibration modes are possible. Each vibration mode has an average energy of $k_B T$ leading to a deflection for each vibration mode i of [82]

$$\langle Z_i^2(L) \rangle = \frac{12 k_B T}{k_c \alpha_i^4} \quad (2.27)$$

with $\alpha_1 = 1.875$, $\alpha_2 = 4.694$, $\alpha_3 = 7.855$, etc. (see Table 1). When summing up all vibration modes the total mean square deflection of the cantilever, as given by $\langle Z_c^2 \rangle = k_B T / k_c$, is again obtained.

In practice, a force curve on a hard substrate is acquired to characterize the sensitivity and then a noise spectrum of the deflection amplitude is taken. This spectrum shows a peak at the resonance frequency, which corresponds to the first vibration mode. The first peak is fitted with a Lorentzian curve and the mean square deflection of the first peak is obtained by integration. For the first vibration mode inserting α_1 leads to

$$\langle Z_1^2(L) \rangle = \beta \frac{k_B T}{k_c} \quad (2.28)$$

with the correction factor $\beta = 0.971$.

The second important effect is that deflection is usually detected with the optical lever technique. The optical lever technique measures the inclination rather than the deflection. Deflection and inclination are still proportional but the proportionality factor is not given by Eq. (2.2) anymore. At the same deflection the inclination of the first vibration mode is lower than the inclination of a cantilever with a vertical end load. Vice versa, if the signal caused by the first vibration mode is similar to the signal of the same cantilever with a vertical end load, the deflection for the first vibration mode is higher. When calibrating the cantilever with the thermal noise method and then applying it to measure forces acting at the end we need to use

$$k_c = \beta^* \frac{k_B T}{\langle Z_1^{*2}(L) \rangle}, \quad (2.29)$$

where Z^* is the effective deflection and $\beta^* = 0.817$. The effective deflection is the deflection you read from the instrument after determining the sensitivity from the contact part of a force curve on a hard substrate (see also Section 3.1). If we use V-shaped cantilever (rather than rectangular ones) finite element analysis showed that the correction factors are $\beta = 0.965$ and $\beta^* = 0.764$ [84]. Proksch et al. point out that the precise position of the laser spot on the cantilever and its size can also influence the result of a thermal noise measurement [97]. The use of the thermal noise method has been confirmed experimentally [43,98]. For completeness we also consider the case that not only the first vibration mode but the total noise is measured. Each mode has an average energy $k_B T/2$ and each mode contributes to the mean deflection. Fortunately, the contributions strongly decrease for higher modes. As a result for rectangular cantilevers with an optical lever detection the total noise is [82] $\langle Z_c^{*2} \rangle = 4k_B T/3k_c$.

Another method is the determination of spring constants from the resonance frequency and the quality factor Q alone. Sader et al. [99] showed that from knowing the two properties and knowing the width and length of a rectangular cantilever, the spring constant can be calculated according to

$$k_c = 0.1906 \rho_f w^2 L Q \Gamma_i(Re) \omega_0^2. \quad (2.30)$$

Here, ρ_f is the density of the fluid surrounding the cantilever. Γ_i is the imaginary part of the so-called “hydrodynamic function”, which is plotted in Ref. [99]. This hydrodynamic function takes the viscosity η of the surrounding fluid into account. It depends on the Reynolds number, which in this case contains the angular resonance frequency:

$$Re = \frac{\rho_f \omega_0 w^2}{4\eta}. \quad (2.31)$$

The direct methods described so far are sometimes difficult to use, in particular if a series of force experiments with different cantilevers is done. In practice it is often more convenient to calibrate a reference cantilever accurately and then use this reference to calibrate all other cantilevers by pressing them against the reference cantilever (Fig. 7) [100]. Therefore one of the cantilevers is mounted on a piezoelectric translator. If Z_c is the deflection of the cantilever and Z_p is the height position of the piezoelectric translator (the zero is when the tip of the cantilever just touches the reference cantilever and the cantilevers are not yet deflected) then the spring constant is given by

$$k_c = k_{\text{ref}} \frac{Z_p - Z_c}{Z_c} = k_{\text{ref}} \frac{1 - Z_c/Z_p}{Z_c/Z_p}. \quad (2.32)$$

Here, k_{ref} is the spring constant of the cantilever. Practically, Z_c/Z_p is the slope of the force curve obtained on the reference cantilever in the contact regime. Different kinds of reference cantilevers have been used:

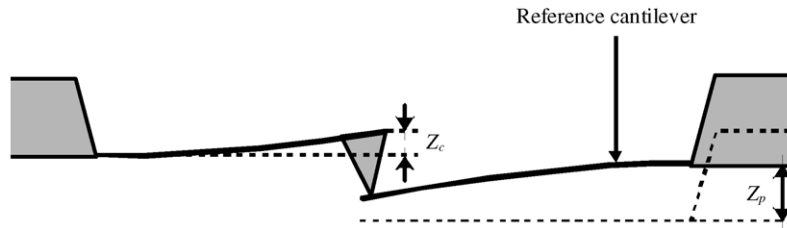


Fig. 7. The unknown spring constant of a cantilever can be determined by pressing it against a reference cantilever (on the right) and measuring its deflection Z_c for a given movement of the piezoelectric translator Z_p .

Microcantilevers, which had been calibrated with one of the direct methods, macroscopic cantilevers [101,102], where the spring constant can be calculated, or microfabricated arrays of reflective springs [103].

When analyzing force curves it is always assumed that the cantilever is oriented horizontally with respect to the sample surface. In reality this is not the case. Usually cantilevers are mounted under a certain tilt ϑ with respect to the horizontal. A tilt is necessary to ensure that the tip, and not the chip onto which the cantilever is attached, touches the sample first. In commercial AFMs the tilt angle ranges from 7° to 20° . This tilt increases the effective spring constant by typically 10–20% [104–106]. The spring constant of a rectangular cantilever of length L can be obtained by dividing the measured spring constant by $\cos^2\vartheta$. Tilt also affects hydrodynamic forces [107].

Another important issue is the precise point where the force is applied [87]. Usually it is only few μm away from the end of the cantilever. If this is not the case the effective spring constant is significantly increased because the effective length is decreased. Walters et al. [43] measured the spring constant and resonance frequencies for rectangular cantilevers of different lengths. They demonstrate that for lengths above 40–50 μm the predicted dependencies $k_c \propto L^{-3}$ and $\nu_0 \propto L^{-2}$ are indeed observed.

2.4. Tip modification and characterization

2.4.1. Modification

Early AFM experiments relied on diamond shards glued to the end of cantilevers [108]. Nowadays microfabricated tips, which is the subject of this section, or particles attached to the end of a cantilever, which will be discussed in Section 2.5, are used. Commercially available microfabricated tips are made from silicon nitride [38] or silicon [109–113]. Both materials are oxidized under ambient conditions. To tune their properties they are often modified (for reviews see Refs. [114,115]). Force measurements with modified (“functionalized”) microfabricated tips or modified colloidal probes are called “chemical force microscopy” (for reviews see [116,117]). Before discussing modification of silicon and silicon nitride tips we mention other tips, prepared by special procedures for particular purposes. One example are photopolymerized polymer tips made of an acrylate and epoxy [118].

Probably the method with the highest reliability of getting a predetermined density of specific groups is a gold-thiol coating. To coat tips with thiols they first have to be coated with a layer of gold either by evaporation or sputtering. Typically the gold layer is 30–100 nm thick. To enhance the adhesion of the gold layer to the silicon nitride or oxide first a 2–5 nm thick layer of titanium or chromium is deposited.

Thiols contain a thiol group (SH), also called “mercapto” group, at one end; their general chemical structure is R–SH or $\text{R}(\text{CH}_2)_n\text{SH}$ if they contain an alkyl chain. Not only thiols but also disulfides ($\text{R}_1\text{–S–S–R}_2$) bind spontaneously to gold and to a lesser degree silver surfaces and form close-packed monolayers [119]. Forming thiol or disulfide monolayers is practically very simple. If they are volatile they readily bind to any gold surface in a closed vessel. Usually however, thiols are dissolved in a suitable solvent like ethanol or dichloromethane at a concentration of typically 1 mM. The surface is immersed in this solution for 1–12 h and then it is rinsed to get rid of excess thiols. The binding energy to gold of approximately 120 kJ/mol is relatively strong and the layer is very stable and free of holes. Layers with defined surface properties can be made by selecting an appropriate functional chemical group which we call rest group. For many applications thiols with a long alkyl chain, $\text{HS}-(\text{CH}_2)_n\text{–R}$, are used. For chain lengths $n \geq 10$ the hydrocarbons tend to form a close-packed, highly ordered and stable layer.

Gold-thiol coatings are used frequently because the self-assembly of thiols on gold is highly reproducible and easy to handle. The density of the thiols or disulfides on the gold surface is well

determined, and as a result forces between defined chemical groups can be measured [120]. Various rest groups have been used such as carboxyl ($-\text{COOH}$) [121], hydroxyl ($-\text{OH}$) [122], methyl ($-\text{CH}_3$), acetate ($-\text{OCOCH}_3$) [123,124], amide [125], and amino [126,127]. One problem of chemically modified tips is that they might be destroyed by the interaction with another surface. Therefore the approach of the tip to the surface needs to be done carefully and force curves should be taken with controlled load. Otherwise the tip gets damaged (Fig. 8) and the analysis of force curves is erratic.

An alternative method to coat tips with defined chemical groups coating is silanization. Silanes consist of a silicon atom which can have up to three reactive groups, X_i , plus one organic rest group R. The rest group is often attached via an alkyl chain. As reactive groups hydroxyl ($-\text{OH}$), chlorine ($-\text{Cl}$), methoxy ($-\text{OCH}_3$), or ethoxy ($-\text{OCH}_2\text{CH}_3$) groups have been used. Silanes react with silanol groups (SiOH) on silicon surfaces according to $\text{SiOH} + \text{SiX}_3\text{R} \rightarrow \text{SiOSiX}_2\text{R} + \text{XH}$.

The same reaction can occur with more than one group. It is usually carried out in organic solvents or in the vapor phase. It is crucial to exclude water molecules from the solvent solution, to avoid back reactions.

On the other hand, water molecules in traces, as they appear on the hydrophilic silica surface, activate the surface as well as the silanes. This is due to the two-step process of silanization. When a silane approaches the surface the groups X will react with the water to form silanol groups, a reaction called hydrolysis. The hydrolysis determines the overall reaction speed and depends on the groups X. It decreases in the order $\text{Cl} > \text{OCH}_3 > \text{OCH}_2\text{CH}_3$. After hydrolysis the silanol condenses in a second step with the silanol groups from the silica surface.

Practically, the functionalization of silicon is carried out in several steps. First, the substrate is hydrophilized by strong acids like sulfuric acid (H_2SO_4) mixed with hydrogen peroxide (H_2O_2) to remove organic residues and/or exposure to a basic mixture of hydrogen peroxide with ammonia to remove metal ions from the silicon surface and create a high hydroxyl group density. To remove water except from surface water, the silicon substrates are washed consecutively with different organic solvents which are less and less polar. For example, we can use the sequence methanol, methanol–chloroform 1:1,

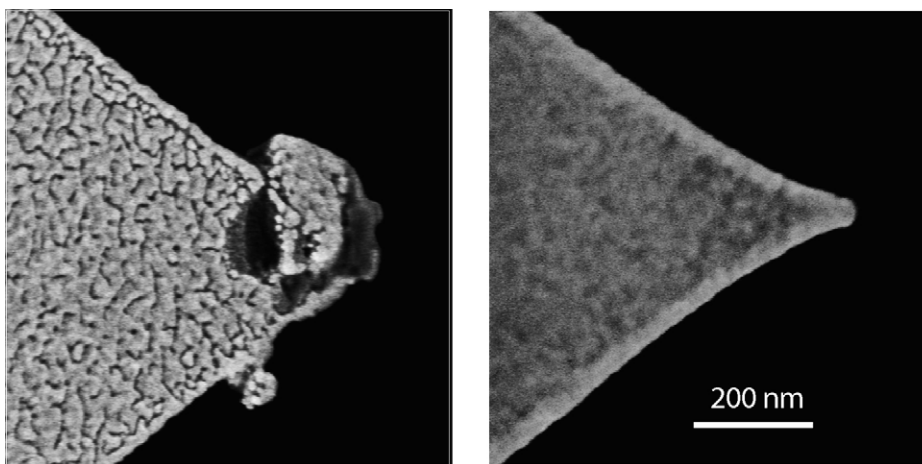


Fig. 8. SEM images of silicon nitride tips coated with a 2–3 nm thick chromium layer, a 30–40 nm thick gold layer and a monolayer of dodecanethiol. The left tip is damaged after taking many force curves with high loads while the right tip is still in good shape.

and finally just chloroform. Afterwards, the silane is dissolved in dry (dry = no dissolved water) organic solvents and the dried substrates are immersed for some hours in the silane solution. Finally, they are taken out and washed with the same solvents as before but in the opposite direction becoming more polar to remove physisorbed silanes.

For the AFM different silane coatings have been used, such as different alkyl-trichloro-silane [128–131], 3-amino-propyl-triethoxy-silane ($\text{H}_2\text{N}(\text{CH}_2)_3\text{Si}(\text{OC}_2\text{H}_5)_3$) [131–133], chloro(sulfonyl)-terminated silanes [131], and fluoroalkyl-trichloro-silanes [134]. Removing the oxide layer of silicon nitride tips with hydrofluoric acid helps in the formation of silane monolayers [135,136].

Silane coupling is also used to couple biomolecules to and graft polymers from tip surfaces. Lee et al. [137] coupled oligonucleotides via silane linkers to tips. Sano et al. [138] first linked allyl-trichloro-silane to the tip. The tip was placed in a solution containing reagents which formed a cross-linked gel of poly-((3-acrylamidopropyl)-trimethylammonium-co-(3-acrylamido)-phenylboronic acid) on the tip. To graft an ionic polymer from a silicon nitride tip Zhang et al. [139] first expose the tip to a vapor containing ethyl cyanoacrylate. Polymerization of the ethyl cyanoacrylate resulted in a thin layer firmly adhering to the tip surface. Then the tip was placed in an aqueous solution containing cationic *N,N*-dimethylaminoethyl methacrylate monomers (and NaIO_4 to remove oxygen) and irradiated by UV. Excessive homopolymer was then removed by rinsing with water.

At this point we would also like to mention an alternative method to graft polymers to tips. Jérôme et al. [140] describe a method in which gold coated tips are electrografted with poly(*N*-succinimidyl acrylate).

Plasma treatment in the presence of defined gases has become an important method to modify tips [141]. A typical plasma set-up consists of a reactor vessel, a gas inlet, a vacuum pump, and a power source. An electric field is applied at a pressure of typically 1 Pa in the presence of a certain gas. Ions and electrons are created by the electric field. For dc and low frequency glow discharge, internal electrodes are necessary. As the frequency increases the electrodes can be placed outside the reaction chamber. Reactions between gas molecules and surface species produce functional groups and cross-links at the surface. Examples include reactions induced by argon, ammonia, carbon monoxide, carbon dioxide, fluorine, hydrogen, nitrogen, nitrogen dioxide, and water. Hydrophobic tips with a low surface energy were produced by plasma treatment in hexafluoropropane [142]. One important modification is the complete oxidation of the entire tip surface. This can be accomplished by exposure to an oxygen plasma, or by UV-radiation in an oxygen-rich atmosphere. UV-radiation in oxygen also removes carbon contaminants [143]. The resulting surface will be terminated with a high density of silanol groups. Unfortunately, this surface readily adsorbs contaminants because of its relatively high surface energy. UV radiation can also be used to bind hydrocarbons or fluorocarbons to tip surfaces [144].

To make AFM tips repelling to proteins, Yam et al. [145] coated tips with oligo-(ethylene glycol). Therefore, first the oxide layer was removed by HF treatment. Then the tips were immersed in a solution containing $\text{CH}_3\text{O}(\text{CH}_2\text{CH}_2\text{O})_3(\text{CH}_2)_9\text{CH}=\text{CH}_2$.

For many experiments probes are required which have a spherical shape and radii of curvature larger than that of microfabricated tips but smaller than typical radii of microspheres. To access the range of tip radii $R = 30\text{--}2000$ nm, Hüttl “etched” commercial silicon tips by putting them in an oven at 800°C for roughly 1 h [146]. With increasing time or temperature the radii of curvature increased.

When force measurements are combined with imaging at high resolution small tips with a sharp end are required. One promising approach is to attach carbon nanotubes to the end of AFM tips (see review [147]). Single wall carbon nanotubes are particularly suited because they have a defined structure and

they are extremely stiff; their Young's modulus is ≈ 1000 GPa [148–150]. In addition they can be chemically activated at the end (e.g. [151]).

2.4.2. Characterization

For quantitative force experiments the geometry of the tip needs to be known. Several procedures have been applied to characterize size and shape of microtips. The standard procedure is to use a scanning electron microscope (SEM). For most SEMs the tip has to be conducting in order to avoid charging. Insulating materials, such as silicon nitride, are coated with a metal layer by sputtering or evaporation. Then the resolution is limited by the thickness of this layer to typically few 10 nm. Only in low-voltage SEMs charging is avoided and even insulating tips can be imaged. The resolution is typically of the order of 10 nm. Imaging tips with a SEM is useful and in many cases necessary to assess tip wear [152]. One should, however, be aware that SEMs do not provide a calibrated image in the normal direction. Therefore, only a semi-quantitative determination of the shape is possible. One should be aware that the electrons together with the almost inevitable hydrocarbon contamination in a SEM creates structures on the surfaces analyzed. Usually this effect is a nuisance. It can, however, also be used to create hydrocarbon tips.

A more quantitative method is to use a transmission electron microscope (TEM) and image the shadow of the tip [153–156]. With a high resolution TEM Chung et al. [157] even succeeded to reveal the crystalline structure of a silicon tip. An alternative which does not require an electron microscope is to image a sharp structure and reconstruct the tip shape from the image [153,158,159]. In this case one relies on a defined structure of the sharp object and the characterization itself might cause damage to the tip. Therefore, characterizing the tip size and shape for routine applications is an unsolved problem, neither the resolution is satisfactory nor are the methods non-invasive.

Tip wear is one of the major problems in force measurements. The assumption, that the surfaces of tip and sample do not change during a force experiment is probably in most cases wrong. Computer simulations showed that a transfer of atoms between the two surfaces is likely as they get into contact [160]. Chung et al. [157] could show that during the first approach significant structural changes of the tip apex can occur, even at low forces.

2.5. Colloidal probes

The colloidal probe technique was introduced in 1991. Ducker et al. [15] glued silica spheres onto cantilevers while Butt used glass spheres [16]. With smooth, spherical particles of defined radius (1) the force can be analyzed more quantitatively; (2) the total force is higher and thus the measurement can be more sensitive; (3) it is possible to make a variety of probes by attaching particles of different chemical composition to the cantilevers; and (4) hydrodynamic force measurements become possible. Two important questions are: How can spherical particles (microspheres) be produced, which have a diameter between 1 and 30 μm and a smooth surface? How can microspheres be attached to cantilevers?

Numerous ways exist to produce microspheres and many types are commercially available (e.g. Bangs Laboratories, Inc., Fishers, IN, USA; Duke Scientific Corp., Palo Alto, CA, USA; Merck KGaA, Germany; Kisker GbR, Germany; Polysciences Inc., Warrington, PA, USA; see a useful list at <http://www.magneticmicrosphere.com/supply.htm>). Often, however, these microspheres are rough on the nm scale or they are porous. The particles may be coated with a layer of physisorbed or bound molecules which helps to keep them in dispersion and to prevent aggregation. Polystyrene particles for example

often come with surfactant or with added sulfonic acid groups on the surface. This changes the surface chemistry. For this reason only few kinds of microspheres are used as colloid probes.

Most widely used are silica microspheres (e.g. [161]). Their rms roughness is typically below 1 nm over $1 \mu\text{m}^2$. They consist of amorphous SiO_2 and are commercially available (e.g. Bangs Laboratories) at different sizes, from a number of sources, and with surface modifications. Silica particles are made by a sol–gel process [162]. Due to the high melting point of silica (1723°C) it is unpractical to sinter them to cantilevers. In this respect glass particles [16,163,164], which are usually made from a borosilicate glass, are easier to sinter since their melting point is below 800°C . Their surface is as smooth as that of silica particles.

Zirconia microspheres were produced by annealing zirconia powder [165]. Spherical agglomerates of zirconia nanoparticles, made by spray drying, were also used as colloidal probes [166]. Alumina (Al_2O_3) microspheres were produced from alumina powder by melting in a hydrogen–oxygen flame [167]. They were, however, relatively rough (rms 21 nm over an area of $5 \mu\text{m} \times 5 \mu\text{m}$). Commercially available alumina particles ($\text{Ø} 10 \mu\text{m}$, Admafine AO-509, Admatechs Co., Ltd., Japan) could even be transformed from $\alpha\text{-Al}_2\text{O}_3$ to $\gamma\text{-Al}_2\text{O}_3$ by annealing at 1300°C [168]. Other important inorganic materials which have been used as colloidal probes are titanium oxide (TiO_2) [169], magnesium oxide (MgO) [170], and zinc sulfide (ZnS) [171–173]. As an example for a metal, gold microspheres were produced by an electric discharge across a gap between two gold wires in an inert atmosphere [174]. Oxidized tungsten (6.3–7.9 μm radius, Bioforce laboratory, USA) were used and analyzed by XPS and zeta potential measurements [175]. In addition to microspheres, irregular particles and single crystals of micron size also have been used as probes. Examples include hydrated calcium sulphate [176].

Polymeric microspheres made of polystyrene [177,178], poly-(methyl methacrylate) or polyethylene can be produced by dispersion polymerization (e.g. [179]) or other techniques and are commercially available. They may be coated with a layer of surfactant which can be washed off by excessive rinsing [180]. In our own experience this should be done before heating them, for example when attaching them to cantilevers; otherwise the surfactant is so strongly bound that it cannot be removed anymore. Drelich, Nalaskowski et al. produced smooth polyethylene microspheres [181] and toner particles [182] by (1) suspending a powder of the material in glycerol; (2) heating the suspension above the melting temperature of the polymer; (3) solidifying the polymer particles by cooling; and (4) filtering, washing and drying the particles. Since the method does not depend on the specific chemical nature of the polymer, it can be applied to other hydrophobic polymers as well. In contrast to many commercial polymer particles these microspheres are not cross-linked. Cellulose is another material which is commercially available from different sources and has been studied by several groups [183–186].

Different ways are used to attach microspheres to cantilevers. First these spheres were glued to cantilevers. As a glue often thermoplastics, i.e., non-cross-linked polymers which melt at a certain temperature, are used. Most long-chain linear polymer can be applied as long as they are pure and do not contain additives. For historic reasons, however, most researchers stick with the epoxy Epicote (Shell Chemical Co.) [187,393]. Frank and Belfort [188] added a solvent (a mixture of dichloromethane and dimethylsulfoxide) to lower its viscosity so that heating was not necessary and the glue hardened when the solvent evaporated. In this case it is important to wait at least 24 h or to expose the cantilever to vacuum to make sure that all solvent has evaporated. Alternatives are two component epoxy glues which cross link upon mixing [186] and low vapor pressure resign sealants used in ultrahigh vacuum technology.

Any glue can introduce contamination. In particular in organic solvents, where a certain amount of the glue might be dissolved and then adsorb to the surfaces, this is unacceptable. Therefore particles are

sometimes melted or sintered onto cantilevers. Polymer particles are placed onto the end of the cantilever and heated to close to the glass transition temperature [189]. Borosilicate glass particles were attached to tipless silicon dioxide and poly-silicon cantilevers by first dipping the free end of the cantilever into a glycerol droplet [190]. Then a particle is picked up from the glass slide. The glycerol serves to hold the particle on the cantilever by capillarity, so that when withdrawing the cantilever from the glass the particle sticks to the cantilever. Cantilevers with particles were then put in an oven and heated up to the softening point of the borosilicate glass ($\approx 780^\circ\text{C}$) for 2 h. All glycerol evaporates in this process, and a strong connection of the particle and the cantilever could be established.

2.6. Deflection detection with an optical lever

The deflection of the cantilever is usually measured using the optical lever technique [28,29] (Fig. 9). A beam from a laser diode is focused onto the end of the cantilever and the position of the reflected beam is monitored by a position sensitive detector (PSD). When a force is applied to the tip, the cantilever bends and the reflected light-beam moves through an angle equal to twice the change of the endslope $\alpha = \Delta(dZ_c/dX)$. If the detector is a distance d away from the cantilever the laser spot moves on the detector through a distance

$$\Delta_{\text{PSD}} \approx 2d \tan \alpha = \frac{FL^2 d}{EI}. \quad (2.33)$$

The deflection of the cantilever is given by

$$Z_c = \frac{FL^3}{3EI} = \frac{\Delta_{\text{PSD}} L}{3d}, \quad (2.34)$$

provided the deflection is caused by an end load. High sensitivity in Z_c is obtained by having the cantilever short compared to its distance from the detector, hence the name light-lever. The resolution of

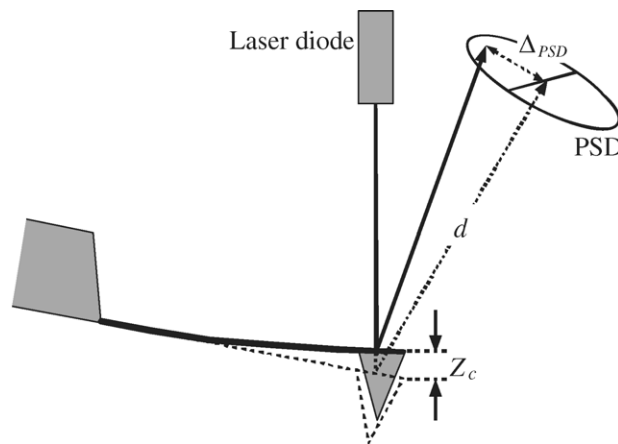


Fig. 9. Schematic of the light lever to detect cantilever deflection. The position sensitive device (PSD) is indicated as a split photodiode. Δ_{PSD} is the distance the laser spot moves on the PSD, d is the distance between the end of the cantilever and the PSD, Z_c is the cantilever deflection.

the optical lever technique is roughly $10^{-13} \text{ m}/\sqrt{t}$ [191], t being the time for measuring a pixel of the force curve in seconds. With typically $t = 0.1 \text{ ms}$ the resolution is of the order of 0.1 \AA .

The position of the reflected laser beam is usually detected by a split photodiode. Denoting the current signal from the top and bottom part of the photodiode as A and B , the signal used to measure deflection is $(A - B)/(A + B)$. At zero deflection the reflected laser beam is positioned in the center of the photodiode so that both segments show the the same current and $A - B = 0$. A deflection leads to a shift of the reflected laser spot and thus to a reduced signal on one segment and an increased signal on the other segment. This scheme is simple and very sensitive. Unfortunately its linear range is rather limited. For larger deflections the difference in the two signals is not proportional to the cantilever deflection anymore because of the distinct shape of the reflected laser beam. To increase the dynamic range the split photodiode has been replaced by a linear position sensitive device or an array detector [79,192,193].

The spot size and shape of the laser beam on the split photodiode influence the sensitivity [194]. This is illustrated in Fig. 10. A given change in the angle leads to a shift in the position of the spot by a distance Δ_{PSD} . For a small, rotational symmetric spot that leads to a significant change in the signal (Fig. 10b). For a larger spot the change in signal, which corresponds to the shaded area relative to the gray area, is lower (Fig. 10c). Also the shape of the spot influences the sensitivity. If the spot is distorted the same deflection can produce a smaller (Fig. 10d) or larger change (Fig. 10e) in relative area. This leads to a lower or higher sensitivity, respectively. One should even keep in mind that the spot shape might change when high forces change the shape of the cantilever.

For very small cantilevers the aperture of the lens in the incident laser beam path has to be adjusted to achieve an optimal signal-to-noise ratio [46]. For higher vibration modes the sensitivity for the different vibration modes is different because the light lever detection integrates over an area of the size of the spot [195]. This affects higher vibration more than the first modes.

In some cases interference can cause a distortion of force curves, which is visible as a periodic signal in the non-contact regime. Light reflected from the back of the cantilever and light being reflected from the sample interfere and give an additional signal at the PSD. In particular for highly reflective samples this effect can severely affect force curves. The periodicity of the distortion is of the order of half the wavelength of the laser [196]. It can be avoided by using less coherent laser light. Infrared laser diodes for example are less coherent than diodes working with visible light. Sometimes realigning the laser so that more light is reflected from the cantilever rather than from the sample helps.

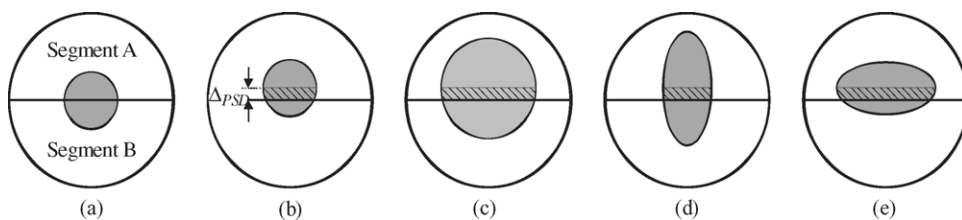


Fig. 10. The effect of laser spot shape on optical lever sensitivity. (a) A centered spot leads to zero deflection signal $(A - B)/(A + B)$. (b) A well-shaped rotational symmetric and small spot produces a large relative area change between the A and B photodiode segments for a given deflection. This corresponds to a high sensitivity. For large deflections, however, the linear regime is small. If the spot is large (c) or distorted (d) the same deflection can produce a smaller change in relative area, hence a lower sensitivity. Also an increased sensitivity for distorted spots is possible (e).

3. Analysis of force curves

3.1. Conversion of force curves and the problem of zero distance

The direct result of a force measurement is a measure of the photodiode current I_{PSD} versus height position of the piezoelectric translator Z_p . To obtain a force-versus-distance curve, I_{PSD} and Z_p have to be converted into force and distance (see also [197]). Therefore two parameters need to be known: the sensitivity and the zero distance. In atomic force microscopy both parameters must be inferred from the force curve itself and not through an independent method. Practically, the linear part of the “contact regime” is assumed to be zero distance and its slope is the sensitivity. In most applications this is correct and poses no significant problem. In some cases, however, this method may cause a false interpretation. This is particularly the case for highly deformable surfaces or if layered structures cause strong repulsive forces (see Section 8). In the following we discuss how to determine sensitivity and zero distance for different types of force curves. We start with simple “ideal” types and proceed to more complicated “real” force curves.

- *Infinitely hard materials, no surface forces.* If no long-range forces are acting and tip and sample are infinitely hard, then the recorded PSD-versus-piezo displacement signal curve consists of two linear parts: The non-contact zero force line and the linearly increasing contact regime (Fig. 11a). The non-contact zero force line defines zero deflection of the cantilever. From the linearly increasing contact part the sensitivity $\Delta I_{\text{PSD}}/\Delta Z_p$ is obtained; it is the slope of the contact part of the force curve. The PSD signal can be converted into a deflection by dividing the PSD signal by the sensitivity, which leads to $Z_c = I_{\text{PSD}}/(\Delta I_{\text{PSD}}/\Delta Z_p)$. Knowing the spring constant of the cantilever the PSD signal can easily be converted into a force: $F = k_c Z_c$. The true distance between the tip and sample is the piezo deflection plus cantilever deflection, $D = Z_p + Z_c$. Here, Z_p is defined as zero at the point where the two linear parts of the force curve cross. We count Z_p positive if it is retracted away from the tip (downward). Then, in the non-contact part of the force curve $D = Z_p$ because in the absence of a force $Z_c = 0$. In the contact part $Z_p = -Z_c$ and $D = 0$.
- *Infinitely hard materials with surface force.* Now we introduce a force between tip and sample. As an example a long-range exponentially decaying repulsive force is considered (Fig. 11b). Contact and non-contact part of the force curve are easily distinguishable. The sensitivity is obtained from the linear contact part and not the exponentially decaying part of the force curve. Zero deflection is determined from the non-contact part at large distance. That is at a distance where surface forces are negligible. Then force curves can be converted as before. The contact point, that is $Z_p \equiv 0$, is now extrapolated from the two linear regimes. In order to do so accurately it is necessary to record force curves from a large distance and also apply a relatively hard force. The degree of extrapolation determines the error in zero distance. The weaker and shorter ranged the repulsive force is and the larger the two linear regimes of the force curves are the more accurate zero distance can be defined. In the non-contact part of the force curve $D = Z_p + Z_c = Z_p + F/k_c$. In the contact part we again have $Z_p = -Z_c$ and $D = 0$.
- *Deformable materials without surface forces.* In reality all solid materials deform and are not infinitely rigid (for details see Section 4). We first ignore surface forces. As a result the non-contact part of the force curve is described by $D = Z_p$ because $Z_c = 0$. More difficult is the description of the contact part. If tip and/or sample deform the contact part of the force curve is in general not linear anymore

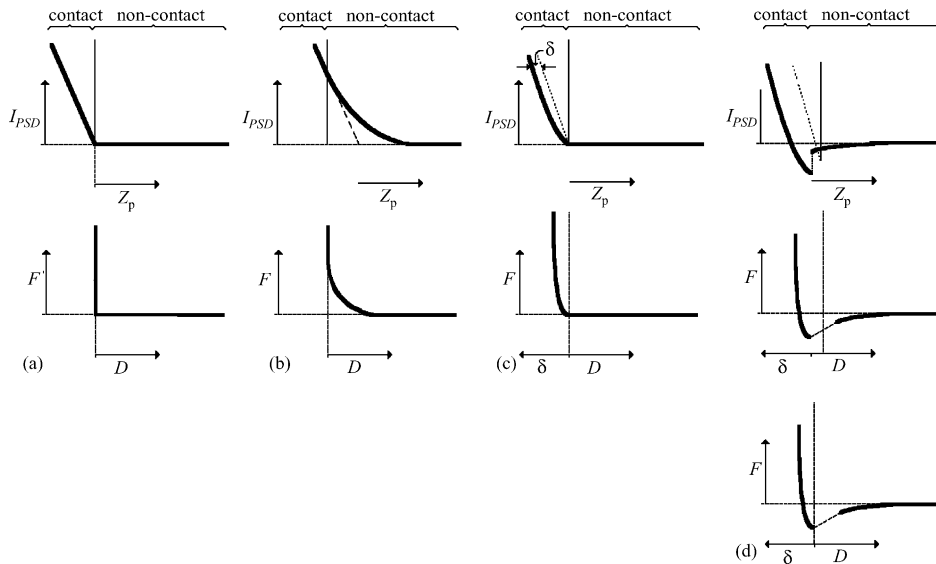


Fig. 11. indicates how the I_{PSD} -vs.- Z_p curves (position sensitive detector current signal vs. piezo position) are converted to force-vs.-distance (F -vs.- D) curves, where D is given by the sum of the cantilever deflection Z_c and the piezo position Z_p . (a) Infinitely hard tip and sample without surface forces. (b) Infinitely hard materials but with a long-range repulsion. (c) Deformable materials without surface forces. In this case we suggest to interpret the negative distance axis as indentation δ . (d) Deformable materials with attraction and adhesion force. The additional bottom figure shows the usual misinterpretation, in which zero distance is placed to the end of the jump-in. For (a) and (b) approaching and retracting parts of force curves are identical. For (c) approaching and retracting parts are identical if the deformation is elastic. For (d) the retraction shows an adhesion force.

(Fig. 11c). For the case of a perfectly elastic tip with a spherical end and a planar sample made of the same material this is described by the Hertz model and given by $F = \delta^{3/2} 2E\sqrt{R}/3(1 - \nu^2)$ (see Section 4.2). Here, δ is the indentation, E the Young's modulus, R the radius of the tip, and ν is the Poisson's ratio. Practically, for many inorganic solids such as silicon wafers or glass and not extremely high spring constants the indentation is small ($\delta \ll Z_c$). Then, for relatively high loads an additional change in the load ΔF leads to an almost corresponding change in cantilever deflection, $\Delta Z_c \approx \Delta F/k_c$ ($\Rightarrow \Delta\delta \ll \Delta Z_c$) and the sensitivity can be determined as before. If this is not the case and the change in indentation is not negligible the specific force curves have to be discussed and an appropriate model to describe indentation has to be found. Such "soft" samples include for example cells, bubbles, drops, or microcapsules. They are discussed in Section 9.

For deformable materials "zero distance" becomes a matter of definition. Obviously, in contact the distance is zero – or to be more precise – it equals an interatomic distance. This, however, does not describe the situation adequately. Indentation and contact area are still changing with the load. For this reason it is more appropriate to use indentation rather than distance once contact has established. As a result, the abscissa would show two parameters: "Distance" before contact and "indentation" once contact has been established.

- *Deformable materials with surface forces.* For deformable surfaces the presence of surface forces can be a problem if they lead to a significant deformation even before contact is established. This is certainly the case for very soft materials. Even for relatively hard materials, attractive forces and adhesion can cause an error and it is practically often difficult to precisely determine where contact is

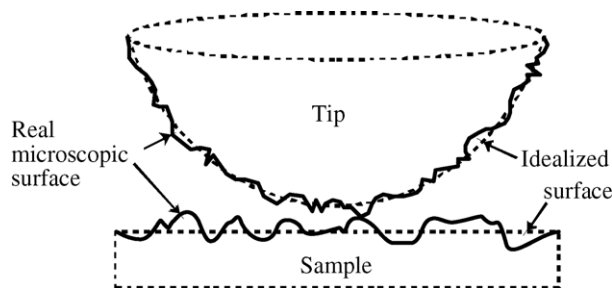


Fig. 12. Effect of roughness on the determination of contact.

established. When the tip approaches a solid surface and it is attracted by for example van der Waals forces at some distance the gradient of the attraction might exceed the spring constant and the tip jumps onto the surface. Immediately after being in contact, adhesion forces set in, draw the tip even more into contact. Adhesion forces add to the spring force and can cause an indentation (Fig. 11d). The total jump distance is therefore the sum of the initial jump due to the instability caused by strong attractive surface forces plus the indentation due to adhesion and the deformability of tip and sample material [198]. In this case it is practically impossible to determine zero distance and one can only assume that the indentation caused by adhesion is negligible.

In summary: For deformable surfaces the uncertainty in a determination of zero distance is proportional to the indentation. In addition, the parameter “distance” is only useful before contact is established. Once tip and sample are in contact other parameters such as the indentation are more appropriate.

Roughness of the sample or tip surface is another problem for interpreting force curves. For rough surfaces of hard materials the first contact of any asperity determines zero distance. This can lead to an erroneous interpretation if contact is taken to be the distance between the average surfaces (Fig. 12). We know of no simple solution to this problem. To be able to estimate the extent of this uncertainty we recommend reporting the roughness, if possible as a peak-to-peak distance over a representative area. The rms, defined as the root mean square deviation of the actual surface from the average surface, is helpful but may in many cases also be misleading. It is helpful because it describes the roughness in a quantitative way. It can be misleading because similar rms values can lead to a different peak-to-peak roughness and thus to different zero distances. In any case, the area over which the roughness was determined should be reported.

One approach to determine the distance from contact independently was developed by Huntington et al. [199] and Ducker et al. [200]. On a transparent sample an evanescent field is formed by the total internal reflection of a laser beam at the sample surface. This field decays roughly exponentially with distance from the surface. When the colloidal probe enters this field light is scattered. Ducker et al. measure the intensity of the scattered light with an inverted light microscope onto which the AFM is mounted. The intensity of the scattered light serves as an independent signal. Huntington et al. use a SNOM probe to detect the evanescent light.

How important is the determination of zero distance? That depends on the specific question tackled by a force measurement. If one is only interested in the aggregation behavior the absolute zero is not important. Particles of the material investigated would disperse or aggregate depending on repulsion or attraction irrespective of the absolute zero. If it comes to a comparison with molecular models or if

quantities like conductivity of aggregates are relevant, then it is important to know whether the surfaces are in real contact or not.

3.2. Difference between approach and retraction

Approaching and retracting parts of force curves are often not identical. This can have various reasons (Fig. 13) In liquids hydrodynamic drag on the cantilever is one of the reasons [201]. It causes a difference in the zero-force line (region A in Fig. 13). This hysteresis is proportional to the approaching/retracting velocity v_0 and it can be prevented by reducing v_0 . If for some reason the velocity cannot be reduced the constant hydrodynamic drag has to be subtracted. This has to be done for approach and retraction separately (for details see Section 10).

Implicit in the measurement of a surface force with a “spring force” is the assumption that the two are equal and opposite and thus the spring is not in motion, or, in other words, that the system “surface + cantilever” is in equilibrium at every distance. However, close above the surface, the change of the spring elastic force with the distance often cannot counterbalance the corresponding change of attractive surface forces, equilibrium is lost and the tip jumps onto the sample surface. The onset of this unstable regime (“jump-in”) is characterized by the point where the gradient of the attractive force exceeds the spring constant [202]. To explain this important condition we use the fact that in equilibrium a system must be insensitive to small changes in the position coordinates. Let us assume the tip moves a tiny distance towards the surface, for example due to a thermal fluctuation. Then the separation D decreases and the deflection increases: $dD = -dZ_c$. This leads to a change of the total force of

$$dF = k_c dZ_c + \frac{dF_{\text{surf}}}{dD} dD = \left(k_c - \frac{dF_{\text{surf}}}{dD} \right) dZ_c, \quad (3.1)$$

where F_{surf} is the distance-dependent surface force. The attractive surface force has a negative sign. Its amount decreases with distance. Thus, the gradient of the attractive surface force is positive: $dF_{\text{surf}}/$

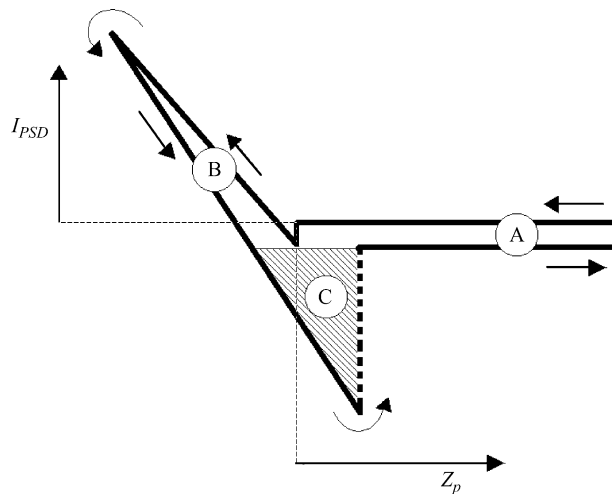


Fig. 13. Schematic position sensitive detector current signal (I_{PSD}) vs. piezo position (Z_p) curve including approaching and retracting parts. Three types of hysteresis can occur: In the zero force line (A), in the contact part (B) and adhesion (C).

$dD > 0$. If the spring constant is higher than the gradient of the attractive force ($k_c > dF_{\text{surf}}/dD$) the total force F increases after a small, virtual movement of the tip. This leads to a restoring positive force, which drives the tip back to its previous position. For $dF_{\text{surf}}/dD > k_c$ the net force is negative, the tip is driven further towards the surface and eventually jumps-in.

To prevent a jump-in contact one can use stiffer cantilevers. Then, however, sensitivity is lost. Therefore, alternative techniques have been employed to access the unstable regime:

- The best but technically most demanding is the application of a force feedback (electric or magnetic) to balance the surface force [203–209]. This also led to the development of devices constructed for force experiments such as the interfacial-force microscope [210,211].
- Kinetic force experiments, that is, measurement of the time-dependent force and displacement in the unstable regime, then calculation of the velocity and acceleration to yield the surface force according to Newton's equation of motion [79,212] (see Section 2.2 for details).
- In liquids and when using a microsphere rather than a microfabricated tip the hydrodynamic drag can be used to compensate for the attraction [201]. For a sphere approaching a flat surface with a velocity v the hydrodynamic force increases with decreasing distance as $F_H = 6\pi\eta vR^2/D$, where η is the viscosity of the liquid (see Section 10 for details) [78].
- One possibility to determine force curves even in the strong attractive regime is to use a dynamic mode with a large vibration amplitude [55,213] (see Section 2.2). In large amplitude dynamic AFM the jump-to-contact is avoided by using stiff cantilevers.

Another instability occurs when tip or sample surface are not perfectly rigid but are deformed by the tip. For that case of elastic deformation Pethica and Sutton showed that at sufficiently small separations, typically 1–2 Å, the tip and the sample will jump together, irrespective of apparatus construction [198]. A similar jump occurs for non-elastic deformations. In this case, however, the jump depends on the rate of the plastic deformation [214].

In the contact regime a difference between the approaching and retracting part is usually caused by plastic or viscoelastic deformation of the sample. An elastic deformation should not lead to a hysteresis. Hoh and Engel pointed out that friction can lead to a hysteresis in the contact part of the force curve [215]. When the tip gets into contact with the sample and the piezoelectric translator keeps approaching, the tip has to slide over the sample surface. The reason is the tilt in the cantilever. The cantilever is not oriented horizontally but it is slightly tilted to ensure that the tip and not another part of the chip is touching the sample first. Typically this tilt is 7–20°. While the cantilever bends upwards, it is bowed forward by the friction. This creates an offset in the contact line (region B in Fig. 13). Practically, however, this effect seems to be rare and not so important in most experiments.

When retracting the tip adhesion often keeps it in contact with the surface until the cantilever force overcomes the pull-off force (also called adhesion force) F_{ad} . This even happens in purely elastic, non-dissipative situations. The energy which has to be overcome is the energy required to bend the cantilever until it reaches F_{ad} . In absence of sample deformations it is given by

$$W_{\text{ad}} = \frac{F_{\text{ad}}^2}{2k_c}, \quad (3.2)$$

and it is equal to the shaded area C in Fig. 13.

3.3. Derjaguin approximation

The force between two surfaces depends on both the material properties and the geometry of the surfaces. Derjaguin [216] approximated the influence of arbitrary geometry on the interaction potential $U(D)$ by reducing it to the simple geometry of two flat surfaces. The Derjaguin approximation relates the energy per unit area between two planar surfaces U_A which are separated by a gap of width x to the energy between two bodies of arbitrary shape U which are at a distance D :

$$U(D) = \int U_A(x) dA. \quad (3.3)$$

Here, dA is the variation of the cross-sectional area of the two real surfaces with increasing separation distance (Fig. 14). The integration runs over the whole cross-sectional area. For forces the analogous expression is

$$F(D) = \int f(x) dA, \quad (3.4)$$

where F is the force between two bodies of arbitrary shape and f is the force per unit area between two flat surfaces.

In colloidal probe experiments the geometry is a sphere approaching a flat planar surface. Also the end of a microfabricated tip is approximately spherical with a radius of curvature R . Then $dA = 2\pi r dr$ and the radial coordinate r and the height are related by

$$x = D + R - \sqrt{R^2 - r^2} \Rightarrow r dr = dx \sqrt{R^2 - r^2}. \quad (3.5)$$

If the range of the interaction is much smaller than R we only need to consider contributions with r much smaller than R and $r dr = R dx$. This is precisely valid if the tip has a parabolic shape with radius of curvature R . A parabolic tip shape is described by $x = D + r^2/2R$. Inserting leads to

$$U(D) = 2\pi R \int_D^\infty U_A(x) dx. \quad (3.6)$$

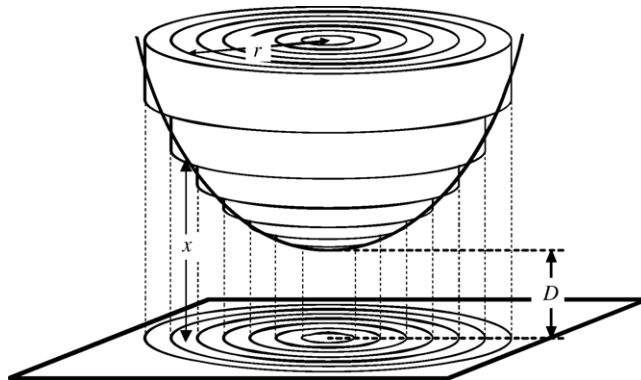


Fig. 14. Schematic illustration of the so-called Derjaguin's approximation. x is the distance between the planar surfaces, D is the distance between the two considered bodies, i.e., between the apex of the tip and planar surface, and r is the radial coordinate.

According to Eq. (3.3) the fundamental property of the material is the interaction energy U_A , per unit area. The most useful measurement is one between two surfaces of known geometry so that U_A (or f) can be determined and thus the interaction energy of all geometries can be calculated.

A useful equation is derived considering that for conservative interactions $F = -dU/dD$ and $f = -dU/dx$. This leads to

$$U_A = \frac{F}{2\pi R}. \quad (3.7)$$

From this relationship it can also be seen that a larger radius results in a higher force, and thus greater sensitivity in U_A . Naturally, this increase in U_A sensitivity comes at the expense of reduced lateral resolution.

It is important to keep in mind that Derjaguin's approximation is valid only if the range of the interactions is much smaller than R . Since in atomic force microscopy the tip radius can be small this condition is not necessarily fulfilled. Indeed, Todd and Eppell [217] found deviations when studying the electrostatic double-layer force and choosing the decay length of the exponentially decaying force 10 nm or larger.

3.4. Electrostatic force

A measurement of electrostatic forces is of a wide interest for a better understanding of electrostatic force microscopy or Kelvin probe microscopy, and also for understanding charging mechanisms per se. For this reason a number of experiments and theoretical approaches are described in the literature. Relatively well understood is the interaction between a metallic tip and a metallic sample. For good conductors the electric potential is the same everywhere and identical to the applied potential. In a calculation that implies that the field lines are oriented perpendicular to the surfaces. A calculation of the electrostatic force is straightforward. The energy is given by $CV^2/2$, where C is the capacitance of tip and sample and V is the applied voltage. The force is the derivative of the electrostatic energy, which for perfectly conducting materials, is given by

$$F = -\frac{1}{2} \frac{dC}{dD} V^2. \quad (3.8)$$

The problem is a precise calculation of the capacitance. Analytical solutions exist. They are, however, all approximations which are only valid in a limited range. The most general approximation is that for a conical tip of half opening angle Θ with a spherical apex of radius R (Fig. 15) given by Hudlet et al. [218]. It was extended by Law and Rieutord [219] to take also the cantilever into account. The cantilever was assumed to be rectangular inclined at an angle ϑ . The electrostatic force is

$$F = \pi\epsilon_0 V^2 g(D). \quad (3.9)$$

The geometrical factor, given by the function $g(D)$, is a sum of three contributions [220], that of the spherical apex of the tip, that of the conical part, and that of the cantilever:

$$g = g_{\text{cone}} + g_{\text{apex}} + g_{\text{cant}}, \quad (3.10a)$$

$$g_{\text{cone}}(D) = \frac{1}{\ln^2(\tan(\Theta/2))} \left[\ln\left(\frac{H}{D + R(1 - \sin \Theta)}\right) - 1 + \frac{R(\cos^2 \Theta / \sin \Theta)}{D + R(1 - \sin \Theta)} \right], \quad (3.10b)$$

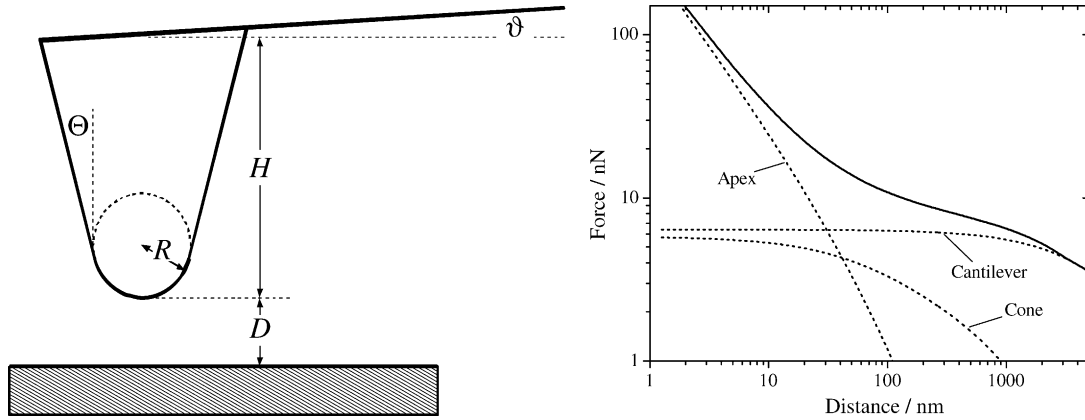


Fig. 15. Left: conical tip with a spherical apex and a rectangular cantilever as used to calculate the electrostatic force in the right part of the figure. Θ is the opening angle, R the apex radius, H the height of the tip, and D the tip–sample distance. Right: force vs. distance curve for an applied potential of 10 V is shown. $\Theta = 15^\circ$, $R = 100$ nm, and $H = 8$ μm . The tip is mounted on a cantilever with length $L = 200$ μm and width $w = 25$ μm , having a tilt $\vartheta = 15^\circ$ with the horizontal surface. In addition to the total electrostatic force the individual contributions of apex, conical part and the cantilever are shown.

$$g_{\text{apex}}(D) = \frac{R^2(1 - \sin \Theta)}{D[D + R(1 - \sin \Theta)]}, \quad (3.10c)$$

$$g_{\text{cant}}(D) = \frac{1}{2\pi} \frac{Lw}{(D + H)^2} \frac{1}{(1 + (L/(D + H)) \tan \vartheta)}, \quad (3.10d)$$

Here, H is the height of the tip, Θ the opening angle and ϑ is the tilt of the cantilever. To calculate the force a small opening angle ($\Theta \leq 20^\circ$) and a small distance ($H \gg D$) was assumed.

It is obvious from Fig. 15 that the different parts contribute in a different way, that is with a different distance dependency. The contribution of the apex dominates at short distances, the conical part is relevant for the intermediate range and at very large distances the cantilever influences the electrostatic force. The validity of the above expression has been confirmed by several experiments (e.g. [221,222]).

The above equation can be regarded as the culmination of a long struggle to quantify electrostatic forces. The first expressions were for a sphere and a flat surface. For large distance the approximation $F = \pi\epsilon_0 R^2 V^2 / D^2$ was used, for small distances the force can be approximated by [13] $F = \pi\epsilon_0 R V^2 / D$. Both are derived from a more general but more inconvenient equation [36,223]. A useful approximation for all distances is

$$F = \pi\epsilon_0 \frac{R^2 V^2}{D(D + R)}. \quad (3.11)$$

This is also derived from the equation above assuming that $\Theta = 0$. Hao et al. [221] derived an equation for a conical tip of small opening angle. It is not identical to the equation of Hudlet et al. [218] but the difference is small. Both use a uniformly charged line model and find a logarithmic distance dependency, which is confirmed by Yokoyama et al. [224]. Also procedures to calculate the electrostatic force between metals precisely but numerically are described [225,226]. The contribution of the cantilever as a correction in particular at large distances was realized and described by several authors [227,228]. The effect of surface roughness was considered by Boyer et al. [229].

The description of non-metallic surfaces is more difficult because the simple boundary condition of constant potential is not valid anymore and no simple analytical expressions can be derived to describe the interaction between insulating tips and samples [230,231]. Two cases have attracted special attention: The interaction between metallic tips and semiconductors [232,233] and the interaction between two metals, one being covered with an insulating layer [234]. The latter case is important for polarization force microscopy [234]. It turns out that the main effect of an insulating layer on a metal is to reduce the electric field in the gap between tip and sample and thus reduce the electrostatic force [235].

4. The contact regime

4.1. Overview

From the contact lines of force–displacement curves it is possible to draw information about the elastic–plastic behavior of materials. In fact, the first force curves taken with the AFM were aimed at analyzing the nanomechanical properties of solid surfaces. Meyer et al. [108] measured force curves between diamond shards and LiF and HOPG. Mate et al. [236] measured the force-versus-distance between a Pt–Rh wire, which was bent like a cantilever and whose deflection was detected via optical interference, and graphite. Burnham and Colton analyzed the elastic properties of HOPG and gold [237]. Mate et al. [238] use the same set-up to study the thickness of liquid polymeric films [239,240]. Moiseev et al. [241] measure forces with an STM-detection AFM between an Al_2O_3 tip and an Al_2O_3 surface. Also the first theoretical analysis of force curves is concerned with the elastic properties of the interacting surfaces [242]. This already reflects the importance of understanding the contact regime of force curves. Still today, the analysis of nanomechanical properties is a very active field of research.

Let us first consider an ideally elastic material. As described in Section 3 the tip deforms the sample by a depth δ . Loading and unloading curves, i.e., the approach and withdrawal contact lines, overlap. If the sample is plastically deformed, the sample undergoes a deformation during the loading curve, and, when the tip is withdrawn, it does not regain its own shape as the load decreases, whereas the penetration depth remains the same. Most samples have a mixed behavior. Hence loading and unloading curves seldom overlap. In particular, at a given penetration depth, the force of the unloading curve is lesser than the force of the loading curve. The difference between the approach and the retraction contact lines is called “loading–unloading hysteresis”. In the following we neglect plastic deformations and review theories dealing with elastic continuum contact mechanics, in which the tip and sample are assumed to be continuous elastic media.

4.2. Theory: Hertz, JKR, DMT and beyond

In the contact part of force curves, both in the approach and in the retraction phase, the elastic deformation of the sample can be related to its Young’s modulus. In order to relate the measured quantities to Young’s modulus, it is necessary to consider the deformation of the sample δ . For elastic deformation it is useful to describe the system by means of a potential energy U :

$$U = U_{cs}(D) + U_c(Z_c) + U_s(\delta) = U_{cs}(D) + \frac{1}{2}k_c Z_c^2 + \frac{1}{2}k_s \delta^2. \quad (4.1)$$

Here, U_{cs} is the tip–sample interaction potential caused by surface forces, U_c the energy due to bending of the cantilever, U_s the elastic deformation energy of the sample, and k_s is the so-called sample stiffness. In general, we can write:

$$D = Z_p + Z_c + \delta. \quad (4.2)$$

In contact $D = 0$ and, if the system is in equilibrium, also $k_s \delta = k_c Z_c$. Substituting, we obtain

$$k_c Z_c = -\frac{k_c k_s}{k_c + k_s} Z_p = k_{\text{eff}} Z_p. \quad (4.3)$$

This simple relation shows that the slope of the force–displacement curve is a measure of the stiffness of the sample. If the sample is much stiffer than the cantilever, that is for $k_s \gg k_c$, then $k_{\text{eff}} \approx k_c$, whereas $k_{\text{eff}} \approx k_s$ when $k_s \ll k_c$, i.e., when the sample is much more compliant than the cantilever. This gives also a rule of thumb for the choice of the cantilever spring constant in experiments dealing with the elastic properties of the sample: If the cantilever spring constant is much lower than the sample spring constant, the force curve will probe primarily the stiffness of the cantilever, and not that of the sample.

The stiffness of the sample is related to its Young's modulus by

$$k_s = \frac{3}{2} a E_{\text{tot}} \quad \text{with} \quad \frac{1}{E_{\text{tot}}} = \frac{3}{4} \left(\frac{1 - \nu_s^2}{E_s} + \frac{1 - \nu_t^2}{E_t} \right). \quad (4.4)$$

Here, ν_t , E_t , ν_s and E_s are the Poisson's ratio and the Young's moduli of tip and sample, respectively, E_{tot} the reduced Young's modulus, and a is the tip–sample contact radius. Young's modulus of silicon nitride is typically 160–290 GPa, the Poisson's ratio is 0.20–0.27, depending on conditions and precise content of silicon and nitrogen (e.g. [43,86,88,243]). For silicon the values are $E = 130$ – 185 GPa and $\nu = 0.26$ – 0.28 , depending on crystallographic orientation (e.g. [244]). Silicon oxide (fused quartz) has a Young's modulus of 72 GPa and a Poisson's ratio of 0.17; all values at room temperature.

In many cases the tip is much stiffer than the sample. If we neglect the deformation of the tip Eq. (4.4) can be approximated by

$$k_s = 2a \left(\frac{E_s}{1 - \nu_s^2} \right). \quad (4.5)$$

Several theories describe the elastic deformation of the sample. Differences in the relations between the applied load F and the contact radius a or the deformation δ are due to the role played by the adhesion in the considered system. Table 2 summarizes the relations between contact radius, the deformation of the sample, and the adhesion force for a spherical tip on a plane surface according to the three most used theories. These theories have been developed by Hertz [245], Johnson–Kendall–Roberts (JKR) [246], and Derjaguin–Müller–Toporov (DMT) [247–249].

In the Hertz model the adhesion of the sample is neglected, whereas the two other theories take account of it outside (DMT) or inside (JKR) the contact area. Hence, Hertz theory can only be applied when the adhesion force is much smaller than the maximum load. In the two other theories, the work of adhesion W can be calculated from the jump-off-contact, if the tip radius R is known. Then it is possible to calculate a as a function of the reduced Young's modulus E_{tot} and finally to obtain E_{tot} as a function of δ , measured from the contact line. The JKR theory can be applied in the case of large tips and soft samples with a large adhesion, the DMT theory in the case of small tips and stiff samples with a small adhesion. Both theories are only approximations.

Table 2

Relation between the contact radius a , the sample deformation δ , and the adhesion force F_{ad} for a spherical tip on a flat surface according to the Hertz, JKR, and DMT theories

	Hertz	DMT	JKR
a	$\sqrt[3]{\frac{RF}{E_{\text{tot}}}}$	$\sqrt[3]{\frac{R}{E_{\text{tot}}}(F + 2\pi RW)}$	$\sqrt[3]{\frac{R}{E_{\text{tot}}}\left(F + 3\pi RW + \sqrt{6\pi RWF + (3\pi RW)^2}\right)}$
δ	$\frac{a^2}{R} = \left(\frac{F^2}{RE_{\text{tot}}^2}\right)^{1/3}$	$\frac{a^2}{R} = \frac{(F + 2\pi RW)^{2/3}}{\sqrt[3]{RE_{\text{tot}}^2}}$	$\frac{a^2}{R} = \frac{2}{3} \sqrt{\frac{6\pi Wa}{E_{\text{tot}}}}$
F_{ad}	0	$2\pi RW$	$\frac{3\pi RW}{2}$

R is the tip radius and W is the adhesion work per unit area. Often the work of adhesion is replaced by twice the surface energy of the solid. R is the radius of the spherical tip, F is the force exerted by the tip on the surface, and E_{tot} is the reduced Young's modulus defined in Eq. (4.4).

At this point it is instructive to consider a typical example. For a silicon nitride tip with $R = 30$ nm, $E = 200$ GPa, $\nu = 0.3$ on silicon nitride we have $E_{\text{tot}} = 147$ GPa. At a load of 1 nN this leads to an indentation of 0.012 nm and a contact radius of 0.59 nm. The mean pressure underneath the tip is thus $P = F/\pi a^2 = 0.9$ GPa or almost 10 kbar.

Maugis [250] has shown that the JKR and DMT models are limits of the same theory, describing the elastic deformations of all samples as a function of the parameter

$$\lambda = \frac{2.06}{D_0} \sqrt[3]{\frac{RW^2}{\pi E_{\text{tot}}^2}}, \quad (4.6)$$

where D_0 is a typical atomic dimension. In the Maugis theory, the deformation and the contact radius are given by a set of parametric equations:

$$\bar{\delta} = \bar{A}^2 - \frac{4}{3} \lambda \bar{A} \sqrt{m_M^2 - 1}, \quad \bar{F} = \bar{A}^3 - \lambda \bar{A}^2 \left(\sqrt{m_M^2 - 1} + m_M^2 \arctan \sqrt{m_M^2 - 1} \right) \quad (4.7a)$$

with

$$\bar{A} = \frac{a}{\sqrt[3]{\pi WR^2/E_{\text{tot}}}}, \quad \bar{F} = \frac{F}{\pi WR}, \quad \bar{\delta} = \frac{\delta}{\sqrt[3]{\pi^2 W^2 R/E_{\text{tot}}^2}}, \quad (4.7b)$$

and

$$\frac{\lambda \bar{A}^2}{2} \left[\sqrt{m_M^2 - 1} + (m_M^2 - 2) \arctan \sqrt{m_M^2 - 1} \right] + \frac{4\lambda^2 \bar{A}^2}{3} \left(1 - m_M + \sqrt{m_M^2 - 1} \arctan \sqrt{m_M^2 - 1} \right) = 1. \quad (4.7c)$$

Here, m_M is the ratio between the contact radius a and an annular region, where the adhesion is taken into account. Eqs. (4.7) reduce to the respective expressions in Table 2 for $\lambda \rightarrow \infty$ (JKR) and for $\lambda \rightarrow 0$ (DMT).

The Maugis theory, experimentally verified by Lantz et al. [251], shows that an exact determination of the Young's modulus E and of the work of adhesion W only from force–distance curves is impossible, because the slope of the contact line and the jump-off-contact depend on each other in a way described by the parameter λ , but in order to calculate λ both E and W must be known.

All equations given till now are valid for spherical tips. Sneddon [252] has shown that for any punch that can be described as a solid of revolution of a smooth function the load–displacement relationship can be written in the form

$$F = \alpha \delta^n, \quad (4.8)$$

where α and n are constants ($n = 1$ for flat cylinders, $n = 2$ for cones, $n = 1.5$ for spheres and paraboloids).

4.3. Plastic deformation

When indenting soft samples, e.g. polymers, plastic deformation may take place. A typical curve with plastic deformation is depicted in Fig. 16. It was acquired on poly(*n*-butyl methacrylate) (PBMA) at 30 °C. The approach contact-line can be divided in two parts, corresponding to elastic and plastic deformations. Also the fit of the elastic region following the Hertz model ($F \propto \delta^{3/2}$) is shown (dashed line). The two regions are separated by a yielding point. When yielding occurs, the cantilever exerts a critical pressure on the sample, and a plastic deformation is obtained. Please note that the stiffness of the sample after the yielding is lower than before the yielding (the indentation obtained in the plastic region at a certain load is larger than the corresponding elastic deformation, indicated by the dashed line).

In presence of a plastic deformation the contact line of the withdrawal curve does not overlap with the approach contact line. This shows that, upon retracting of the tip, the sample cannot regain completely its shape, as implied by the definition of plastic deformation. As shown in Fig. 17, we can define the elastic recovery $Z_p^{\max} - p$, where p , the permanent plastic deformation, is the intercept between the withdrawal

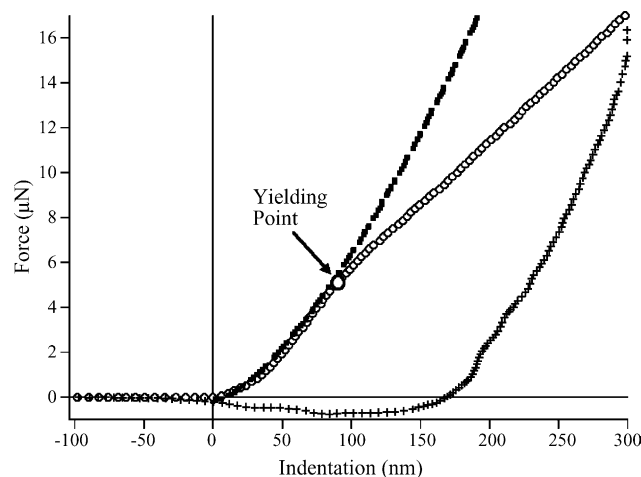


Fig. 16. Force–distance curve in air on PBMA at 30 °C. The approach curve is drawn with open circles, whereas the retraction curves is drawn with crosses. The contact line of the approach curve can be divided in two parts, i.e., the elastic and the plastic region, divided by a yielding point. Also the fit of the elastic region following the Hertz model ($F \propto \delta^{3/2}$) is shown (dashed line). After the yielding point the sample has become softer, because of the onset of plastic deformations.

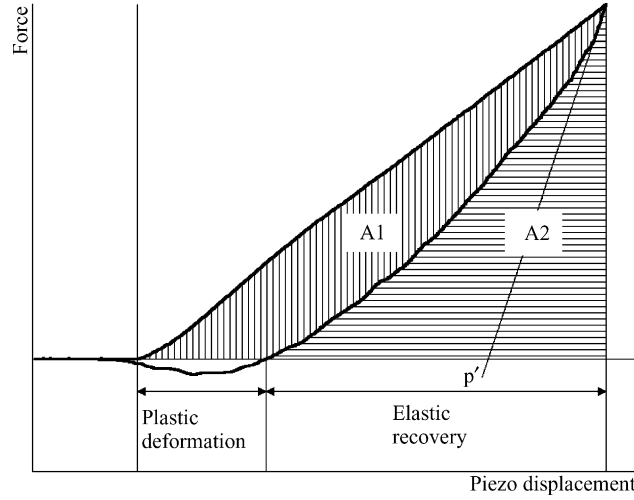


Fig. 17. Schematic force–distance curve with plastic deformations. The permanent plastic deformation, p , is the intercept between the withdrawal contact line and the axis $F = 0$; A_1 is the area between the two contact lines above the axis $F = 0$; A_2 is the area between the retraction contact line and the axis $F = 0$, p' is the intercept between the axis $F = 0$ and the tangent to the unloading curve for very high loads.

contact line and the axis $F = 0$. For a totally elastic sample would be $p = 0$ and the elastic recovery would be equal to Z_p^{\max} ; for a totally plastic sample would be $Z_p^{\max} = p$ and the elastic recovery would be zero.

The area between the two contact lines above the axis $F = 0$, that is A_1 , is a measure of the energy needed for the deformation and dissipated into the sample [253], whereas the sum $A_1 + A_2$ is the work done on cantilever and sample, i.e. the maximal energy that could be stored in the sample during the indentation. We can define a plasticity index in the form

$$\psi_P = \frac{A_1}{A_1 + A_2}. \quad (4.9)$$

For a totally elastic sample would be $A_1 = 0$ and $\psi_P = 0$, for a totally plastic sample would be $A_2 = 0$ and $\psi_P = 1$.

In several experiments the AFM is used as an indenter in order to measure the Young's modulus and the hardness H of the sample. The basic empirical equations, valid in the plastic regime, are reported by Oliver and Pharr [254,255]:

$$\left. \frac{dF}{d\delta} \right|_{\delta_{\max}} = \frac{2\beta_1}{\sqrt{\pi}} E_{\text{tot}} \sqrt{A_{\max}}, \quad (4.10)$$

$$H = \frac{F_{\max}}{A_{\max}} = \frac{F_{\max}}{\beta_2 p'^2}. \quad (4.11)$$

Here, β_1 and β_2 are parameters depending on the indenter geometry, A_{\max} the projection of the contact area between the indenter and the sample at the maximal indentation δ_{\max} , and p' is the intercept between the axis $F = 0$ and the tangent to the unloading curve for very high loads. A_{\max} can be calculated only if the shape of the tip is exactly known. Alternatively it can be measured by imaging the sample after indentation.

In such experiments the AFM is employed as an indenter and force–displacement curves are not of primary interest. The measurement is focused on the result of a given indentation, i.e., on the shape of the “imprinted” hole, and not on the dependence of the deformation on the load. Hence, we refer the reader to other reviews [256] and to some recent works [257–260].

4.4. Experimental results

The Maugis theory has put an end to the dispute between DMT and JKR model in the 1970s and is nowadays accepted as the only general theory fully describing the elastic deformation of samples. Therefore little work has been done in the last years from the theoretical point of view. In an extensive MD simulation study Patrick et al. [261] have checked the accuracy of the three models in predicting numerical simulation results.

The determination of the elastic properties of hard, non-deformable samples by means of AFM has become a relatively unproblematic task [262]. The most serious limits and sources of errors are the uncertainty of the tip shape and the choice of one of the elastic continuum theories.

A challenging experiment is that of Shulha et al. [263], who have probed the elastic properties of dendritic molecules with dimensions below 3 nm and have shown that it is possible to recognize two different molecules via their different Young’s modulus.

In recent experiments the interest has been refocused on compliant, easily deformable samples, such as polymers or biological samples. For such samples, additional limitations to the quantitative determination of nanomechanical properties are the occurring of plastic deformations and the effect of substrate stiffness. Also the difficulty in establishing when contact occurs on a soft material may engender serious errors, critically discussed in the study of Dimitriadis et al. [264].

In the study of Mailhot et al. [265], this problem is bypassed by comparing relative values of the stiffness of samples (see also Refs. [266,267]). The authors showed that the elastic properties of polymer films are related to the photooxidation by comparing the stiffness measured at different depths.

Also in the case of polymers the determination of the elastic behavior of the sample by means of AFM is very common. Usually the Hertz theory is employed [268–273], due to the low adhesion of the tip with most of polymeric films. In some cases, however, the JKR [274] or even the Maugis model [275] yield more satisfactory results. A comparison of the reliability of Hertz and JKR theories on polymers can be found in Refs. [276,277]. Also the effect on the sample deformation of maximum load [278], contact time [279], and loading rate [280] have been characterized.

An accurate description of the tip shape is essential for the quantitative determination of elastic properties. Several equations describing the load-indentation dependencies with different tip shapes, e.g. conical, paraboloidal, and hyperboloidal, have been tested in recent works, both for Hertz [281,282] and JKR model [275]. In order to avoid errors due to uncertainties in the characterization of the tip shape, Dimitriadis et al. [264] suggest to use microspheres as probes and discuss their advantages relative to common tips.

For thin deformable films the effect of the substrate cannot be neglected [264,280,283]. When working with thick samples, indentations are limited to depths much smaller than the total thickness of the sample (10–20%), in order to eliminate the influence of the substrate. In case of very thin samples (2–20 nm) indentations should therefore be limited to 1–4 nm, and probing such depths is unstable. This important issue has been addressed especially by the researchers in the group of Tsukruk, who have exploited a semi-empirical formula of Shull et al. [284] to model the deformations of thin polymeric films [285] and

of polymer nanocomposite layers [286]. Such a formula gives the indentation depth as in the Hertz theory ($\delta = a^2/R$), but the contact radius is a function of the Young's moduli of the film material (E_F) and the underlying substrate (E_S) and of the thickness of the sample t :

$$\frac{a}{a_{\text{Hertz}}} = \sqrt[4]{\frac{J^{4/3} + 0.8t/a_{\text{Hertz}}}{1 + (0.8t/a_{\text{Hertz}})^2}} \quad (4.12)$$

where $J = (E_F/E_S)(1 - \nu_S^2)/(1 - \nu_F^2)$, ν_S (ν_F) is the Poisson's ratio of the substrate (film), and a_{Hertz} is the contact radius that be would be obtained on the sample when neglecting the effect of the substrate. This model has been exploited by Rabinovich et al. [287] in order to determine the mechanical properties of self-assembled surfactant aggregates on mica or silica at concentrations higher than the critical micelle concentration, as shown in Fig. 18.

By determining the Young's modulus of the samples Lubarsky et al. [274] could demonstrate the differences between polystyrene surfaces exposed to three different modification processes. Similarly, stiffness measurements have been exploited to characterize heterogeneity in thin film blends of polystyrene and polybutadiene [288,289] and in polymer brush layers from poly(styrene-co-pentafluorostyrene) and polymethylacrylate [290]. In this last study the temperature dependence of the elastic response of polymer brushes also is addressed, showing that changes in the elastic behavior of the polymer sample, probed through force–displacement curves, can be exploited to determine the glass transition temperature of the polymer. Similarly, Yao et al. [291] have monitored the changes in the Young's modulus of chitosan/gelatin hybrid polymer network gels as a function of swelling time.

The determination of the glass transition temperature of polymer sample via the characterization of the stiffness, of the adhesion, and/or of the elastic–plastic behavior as functions of temperature, has been attempted also with polymer films [292–294]. Cappella et al. [295] have measured the yielding force and the Young's modulus of PBMA as a function of temperature, showing a very good agreement between

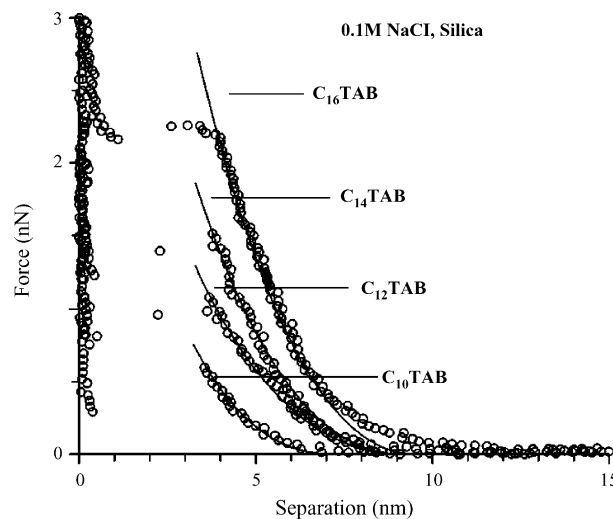


Fig. 18. Experimental force–distance curves (circles) measured between an AFM tip and cetyltrimethylammonium bromide (C_n TAB) aggregates on a silica substrate. Theoretical (solid) curves are plotted using the model of Shull. Reprinted from Ref. [287] with permission from Elsevier.

AFM and dynamic mechanical analysis (DMA) data, and have also determined the coefficients of the Williams–Landel–Ferry equation, in agreement with broadband spectroscopy and DMA (see also [294]).

Polymer samples are likely to be plastically deformed for small loads. Several recent works deal with plastic deformations of polymer samples [296,297]. Hence, the model of Oliver and Pharr can be applied successfully also to polymers, as shown by several works [298,299].

Cappella et al. [295] have presented a mathematical model of plastic deformations of polymers, in which the polymer is modeled as a two-layer system with different stiffness, before and after the yielding force, i.e., before and after the onset of plastic deformations. Following this model, plastic deformations are handled like elastic (hertzian) deformations occurring for forces larger than the yielding force with a lower stiffness, and a shift of the origin in the force–deformation plot accounts for the effect of plasticity, similarly to the DMT theory, where a shift of the origin accounts for adhesion. A similar approach is used in some studies in order to characterize the deformations of viscoelastic samples [280,296,300].

The characterization and quantitative determination of elastic properties of the sample via force–displacement curves has been attempted also with biological samples. Due to the usually very small Young’s modulus of such samples and to their high deformability, the technical problems and sources of error mentioned above are particularly important in experiments with biological samples. Nevertheless, an analysis of force–displacement curves following the Hertz theory has been applied in the study of tissues [301], microbial cells [302,303], platelets [304], and other biological samples [305–308]. For more details on the determination of the Young’s modulus of cells, see Section 9.

5. van der Waals forces

5.1. Theory

In this section only some basic equations, necessary for the comprehension of the experimental sections, are summarized. An general introduction on van der Waals force can be found in Ref. [309]. The van der Waals force between atoms and/or molecules is the sum of three different forces, all proportional to $1/r^6$, where r is the distance between the atoms or molecules. The corresponding potentials are the orientation or Keesom potential $w_K(r)$, the induction or Debye potential $w_D(r)$, and the dispersion or London potential $w_L(r)$.

The Keesom potential originates from the angle-averaged dipole–dipole interaction and is [309]:

$$w_K(r) = -\frac{C_K}{r^6} = -\frac{u_1^2 u_2^2}{3(4\pi\epsilon_0\epsilon)^2 k_B T r^6}, \quad (5.1)$$

where u_1 and u_2 are the dipole moments of the molecules, ϵ the dielectric constant of the medium, k_B the Boltzmann’s constant, and T is the temperature.

The Debye potential is the angle-averaged dipole-induced dipole interaction between two atoms or molecules:

$$w_D(r) = -\frac{C_D}{r^6} = -\frac{u_1^2 \alpha_{02} + u_2^2 \alpha_{01}}{(4\pi\epsilon_0\epsilon)^2 r^6}, \quad (5.2)$$

in which α_{01} and α_{02} are the electronic polarizabilities of the molecules.

The dispersion force is the most important contribution to van der Waals force, because it acts between all molecules or atoms. The dispersion force is the dipole–induced dipole interaction, and is of quantum-mechanical nature. The corresponding potential, calculated in 1930 by London [310], is

$$w_L(r) = -\frac{C_L}{r^6} = -\frac{3}{2} \frac{\alpha_{02}\alpha_{01}}{(4\pi\epsilon_0)^2 r^6} \frac{h\nu_1\nu_2}{\nu_1 + \nu_2}. \quad (5.3)$$

Here, $h\nu_1$ and $h\nu_2$ are the first ionization potentials of the molecules and h is the Planck's constant.

The total van der Waals potential is the sum of the three terms and can be written in the form $w_{\text{vdW}} = (C_K + C_D + C_L)/r^6 = C/r^6$ or [311]:

$$w_{\text{vdW}}(r) = -\frac{3k_B T}{(4\pi\epsilon_0)^2 r^6} \left(\frac{u_1^2}{3k_B T} + \alpha_{01} \right) \left(\frac{u_2^2}{3k_B T} + \alpha_{02} \right) - \frac{3}{2} \frac{\alpha_{01}\alpha_{02}}{(4\pi\epsilon_0)^2 r^6} \frac{h\nu_1\nu_2}{\nu_1 + \nu_2}. \quad (5.4)$$

The first term of Eq. (5.4) contains the Keesom and Debye energies. This term acts only between polar molecules and is called polar or entropic contribution. The second term is called dispersion contribution and acts between every molecule.

So far we have implicitly assumed that the molecules stay so close to each other that the propagation of the electric field is instantaneous. For the London interaction this is not necessarily true. To illustrate this we consider a spontaneous random dipole moment that arises in one molecule, which generates an electric field. The electric field, expanding with the speed of light, polarizes the second molecule, whose dipole moment in turn causes an electric field that reaches the first molecule with the speed of light. Covering the distance r between the molecules takes a time $\Delta t = r/c$, where c is the speed of light. If the first dipole changes faster than Δt , the interaction becomes weaker. The time during which the dipole moment changes is in the order of $1/\nu$. Hence, the interaction takes place as considered only if $r/c < 1/\nu$. ν , corresponding to the ionization of the molecules, is typically 3×10^{15} Hz. Thus, for $r > c/\nu \approx 10$ nm the van der Waals energy decreases more steeply (i.e. for molecules with $1/r^7$) than for smaller distances. This effect is known as retardation. Usually it is not relevant for AFM force experiments.

The van der Waals force can be calculated also for atoms or molecules of dielectric constant ϵ_1 and ϵ_2 in a medium of dielectric constant ϵ_3 . In this case it is necessary to consider the excess polarizability of the molecule of radius R_m given by the Clausius–Mossotti equation [312]:

$$\alpha_{\text{exc}}(\nu) = 4\pi\epsilon_0\epsilon_3(\nu) \frac{\epsilon_1(\nu) - \epsilon_3(\nu)}{\epsilon_1(\nu) + 2\epsilon_3(\nu)} R_m^3. \quad (5.5)$$

Inserting Eq. (5.5) into Eq. (5.4) the entropic and the dispersion terms are given by

$$w_{\text{ent}}(r) = -\frac{3k_B T R_{m1}^3 R_{m2}^3}{r^6} \left(\frac{\epsilon_1(0) - \epsilon_3(0)}{\epsilon_1(0) + 2\epsilon_3(0)} \right) \left(\frac{\epsilon_2(0) - \epsilon_3(0)}{\epsilon_2(0) + 2\epsilon_3(0)} \right), \quad (5.6a)$$

and

$$w_{\text{disp}}(r) = -\frac{\sqrt{3}}{2} \frac{h\nu_e R_{m1}^3 R_{m2}^3}{r^6} \frac{(n_1^2 - n_3^2)(n_2^2 - n_3^2)}{\sqrt{(n_1^2 + 2n_3^2)}\sqrt{(n_2^2 + 2n_3^2)} \left[\sqrt{(n_1^2 + 2n_3^2)} + \sqrt{(n_2^2 + 2n_3^2)} \right]} \quad (5.6b)$$

in which ν_e is the mean absorption frequency and n_1 , n_2 , and n_3 are the refractive indices of tip, sample, and the medium in between, respectively.

Table 3
van der Waals interaction laws for most common AFM geometries

Geometry	Force
Two flat surfaces	$f = -\frac{A_H}{6\pi D^3}$ per unit area
Two spheres	$F = -\frac{A_H}{6D^2} \frac{R_1 R_2}{R_1 + R_2}$
Sphere—flat surface	$F = -\frac{A_H R}{6D^2}$
Cone—flat surface	$F = -\frac{A_H \tan^2 \theta}{6D}$
Paraboloid—flat surface	$F = -\frac{A_H}{12D^2} \frac{l_{xy}^2}{l_z}$
Cylinder—flat surface	$F = -\frac{A_H R^2}{6D^3}$

A_H is the Hamaker constant, D is the distance, R is the radius of the sphere or of the cylinder, θ is the semi-aperture of the cone, l is the semi-axis of the paraboloid. $A_H = \pi^2 C \rho_1 \rho_2$, where C is the constant in the atom–atom pair potential and ρ_1 and ρ_2 are the number of atoms per unit volume.

In order to model the interactions taking place in AFM, it is necessary to consider macroscopic bodies rather than individual atoms or molecules. van der Waals energies between macroscopic bodies may be computed via integration only in the approximation that the van der Waals force is considered additive and non-retarded. The interaction laws obtained via integration using Derjaguin’s approximation (Section 3.3) are listed in Table 3 for common geometries. All interaction laws depend on geometrical features of the bodies and on the Hamaker constant A_H , which includes all physico-chemical information [313]:

$$A_H = \pi^2 C \rho_1 \rho_2, \quad (5.7)$$

in which C is the constant in the atom–atom pair potential and ρ_1 and ρ_2 are the number of atoms per unit volume. Typical values of the Hamaker constant of condensed phases in vacuum are about 10^{-19} J.

By assuming the additivity of the van der Waals force, the influence of nearby atoms on the couple of interacting atoms is neglected, thus introducing large errors in the calculation of the Hamaker constant. Lifshitz [314] circumvented this problem via an alternative approach in which each body is considered as a continuum with certain dielectric properties, thus incorporating automatically many-body effects. All expressions in Table 3 remain valid. Only the computation of the Hamaker constant changes. In Lifshitz theory, the Hamaker constant for the interaction of media 1 and 2 across the medium 3 may be expressed as

$$A_H \cong \frac{3}{4} k_B T \frac{\varepsilon_1 - \varepsilon_3}{\varepsilon_1 + \varepsilon_3} \frac{\varepsilon_2 - \varepsilon_3}{\varepsilon_2 + \varepsilon_3} + \frac{3h\nu_e}{8\sqrt{2}} \frac{(n_1^2 - n_3^2)(n_2^2 - n_3^2)}{\sqrt{|n_1^2 - n_3^2|} \sqrt{|n_2^2 - n_3^2|} [\sqrt{|n_1^2 - n_3^2|} + \sqrt{|n_2^2 - n_3^2|}]}. \quad (5.8)$$

For two identical media ($\varepsilon_1 = \varepsilon_2 \neq \varepsilon_3$, $n_1 = n_2 \neq n_3$), Eq. (5.8) becomes:

$$A_H \cong \frac{3}{4} k_B T \left(\frac{\varepsilon_1 - \varepsilon_3}{\varepsilon_1 + \varepsilon_3} \right)^2 + \frac{3h\nu_e}{16\sqrt{2}} \frac{(n_1^2 - n_3^2)^2}{\sqrt{(n_1^2 + n_3^2)^3}}. \quad (5.9)$$

Eq. (5.8) reveals two important aspects:

1. The van der Waals force between two identical bodies in a medium is always attractive (A_H is positive), whereas the force between two different bodies may be attractive or repulsive.
2. The van der Waals force between any two condensed bodies in vacuum or in air ($\varepsilon_3 = 1$ and $n_3 = 1$) is always attractive.

For interactions between conductive bodies such as metals, Eq. (5.8) cannot be applied, since ε is infinite. For two metals in vacuum the Hamaker constant is

$$A_H \cong \frac{3}{8\sqrt{2}} h \frac{\nu_{e1}\nu_{e2}}{\nu_{e1} + \nu_{e2}} \cong 4 \times 10^{-19} \text{ J}. \quad (5.10)$$

Here, ν_{e1} and ν_{e2} are the plasma frequencies of the two metals.

In order to determine Hamaker constants from measured force–distance curves, three approaches can be followed. In all three methods the geometrical characterization of both tip and sample is necessary. The first method consists in fitting the attractive part of the force–distance curve with one of the force laws listed in Table 3, depending on the geometry [315]. This procedure can be somewhat difficult due to the short interaction range and the very small forces. Therefore it requires a very good distance and force resolution and yields better results only when techniques eliminating the jump-to-contact are employed.

The second method exploits the jump-to-contact force. The tip jumps onto the sample when the force gradient exceeds the spring constant of the cantilever (Section 3.2). For a sphere–plane system it can be shown that the cantilever deflection and the distance at the jump-to-contact are given by

$$(Z_c)_{\text{jtc}} = \frac{1}{2} \sqrt[3]{\frac{1}{3} \frac{k_{\text{eff}}^2}{k_c^3} A_H R}, \quad D_{\text{jtc}} = 2 \frac{k_c}{k_{\text{eff}}} (Z_c)_{\text{jtc}} = \sqrt[3]{\frac{A_H R}{3k_{\text{eff}}}}. \quad (5.11)$$

Eq. (5.11) permits to calculate A_H and R (k_{eff}) from the measured $(Z_c)_{\text{jtc}}$ and D_{jtc} once the elastic constant of the cantilever k_c and the effective elastic constant of the system k_{eff} , defined in Eq. (4.3), or the tip radius R are known.

The third method consists in calculating the work of adhesion according to the DMT ($F_{\text{ad}} = 2\pi RW$), JKR [316] ($F_{\text{ad}} = 3/2\pi RW$), or Maugis theory, and then relating it to the Hamaker constant through

$$W = \frac{A_H}{\beta D_0^n}, \quad (5.12)$$

where β and n depend on the geometry of the system and can be calculated from the force laws listed in Table 3 (e.g., $\beta = 6/R$, $n = 1$ for a sphere–plane system). D_0 is an interatomic spacing [309]. Often $D_0 = 0.165$ nm yields good results, except for highly polar H-bonding liquids. In addition to the geometrical characterization of the system, uncertainties on D_0 and most of all the choice of an appropriate elastic continuum theory are serious sources of error in this method.

The work of adhesion can be related to the surface energies of tip and sample in a medium by the Dupré equation [309]:

$$W_{\text{smt}} = \gamma_{\text{tm}} + \gamma_{\text{sm}} - \gamma_{\text{st}}. \quad (5.13)$$

When considering polar surfaces, the total surface energy γ should be the sum of two components [317], the Lifshitz–van der Waals surface energy γ^{LW} and the acid–base surface energy $\gamma^{\text{AB}} = 2\sqrt{\gamma^+ \gamma^-}$,

where γ^+ and γ^- are the electron acceptor and the electron donor components, respectively. For the two components γ^{LW} and γ^{AB} of a binary system the Good–Girifalco–Fowkes combining rules [318] are applicable:

$$\gamma_{12}^{LW} = \gamma_1^{LW} + \gamma_2^{LW} - 2\sqrt{\gamma_1^{LW}\gamma_2^{LW}}, \quad (5.14a)$$

$$\gamma_{12}^{AB} = 2\left(\sqrt{\gamma_1^+\gamma_1^-} + \sqrt{\gamma_2^+\gamma_2^-} - \sqrt{\gamma_1^+\gamma_2^-} - \sqrt{\gamma_1^-\gamma_2^+}\right). \quad (5.14b)$$

Hence, for the interaction of a polar tip with a polar sample across a polar medium we obtain:

$$\begin{aligned} \frac{W_{smt}}{2} = & \sqrt{\gamma_s^{LW}\gamma_t^{LW}} - \sqrt{\gamma_s^{LW}\gamma_m^{LW}} - \sqrt{\gamma_t^{LW}\gamma_m^{LW}} + \gamma_m^{LW} + \sqrt{\gamma_m^+}(\sqrt{\gamma_m^-} - \sqrt{\gamma_s^-} - \sqrt{\gamma_t^-}) \\ & + \sqrt{\gamma_m^-}(\sqrt{\gamma_m^+} - \sqrt{\gamma_s^+} - \sqrt{\gamma_t^+}) + \sqrt{\gamma_s^+\gamma_t^-} + \sqrt{\gamma_s^-\gamma_t^+}. \end{aligned} \quad (5.15)$$

The method of determining van der Waals constants from adhesion experiments is, however, of limited use because it relies on the assumption that the solid surfaces do not change upon contact. Considering the high pressures underneath the tip in the contact region this is often not fulfilled.

5.2. Determination of Hamaker constants, adhesion and surface energies

Experiments before 2000, reviewed in Ref. [319], had already demonstrated the capability of AFM in probing van der Waals force with high distance and force resolution. Further measurements and characterizations of van der Waals forces with different tip–sample systems can be found for different systems, such as silicon nitride/silicon nitride in diiodomethane [320], Teflon AF/silica or alumina [321], silica/mica in water [322], silicon nitride/various samples in water, ethanol, ethylene glycol, and formamide [323], and poly(tetrafluoroethylene)/silica or alumina [324]. An overview over Hamaker constants is given in Table 4.

Several experiments in recent years have been refocused on the elucidation of artifacts and on the elimination of the main limits and sources of error. When determining the Hamaker constant of the system by fitting the attractive part of the approach curve, the main problem is the presence of the jump-to-contact. Ashby et al. [330] have taken advantage of a magnetic feedback AFM to probe the complete force profile between OH- and COOH-terminated self-assembled monolayers on gold in water solution, as shown in Fig. 19. The authors could show that the Hamaker constant is dominated by the underlying gold support (for a calculation of the Hamaker constant of SAMs on metal supports as a function of the thickness of layers see also [347]). The same result has been found by Seog et al. [348] by measuring the forces between glycosaminoglycan on gold and by Vezenov et al. [349].

Another major problem in measuring the van der Waals force is the characterization of the geometrical properties of tip (tip shape) and sample (roughness). The theoretical calculation of the van der Waals interaction between bodies with particular geometries has been adapted to common AFM configurations. For example, Zanette et al. [350] have calculated the van der Waals force between a plane sample and a tip in the form of a four-side truncated pyramid with a spherical cap on the top. The authors have verified the accuracy of their approximations by measuring and fitting the van der Waals force between a silicon nitride tip and a gold film.

Table 4

List of measurements of the Hamaker constant between materials commonly used in atomic force microscopy

Material 1	Material 2	Medium	Calculated A_H ($\times 10^{-20}$ J)	Reference	Experimental A_H ($\times 10^{-20}$ J)	Reference
TiO ₂	TiO ₂	Water	6 5.3–5.7	[325] [326]	6 ± 2	[169]
Au	Au	Water	40	[309]	7–25 25 10	[327] [328] [329,330]
Ag	Ag	Vacuum	20–49	[315]	38.5 ± 0.5	[315]
Cu	Cu	Vacuum	25–40	[315]	27.5	[315]
Ag	Cu	Vacuum	22–44	[315]	32.6–34	[315]
Si ₃ N ₄	Si ₃ N ₄	Water	4.8–5.9	[326]	6.1	[331]
Si ₃ N ₄	Mica	Water	2.45	[326]	3.4	[331]
Si ₃ N ₄	Mica	Ethanol			11.6	[332]
SiO ₂	SiO ₂	Ethanediol	0.6	[333]	0.2	[333]
SiO ₂	SiO ₂	Water	0.77–0.84 0.46–0.7 0.85	[334] [326] [333]	1 0.85	[335] [336]
SiO ₂	Air	Water	–1	[309]	–1	[337]
SiO ₂	Au	Air			2.2–4.1	[338]
SiO ₂	Au	Water			12–15	[338]
SiO ₂	Ag	Vacuum	11–18	[315]	13	[315]
SiO ₂	Cu	Vacuum	12–17	[315]	14	[315]
SiO ₂	TiO ₂	Water	0.69	[326]	1.4	[339,340]
SiO ₂	Teflon	Cyclohexane	–0.54	[341]	–0.41	[341]
SiO ₂	Mica	Water	1.2 1.16	[334] [326]	1.2	[322]
ZrO ₂	ZrO ₂	Water	7.2–8.1	[326]	6	[342]
Al ₂ O ₃	Al ₂ O ₃	Water	5.3	[333]	5.3	[343]
Mica	Mica	Water	2–2.2 1.3–1.9	[334] [326]	2.2	[344]
Teflon	Teflon	Air			3.9	[345]
BSA	BSA	Water			0.4	[346]

Only measurements performed with AFM are listed.

The problem of the roughness of surfaces and the presence of asperities has been handled mainly by researchers dealing with the adhesion of particles, i.e., in experiment measuring forces and adhesion between a sample and a (rough) particle fixed on the cantilever and used as a tip. Hence, we refer to Section 7.2. Yet some theoretical results [351–354] are generally valid, also for usual AFM-tips on rough samples.

The surface energy of polar materials has been the object of several theoretical and experimental works in the past few years. Experimental works have been carried out usually with colloidal functionalized probes, in order to define accurately the geometry and the chemical composition of the system.

Freitas and Sharma [355] have measured the hydrophilic–hydrophilic, hydrophilic–hydrophobic and the hydrophobic–hydrophobic adhesion in water and ethanol, obtaining a good qualitative agreement with the values predicted by the acid–base theory. In water the higher adhesion is obtained for the hydrophobic–hydrophobic system, followed by the hydrophilic–hydrophobic and by the hydrophilic–hydrophilic system, as confirmed also by Duwez et al. [356], who measured the adhesion of –OH and –CH₃

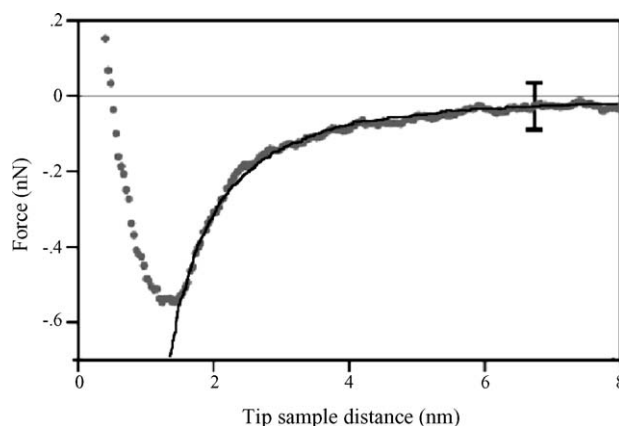


Fig. 19. Approach force–distance curve for hydroxyl-terminated SAMs in deionized water. Experimental data are circles and the fit to the sphere–plane van der Waals force is the solid line. Reprinted from Ref. [330], Copyright 2000, with permission from the American Chemical Society.

functionalized tips and samples in water, ethanol, hexane and nitrogen atmosphere. The authors find that the tendency in nitrogen atmosphere is inverted: OH/OH adhesion is much larger than CH₃/CH₃ adhesion. The authors also exploit the capabilities of force–displacement curves with functionalized tips in order to characterize the adhesion of several polymer additives with –OH and –CH₃ terminated tips in water and nitrogen atmosphere and to recognize them at the surface of polypropylene films.

Nalaskowski et al. [357] have measured the adhesion between polyethylene and silica in water, previously calculated via Eq. (5.15) and the JKR theory. Discrepancies between the theoretical and the experimental values are attributed to surface roughness.

A complete study is that of Vezenov et al. [349]. The authors measured the adhesion between CH₃-terminated SAMs in several solvents (decane, benzene, propanol, butanol, hexanol, ethanol, methanol, water, and other solvents) and found that it greatly varies depending on the medium. In order to get further insights in this phenomenon, they measured the jump-to-contact of CH₃-terminated SAMs and the adhesion of CF₃–CF₃, CH₃–CH₃, CH₃–COOH, COOH–COOH, CH₂Br–CH₂Br and epoxy–CH₃ SAMs in methanol–water mixtures. The authors confirmed that the van der Waals interaction at large distances is dominated by the underlying gold layer and corroborated this result by studying the effect of chain length on the jump-to-contact: the jump-to-contact distance reproduces the change in SAM chain length (see also [358]).

The authors saw that the jump-to-contact distance does not depend on medium composition, whereas there is a clear trend for the adhesion of all measured systems: the adhesion increases with the fraction of water in the medium. The authors claim that this is due to intrasolvent polar interactions occurring, to different extent, also for the other solvents, and support their assumptions with theoretical reasons based on the acid–base theory (see also [359]).

A challenging experiment is that of Noy et al. [360], who have measured the adhesion as a function of temperature (in the range –30 to 30 °C) for COOH–COOH, Si₃N₄–mica (mainly hydrogen bond interactions), CH₃–CH₃, and Au–Au (mainly van der Waals interactions) in ethanol and hexane. In hexane the adhesion decreases slightly with increasing temperature for all four systems. In ethanol the adhesion increases considerably with increasing temperature for COOH–COOH and Si₃N₄–mica, slightly for CH₃–CH₃ and does not increase for Au–Au. The authors explain these results through a

“solvent ordering effect”: the increase in adhesion is a consequence of the energy needed to order solvent molecules at hydrophilic interfaces when the tip–sample surfaces are separated. The energy needed increases with temperature and is higher for polar solvents.

The jump-to-contact and the adhesion has been measured with functionalized tips also for the following systems: $-\text{NH}_2$, $-\text{CH}_3$, and $-\text{COOH}$ pairs in water [361,362], $-\text{OH}$ and $-\text{CH}_3$ terminated samples and tips in different liquids (water, hexadecane, perfluorodecaline, dodecane, octanol) [363], $-\text{OH}$, $-\text{COOH}$, and $-\text{CH}_3$ terminated samples and tips in different liquids (water, hexadecane, perfluorodecaline, dodecane, ethanol) [364], $-\text{COOH}$ terminated tips on $-\text{NH}_2$, $-\text{CH}_3$ terminated samples and allylamine films [365], mixed films of $\text{HS}(\text{CH}_2)_{11}\text{OH}$ and $\text{HS}(\text{CH}_2)_{11}\text{CH}_3$ with $-\text{C}_{10}\text{COOH}$ and $-\text{C}_{11}\text{CH}_3$ tips [366], cholesterol monohydrate in water and ethylene glycol with $-\text{COOH}$ and CH_3 tips [367], and also several proteins and NH_2 -, CH_3 -, OH - and COOH -terminated samples in water and PBS buffer [362,368,369].

In the extensive work of Clear and Nealy [370] the adhesion of different systems ($-\text{CH}_3$ / $-\text{CH}_3$, $-\text{COOH}$ / $-\text{COOH}$, $-\text{CH}_3$ / $-\text{COOH}$, $-\text{CH}_3$ or $-\text{COOH}$ /octenyl-trichlorosilane) is measured in different liquids (water, hexadecane, ethanol, 1,2- and 1,3-propanediol). The surface energies, calculated following the acid–base theory, are compared with experimental values and good agreement is found for the $-\text{CH}_3$ / $-\text{CH}_3$ system.

Work of adhesion between a Si_3N_4 AFM tip and methyl (CH_3), amine (NH_2), methyl fluoride (CF_3), and ester ($\text{CO}(\text{OCH}_3)$) end-group SAMs, as well as hydroxyl (OH) functionalized surfaces showed quantitative agreement with contact angle measurements of the surface energies [371]. Comparison with the work of adhesion on soft polymer surfaces with same surface chemistry allowed separating chemical and mechanical contributions to the work of adhesion [372]. Tormoen et al. [373] used tips and surface coated with SAMs (thiols on gold) terminated with OH , CH_3 , COOH and NH_2 groups. Taking into account the granular structure of the evaporated gold, good agreement with values from contact angles was achieved. Work of adhesion between Si_3N_4 tip coated with indium tin oxide (ITO) and model surfaces with various functional groups (Cl , NH_2 , CH_3 , and CF_3) was determined using the DMT theory for data evaluation [374]. Both dispersion and polar surface tension are taken into account. Values correlated well with results from measurements with a JKR apparatus and contact angles. The adhesion of a Si_3N_4 tip to 3d transition metal surfaces was found to be correlated to the electronic work function of the surface, decreasing with increasing work function [375].

An increase in surface energies of polypropylene films after UV/ozone treatment [376] or mechanical scratching [377] was observed. Surface tensions of bovine serum albumine (BSA) and hyaluronate layers were estimated from adhesion forces [378]. Relative changes in surface energies for the surfaces of fused-silica capillary tubes by etching, silanization and octadecyl functionalization were determined by Pullen et al. [379].

Jänchen et al. [380] determined the adhesion energy for the interaction of a polystyrene sphere coated with a titanium film with collagen films coated on a titanium substrate. Si_3N_4 tip interactions with various materials ($\text{Si}(1\ 0\ 0)$, $\text{Si}(1\ 1\ 1)$, silica glass, titanium nitride, and diamond-like carbon) in four different liquid media (water, ethanol, ethylene glycol, and formamide) showed close correlation between the measured adhesion forces and calculated values using surface energies, except in water, where AFM experiments showed stronger adhesion [323]. Schneider et al. [381] studied the action of Cr as an adhesion promoter by the interaction of a silica AFM tip with and without chromium coating with silica, mica, gold and silver surfaces. Adhesion was higher for Cr than for SiO_2 tips and surface energies for these materials were calculated from the results. Relini et al. [382] determined the surface energy of a

streptavidin crystal from adhesion of a streptavidin functionalized tip to a crystal face. Beach et al. [383] used gold coated AFM tips and silicon wafers with a hexadecanethiol SAM. The measured pull-off force value remained practically unaffected by a variation of the maximum applied load in a range of 5–80 nN and corresponded to surface energies of 24–27 mJ/m². These surface free energies matched closely the results obtained from contact angle measurements on these SAMs. Organic coating of silicon oxide and silicon nitride by 1-octadecene decreased the surface energies by a factor of ~1.5 as deduced from adhesion force measurements and contact angles [384].

Rixman et al. [385] compared the results obtained by the JKR and DMT theory. Drelich et al. [353] have collected the data of several articles and calculated again the adhesion with the Maugis theory. They have shown that in some cases the JKR or the DMT approximation yield satisfactory results. In several other works discrepancies between experimental and theoretical data arise due to a false choice of the elastic continuum model, i.e., because researchers apply the DMT model to systems that would be described better by the JKR theory, or vice versa. The authors show that such discrepancies can be overcome by calculating again the data with the “right” theory. The authors also discuss critically several sources of error, i.e., tip characterization, heterogeneity, plastic deformations, and roughness.

The acid–base theory also has been applied to the adhesion between cells and biological materials [386], to the adhesion between blood proteins and several functional groups [362].

In recent years the research dealing with the determination of individual chemical bonds has made great strides. Two approaches, described in the following, are usually followed: “force quanta” measurement and Poisson statistics (for a dynamic simulation of both methods see [387]).

In the first approach, pull-off forces between AFM tips and substrates capable of specific chemical binding are measured. Since the contact area is on the order of a few nm², the pull-off involves breaking a small integer number of bonds. Fluctuations in the number of discrete bonds formed and broken in consecutive pull-off measurements give rise to a distribution of forces. This distribution, plotted as a histogram of pull-off forces, can be analyzed to determine the “force quantum” corresponding to the rupture of a single chemical bond.

The work of Skulason and Frisbie [388] deals with the adhesion between gold and S-acetate-, O-acetate-, SH- and OH-terminated SAMs in different solvents, and the accent is put on the detection of the discrete rupture forces or force quanta (see also [389]). The authors found a force quantum of 0.1 nN in histograms of the adhesion force and assigned it to the rupture of individual chemical bonds. The presence of a force quantum is strongly solvent-dependent.

Later [390] the same authors studied theoretically the possibility to detect force quanta in histograms of adhesion force depending on the surface energy of the solvent, the binding probability of the materials, and the tip radius. The authors express the effective force resolution ξ in the form:

$$\xi = \sqrt{\frac{W_{\text{smt}}}{\gamma_{\text{m}}}} \frac{1}{\sqrt{1 + \sqrt{n_{\text{max}}(1 - P)}}}, \quad (5.16)$$

where n_{max} is the maximum number of bonds possible with the considered interaction area and P is the binding probability. The authors show that the effective force resolution and hence the possibility to detect quantized adhesion forces decreases with increasing solvent surface energy, increasing tip radius, and decreasing binding probability.

In other works the determination of the single bond is achieved following a method based on the assumption that the ruptures obey Poisson statistics [125,391]. In this method chemical bonds, hydrogen

bonds and van der Waals force are considered as specific interactions yielding a total adhesion force F_{ad} that is the sum of any possible discrete bond. The second assumption of this method is that the bonds form randomly and have all the same value F_i . Under these assumptions, the distribution of the number n of interacting bonds formed at the jump-off-contact follows Poisson statistics, and

$$\begin{cases} F_{\text{av}} = n_{\text{av}}F_i + F_0 \\ \sigma_{\text{F}}^2 = (\sigma_{\text{n}}F_i)^2 = n_{\text{av}}F_i^2 \end{cases} \Rightarrow \sigma_{\text{F}}^2 = F_{\text{av}}F_i - F_iF_0, \quad (5.17)$$

where F_{av} (n_{av}) and σ_{F}^2 (σ_{n}^2) are the average force (number of bonds) and the force (number of bonds) variance, and F_0 is the non-specific interaction. Thus, a plot of σ_{F}^2 against F_{av} yields F_i as the slope and $-F_iF_0$ as the intercept. This technique has been employed recently to determine the interaction between single molecular pairs [370,392,393].

6. Forces in aqueous medium

6.1. Electrostatic double-layer force and DLVO theory

At the end of the 19th century it was well known that many colloids in aqueous medium coagulate after the addition of salt. It was even known that di- or trivalent ions are much more efficient in destabilizing dispersions than monovalent ions. The explanation for this behavior was eventually given in a quantitative way with the DLVO theory, named after Derjaguin, Landau, Verwey, and Overbeek [394,395]. In DLVO theory the interaction between two particles is assumed to consist of two contributions: The van der Waals attraction and an electrostatic double-layer repulsion. At low salt concentration the double-layer repulsion is strong enough to keep the colloidal particles apart. With increasing salt concentration the electrostatic repulsion is more and more screened. At a certain concentration the van der Waals attraction overcomes the repulsive electrostatic barrier and coagulation sets in.

The electrostatic double-layer force arises because of surface charges at interfaces. Water has a high dielectric constant. Thus, surface dissociation or adsorption of a charged species in water is very common. The surface charge is balanced by dissolved counterions which are attracted back to the surface by the electric field, but spread away from the surface to increase the entropy. Together the ions and charged surface are known as the electric double layer. When another surface approaches, the double layer is perturbed, and the resulting force is known as the double-layer force. When the approaching surface charges have the same sign, the concentration of ions between the surfaces always increases. This results in a repulsive force [395,396]. At large distances, this electrostatic double-layer force decays roughly exponentially. The decay length is the so-called Debye length. For a monovalent salt it is

$$\lambda_{\text{D}} = \sqrt{\frac{\varepsilon\varepsilon_0k_{\text{B}}T}{2ce^2}}. \quad (6.1)$$

The Debye length λ_{D} is determined by the salt concentration; c is the salt concentration in mol/L. For water at 25 °C Eq. (6.1) can be reduced to $\lambda_{\text{D}} = 3.04/\sqrt{c}$ Å. If also ions of higher valency Z_i are present, $2c$ has to be replaced by $\sum c_iZ_i^2$. Here, c_i is the bulk concentration of the i th ion species. The sum runs over all ions present.

The electrostatic double-layer force can be calculated using continuum theory. This is based on a theory of Gouy, Chapman [397,398], Debye, and Hückel [399] for electric double layers. Therefore, first

the potential distribution between the two surfaces is calculated (see [115,309,400]). In continuum theory the potential distribution is determined from the Poisson–Boltzmann equation which is a second-order differential equation. To solve this equation certain boundary conditions have to be assumed. Two boundary conditions are often used: Either it is assumed that upon approach the surface charges remain constant (constant charge) or that the surface potentials remain constant (constant potential). These boundary conditions have a strong influence on the electrostatic force at distances below roughly $2\lambda_D$. Two surfaces with constant charge of equal sign always repel each other for $D \rightarrow 0$. Two surfaces with constant potential are attracted for $D \rightarrow 0$ even when the surface potentials have the same sign (except for the hypothetical case that the potentials are precisely equal in magnitude and sign)[401]. The force between an AFM tip with a parabolic end of radius of curvature R and a flat surface is given by [402,403]

$$F_{el}^{cp} = \frac{2\pi R \epsilon \epsilon_0}{\lambda_D} [2\psi_S \psi_T e^{-D/\lambda_D} - (\psi_S^2 + \psi_T^2) e^{-2D/\lambda_D}], \quad (6.2a)$$

assuming constant potentials of the sample ψ_S and the tip ψ_T . For constant charge conditions the electrostatic double-layer force is [403,404]

$$F_{el}^{cc} = \frac{2\pi R \lambda_D}{\epsilon \epsilon_0} [2\sigma_S \sigma_T e^{-D/\lambda_D} + (\sigma_S^2 + \sigma_T^2) e^{-2D/\lambda_D}], \quad (6.2b)$$

where σ_S and σ_T are the surface charge densities of sample and tip. In both cases it is assumed that the surface potentials are low ($\psi_S, \psi_T \leq 50$ mV).

In addition to the requirement that the potentials should be low there are two more limitations: The radius of curvature has to be large ($R \gg \lambda_D$) and Eqs. (6.2a) and (6.2b) are only valid for $D \geq \lambda_D$. For very large distances ($D \gg \lambda_D$) the equation becomes even more simple and the difference between constant surface potential and constant surface charge is negligible:

$$F_{el} = \frac{4\pi R \sigma_S \sigma_T \lambda_D}{\epsilon \epsilon_0} e^{-D/\lambda_D} = \frac{4\pi R \epsilon \epsilon_0 \psi_S \psi_T}{\lambda_D} e^{-D/\lambda_D}. \quad (6.3)$$

To demonstrate the effect of boundary conditions Fig. 20 shows the force between a microsphere of 3 μm radius interacting with a flat surface versus distance. The force was calculated with the nonlinear Poisson–Boltzmann equation which is valid for potentials above 50 mV. A salt concentration of 1 mM was chosen resulting in a Debye length $\lambda_D = 9.6$ nm. At close distances the force calculated with constant charge boundary conditions is much higher than the force calculated assuming constant potential. For $D \gg \lambda_D$ the forces calculated with constant charge and constant potentials are equal and surface charges and potentials can be converted according to $\psi_S = \lambda_D \sigma_S / \epsilon \epsilon_0$ and $\psi_T = \lambda_D \sigma_T / \epsilon \epsilon_0$. Also approximation (6.3) is plotted. It lies between the two extreme cases. For more detailed calculations which also are valid at higher potentials and which explicitly take into account the geometry see Refs. [405–409].

Which boundary condition is more realistic depends on the materials used. In addition, the electrolyte and the speed of the approach might have an influence. Prica et al. measured force curves between zirconia plates which showed a constant charge behavior [410]. Also the force between two surfaces coated with densely packed carboxylic groups followed constant charge conditions [411]. In other cases constant potential conditions are more appropriate. Most cases, however, lie between the two extremes. Then a charge regulation model is often applied [412]. In this model the surface charge is caused by the dissociation of ions from surface groups. The dissociation constant, and as a consequence the surface charge, depends on the potential. This explains the often observed dependency of the surface charge on

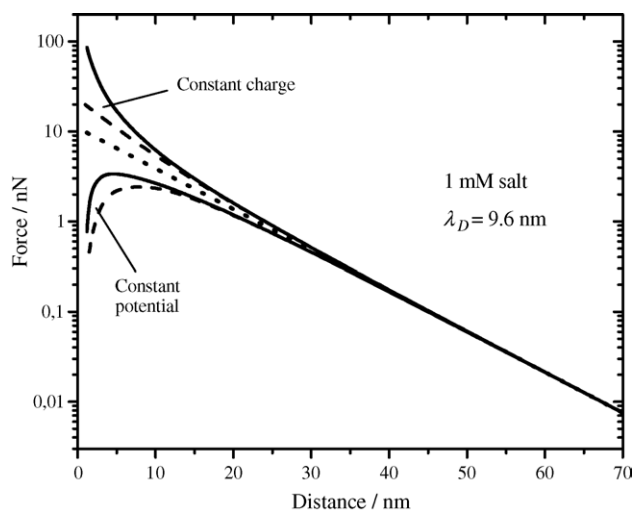


Fig. 20. Electrostatic double-layer force acting on a sphere of 3 μm radius in water containing 1 mM monovalent salt. The force was calculated for constant potentials (the potential of the tip is $\psi_T = 80$ mV, that of the sample is $\psi_S = 50$ mV) and for constant surface charge (the surface charge of the tip is $\sigma_T = 0.0058$ C/m² = 0.036 e/nm², that of the sample is $\sigma_S = 0.0036$ C/m² = 0.023 e/nm²) using Derjaguin's approximation. The surface charge was adjusted by $\sigma_{T/S} = \epsilon\epsilon_0\psi_{T/S}/\lambda_D$ so that at large distances both lead to the same potential. The continuous lines show the solution of the full nonlinear Poisson–Boltzmann equation. The results of Eqs. (6.2a) and (6.2b) are shown as dashed lines. In addition, the force expected with approximation (6.3) is plotted as a dotted line.

pH and the salt concentration. The charge regulation model is successfully applied to many materials, especially those where the surface charge is mainly determined by pH, such as oxides, silicon nitride [334,413–415], mica [416–419] and biological materials.

In the continuum Poisson–Boltzmann theory of the electric double layer several assumptions were made [420]: The finite size of the ions was neglected, ions in solution were considered as a continuous charge distribution rather than discrete particles, all non-coulombic interactions were disregarded, the solvent was supposed to be continuous with constant permittivity, all surfaces were assumed to be flat on the molecular scale, and image forces between the ions and the surface were ignored. Despite these strong assumptions, the DLVO theory describes the electric double-layer force surprisingly well. The reason is that errors lead to opposite effects and compensate each other. Including non-coulombic interactions leads to an increase of the ion concentration at the surface and a reduced surface potential. On the other hand, taking the finite size of the ions into account leads to a lower ion concentration at the surface and thus an increased surface potential. A reduction of the dielectric permittivity due to the electric field increases its range but at the same time reduces the surface potential because fewer ions dissociate or adsorb.

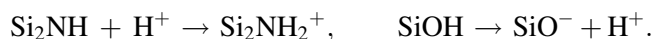
In summary: For aqueous solutions the DLVO theory provides relatively good predictions for monovalent salts at concentrations below 0.2 M and for potentials below 50–80 mV. The fact that the surface charge in reality is not continuously but discretely distributed, leads to deviations only with bivalent and trivalent ions.

In this context we would like to recall another principal problem. With any surface force measuring device the total force between two surfaces is determined. The origin of all surface forces is the interaction between electric charges. Under normal circumstances it is, however, practical to separate the

total force into several components and take the components as being additive (for a critique see [421]). These components are the van der Waals forces, the electrostatic double-layer force, the hydration repulsion (between hydrophilic surfaces) and the hydrophobic attraction (between hydrophobic surfaces). To analyze the electrostatic double-layer force one needs to separate it from all other components. This is usually done by assuming a certain distance dependency for the van der Waals force and the electrostatic force. In addition, the electrostatic force can be identified by means of the influence of salt.

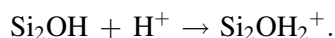
According to the above equations it is important to know how charges arise on the tip. Silicon and silicon nitride tips dominate the vast majority of applications. Some microfabricated tips are, however, produced from other materials, such as CVD diamond [422], or GaAs [423].

Silicon nitride is an important industrial material used in ceramics processing. Therefore various aspects of its surface chemistry have been studied in detail ([334,424,425] and references therein). It has been shown that conditions of preparation can strongly influence the acid–base balance at the surface. This results in a wide interval of pH values where the isoelectric point can occur (3.5–8.0) with an average around pH 6 [424]. The isoelectric point is the pH value at which the density of negative charges is equal to the density of positive charges and surface is electrically neutral. It has also been established that the charge behavior of the surface of silicon nitride in an aquatic environment is governed by protolytic reactions involving two major types of functional groups: namely, silanols which are bearers of acidic properties, and secondary amino groups (Si_2NH) bearing basic properties:



Both the hydrolytic instability of the surface and its proneness to oxidation lead to gradual development of a silica (SiO_2) layer covering the surface of silicon nitride. The thickness of this layer may reach several nanometers [425].

For silicon oxide the surface charge is determined by the second reaction. The first reaction does not exist. At very low pH silicon oxide can acquire a positive surface charge due to the reaction



The isoelectric point is around pH 2–3 [426]. Zhmud et al. determined the equilibrium constants for the last two reactions from surface force experiments between two silicon oxide surfaces using a charge regulation model [427]. For 1 mM aqueous electrolyte at 25 °C they found $[\text{SiOH}_2^+]/[\text{SiOH}][\text{H}^+] = 1.03 \times 10^{-3} \text{ L/mol}$ and $[\text{SiO}^-][\text{H}^+]/[\text{SiOH}] = 1.86 \times 10^{-4} \text{ mol/L}$ assuming a density of silanol groups of $1.25 \times 10^{-7} \text{ mol/m}^2$.

With the AFM DLVO forces were measured between several materials which are of special interest in colloidal science, e.g. glass, silica, and silicon nitride [15,16,187,427–434]; gold [327,429,435,436]; copper and nickel [437]; zinc and lead sulphide [171,172,438]; titanium oxide [169,339,340]; zirconia [165,166,410]; iron oxide [439]; tungsten [175]; cobalt [175]; and alumina [16,439–442]. Different polymers [177,189,443–447], Langmuir–Blodgett and other thin organic layers [126,329,411,448,449] have been analyzed. In recent years special interest in biologically relevant surfaces materials evolved. Examples are surfaces coated with poly(amino acids) [450,451] and hydroxyapatite ($\text{Ca}_5(\text{PO}_4)_3\text{OH}$) [452]. Forces on surfactant layers, lipid membranes and biological structures are discussed later. In all cases the force could be well described by DLVO theory. Independently measured surface potentials (or charge densities) and Hamaker constants agreed with AFM results. At separations below 1–5 nm differences occurred (see for instance [16,432,453,454]), particularly at high ionic strength. These are usually attributed to hydration forces.

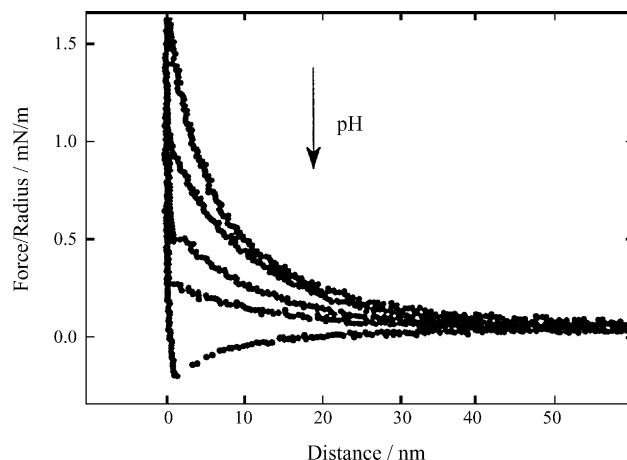


Fig. 21. Force between a silica (SiO_2) microsphere of $2.5 \mu\text{m}$ radius and a titania (TiO_2) crystal vs. distance. The force is scaled by the radius of the sphere. The curves were recorded at pH values of 8.8, 7.2, 6.3, 5.3, and 3.0 from top to bottom with 1 mM KNO_3 background electrolyte. The figure is reproduced with kind permission from Drummond [339].

As one example the force-versus-distance between a silica particle and a titania flat is shown in Fig. 21 [339]. Like in many publications the force is scaled by division through the radius of the silica microsphere. According to Derjaguin's approximation (Eq. (3.7)) the scaled force, F/R , is equal to $2\pi U_A$. Force curves were recorded at different pH values ranging from pH 8.8 for the top curve to pH 3.0 for the bottom curve. The surface charges of both materials are mainly determined by the pH. Silica has an isoelectric point around pH 3.0, while the isoelectric point of titania is pH 5.6. As a consequence at high pH, where both materials are negatively charged, an electrostatic repulsion is observed. The repulsion decreases as the pH decreases, and at pH 3.0, i.e. below the isoelectric point of titania, there is an electrostatic attraction as well as a van der Waals force resulting in an overall attraction between the two surfaces.

On oxides the density of hydroxyl and other active surface groups depends sensitively on the pre-treatment. Heating often removes hydroxyl groups while the presence of water increases the density of hydroxyl groups. A way of measuring the force between two surfaces with a well-defined density of functional groups is to coat the tip with thiols or disulfides. Titration experiments have been done with a number of differently coated surfaces [121,122,124–127].

With classical surface force measuring techniques it is impossible to analyze the electrostatic double layer of solid surfaces at surface potentials significantly higher than 0.1 V. The reason is that high surface potentials can only be obtained by applying an external potential to a metallic or conducting sample. With the AFM, however, this is quite possible by using either a conducting surface or a metal coated tip as the working electrode in an electrochemical cell. Ishino et al. [455] coated a microfabricated AFM tip with gold and used it as working electrode. They indeed observed a variation of the force with the applied potential when measuring the interaction between the gold coated tip and a stearic acid monolayer. An electrostatic repulsion was observed at negative applied potentials and attractive forces were measured at positive potentials. Since the stearic acid monolayer was negatively charged such a behavior is expected.

A more convenient setup consists of a conducting sample, which serves as a working electrode, and an insulating probe [456]. Raiteri et al. and Döppenschmidt and Butt [457,458] measured the force between a gold, platinum, or graphite sample and a silicon nitride tip. Campbell and Hillier determined the force

between a silica sphere as probe and carbon or gold [338,459]. Barten et al. concentrated on the gold surface probed by a silica sphere [460]. Dedeloudis et al. probed the electric double layer on a copper electrode with a silica sphere [461]. The results obtained with silica microspheres on gold [338,460] and with microfabricated silicon nitride tips [457] qualitatively agree. In all cases the silica microsphere (or tip) is repelled at negative potentials of the gold. When changing the potential to more positive values the repulsion decreased and finally attractive forces are observed. For separations larger than 10 nm the force curves could be described by DLVO theory. For smaller separations measured force curves deviated from calculated force-versus-distance curves. Hillier et al. attribute this discrepancy to several factors: An overestimation of the Hamaker constant, the roughness of the two interacting surfaces, and hydration effects.

Despite the qualitative agreement, there are differences between the results: The force observed between silica and gold changed almost linearly with the applied potential in a range from -0.6 to $+0.4 V_{SCE}$ (V_{SCE} is the potential at the saturated calomel electrode) [338,460]. Since the force curves reflect the surface effective surface potential of the gold surface this indicates that the surface potential also changes over a range of 1 V. Raiteri et al. observed a change of the force only in a narrow potential range of roughly 0.4 V. Above and below this voltage range the force saturated. This saturation behavior is also predicted by DLVO theory. The different potential range, where the force changed, can be caused by a large potential drop across an oxide layer or a Stern layer on the gold surface [460], which causes a large potential and might have been present in Refs. [338,460] but was less significant in Ref. [457].

Also preliminary experiments are done for the symmetric case of gold interacting with gold [174]. Both gold surfaces were electrically connected and served as working electrodes. In this case a repulsion was observed at high positive potentials and high negative potentials. In between, around the point of zero charge, the repulsion was reduced. This behavior agrees with predictions of continuum theory. Later Kleijn et al. use the same method to characterize the electrochemical properties of a gold surface in order to understand the adsorption of macromolecules from solution [462].

Besides measuring the distance dependency of a force it is sometimes interesting to know how the force changes from one place on the sample to another. To obtain this lateral information Senden et al. [463] imaged a silicon nitride surface at low force. In these experiments the image obtained is not solely an image of the charge distribution but it is a mixture of topography and charge density. Heinz and Hoh [464] developed a protocol, called D-minus-D mapping, in order to separate the two contributions. Therefore they take isoforce images at different salt concentrations to remove topography and isolate electrostatic contributions to the tip-sample interaction. A similar procedure was also used by Hafner et al. [465].

To get more quantitative information on the surface charge density whole force curves must be taken at each individual point of the sample. In this way differences between the charge densities of different regions on a sample can be obtained. This not only allows to distinguish regions based on their electric properties but also opens the possibility to measure quantitative charge densities with a standard AFM tip. Therefore the size of the tip and the surface charge density of the tip needs to be known accurately. One way to “internally” calibrate the tip is to deposit the material studied on a substrate with known charge density. Some regions of the substrate must be kept free. Then force curves are taken on the substrate and on the deposited material [466]. Rotsch and Radmacher [467] verified the positive surface charge of dimethyldioctadecylammonium bromide (DODAB) patches on negatively charged mica. At neutral pH they observed a repulsive force between the negatively charged mica and the negatively charged silicon

nitride tip. On a DODAB patch an electrostatic attraction was observed, indicating that the patch is positively charged. Electrostatic interactions were also mapped for polyelectrolyte complexes adsorbed to silicon wafers [468].

Electrostatic double-layer forces occur mainly in aqueous medium because of the high dielectric permittivity of water. They can, however, also be present in apolar media when adding certain surfactants. The surfactants form reverse micelles and dissolve free ions in the liquid and at the same time charge the surfaces. This was demonstrated by McNamee et al. [469]. They measured the force between two silica surfaces in *n*-dodecane with dissolved anionic surfactant AOT (bis(2-ethylhexyl)-sulfosuccinate). They could observe the exponentially decaying electrostatic double-layer force.

6.2. Hydration repulsion

The DLVO theory treats the intervening medium as continuous, so it is not surprising that the model breaks down when the liquid medium between two surfaces is only few molecular diameters in width. When two hydrated surfaces are brought into contact repulsive forces of about 1–3 nm range have been measured in water between a variety of surfaces: Clays, mica, silica, alumina, lipids, DNA, and surfactants. Because of the correlation with the low (or negative) energy of wetting of these solids with water, the repulsive force has been attributed to the energy required to remove the water of hydration from the surface, or the surface adsorbed species (secondary hydration), presumably because of strong charge–dipole, dipole–dipole or H-bonding interactions. These forces were termed hydration forces (reviews: [470–472]). The existence of hydration forces was already deduced from the observation that some dispersions are stable even at high ionic strength and from the swelling of clays in water (e.g. [473–475]).

Hydration forces are relatively short-ranged so that at salt concentrations below 0.1 M they can easily be distinguished from the longer range electrostatic and van der Waals forces. They are repulsive and, except for the case of molecularly smooth surfaces and low salt concentrations where force oscillations were observed [476], decay exponentially with distance:

$$U_A = A e^{-x/\lambda_H}. \quad (6.4)$$

Characteristic decay lengths λ_H determined with the SFA, the osmotic stress method, or the AFM range from 0.2 to 1.4 nm. Typical amplitudes are $A = 10^{-3}$ to 10 J/m^2 . In contrast to the electrostatic double-layer force, hydration forces tend to become stronger and longer ranged with increasing salt concentration, especially for divalent cations.

The origin of hydration forces is not clear. Several effects are discussed in the literature [477–479]. Certainly the fact that one layer of water molecules is bound to the solid surfaces is important. The hydration force, however, extends over more than two water layers. Israelachvili and Wennerström [472] point out that the effect of the first water layer should not be called hydration force because it is caused by the interaction between water molecules and the solid surface and not by water–water interactions. In a classic paper Marcelja and Radic proposed an elegant theory to explain the short-range repulsion by a modification of water structure near hydrophilic surfaces [480]. The water molecules near the interface are more ordered than water molecules in the bulk. Modern theories take additional effects into account. In fact, short range monotonically repulsive forces observed between inorganic surfaces are probably not only due to structured water layers propagated away from the surfaces, but to the osmotic effect of hydrated ions which are electrostatically trapped between two approaching surfaces [481]. For example the role of adsorbed ions on silica and mica was studied extensively by Vakarelski et al. [279,322].

It is quite possible that several effects contribute to the short-range repulsion. This is especially likely for the interaction between flexible surfaces such as lipid bilayers [482,483]. Molecular-scale fluctuations of hydrocarbon chains and a steric repulsion between mobile head groups may significantly contribute [484]. Molecular scale corrugations can cause a short range repulsion [485].

With the AFM the range of materials which can be analyzed has increased dramatically. The natural materials to use with an AFM are silicon nitride and silica. Short range repulsive forces were observed between silicon nitride and mica at neutral pH and in the presence of more than 30 mM MgCl_2 [16]. Meagher measured a short range repulsion between a silica sphere and an oxidized silicon wafer at pH 4.1 and with 10 mM CaCl_2 [432]. At high pH or with high concentration CaCl_2 the repulsion disappeared. Veeramasuneni et al. attached polystyrene microspheres functionalized with amino groups and silica particles to cantilevers and measured their interaction with quartz (SiO_2), sapphire (Al_2O_3) plates [454], and alkali halide crystals (NaCl and KCl) [486] at high ionic strength. Short-range repulsive forces ($\lambda_H = 0.1\text{--}1.4$ nm) were measured between similarly charged surfaces while relatively long-range attractive forces ($\lambda_H = 4\text{--}9$ nm) were observed between oppositely charged hydrophilic surfaces at high ionic strength. These results indicate that surface charges influence the hydration force.

In order to find out whether the specific structure of water is essential for the hydration interaction various authors measured forces in mixtures of water with alcohols and other organic solvents. Yoon and Vivek measured a hydration repulsion between a glass microsphere and a silica surface in pure water [453]. Addition of only 10% methanol lead to a complete disappearance of the hydration repulsion. Ethanol also decreases the repulsion and reduces the decay length. Pyridine or trifluoroethanol did not decrease the hydration repulsion. Kanda et al. observed a gradual decrease of the hydration repulsion with increasing propanol content between two silica surfaces [487]. The authors claim that alcohol reduces the hydration repulsion by replacing the first layer of water on the hydroxylated silica surfaces.

When reviewing the literature about AFM force measurements in aqueous medium many papers do not mention hydration forces. One might be tempted to conclude that most researchers did not find hydration forces. Most publications are concerned with long-range forces such as the electrostatic double-layer and the van der Waals attraction. The fact that only few papers deal explicitly with hydration forces is probably due to the problems involved. Problems arise due to deformation of the sample, the precise determination of zero distance, and contamination, which can cause a steric repulsion.

There are several reports about force curves taken between protein layers [488–491] or on biological membranes [466,492,493]. In most cases no short-range repulsive forces could unambiguously be identified. One should, however, not conclude that hydration forces were absent. The reason that short-range repulsive forces could not be identified is probably due to the facts that it is difficult to take accurate force curves on biological materials and that elastic and non-elastic deformation takes place. Often the material is pushed to the side by the tip. Some authors explicitly mention that hydration forces might have been present but that this cannot be safely concluded from the recorded results.

6.3. Hydrophobic attraction

Hydrophobic surfaces in water attract each other [494,495]. This attraction is called hydrophobic interaction. It is observed between surfaces with contact angles around or higher than 90° . For one hydrophobic and one hydrophilic surface no long-range attraction is observed [355,496]. The first direct evidence that the interaction between solid hydrophobic surfaces is stronger than the van der Waals attraction was provided by Israelachvili and Pashley [497,498]. With the SFA they observed an

exponentially decaying attractive force between two mica surfaces with an adsorbed monolayer of the cationic surfactant cetyltrimethylammonium bromide (CTAB). Since then the hydrophobic force has been studied extensively. Hydrophobic surfaces were not only made by physisorption of cationic surfactants to mica, but also by Langmuir–Blodgett deposition of surfactant monolayers [499,500]. Most of the experiments relied on the SFA and thus the restriction to mica. Some were performed with specialized set-ups such as the bimorph surface force apparatus. In these devices hydrophobic surfaces could be produced also by other methods, for example by silanizing inorganic surfaces with hydrophobic substances [501,502] and by coating surfaces with gold and alkanethiols [503]. However, routine force measurements with differently prepared hydrophobic surfaces became possible only with the AFM [504]. These include:

- silica, oxidized silicon wafers, and glass surfaces treated with octadecyl-trichloro-silane (OTS, $\text{CH}_3(\text{CH}_2)_{17}\text{SiCl}_3$) [355,496,505,506], trimethyl-chlorosilane [505,507], dichloro-dimethyl-silane [508], in fluorinated dichlorosilane [509], and hexamethyl-disilazane [180];
- hydrophobic polymer surfaces such as polystyrene [189,510], polypropylene [511], polyethylene [512];
- gold-alkanethiol coated surfaces [513];
- silica, oxidized silicon wafers, and glass surfaces with physisorbed CTAB [514,515].

Still, no single theory is available to account for all observed experimental behaviors. Even experimental results on seemingly similar systems are often contradictory, so that an understanding of the origin of the hydrophobic force remains elusive. In many cases two components of the attraction are observed [499,503,516–519]. One is short-range and decays roughly exponentially with a decay length of typically 2–6 nm. The second component is long-ranged and in some cases extends out to 100 nm.

Several hypothesis have been invoked to explain the origin of the hydrophobic force. An early theory attributes the hydrophobic attraction to surface induced change in water structure propagating between the two surfaces [520–522]. This explanation can only hold for the short-range component because it is known from simulations and other evidence that the change in structure of the liquid near a surface only persists for several molecular diameters.

Several theories assert that electrostatic correlations, electrolyte fluctuations or correlated charge domains are responsible for the attraction. All these theories predict an exponentially decaying force with a decay length of half the Debye length. Experiments, however, show that the hydrophobic force is independent of the ionic strength [509,523–525].

Force experiments with physisorbed, charged surfactants indicate that the correlated rebinding of ions, which were previously dissociated from the surfactants and the sample surface, might lead to a net attractive force [526,527]. Again, the range of the predicted interaction is much too small to account for the long-range component.

In another theory it is proposed that the attraction is due to separation induced cavitation [501,528,529]. A simple thermodynamic calculation shows that for surfaces with contact angles above 90° a vapor bridge is stable out to distances of few 100 nm [530] and should lead to an attraction [531]. The question is whether there exists a spontaneous (spinodal) formation of such a cavity when the two surfaces approach each other. Estimations of the rate of cavitation result in much too low values. Upon separation such cavities have been observed [532–534].

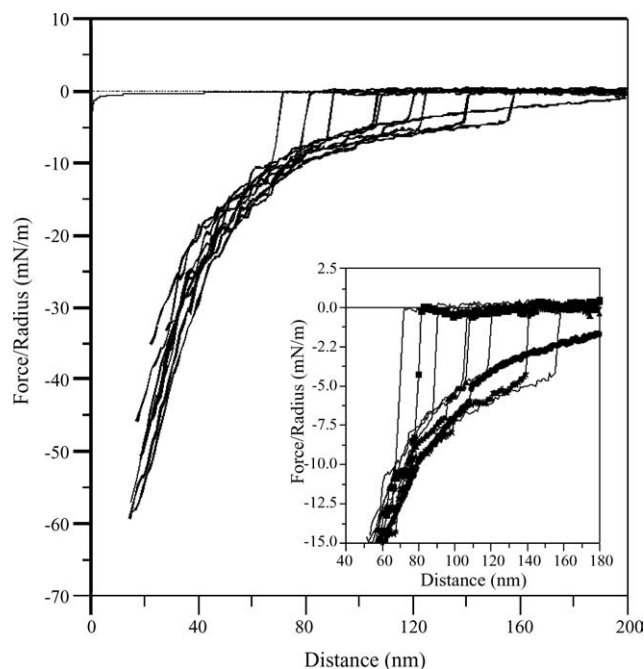


Fig. 22. Typical force curve between PE colloidal probe and silanated silica surface in nitrogen-saturated water. Separate, single measurements are shown. Thin solid line represents theoretical van der Waals forces for PE–silica system in water ($A_H = 0.72 \times 10^{-20}$ J). Inset shows subtle structure of discontinuities region. Image was adapted with kind permission from Nalaskowski et al. [538].

A last hypothesis is that submicroscopic gas bubbles, also called nanobubbles, preexist on the hydrophobic surfaces. Upon approach the bubbles form bridges between the two surfaces. Bridging bubbles give rise to the attraction. Once these gas bubbles get into contact they fuse or they serve as nucleation sites for the formation of cavities [535] and cause a strong attraction due to the meniscus force [536]. Much of this evidence for the existence of nanobubbles is provided by AFM experiments:

- Force measurements revealed steps and discontinuities at long separations [503,512,513,535,537] (Fig. 22). Each step was taken to represent the attachment of the approaching surface to a bubble on the opposite surface. After bridging the bubble grows laterally and forms a meniscus.
- Dissolved air and other gases seem to influence the long-range component of the hydrophobic force. In deaerated water, i.e., water in which dissolved gases have been taken out as much as possible, the formation of nanobubbles is very much reduced, and the force is of shorter range [507,511,514,537,539,540].
- Nanobubbles on hydrophobic surface could be imaged with the AFM in tapping mode [541–545] (Fig. 23). Being able to image nanobubbles confirms that they can be stable on hydrophobic surfaces on the time scale of an AFM experiment. It is, however, not clear whether they form spontaneously under normal conditions or only if the dissolved gas is supersaturated [545], the samples were in contact with air before being immersed in water [542], or the AFM tip itself induced bubble formation [546].

Other experiments lead to conflicting results: Neutron reflectivity on polystyrene in contact with D_2O showed a depletion layer at the interface indicating the existence of nanobubbles [544]. Neutron [547]

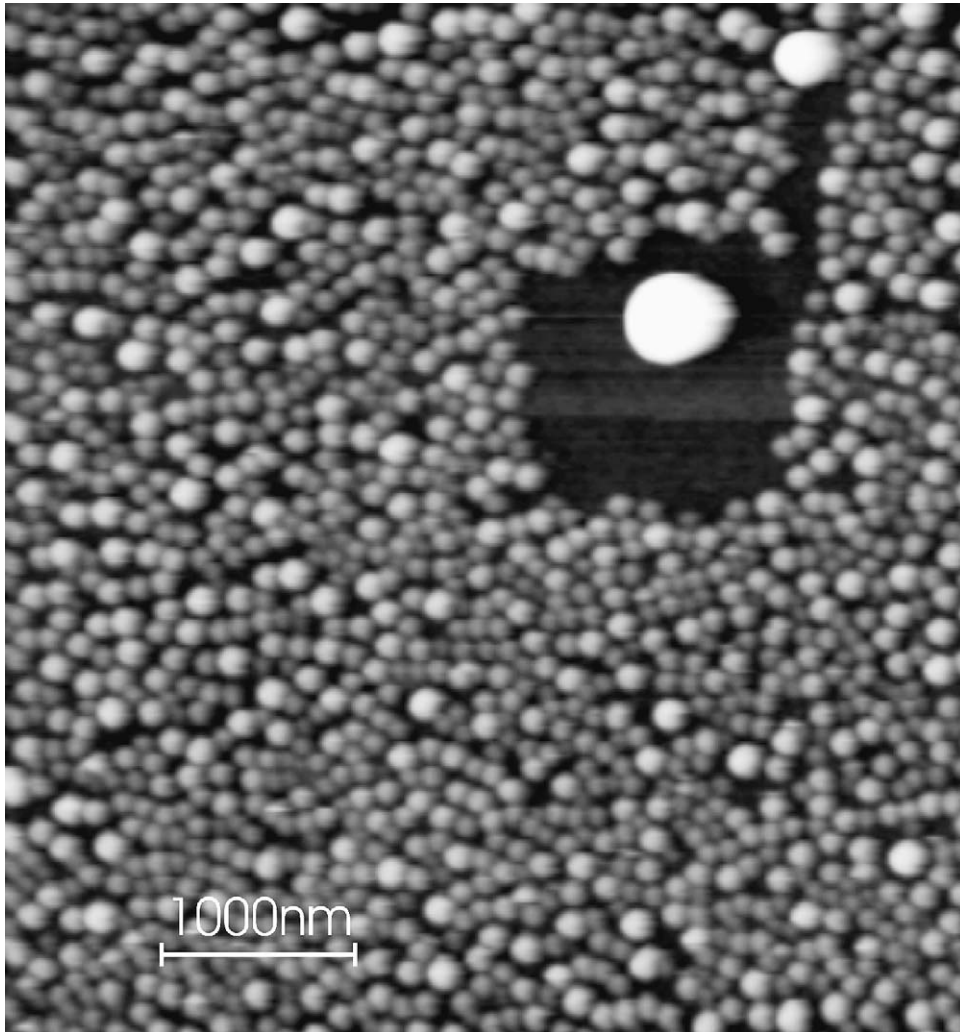


Fig. 23. AFM image of nanobubbles spontaneously formed by immersion of a hydrophobic polystyrene surface. The image was taken in tapping mode. By scanning a small region with increased tapping amplitude, the nanobubbles in this region fused to one bigger bubble. The figure was kindly provided by Klösigen [546].

and X-ray [548] reflectivity experiments confirmed the observed reduced density of water at the interface, while experiments with an ellipsometer excluded nanobubbles on silanated silica [549]. There is now strong evidence, that bridging bubbles contribute to the long-range hydrophobic attraction in many experiments [495] but the whole hypothesis and the effect of nanobubbles are still being debated [550].

One issue which is still discussed is whether the nanobubbles form spontaneously and always reside on the surfaces or if they are created by an approaching surface or even by a previous contact. In the later case the long-range component of hydrophobic force is not a “real” surface force but an interaction which is initiated by a previous contact. In fact, very long-range forces were only observed in experiments where force curves are repeatedly measured in fast succession. For AFM (and also for the bimorph surface force apparatus) this is always the case unless special care is taken. In commercial

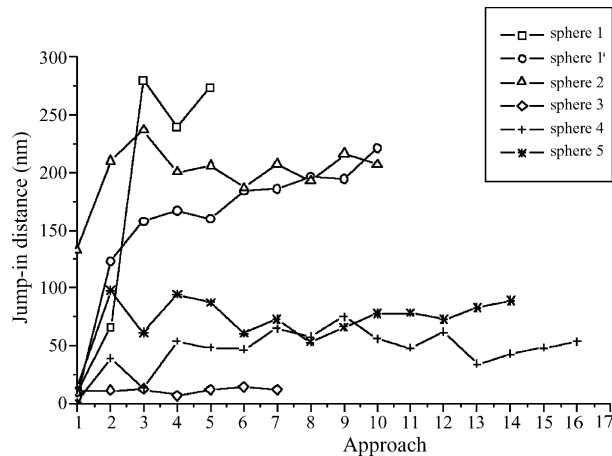


Fig. 24. Jump-in distance for different approaches between five silica spheres ($R = 2.4 \mu\text{m}$) and a silicon wafer all hydrophobized in a hexamethyldisilazane vapor. Forces were measured in pure water. Except for sphere 3 the jump-in distance increased many fold after the first force curve. Sphere 1' is sphere 1 after immersing in water for several hours. Figure was adapted from Ref. [180].

AFMs force curve are taken periodically. Usually the first force curve is not even displayed. If something changes at the first few contacts, this is likely to be overlooked. In fact when measuring the jump-in distance between two hydrophobic surfaces for the first, second, etc. contacts a strong increase was observed [180] (Fig. 24). This demonstrates that something changes at the first contact, presumably a bubble is created and in subsequent contact the interaction between the hydrophobic surface and the bubble or even between two bubbles is measured.

7. Adhesion

When retracting the tip from the sample surface, the tip stays in contact with the surface until the cantilever force overcomes the adhesive tip–sample interaction. First measurements of this pull-off force or adhesion force F_{ad} were performed by Martin et al. [551] and Erlandson et al. [552]. In the most general case the adhesion force F_{ad} is a combination of the electrostatic force F_{el} , the van der Waals force F_{vdW} , the meniscus or capillary force F_{cap} and forces due to chemical bonds or acid–base interactions F_{chem} :

$$F_{\text{ad}} = F_{\text{el}} + F_{\text{vdW}} + F_{\text{cap}} + F_{\text{chem}}. \quad (7.1)$$

In gaseous environments, significant contributions from electrostatic forces are to be expected mainly on insulators and at low humidity, when charge dissipation is ineffective. In aqueous solutions, most surfaces become charged due to dissociation of surfaces groups and electrostatic forces are important, but their magnitude also depends on electrolyte concentration (see Section 6.1). The van der Waals force (see Section 5) always contributes and in most cases it is attractive. At ambient conditions, a water neck forms between AFM tip and substrate due to capillary condensation and adsorption of thin water films at surfaces. This attractive interaction depends on the relative humidity and the hydrophilicity of tip and sample. A more detailed discussion of the meniscus force follows in Section 7.4. Depending on the

chemical end-groups present on tip and substrate, chemical bonds may form during contact or other specific chemical interactions (e.g. receptor–ligand) may occur and then often dominate the adhesion force (see Section 11.2).

In many of the AFM studies on adhesion force, conditions were chosen such that the van der Waals forces were expected to dominate. In this case F_{ad} should be given by the Hamaker constants of AFM probe and sample and by the contact geometry. Quantitative comparison of such experiments with theoretical predictions is hampered by several factors:

- Surface roughness has a pronounced influence on adhesion force that is hard to quantify.
- The precise contact geometry is often hard to determine.
- Adsorption of contaminants on high energy solid surfaces leads to chemical inhomogeneities of the surfaces.

Nevertheless, AFM force–distance curves have become an important method for studying adhesion properties, especially due to the possibility to detect spatial variations at the nanometer level.

7.1. Influence of roughness on adhesion

Already some of the early measurements of surface/particle adhesion with the colloid probe technique showed much lower values of adhesion than expected for a simple sphere/plate geometry and this was attributed mainly to the roughness of the contacting surfaces [553,554].

A simple theoretical model to describe the influence of surface roughness on adhesion was introduced by Rumpf [555]. It describes the force between spherical particle and a surface with a small hemispherical asperity centered below the particle (Fig. 25, left). The interaction force in this model is given by

$$F_{\text{ad}} = \frac{A_{\text{H}}R}{6D_0} \left[\frac{r}{r+R} + \frac{1}{(1+r/D_0)^2} \right], \quad (7.2)$$

where R is the particle radius, r the asperity radius, A_{H} the Hamaker constant and D_0 is the minimum distance between sphere and asperity (interatomic spacing). The first term of Eq. (7.2) in the bracket

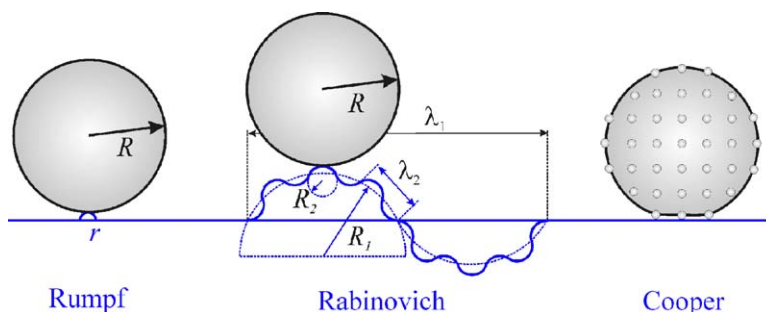


Fig. 25. Schematics of models considering the influence of roughness on adhesion. Left: model by Rumpf [555] with a single asperity of radius r . Middle: model of Rabinovich et al. [557], that considers different length scales λ_1 and λ_2 of the surface roughness, with radii R_1 and R_2 . Left: model by Cooper et al. [558], that assumes an even distribution of asperities.

describes the van der Waals force between particle and asperity and the second between particle and planar surface. The effect of the asperity is to avoid a closer contact between particle and surface, thus reducing the adhesion force. Since surface roughness is usually not determined as a mean asperity radius but typically by a root mean square (rms) value, a more applicable formulation of the Rumpf model was suggested by Rabinovich et al. [556]. They derived a relationship between rms roughness and r based on a surface model of close packed hemispherical peaks and valleys and obtained the modified equation (with rms being the rms value of the surface roughness):

$$F_{\text{ad}} = \frac{A_{\text{H}}R}{6D_0} \left[\frac{1}{1 + (R/1.48 \text{ rms})} + \frac{1}{(1 + 1.48 \text{ rms}/D_0)^2} \right]. \quad (7.3)$$

The same authors proposed a more sophisticated model that uses spherical caps instead of hemispheres [556] and can be expanded to take into account surface roughness of different length scales (Fig. 25, middle) [557]. For this model, they obtained

$$F_{\text{ad}} = \frac{A_{\text{H}}R}{6D_0} \left[\frac{1}{1 + (58R \text{ rms}_2/\lambda_2^2)} + \frac{1}{(1 + (58R \text{ rms}_1/\lambda_1^2))(1 + 1.82 \text{ rms}_2/D_0)^2} + \frac{D_0}{(1 + 1.82(\text{rms}_1 + \text{rms}_2))^2} \right], \quad (7.4)$$

where rms_1 and rms_2 are the rms values of roughness on the length scales λ_1 and λ_2 , respectively. The model was found to adequately describe the decrease in adhesion for increasing roughness on titanium deposited on silicon wafers [557]. Beach et al. [352] applied this model successfully to analyze pull-off forces of glass and lactose particles from rough surfaces (series of polypropylene coatings, polycarbonate, and acrylonitrile–butadiene–styrene). The adhesion of beclomethasone dipropionate and polystyrene particles to polypropylene was underestimated by about an order of magnitude. This was attributed to the deformation of the beclomethasone dipropionate and polystyrene particles.

Cooper et al. [558] developed a model for the adhesion of a rough particle on a smooth substrate (or vice versa), where they assumed a homogenous distribution of hemispherical asperities on a spherical particle (Fig. 25, right). The total adhesion force was then calculated as the adhesion of a single asperity times the number of asperities in contact to the surface plus the force between sphere and surface at the distance $r + D_0$. They obtained

$$F_{\text{ad}} = \left[1 + \sum_{i=1}^{i < a/x} \frac{360}{\arccos(1 - 1/2i^2)} \right] \left[\frac{A_{\text{H}}r^4}{6D_0^2(D_0 + r)^3} \left(1 + \frac{2D_0}{r} \right) \right] + \frac{A_{\text{H}}R}{6(r + D_0)^2}, \quad (7.5)$$

where a is the contact radius (which has to be calculated using one of the models of contact mechanics), r again the asperity radius, and x the distance between them. This model was applied to colloid probe measurements between polystyrene spheres and a silicon wafer at different pH values that caused different surface roughness [559] and measured adhesion forces agreed much better with this model than with DLVO theory of a sphere/plane geometry. On the basis of this model, Cooper et al. [351,560] generated computer representations of surface topographies as obtained by AFM imaging by distributions of hemispherical asperities and simulated adhesion forces between these surfaces. In a recent publication [561] rough surfaces were also modeled by fractals and a fast Fourier transform algorithm. The results of the theoretical computations yielded good agreement with adhesion force measurements.

The decrease of adhesion with surface roughness can be exploited to influence particle adhesion. Zhou et al. [562] showed that the adhesion between polystyrene spheres, alumina particles and toner particles of irregular shape with substrates of defined roughness (silicon wafers, polished and PVD-coated aluminum) can be minimized by tailoring the roughness of the contacting materials. The mean roughness alone (e.g. given by the rms value) is not sufficient to predict the adhesion behavior. As an example, Bowen et al. [563] found an increase of adhesion between a single polymer latex particle to stainless steel surfaces with decreasing roughness. On the smoothest surface, however, that exhibited regular surface features on the length scale of the particle, the adhesion was highest, probably due to high particle adhesion in valleys. It is known from powder technology that coating particles with second fraction of much smaller ones, the flowability can be improved. Quintanilla et al. [564] showed that addition of submicron sized fumed silica reduced adhesion between xerographic toner particles. Jonat et al. [565] measured a reduction in adhesion force between microcrystalline cellulose particles by addition of colloidal silicon dioxide that correlated well with macroscopic angle of repose experiments. For the adhesion between polyethylene spheres and nanostructured silicon surfaces in UHV, Meine et al. [566] found that the correlation between adhesion and effective contact area could be explained with JKR theory only if a change of the surface energy was assumed by the nanostructuring. Surface roughness not only reduces the adhesion force but also leads to strong spatial variations. For the adhesion between gold particles with diameters between 5 and 20 μm and nanostructured substrates with defined roughness, three types of distribution functions were identified [567]: for surfaces with a narrow size distribution of the asperity radii Weibull distributions are expected (a simple Weibull distribution if the particle is smooth, a bimodal one if the particle roughness is comparable to that of the substrate). For a substrate with an inhomogenous roughness, a log-normal distribution of the adhesion forces is found.

For very soft surfaces, adhesion may even increase with increasing roughness [568,569]. This happens if deformations become large enough to induce an intimate contact between surfaces. In this case the contact area will be increased compared to smooth surfaces, resulting in higher adhesion.

As Méndez-Vilas et al. showed [570], not only surface roughness but also the influence of surface geometry has to be considered. When measuring the adhesion between an AFM tip and spherical particles, they found a significant decrease of adhesion far from the top of the spheres. Sphere material and roughness had not much influence on this effect. In a later paper [571], a ratio of 1.6 for adhesion of an AFM tip on a horizontal surface versus adhesion on a surface inclined by 45° was found.

7.2. Particle adhesion

Adhesion of particles to surfaces is important in many technical applications. With the ever shrinking structural dimensions in semiconductor industry and increasing importance of nanotechnology, preparation and maintenance of clean surfaces is a prerequisite. Appropriate cleaning methods become increasingly difficult with decreasing size of the contaminants, and a proper understanding of adhesion and removal forces is important for process optimization, e.g. for chemical mechanical polishing of silicon wafers. Another growing field is the study of granular matter. Granular materials are the second-most handled material in industry (after water) [572] and can show a complex flow behavior that is hard to predict, since no rheological law exists. Therefore industrial processing of granular matter is based on empirical observations. The combination of single-particles forces with numerical simulations can lead to better predictions of powder behavior – especially highly cohesive powders as nanoparticles – and better performance in powder processing [573,574].

A well-established method to study adhesion forces between particles and planar surfaces is the centrifugal method that has been used for more than 40 years [575–582]. A significant part of the knowledge about the behavior of powders stems from such experiments. Usually the detachment force of many particles is measured in a single experiment, allowing statistical evaluation of the data. This is especially useful in the case of irregular shaped particles where the contact area and adhesion force depends on the random orientation of the particles relative to the surface. Therefore, the centrifuge technique has been used to characterize the behavior of industrial powders in pharmaceutical [583–589] or food applications [590]. There are, however, also disadvantages of this technique. One limit is that the rotational speed of the available ultra-centrifuges is limited due to the material stability of the rotor. This restricts adhesion measurements with the centrifuge method to particles larger than a few micrometer. Otherwise, the centrifugal force is not strong enough to detach the adhering particles from the surface.

A new approach for measuring the adhesion of particles to surfaces has been introduced by Hein et al. [591] who optically detected the detachment of particles from surfaces mounted onto a piezotransducer. The surfaces can be oscillated with high frequencies and the detachment force can be calculated from the particles size and the acceleration due to the oscillation. Limitations are the optical detection that set the limit for the particle size and that no defined loading force can be applied.

The introduction of the colloid probe technique [15,16] opened new possibilities to study the interaction between micrometer-sized particles and surfaces as well as interparticle forces and has led to a large diversity of research based on this method [354,592].

Biggs and Spinks [593] found an increase in adhesion of a polystyrene sphere to mica with increasing load or contact time due to plastic deformation. For a similar system (PS on Si wafer), load dependence and contact time dependence also indicated plastic and viscoelastic deformation which was indeed found by SEM imaging after the experiment [594]. The adhesion of polystyrene spheres to elastomers surfaces was higher for the more compliant materials [595]. Toikka et al. [596] combined AFM and SEM to evaluate the contact area between a glass particle and a soft PDMS surface during force measurements. Furthermore, for the adhesion between a spherical zirconia particle and a polyester film they found an increase by almost 2 orders of magnitude as the polymer was heated above its glass transition temperature. A linear dependence of adhesion force on the reduced radius $R_{\text{eff}} = R_1 R_2 / (R_1 + R_2)$, where R_1 and R_2 are the radii of the two particles, was found by Heim et al. [597] for the adhesion between silica spheres, proving the validity of the DMT theory also for particle sizes down to dimensions below 1 μm . The data of this experiment are shown in Fig. 26. It also demonstrates the relatively large scatter of the adhesion force values in spite of the fact that an almost ideal system with well-defined surface chemistry and minimal surface roughness was used. The variation of adhesion forces for consecutive force cycles was very small (error bars equal to the size of the single data points). But when the adhesion between two different pairs of particles with the same radius is compared, the large deviations are observed. The forces between spherical PS and Au particles did not show any dependence on number of contacts or on load for forces up to 1 μN [598]. The linear dependence on particle radius was also confirmed by Skulason and Frisbie [316] for even smaller radii using AFM tips. The force between a gold coated tip and a gold surface was measured by AFM and the shape of tip and sample as well as the size of the contact area were imaged by a transmission electron microscope [599]. The results were found to agree with the Maugis theory. Adhesion forces observed between spherical alumina particles [600] and these particles and ceramic surfaces [601] could be modeled by the van der Waals forces between the particles taking into account an adsorbed layer of water at the surfaces and deformation of the surfaces. Interaction of AFM tip

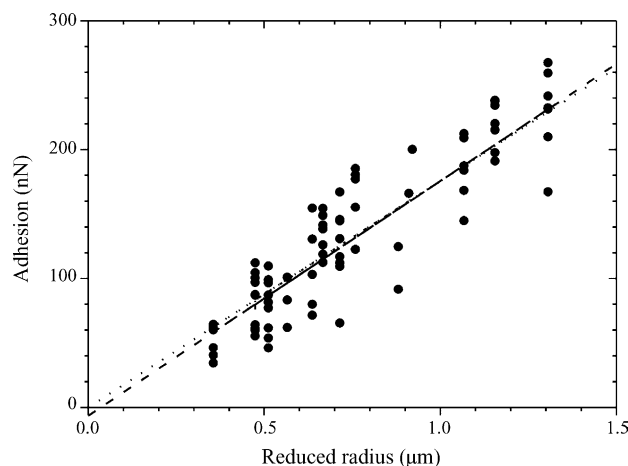


Fig. 26. Dependence of the adhesion force between pairs of silica particles on the reduced radius $R_{\text{eff}} = R_1 R_2 / (R_1 + R_2)$, where R_1 and R_2 are the radii of the two particles [597]. Each data point is an average of seven adhesion measurements obtained with one pair of microspheres. The linear dependence of adhesion on reduced radius as predicted by the JKR and DMT theory is confirmed. The dashed line is a linear regression fit of the measured data; the dotted line is the best linear fit of the data that passes through the origin.

with an Al–Ni–Co quasicrystal surface was found to lead to tip deformation and material transfer for the clean high energy surface in UHV, after surface oxidation tip deformation did no longer occurred [602].

Adhesion between silica nanoparticles (50 nm diameter) and a silicon nitride tip was measured by Batteas et al. [603] in aqueous solution as a model for inter-particle forces. pH was varied between 3 and 9, and the maximum adhesion force was found to occur at pH 4–5. Surface energy of the silanol-covered surfaces was found to be 7.5 mJ/m^2 . Effect of different cleaning solutions used in chemical mechanical polishing of wafers in the semiconductor industry on the adhesion force was evaluated with silica colloid probes [604]. Lowest adhesion was found in a solution with citric acid, benzotriazole and NH_4OH which also exhibited the best cleaning performance. Cooper et al. [605] measured the adhesion of alumina particles to copper, SiO_2 , and tungsten films in solutions common in semiconductor processing. Adhesion of polystyrene and glass particles on a copper electrode during the electrodeposition of copper was studied by Dedeloudis and Fransaer [606]. Results of interaction forces correlated well with sedimentation co-deposition experiments. As a model for salt aerosol retention at surfaces, interaction of a salt crystal colloid probe and a metal oxide surface was studied, taking into account probe dimensions, surface chemistry, and relative humidity [607]. Meurk et al. [608] found an increase of adhesion for silicon nitride granules from spray drying with content of polyethylene glycol (PEG) binder and humidity that leads to a softening of the PEG binder. Adhesion between two gypsum ($\text{CaSO}_4 \cdot 2\text{H}_2\text{O}$) crystals in air and ionic solutions as a model system for solidification of plaster was studied by Finot et al. [176,609,610]. In cement paste, cohesion results from the interactions between calcium silicate hydrate (CSH) surfaces in an interstitial ionic solution. AFM between CSH surfaces in different electrolytic solutions ($\text{Ca}(\text{OH})_2$, CaCl_2 , NaCl and NaOH) showed that forces were electrostatic in origin, but differed from DLVO theory [611]. Paiva et al. [612] used the AFM as a micro-tack-tester for pressure sensitive adhesives to probe the local variations in adhesion depending on the tackifier distribution in the material. In a similar way, adhesion of an AFM tip was used as a micro-tack test to monitor the curing behaviors of

Korean Dendropanax lacquer in order to optimize curing conditions [613]. Barber et al. [614] mounted multiwalled carbon nanotubes AFM tips and immersed them into molten polymer. Pullout from the polymer matrix after air cooling showed high interfacial shear strength ($4\text{--}70\text{ J/m}^2$) that increased for smaller nanotube diameters. Force curves on layers of entangled multiwall carbon nanotubes were recorded with Si_3N_4 tips [615]. Depending on the maximum applied force, the response of one or several nanotubes was probed. The resulting jump features could be reproduced in numerical simulations of the layer-AFM tip system mechanical analysis. Poggi et al. measured the interaction between SAM coated AFM tips and a single walled carbon nanotube. They observed a direct correlation of adhesion force to the thiol terminal group ($\text{NH}_2 > \text{CH}_3 > \text{OH}$).

The application of the colloid probe technique to the study of systems relevant for the flotation technique has not been limited to bubble particle interactions (see Section 9.1), but also interparticle forces have been investigated. Muster et al. [616] studied the interaction between zinc sulfide particles under conditions typical for the refinement of zinc ores. Surface forces between a fractured sphalerite surface and a silica particle at different pH and ionic conditions were found to correlate with sphalerite–silica heterocoagulation tests [617]. Fa et al. [618] prepared spherical particles of calcium dioleate which is used as collector colloid in flotation of calcites and fluorites. A much stronger attractive force and adhesion was found for fluorite surfaces compared to calcite surfaces. The interactions between cleaved talc surfaces and toner particles, as a model for the improved ink removal by a talc-assisted deinking process were studied by Chi et al. [619]. The comparison of measured force profiles with those calculated using the classical DLVO theory indicated the presence of hydrophobic attractive forces. Nalaskowski et al. [620] measured the interaction of polyethylene particles and silica surfaces in aqueous solution as a model for oil release from soil particles. Omoike and Horton [621] investigated the adhesion between aluminum hydroxide particles and a Si_3N_4 tip in presence of phosphate and tannic acid as a model for removal of phosphate and other contaminants in wastewater treatment. To model the immobilization of actinides by humic acid, Plaschke et al. [622] measured the adhesion force between an AFM tip covered with humic acid and a mica surface in aqueous solution in presence and absence of Eu(III). Adhesion increased one order of magnitude by addition of Eu(III). Sticking probabilities for $2\text{ }\mu\text{m}$ carboxylated polystyrene microspheres on a silica glass plate in aqueous solutions of different pH and ionic strength were found to be higher in AFM force measurements than expected from DLVO model calculations [623]. Adhesion force characteristics of stainless steel, polymethylmethacrylate and polytetrafluoroethylene coupons correlated with the rate of struvite ($(\text{NH}_4)\text{MgPO}_4\cdot 6(\text{H}_2\text{O})$) mineral deposition, indicating that lower energy materials are less prone to unwanted build-up of struvite layers.

7.2.1. Adhesion of drug substances

Inhalation of aerosols is an important route for pulmonary drug delivery, e.g. in asthma treatment. For efficient penetration of the drug particles deep into the lung, their aerodynamic diameter should be smaller than $5\text{ }\mu\text{m}$. With the ban of chlorofluorocarbon propellants due to environmental risks, dry powder inhalers have been introduced. Delivery of the correct dose to the respiratory tract depends on the cohesive and adhesive properties of the powder formulations. Often carrier based powder formulations are employed, where drug particles adhere to larger carrier particles – usually lactose – to avoid drug particle agglomeration. During the inhalation process, the drug particles must be set free from the carrier particles in order to be delivered to the target. Since the control of particle size and interparticle force is fundamental for the function of dry powder inhalers, quite a few studies have applied the AFM colloid probe technique to this field (for a review see Ref. [624]).

Sindel and Zimmermann [625] studied the adhesion between crystalline α -lactose monohydrate (Granulac 200) particles and a Granulac 200 pellet. Muster and Prestidge [626] measured adhesion forces of a hydrophobic colloid probe with different faces of the model pharmaceutical crystals *N,n*-octyl-D-gluconamide and sulfathiazole. Results were found to correlate well with contact angle values on the different crystal faces. The interaction forces of micronized salbutamol particles (colloid probe) with different substrates yielded a ranking of adhesion as glass > lactose > salbutamol > polytetrafluoroethylene (PTFE) [627]. Tribocharging was observed for PTFE on repeated contact. Berard et al. [628] studied influence of humidity on the adhesion between lactose particles and the surface of zanamivir crystals. By comparing cohesive versus adhesive forces, Beagat et al. [629] concluded that a budesonide/lactose powder formulation would exhibit poor blend homogeneity, whereas for salbutamol/lactose good blending is expected. A possible approach to reduce adhesion forces between drug and carrier particles are ternary blends with additional small particle fractions that reduce the effective contact area [630].

Porous silica particles were found to be more effective as flow agents than solid ones due to their higher surface roughness that resulted in lower adhesion [631]. Adhesion forces between probes of salmeterol xinafoate or silica and different lactose surfaces were higher for those lactose samples, where small particle fractions have been removed [632]. The adhesion of steroid type drug particles decreased with increasing roughness of the lactose substrate. Adhesion was higher on stainless steel, and increased with humidity [633]. Young et al. used beclometasone dipropionate probes to test the effect of different surface modifications of the lactose carrier surface on the adhesion force.

Adhesion forces between salbutamol sulphate and triamcinolone acetonide drug particles increased with humidity, whereas it decreased for a disodium cromoglycate (DSCG) surface due to decreased electrostatic attraction [634]. Adhesion of individual lactose particles to the surface of gelatin capsules employed in dry powder inhalant drug delivery systems showed that gelatin surfaces with higher surface heterogeneity and higher-contrast friction exhibited higher adhesion and that contaminations by mould release agents from capsule production can be a key factor for the adhesion properties [635]. Young et al. [636] probed the adhesion of salbutamol sulfate to pressurized metered dose inhalers canister materials in a model propellant. Median separation energy values followed the rank order borosilicate glass > aluminum > PTFE, suggesting PTFE to be the most suitable canister coating. To model the interactions in a pressurized metered dose inhaler (pMDI), the interaction forces between inhalable formoterol fumarate dihydrate particles and aluminum surfaces were measured in the model propellant 2H, 3H perfluoropentane in presence and absence of stabilizing polymers (PEG 1000 and PVP K25) [637]. Addition of the polymers reduced the attractive forces, but could not completely suppress them. Hooton et al. compared the adhesion force between micronized and SEDS (solution-enhanced dispersion by supercritical fluids) prepared salbutamol sulphate particles in a liquid environment consistent with that of a pressurized metered dose inhaler with HOPG. Work of adhesion was found to be lower on the SEDS particles [638]. The adhesion between AFM tips and pellets of the above salbutamol sulphide particles and the particles and HOPG in humid air showed a maximum in adhesion at low (22%) to medium (44%) values, depending on the surface roughness [639].

Interaction of an iron coated AFM tip and different drug compounds (ibuprofen, ketoprofen, and flurbiprofen) was studied as a model for adhesion in tablet compression [640]. Ranking of work of adhesion was in agreement with molecular simulations. Magnesium stearate and sodium stearyl fumarate have found usage as lubricants in a wide range of pharmacological formulations. Adhesion forces for these lubricants were found to be typically half of the values for lactose, 4-acetamidophenol, and

naproxen by measuring the forces between a steel colloid probe and surfaces of pellets of these materials [641].

7.2.2. Interaction of membranes and particles

An industrial application where the interaction of small particles with surfaces is of critical importance is filtration. High adhesion of particle to the filtration membrane will promote membrane fouling increasing operation costs. Therefore AFM force–distance curves have been used to characterize interaction forces between different colloid probes and filtration membranes (reviewed by Hilal et al. [642]).

Bowen et al. [643] used a bovine serum albumin coated colloid probe and a yeast cell probe with different polymeric ultrafiltration membranes (ES 404 and XP 117, PCI Membrane Systems, UK). They showed lower adhesion at the XP 117 membrane that is made from a mixture of polymers chosen with the aim of achieving low fouling. Adhesion force between a silica colloid probe and a rough reverse osmosis membrane (AFC99) in NaCl solutions was found to be smaller on roughness peaks and higher inside of valleys [644]. Hence, the authors suggest the use of membranes with tailored roughness to avoid membrane fouling by particles. Adhesion of polystyrene particles to three different nanofiltration membranes was greater than that of silica particles, due partly to greater electrostatic double-layer repulsion between the negatively charged membranes and silica, and partly to short-range repulsive interactions associated with the silica surface [645]. Electrical double layer interactions between a silica particle and a Desal nanofiltration membrane were measured in electrolyte solutions [646]. With increasing ionic strength and membrane roughness, experimental results began to deviate from theoretical DLVO predictions. The interactions between laboratory manufactured polysulfonate membranes (SPEEK/PSU and PSU) and two commercial membranes (PCI ES404 and EM006) with different solutes (silica, latex, cellulose, BSA, yeast, spores) have been directly measured and linked to process performance [647]. A colloid probe coated with molecular imprinted polymer [648] was used to test the adhesion of this type of polymer to different microfiltration membranes (polyvinylidene fluoride, hydrophilic and hydrophobic versions and polyethersulfone) for the development of membranes that show specific interaction with biomolecules [649]. Adhesion of a silica sphere coated with BSA to polyethersulfone membranes was tested by the same group [650]. Photografting of a polymer (quaternary 2-dimethylaminoethylmethacrylate) to the membrane lead to a reduction of adhesion and was therefore proposed as promising way to improve fouling resistance. Forces between colloid probes (silica, alumina and polystyrene) and reverse osmosis membranes (Desal CD and SG) on approach were analyzed by Brant and Childress [651] and were found to be well described by DLVO/extended DLVO theory. In a later study of these authors [652], adhesion of a silica and polystyrene colloid was measured on three commercially available hydrophilic water treatment membranes. The results could not be resolved through classic DLVO analysis alone but could be explained by considering the magnitude of the surface's electron-acceptor and electron-donor components. By measuring the adhesion between a series of membrane substrates of different surface energies (polyvinylidene fluoride, regenerated cellulose and polyethersulfone) and an extracellular polysaccharide secreted by *Pseudomonas atlantica*, Frank and Belfort [653] showed that the ionic strength of the aqueous solution critically determines their mutual adhesion. Adhesion of polystyrene and silica particles to HYFOLN AD membranes was measured in NaCl solution at three different concentrations to quantify their likely fouling tendencies [654]. A carboxylate modified AFM colloid probe was used as a surrogate for humic acid, the major organic foulant in natural waters to test the adhesion of foulants to nanofiltration membranes. Ca^{2+} ions were confirmed to enhance natural organic matter

fouling by complexation and subsequent formation of intermolecular bridges among organic foulant molecules [655].

7.3. Adhesion in MEMS and proteins

For MEMS, stiction between the components can lead to permanent failure of the devices. AFM has proven as a valuable tool to study friction at the micro- and nano-level and is widely used in testing anti-stiction coatings for MEMS (reviews [656,657]). Vögeli and von Kanel [658] used AFM force measurements to approach the problem of sticking for the construction of a microgripper. Another possible application of AFM in the field of MEMS can be a direct test of the forces necessary to move single parts of a MEMS device. Examples for a common MEMS device are digital mirror devices used in digital projection displays (DMDs). Liu and Bhushan [659–662] used an AFM to test the frictional and mechanical properties of the hinge of the DMD and the force necessary to tilt the mirrors. The adhesive force on the landing sites were measured for different materials. This type of approach can give useful information to avoid stiction problems in MEMS devices.

Adhesion of proteins to surfaces is important in biology and for medical and industrial applications. Depending on the application, protein adsorption should be minimized, e.g. to avoid thrombosis or inflammation by bacterial adhesion, or maximized. Furthermore, adsorption of proteins to surfaces can also be used to reduce adhesive properties due to steric repulsion from the protein layer.

Snellings et al. [663] found reduced adhesion of human serum albumin (HSA) coated tips to surfaces coated with PEG polymer brushes. Force–distance curves with a Si_3N_4 tip (uncoated or coated with polypropylene or fibrinogen) on PMMA intraocular lenses (used for surgical replacement of natural lenses) with and without hyaluronan coating were studied by Casinelli et al. [664] in 0.1 M NaCl. Hyaluronan coating leads to complete suppression of adhesion except for the fibrinogen, where adhesion was reduced strongly. Ocular mucins of humans were covalently bound to an AFM tip and adhesion forces between such tips and mica were measured [665]. Mucin functionalized tips did not adhere to layers of mucins deposited on mica. This matches the nonadherence of the mucin gels on the eye lid and cornea during blinking. Adhesion of interferon alpha-2a to borosilicate glass could be reduced by 40% by a new commercial coating for reduced protein adsorption [666]. Sethuraman et al. [667] studied protein adhesion surfaces functionalized with different endgroups, using colloid probes coated with proteins (ribonuclease A, lysozyme, bovine serum albumin (BSA), immunoglobulin, γ -globulins, pyruvate kinase, and fibrinogen). Adhesion increased with hydrophobicity of the surfaces, and the self-adhesion of proteins increased with protein size. Adhesion in aqueous buffer solution between AFM probes functionalized with BSA were employed to recognize liposome adsorption on dextran coated surface plasmon sensor chips [668]. Analysis of the maximal adhesive force and adhesion energy reveals a stronger interaction between BSA and the dextran matrix compared to the lipid covered surfaces. It could be concluded that the sensor chip surface gets completely covered by lipid when injecting lipid vesicles. The adhesion force between Si_3N_4 AFM tips in water and HSA adsorbed on CH_3 - and COOH -terminated SAMs was found to decrease with time on the CH_3 surface but to stay constant on the COOH -terminated surface [669]. This was interpreted in terms of a stronger interaction of HSA with the COOH surface that did not allow reorganization of the HSA layer. BSA coated AFM tips were used to probe the interaction with BSA, anti-BSA, SAMs (CH_3 , OH , COOH , and NH_2), and dextran [368]. No adhesion to the dextran surfaces was found due to steric repulsion or hydration pressure. Adhesive properties of a recombinant mussel adhesive protein Mgfp5 expressed in *Escherichia coli* were shown to be superior as compared to a

commercial mussel adhesive extract (Cell-Tak) by measuring the adhesion between a glass bead and a glass slide in the presence of the Mgf5 in solution [670]. The dominant interactions between a marine mussel adhesive protein, *Mytilus edulis* foot protein 1 (Mefp-1), and polymeric surfaces in seawater appeared to be polar in nature (and possibly chemically specific pi–pi interactions for one of the surfaces) and not dispersive [671]. The influence of ionic conditions on the adhesion of Mefp-1 on a silica substrate was also studied [672]. The increase in adhesion was smallest for monovalent ions (NaCl, KCl), intermediate for divalent ions (MgCl₂, CaCl₂, Na₂SO₄) and strongest for trivalent ions (FeCl₃). Luckham [320] used an AFM tip coated with the Cholera toxin B subunit and a lipid monolayer containing the glycolipid GM₁ as model for viral attachment to cell surfaces. Binding forces between GM₁ coated tip and cholera toxin B immobilized on silica surface were three times higher in distilled water than in PBS buffer, and a dramatic increase of adhesion with decrease of velocity of the force-curve (Z-scan rate) was observed [673]. The forces between the siderophore azotobactin linked covalently to an AFM tip and the minerals goethite (alpha-FeOOH) and diaspore (alpha-AlOOH) were measured in aqueous solution [674]. Specific interaction of azotobactin with the iron oxide surface could be observed and responded to changes in pH and ionic strength in the expected manner. Pluronic-PAA, a copolymer composed of side chains of poly(acrylic acid) (PAA) grafted onto a backbone of Pluronic copolymer, is of interest as a vehicle for controlled drug release. Pluronic-PAA modified microsphere and mucous substrates were used to test its bioadhesive properties [675]. Chitosan membranes where butyl, octyl and hexadecyl moieties had been introduced into chitosan were probed with BSA-coated AFM tips [676]. It is proposed that protein adsorption can be tuned by adjusting the lengths of the introduced side-alkyl moieties. Adhesion between calcium oxalate monohydrate, the primary constituent of kidney stones, and different functional groups was found to depend on the crystal faces and the presence of soluble additives, including urinary macromolecules [677].

7.4. Meniscus force

When imaging fragile samples with the AFM, forces between tip and sample should be minimized as far as possible to avoid damage. Under ambient conditions, reduction of forces is limited by the existence of the meniscus force that arises from capillary condensation around the contact sites between tip and surface. One way to avoid the meniscus force is to do imaging in water [6].

The fundamental equation for capillary condensation is the Kelvin equation. It describes the dependence of vapor pressure of a liquid on the curvature of the liquid:

$$RT \ln \frac{P}{P_0} = \gamma V_m \left(\frac{1}{R_1} + \frac{1}{R_2} \right). \quad (7.6)$$

Here R is the gas constant, T the temperature, V_m the molar volume of the liquid, P_0 the vapor pressure of the planar liquid, P the vapor pressure of the liquid with the curved surface, γ the surface tension of the liquid, and R_1 and R_2 are the principal radii of curvature. A consequence of the dependence of vapor pressure on curvature is the phenomenon of capillary condensation. The effective vapor pressure for a curved surface of a meniscus between a sphere and a planar surface as in Fig. 27 is reduced compared to a planar surface and therefore condensation can occur already at relative humidity much below 100%, if the radii of curvature are small. The formation of a meniscus by capillary condensation leads to an attractive force between sphere and plate. This so-called meniscus or capillary force is caused by the pressure difference between the liquid and the surrounding vapor phase (additionally, there is also a

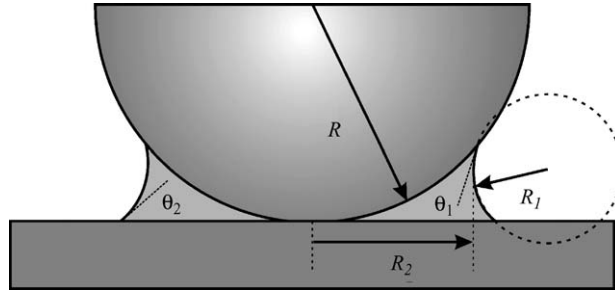


Fig. 27. Schematic of a water meniscus between a sphere with radius R and a plate. R_1 and R_2 are the two principal radii of curvature for the water meniscus, θ_1 and θ_2 are the contact angles for water on the sphere and the plate, respectively.

contribution from the surface tension of the liquid pulling at the three phase contact lines, but this contribution is usually smaller). It is given by the Young–Laplace equation:

$$\Delta P = \gamma \left(\frac{1}{R_1} + \frac{1}{R_2} \right). \quad (7.7)$$

The resulting capillary force F_{cap} between a plate and a sphere with radius R has been calculated by O’Brien and Hermann [678] to be

$$F_{\text{cap}} = 2\pi R\gamma(\cos \theta_1 + \cos \theta_2), \quad (7.8)$$

where θ_1 and θ_2 are the contact angles between the two surfaces and the liquid. The validity of this equation has been proven for meniscus dimensions of ~ 1 nm [679,680]. The total adhesion force in presence of a meniscus will then be given by the sum of the meniscus force and the direct solid–solid contact adhesion. The relative contributions of meniscus, van der Waals and electrostatic force under ambient conditions (50% humidity) for the adhesion of an AFM tip to graphite, mica and MoS_2 were elucidated by Ouyang et al. [681]. In all cases, the meniscus force was found to give the largest contribution. As obvious from Eq. (7.8), meniscus forces are expected to be maximal for hydrophilic surfaces (small contact angle) and to vanish for very hydrophobic surfaces. The expected decrease of the adhesion force with increasing hydrophobicity has indeed been observed by several authors [682–688].

An obvious limitation of Eq. (7.8) is the fact that it does not contain any dependence on the value of relative humidity, which does not reflect our childhood experience that meniscus forces increase with humidity: building a sand castle will not work with dry sand but very well with wet one. More generally speaking, granular matter is known to become more cohesive with increasing humidity and often a critical humidity is observed above which handling of the powders gets difficult. Bocquet and Barrat [689] introduced a model that includes effect of surface roughness. Capillary condensation occurs at the small nano-sized contacts of the surface asperities, leading to many small menisci instead of one large (Fig. 28). Formation of liquid bridges by filling the pores between the asperities would finally result in one large meniscus and a high meniscus force. Assuming that capillary condensation is an activated process (energy barrier to condensate enough liquid to fill the pore volumes from undersaturated vapor) they get a humidity and time-dependent meniscus force:

$$F_{\text{cap}}(t) \approx \gamma d \frac{1}{\ln(P_0/P)} \ln \left(\frac{t}{\tau_0} \right) \quad (7.9)$$

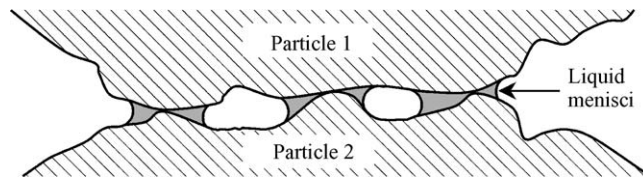


Fig. 28. Schematic diagram of capillary condensation between rough surfaces. At lower humidity, menisci will form only at the contacts of the asperities.

where P/P_{sat} is the relative humidity, τ_0 is a time constant of the order of the time needed to condense one liquid layer, and d is an effective distance taking into account the geometrical characteristics of the contacts. They observed good agreement with this model when looking at the increase in angle of repose of model substances with time and humidity. An analogous experiment on the nanoscale was done by Ando [690]. They used microfabricated silicon arrays of asperities and AFM silicon probes with a flat of $0.7 \mu\text{m} \times 0.7 \mu\text{m}$ at the end. Adhesion forces increased with humidity on the arrays but did not on single asperities, indicating that humidity increased the number of asperities contacted by the flat tip. Fuji et al. [691] found a reduced dependence of adhesion on relative humidity for porous silica particles compared to solid ones. This was attributed to the larger roughness/pore size of the porous particles that hindered the formation of capillary bridges. Ata et al. [692] showed by experiments with a smooth spherical particle and flat surfaces of alumina, silver, and titanium-coated Si wafers that surface roughness can lead to an almost complete reduction of the capillary force. This was attributed to an interaction geometry, where the meniscus is formed between a small asperity and the particle. In this case the meniscus is expected to be very thin and will not much affect the adhesion force. Rabinovich et al. [693] developed a model for the influence of roughness on meniscus force similar to the Rumpf model (see Fig. 25, left), where a single asperity between tip and surface is completely covered by the meniscus and verified it by AFM experiments. Biggs et al. [694] found that forces between a silica sphere and a silica plate increased by a factor of 5–7 for humidity above 60%, but absolute adhesion force values were always smaller than expected. This was attributed to surface roughness. Upon retraction of the colloid probe from the surface, long range force indicated neck formation and pooling of liquid between the surfaces immediately after the neck is broken.

It should also be noted, that Eq. (7.9) describes the maximum capillary force that is acting when the surfaces are in contact. As soon as the surfaces start to separate, the liquid meniscus has to decrease rapidly in order to maintain its equilibrium radius. Thus, the meniscus force should decrease rapidly leading to a jump-out of the cantilever. However, in the case of nonvolatile liquids, or high enough retraction speeds, the liquid volume would be conserved, leading to a different behavior. Rabinovich et al. [695] studied the meniscus force between glass microspheres and silica substrates in presence of an oil droplet and found good agreement with theoretical predictions using a constant volume boundary conditions. The influence of the retract speed was probed by Wei and Zhao [696] who found an increase of measured meniscus force with tip velocity.

More elaborate theoretical models to describe the meniscus force have been developed in recent years by de Lazzer et al. [697] and Stifter et al. [698] to describe the interaction of an AFM tip with a planar surface. Sirghi et al. [699] extended the model by de Lazzer [697] to include local curvature of the sample surface. It was shown both theoretically and experimentally that the sample local curvature strongly affects the adhesion force. Compared to a flat sample surface, a larger/smaller adhesive force for a

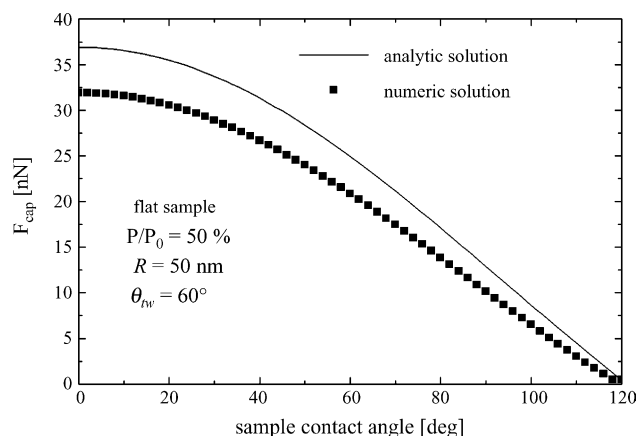


Fig. 29. Dependence of the AFM tip–sample meniscus force on the sample contact angle as calculated by Sirghi et al. [701] for a tip radius of 50 nm, a tip contact angle of 60° and a relative humidity of 50% (from [701] with kind permission from Sirghi).

concave/convex local curvature is found. Sedin and Rowlen [700] proposed a model where humidity dependence shows a step-like behavior: For humidity below a critical threshold value, the adsorbed amount of water is too small to form a meniscus, above the critical value enough water is always present and adhesion becomes high. Such a step-like behavior was observed for experiments with silica, quartz, mica, and HOPG. Sirghi et al. [701] developed a model for the dependence of the meniscus force on water contact angle (see Fig. 29) to tip and substrate and used it to characterize the hydrophilicity of TiO_2 films. The macroscopically observed changes in contact angle induced by UV treatment were reflected in the changes in adhesion force and width of force distributions gave insight in the homogeneity of the surface chemistry. Xiao and Qian [684] developed a theoretical description that includes capillary force, surface tension force, the van der Waals force in presence of the meniscus, and takes into account the precise tip shape. The contributions of the different components of the total adhesion force in dependence on humidity are plotted in Fig. 30. For strongly hydrophilic surfaces the model predicts an increase followed by a decrease of adhesion with humidity, whereas for hydrophobic materials no significant influence is expected. This was indeed observed for Si_3N_4 tips on a silicon wafer and a *N*-octadecyltrimethoxysilane SAM, respectively. Furthermore, a strong influence of tip geometry on the humidity dependence was found.

Jones et al. [686] found that adhesion on hydrophobic substrates increased uniformly with humidity and values for small contacts were predicted by simple Laplace–Kelvin theory. For microspheres, values were too small compared to theory, due to surface roughness. For a hydrophobic glass surface, an anomalous behavior was observed: Pull off force was maximal for 20–40% relative humidity and decreased again for higher humidity.

Due to the significant impact of meniscus forces on the flow behavior of powders, several studies have focused on the humidity dependence of adhesion for several commercially relevant powders like hydrated alumina, a silica aerogel, limestone, titania and zeolite [702] or pharmaceutical products like α -lactose monohydrate, salbutamol sulphate, budesonide, triamcinolone acetonide, and disodium cromoglycate [634,703,704]. Duong et al. [705] used force–distance curves on 900–1100 μm glass beads that were exposed to different amount of water in a shaker. A clear correlation between amount of

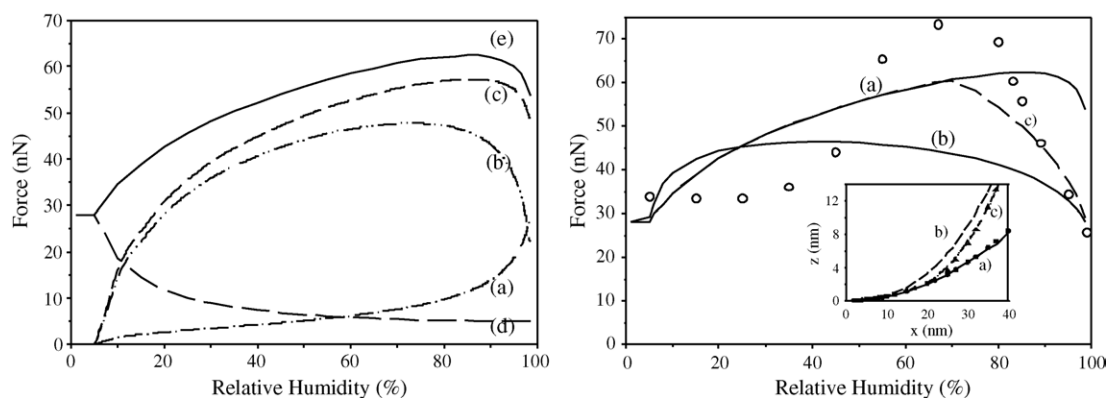


Fig. 30. Left: contributions of (a) surface tension force, (b) capillary pressure force, (c) total meniscus force, (d) van der Waals force, and (e) total (adhesion) force for different values of relative humidity. Parameters used were: tip radius $R = 100$ nm, tip–plane separation 2.5 Å, contact angles $\theta_1 = 60^\circ$ and $\theta_2 = 0^\circ$, surface tension $\gamma = 73$ mJ/m², and volume per molecule 0.03 nm³. Right: adhesion force between a Si₃N₄ tip and a SiO₂ surface for different tip profiles. The inset shows one half of the symmetric tip profiles, x is the lateral distance from the tip apex. (a) Parabolic tip, (b) and (c) “dull” tips. Lines show calculated values, open circles are experimental results (both figures from [684]).

water, adhesion force of the AFM tip due to capillary forces and particle size segregation in the shaker was observed.

As a summary, meniscus forces can show a complex and rich behavior depending on surface roughness, interaction geometry and hydrophilicity. Often quite different dependencies of adhesion force on humidity are reported for the same system, e.g. for mica [700,706,707], and the increase of adhesion with humidity is either reported to be step-like [694,700], linearly increasing [686,708] or exhibiting a maximum at intermediate values [707,684]. These discrepancies need clarification. Kinetics of neck formation and distribution of water layers at the surface are still open questions. Last but not least, capillary condensation can occur not only from the vapor phase but was also found in binary mixtures [709,710].

8. Confined liquids: solvation forces and adsorbed layers

8.1. Overview

Often the liquid structure close to an interface is different from that in the bulk. For many fluids the density profile normal to a solid surface oscillates about the bulk density with a periodicity of about one molecular diameter, close to the surface. This region typically extends over a few molecular diameters and is particularly pronounced for a strong liquid–wall interaction. In this range the molecules are ordered in layers. When two such surfaces approach each other, layer after layer is squeezed out of the closing gap. Density fluctuations and the specific interactions cause an exponentially decaying oscillatory force; the period of the oscillations corresponds to the thickness of each layer (Fig. 31). Such forces were termed solvation forces because they are a consequence of the adsorption of solvent molecules to solid surfaces [711]. Exponentially decaying oscillatory solvation forces across confined liquids were first predicted by computer simulations and theory [711–723]. Experimental proof came a

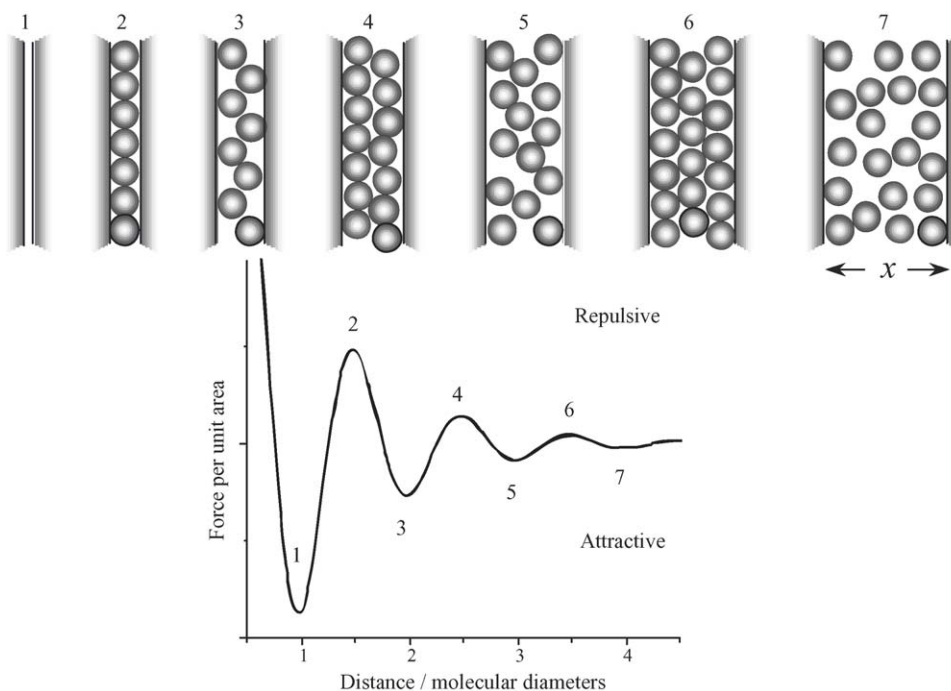


Fig. 31. Schematic structure of a simple liquid confined between two parallel walls. The order changes drastically depending on distance, which results in an oscillatory force.

few years afterwards [724–727]. Solvation forces are not only an important factor in the stability of dispersions. They are also important for analyzing the structure of confined liquids.

In this section we also discuss force curves measured on solid supported lipid bilayers [728–731], surfactant layers [732–737] and adsorbed layers on solid surfaces. Lipids or surfactants can form adsorbed layers at the solid surface. Often these layers are two-dimensional liquids: Individual molecules can more or less diffuse laterally but are still confined in normal direction. The AFM tip penetrates this layer when the load is high enough. Then a sudden jump into direct contact with the solid surface occurs. Molecular layers adsorbed to surfaces are closely related to the layering of simple liquids in confined geometries because confined liquids can be viewed as multilayers. In fact, lipid layers on solid supports in some cases also form multilayers [738] resulting in force curves similar to solvation force curves, so the distinction between adsorbed multilayers and solvation forces becomes artificial. Still, one difference is the fact that for surfactants or lipid layers two components are present: The solvent and the dissolved substance, while solvation forces occur in pure liquids.

8.2. Solvation forces

Solvation forces are often well described by an exponentially decaying oscillating function of the form

$$f = f_0 \cos\left(\frac{2\pi x}{\sigma}\right) e^{-x/\lambda_s}. \quad (8.1)$$

Here, σ is the molecular diameter, λ_S the decay length, and x is the distance between the walls. Then Derjaguin's approximation is used to calculate the force between a sphere of radius R approaching a planar surface [726]:

$$F = F_0 \cos\left(\frac{2\pi D}{\sigma} + \varphi\right) e^{-D/\lambda_S}. \quad (8.2)$$

Phase shift φ and the measured force amplitude are given by $\tan \varphi = \lambda_S/\sigma$ and $F_0 = R f_0/\sqrt{(2\pi\lambda_S)^{-2} + \sigma^{-2}}$. One result of the phase shift in Eq. (8.2) is that the jump distance observed for the inner layer (which is the one being squeezed out last) is supposedly smaller than the distances between the other layers. Based on a model of de Gennes [739], Richetti et al. [740] suggested an almost similar equation to describe the interaction between two surfaces across a smectic liquid. It was used to analyze AFM results [741].

During recent years solvation forces in different liquids were studied with the AFM [741–746]. Examples are OMCTS (octamethyl-cyclo-tetra-siloxane) [747,748], 1,3,5-trimethylbenzene ((CH₃)₃C₆H₃) [747], and *n*-alcohols [749–751]. As one prominent example Han and Lindsay [747] analyze the layering of OMCTS and trimethylbenzene on HOPG with an AFM. They attached a magnetic bead to the end of the cantilever, let it vibrate at 200–500 Hz (below resonance frequency) by applying an oscillating field, and detected the amplitude versus distance. In this way they could detect stiffness in addition to the normal force curve. They observed exponentially decaying oscillating forces with periods of 0.88 nm (OMCTS) and 0.65 nm (trimethylbenzene) which corresponds to the molecular size. The stiffness of the layers measured at the peak force decreases exponentially.

One inherent problem in AFM measurements of solvation forces is the lack of independent zero distance definition. Usually one relies on defining zero as the distance of closest approach. There may, however, be still several layers present which are not penetrated. In fact, combining force and conduction measurements Klein and McEuen found indications for just that [743]. They studied hexadecane on graphite with a tip coated with platinum. Typically five repulsive maxima and five jumps were observed in the force experiment when forces up to 40 nN were applied. At even higher forces (where a force detection was not sensitive enough anymore) jumps in the electric conduction indicated another 15 monolayers.

8.3. Lipid layers

8.3.1. Theory

Forces observed on adsorbed layers are treated in a completely different way and with a different model. Here we focus on layers with a defined structure normal to the solid surface such as lipid bilayers or surfactant layers. Before starting it is instructive to consider a typical force curve measured on a thin film to justify certain assumptions (Fig. 32). The force curve was recorded on a lipid bilayer of ≈ 4 nm thickness in aqueous electrolyte. No interaction is observed at distances much larger than the film thickness. At closer distance the tip experiences a short-range repulsive force and the film is elastically compressed. Here, “elastic” refers to the fact that when retracting the tip before the film ruptures the retracting part of the force curve is identical to the approaching part. Once a certain threshold force is exceeded the layer ruptures and the tip jumps into contact with the solid support. Such jumps are not only observed on lipid layers but also on different systems such as surfactant layers (see Section 8.4) and even protein crystals (e.g. [752]). One attempt to describe the rupture process is to treat the lipid layer or

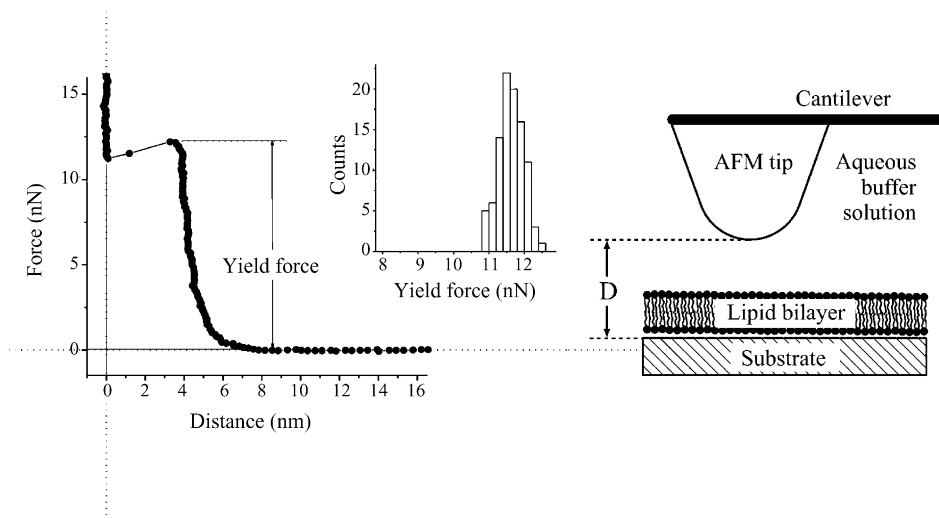


Fig. 32. A typical force curve measured on a lipid bilayer of dioleoyloxypropyl-trimethylammonium chloride (DOTAP) in aqueous electrolyte (150 mM NaCl, 5 mM KH_2PO_4 , pH 7.4) taken at an approaching speed of $v_0 = 2 \mu\text{m/s}$. The tip was coated with gold and a monolayer of hydroxy undecanethiol (tip radius $R = 67 \text{ nm}$, spring constant of cantilever $k_c = 0.40 \text{ N/m}$). The inset shows the histogram of yield forces. The right inset shows the geometry of the tip-sample system. See Ref. [755] for details.

surfactant film as a continuous elastic layer which yields at a certain stress [287]. Such a description ignores the molecular nature of the layer and in particular the fact that the interaction in lateral direction is in general different from the interaction in normal direction.

To take the discrete nature of molecular layers into account we first have to consider that the rupture observed is a statistical process. The tip has a certain probability $P(F)$ to break through the layer at a given applied force. This probability increases with increasing force and applied pressure. Thus, there is a distribution of yield forces and not one definite value. The aim of any theory of the jump-in is to calculate this distribution of yield forces and relate microscopic parameters to measurable quantities. Therefore, rupture of the layer can be described as an activated process [753]. An energy barrier has to be overcome for the formation of a hole in the layer, which is large enough to initiate tip penetration. This activation energy decreases with increasing applied force. The probability distribution could be expressed by the force-dependent activation energy U_0 and the approaching velocity v_0 :

$$\ln P(F) = -\frac{\Omega}{k_c v_0} \int_{F_S}^F e^{-U_0(F')/k_B T} dF', \quad (8.3)$$

for $F > F_S$ and $P = 1$ for $F \leq F_S$. Here, P is the probability to find the tip still on top of the layer. Ω is a frequency factor, which describes the number of hypothetical attempts of the tip to penetrate through the layer. As a first approximation, Ω is equal to resonance frequency of the cantilever. The lower integration limit is given by the “starting force” F_S . This is the force where a breakthrough leads to an energetically favorable situation at all. The remaining task is to find an equation for the activation energy.

Before doing so we would like to mention a universal law concerning the breakthrough process: The mean breakthrough or jump-in force F_j increases with increasing approaching velocity. This can easily be

verified. All experiments showed that the relative width of the distribution of yield forces is narrow and the mean yield force is similar to the force at which the probability is one half: $P(F_j) = 0.5$. With $\ln 0.5 = -0.693$ we can simplify Eq. (8.3):

$$v_0 = \frac{\Omega}{0.693k_c} \int_{F_S}^{F_j} e^{-U_0(F')/k_B T} dF'. \quad (8.4)$$

Since the integral increases monotonically with F_j , Eq. (8.4) directly shows that v is a monotonically increasing function of F_j , and vice versa: the mean yield force increases with the loading rate. This was indeed observed [754,755].

To calculate the activation energy versus applied force two models were used, a continuum nucleation model and a discrete molecular model. In the nucleation model a molecular thin, homogeneous film is considered, which is confined between the solid sample and the tip. The film is supposed to be laterally in a liquid state, but vertically its structure is well defined. At a high enough force a hole nucleates in the layer and the tip jumps through the layer. Using the elastic foundation or “mattress” theory [756] the activation energy can be calculated:

$$\Delta U = \frac{2\pi^2\kappa^2 R}{F - 2\pi RS}. \quad (8.5)$$

Here, the tip is assumed to be a paraboloid with radius of curvature R , κ is a line tension associated with the unsaturated bonds of the molecules at the periphery of the hole. S was called spreading pressure because it is the energy per unit area gained by the layer when spreading into the gap between tip and substrate. Applying a force reduces the activation energy. Inserting Eq. (8.5) into Eq. (8.4) leads to the probability distribution:

$$\ln P(F) = -\frac{\Omega}{k_c v_0} \int_{F_S}^F \exp\left(-\frac{2\pi^2\kappa^2 R}{k_B T(F' - F_S)}\right) dF' \quad (8.6)$$

with $F_S = 2\pi RS$. The distribution of yield forces is given by $|dP/dF|$. Unfortunately, the integral does not lead to a simple analytical expression and has to be solved numerically. For one example this is shown in Fig. 33. With increasing line tension hole formation requires a higher and higher force. For an easier comparison with experimental results Fig. 33 shows the yield probability $|dP/dF|$ instead of $P(F)$.

An alternative is the discrete molecular model. It is related to the model developed by Galla et al. [757] which describes lateral diffusion in lipid bilayers. In the molecular model each molecule in the film has certain binding sites which are energetically favorable positions. These binding sites might be formed by the substrate or by the surrounding molecules. To jump from the initial position into an adjacent free position a potential energy barrier has to be overcome. In the absence of the tip adjacent binding sites are energetically equivalent. When the tip is pressed onto the film a pressure gradient is applied which increases the energy of the molecules. The pressure is maximal in the center of the tip and it decreases with increasing radial distance until it becomes zero at the contact periphery. This pressure gradient at the same time lowers the activation barrier. In a simple version of this model the change in activation energy is

$$\Delta U_0 = U_0 - \frac{\alpha VF}{2\pi hR}. \quad (8.7)$$

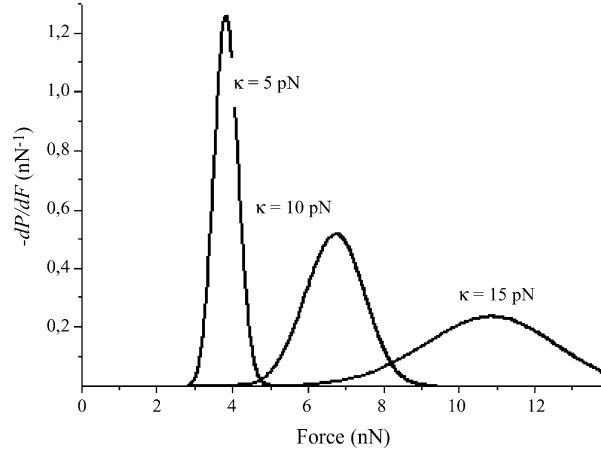


Fig. 33. Probability of a rupture $|dP/dF|$ as derived with the nucleation model Eq. (8.6) using $\Omega = 10^4$ Hz, $k_c = 0.1$ N/m, $v = 1 \mu\text{m/s}$, $S = 0.01$ N/m, and $R = 40$ nm for different values of the line tension κ .

Here, $\alpha \approx 0.5$ is a geometry factor, V the activation volume, and h is the thickness of the layer. Inserting this into Eq. (8.3) and integrating leads to

$$\ln P = -\frac{k_0 F_T}{k_c v_0} (e^{F/F_T} - 1) \quad (8.8)$$

with $k_0 \equiv \Omega \exp(-\Delta U_0/k_B T)$ and $F_T \equiv 2\pi h R k_B T / \alpha V$. The “frequency factor” k_0 is the rate of spontaneous hole formation. To be more precise: It is the rate at which hole of sufficient size, that is of size V , would form spontaneously without the influence of a force by the tip.

The dependence of the mean yield force on the loading rate can be calculated with Eq. (8.4):

$$F_0 = F_T \ln \left(\frac{0.693 v_0 k_c}{k_0 F_T} + 1 \right). \quad (8.9)$$

The mean yield force is proportional to $\ln v_0$, which was indeed observed [754,755].

8.3.2. Preparation of solid supported lipid bilayers

Lipid layers for AFM studies are usually prepared by the Langmuir–Blodgett (LB) technique or spontaneous vesicle fusion [758]. In the LB technique lipid monolayers can be transferred layer-by-layer onto solid substrates (Fig. 34) [759,760]. This is done with a film balance, also called a Langmuir trough. The modern version of a film balance consists of a temperature-controlled trough, which contains the aqueous medium, called “subphase”. Lipids are not (or only weakly) soluble in water and go to the surface, where they form a monolayer. Via a movable barrier the film balance allows to adjust the density of molecules on the aqueous surface by compression or expansion of the film. The film pressure π is defined as the difference between the surface tension of the bare aqueous medium γ_0 and the surface tension of the subphase in the presence of lipids γ : $\pi = \gamma_0 - \gamma$. The film pressure is determined by the Wilhelmy plate method, which usually contains a piece of absorbent paper hanging into the aqueous subphase. The force acting on this piece of paper having a width l is $2l\gamma$. By measuring this force the surface tension and thus the film pressure can be determined. If we compress

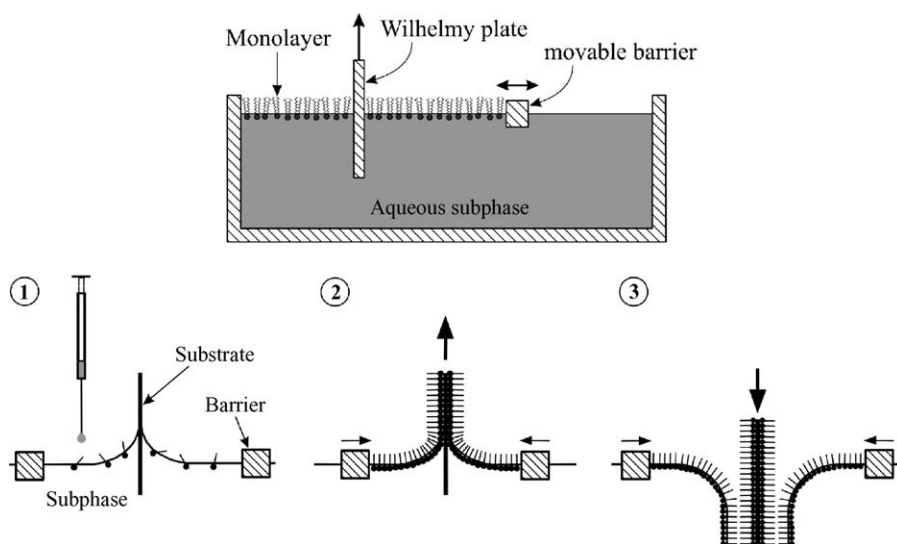


Fig. 34. Langmuir–Blodgett trough (top) and the three main steps in Langmuir–Blodgett transfer of lipid monolayers from water onto a solid substrate. The Wilhelmy plate method is used to measure the surface tension of the subphase. (1) The lipid is dissolved in a solvent which evaporates easily. After the hydrophilic solid substrate has been moved into the pure water subphase, drops of the lipid-containing solvent are set carefully onto the water surface between the movable barriers by a syringe (“spreading”). After solvent evaporation the monolayer is compressed to the desired pressure, usually some 20–40 mN/m. (2) The hydrophilic substrate is moved continuously out of the water subphase at constant film pressure. During the upstroke the monolayer is transferred onto the wafer with the head groups oriented towards the solid substrate and the alkyl chains exposed to the air. This renders the solid surface hydrophobic. By a consecutive down stroke (3) into the subphase through the floating monolayer a second layer can be transferred, with the alkyl chains oriented towards the solid substrate in a “tail-to-tail” configuration. The picture was reproduced from Ref. [115].

a surfactant film on water we observe that the surface tension decreases and the surface pressure increases.

To deposit a lipid monolayer onto a hydrophilic substrate such as a silicon wafer or mica (Fig. 34, bottom) the lipid is dissolved in a solvent, which evaporates easily and is not miscible with water (usually chloroform). After the hydrophilic solid substrate has been moved into the aqueous subphase, drops of the lipid-containing solvent are set carefully onto the water surface between the movable barriers by a syringe (“spreading”). After solvent evaporation the monolayer is compressed to the desired pressure, typically 20–40 mN/m. Then the substrate is moved continuously out of the water subphase at constant film pressure. During the upstroke the monolayer is transferred onto the wafer with the headgroups oriented towards the solid substrate and the alkyl chains exposed to the air. This renders the hydrophilic solid surface hydrophobic.

To prepare a bilayer the substrate is moved into the subphase again. Thereby another monolayer is deposited onto the first monolayer. The alkyl chains are oriented towards the solid substrate in a “tail-to-tail” configuration. As a result a lipid bilayer is formed. This has to be kept in water all the time. Otherwise it is immediately destroyed since the hydrophobic effect, which holds the bilayer together, does not exist in air. In this way lipid bilayers can be formed from a large variety of lipids. The density of molecules in a monolayer can be adjusted by choosing the appropriate film pressure. A possible drawback is that in some cases it is difficult to produce homogeneous films covering a large area. This,

however, is not a severe limitation in AFM studies because inhomogeneities are usually spaced more than several micrometers and are easily detected. Also multilayers can be made by repeating the procedure.

Lipid bilayers are likely to form vesicles. A vesicle is a lipid bilayer which forms a closed sphere. Under appropriate conditions vesicles spontaneously adsorb, spread, and form a bilayer on different surfaces such as glass, silicon oxide, silicon nitride, alumina, titanium oxide, mica, and some thiol-coated gold surfaces [761–765]. This process is called vesicle fusion. Vesicle fusion provides a technique which is easy to handle and which leads to spontaneous formation of a bilayer in the liquid cell of the AFM [766,767]. The lipids are able to diffuse laterally or they are immobile. The mobility depends on the substrate, the lipid, the pH, and salts present in the solution, but also on the presence of a molecular layer of water between the substrate and the lipid bilayer [768].

8.3.3. Force curves on lipid bilayers

A typical force curve recorded on a lipid bilayer shows a repulsive component until the film ruptures and the tip jumps into direct contact with the substrate surface (Fig. 32). Such jumps were observed on a number of different bilayers [728,730,753,755,769–773]. In a series of papers Schneider, Dufrêne, Lee et al. [728,730,769] studied the influence of the tip chemistry on the tip–lipid bilayer interaction. Using gold-thiol coated tips (mercapto hexadecanol or mercapto hexadecane) they studied different lipid bilayers formed by LB transfer on mica. The first monolayer was 1,2-distearoyl-*sn*-glycero-3-phosphoethanolamine (DSPE), which provides a relatively rigid substrate for the second leaflet of DSPE, monogalactosyl-diglyceride (MGDG), DGDG (digalactosyldiglyceride), or DOPE (1,2-dioleoyl-*sn*-glycero-3-phosphodylethanolamine). With hydrophilic tips they observe breakthrough forces which depend on the lipid. It is zero for DOPE in the second layer and increases from DSPE to MGDG and to DGDG. With hydrophobic tips the breakthrough force is always zero. Also pull-off forces are much higher with hydrophobic tips. This is a demonstration that the tip chemistry drastically changes force curves.

Dufrêne et al. [730] also started analyzing force curves quantitatively. Before the tip jumps through the bilayer, the bilayer is compressed. They fit this first part of the force curve using Hertz model of elastic compression [245].

One promising step forward with respect to a quantitative evaluation of force curves is the cluster analysis introduced by Janshoff et al. [772]. In a cluster analysis not only the distribution of one parameter is plotted but it is correlated with another parameter (Fig. 35). For example, rather than just plotting how often a certain breakthrough force is observed the breakthrough force and the breakthrough distance are plotted on the two axes and each result is represented by one point in this plot. From the density of points the distribution and at the same time a possible correlation between the two parameters is deducible.

The force measurements discussed until now were done in order to better interpret images of solid supported bilayers and to get more information about the stability and formation of solid supported membranes. In addition, the AFM can be used to study bilayer–bilayer interaction. The interactions between lipid bilayers have been studied for the last 30 years, with different methods and under various conditions [484,774–779]. The motivation comes from two directions, one biological and one physico-chemical. From the biological point of view, knowledge about the interaction between membranes is essential to understand biological processes such as exo- and endocytosis, intracellular trafficking, cell division, adhesion, fusion and metastasis (such processes are only listed as a kind of “keywords list”, without going in further details). From the physico-chemical point of view, lipid bilayers are one possible stable phase, namely a lamellar phase, adopted by amphiphilic molecules in aqueous medium. Questions

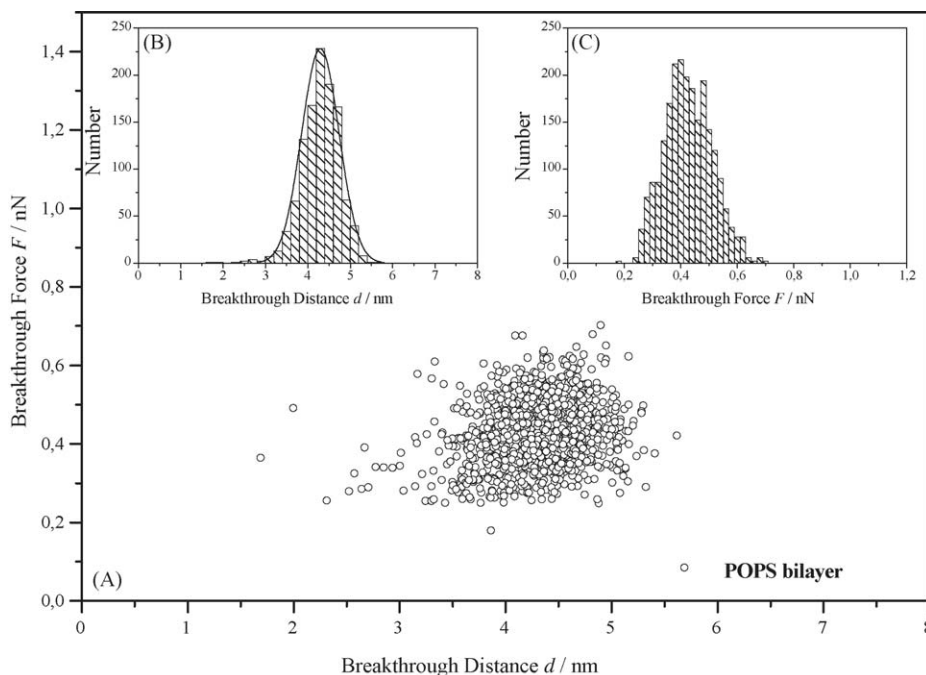


Fig. 35. Distribution of breakthrough forces and jump-in distances shown in a two-dimensional plot. The figure shows results of an AFM experiment with a 1-palmitoyl-2-oleoyl-*sn*-glycero-3-phospho-L-serine (POPS) bilayer on mica. The figure was kindly provided by Janshoff [772].

related to the properties of membranes, the internal organization of a bilayer, the understanding of vesicle fusion by rupturing the bilayers, and the forces governing this interaction may be investigated. By clarifying this latter aspect, a quantitative answer to some of the biological questions may be obtained.

Several forces governing bilayer–bilayer interactions have been identified [484]. The van der Waals force is long-range, attractive and relatively weak. It is opposed by a short-range repulsive force. This repulsive force decays exponentially with a typical decay length of 0.2–0.5 nm. It is not yet clear which effect dominates this short range repulsion: the hydration pressure, arising from ordering of water molecules by the hydrophilic head groups of the lipids, or an entropic “protrusion” effect of molecular groups that are thermally excited to protrude from the fluid-like lipid bilayers [484,780,781]. Charged lipids repel each other by electrostatic double-layer forces. For bilayers, which are not supported on a solid surface, an undulation or fluctuation pressure, due to thermally driven undulations of the entire bilayer surface which couple hydrodynamically to other bilayers keeps the surface apart.

To measure forces between two lipid bilayers with the AFM we need to form a lipid bilayer not only on the sample but also on the tip. Unfortunately this is difficult to achieve. Though many researchers believe that often a second bilayer has formed on the tip, it seems to be not reproducible, and the force to break through the bilayer on the tip seems to be insignificantly small (e.g. Ref. [771]). Why are bilayers at the tip surface so unstable? One possible reason why bilayers adsorb spontaneously to a planar surface, but not to the tip, is the high curvature. The energy per unit area required to bend a bilayer with zero spontaneous

curvature to a spherical cap is $2\kappa/R^2$. Here, κ is the bending rigidity, also called bending elastic modulus. For phosphatidylcholine bilayers in the liquid phase κ is typically 10^{-19} J [782–786]. For the spontaneous adsorption of a bilayer, the adsorption energy must be higher than the bending energy. With typical adsorption energies per unit area of $W_A = (0.2\text{--}2) \times 10^{-4}$ J/m² [782,787] the minimal radius of curvature is estimated to be $R = \sqrt{2\kappa/W_A} = 100\text{--}32$ nm, respectively. We expect that the tip surface is covered only for a strong adhesion between the bilayer and the solid surface. The stronger the adsorption, the smaller the tip can be. In any case: very sharp tips are not going to be covered by bilayers.

To overcome this problem, Pera et al. [738] first coated tips with gold and a monolayer of mercapto undecanol. Calculations indicate that long-chain hydroxyl terminated alkyl thiols tend to enhance spontaneous vesicle fusion because of an increased van der Waals attraction as compared to short chain thiols. When coating AFM tips in this way indeed two jumps of typically 4 nm were observed (Fig. 36). In this way the interaction between 1,2-dioleoyl-*sn*-glycero-3-phosphocholine (DOPC), 1,2-dioleoyl-*sn*-glycero-3-phospho-L-serine (DOPS), and 1,2-dioleoyl-3-trimethylammonium-propane chloride (DOTAP) bilayers could be measured.

Retracting force curves observed on lipid bilayers tend to vary from experiment to experiment and are not as reproducible as approaching force curves. Several types are often observed:

- In some cases “partially reversible” force curves were observed. There the tip is released from direct contact at a positive force. The bilayer has a strong tendency to coat the surfaces, so that it pushes the tip away from the surface. After being released from direct contact approaching and retracting force curves are identical. Such reversible force curves were for example described by Grant and Tiberg on DOPC bilayers coadsorbed with dodecylmaltoside [771].
- In many cases, “contact adhesion” was observed. A certain force, the adhesion force, had to be applied to pull the tip off from direct contact with the solid planar surface. Once released, the tip jumps back to the approaching force curve and from that point on the force curve is reversible.
- When two bilayers are present, contact adhesion can occur twice [738]: First the adhesion between tip and planar surface and then the adhesion between one bilayer and the tip. Contact adhesion was

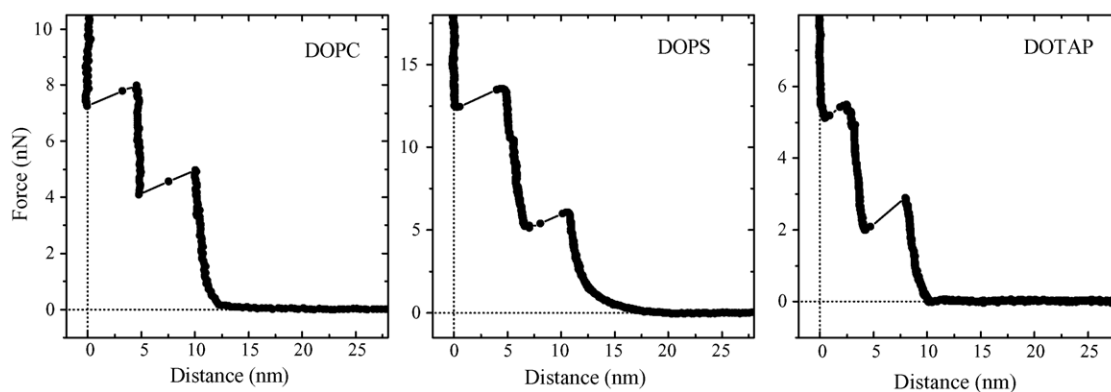


Fig. 36. Typical force-versus-distance curve measured on a planar mica surface in buffer after exposure to 1,2-dioleoyl-*sn*-glycero-3-phosphocholine (DOPC), 1,2-dioleoyl-*sn*-glycero-3-phospho-L-serine (DOPS), and 1,2-dioleoyl-3-trimethylammonium-propane chloride (DOTAP) vesicles. The AFM tips were first coated with chromium and gold and then with a monolayer of mercapto undecanol (HS(CH₂)₁₁OH). For details see Ref. [738].

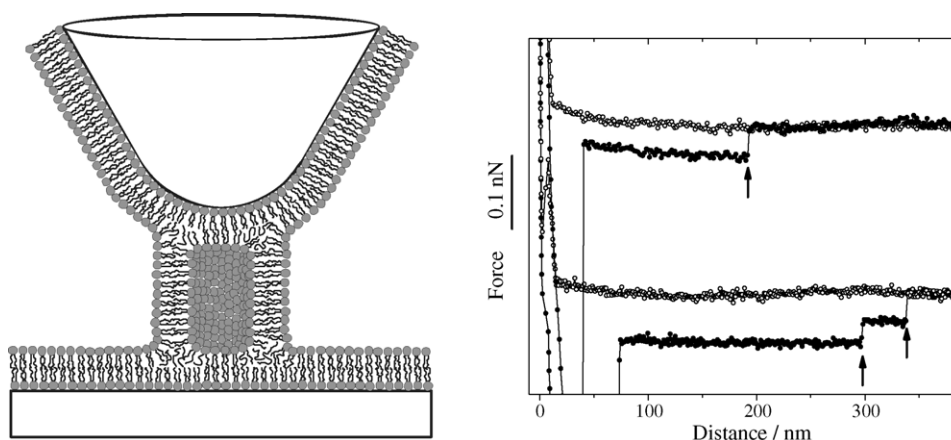


Fig. 37. Schematic of tether formation and experimental force curves interpreted as tether formation (adapted with kind permission from [788]). The curves are acquired on mica with silicon nitride cantilevers and tips, which were rendered hydrophilic by a water plasma treatment prior to use. The two typical force curves show a long-range attraction on the retracting part (full circles) which abruptly stops at a distance of few hundred nm, presumably when tether rupture. Two ruptures are interpreted as two bilayer tethers, one inside the other.

observed and analyzed by Schneider et al. [769] on different lipid bilayers prepared by LB transfer with thiol-coated tips and by Künnecke et al. [772] with uncoated tips on bilayers prepared by vesicle fusion. Schneider et al. conclude that adhesion forces can be analyzed in terms of classical theories of contact mechanics such as the JKR theory.

- In few cases a “weak long-range attraction” was observed in addition to the above-mentioned features. It is at least 10 times lower than the breakthrough force and certainly below 1 nN. It does not depend strongly on distance and is sometimes relatively constant until it drops to zero at distances of up to 20 nm [770,788]. Such weak long-range attraction indicates that some kind of contact is maintained over distances exceeding the thickness of the two bilayers. A possible mechanism leading to the weak long-range attraction is the formation of a bilayer tether between the tip and planar surface (Fig. 37) [738,788]. Such membrane tethers have also been observed on various whole cells by different methods (e.g. [789–791]). The force required to extend such a tube is $F \approx 4\pi r\gamma$, where γ is the surface tension of a lipid bilayer and r is the radius of the tube. With $r = 10$ nm and $\gamma = 0.001$ N/m we estimate a force of 0.13 nN.

Recently not only solid supported bilayers but also whole vesicles are studied by force measurements. In these experiments two rupture events are observed, corresponding to the two bilayers which are penetrated before the tip gets into contact with the substrate. Such experiments give information about the mechanical bending rigidity of the lipid bilayers. For example, Ling et al. [792] observed a stiffening of eggPC vesicles when adding cholesterol to the lipid phase.

8.4. Adsorbed surfactants

One of the significant contributions of the AFM to our understanding of interfaces concerns surfactants adsorbed to solid surfaces. Using the AFM, the structure of such surfactants was revealed. Most of the

Table 5
Surfactants adsorbed to surfaces analyzed by AFM imaging at low forces in aqueous medium

	HOPG	Mica	Silicon oxide	Silicon nitride	Hydroph. silicon oxide	Gold
SDS	[794]				[736]	[732,735]
DDAPS	[795]	[796]	[795]		[736]	
TTAB	[793]	[793]	[793]			[735]
CTAB	[734]	[797–800]	[801]			
CTACl	[802]	[797,802]	[801,802]			
CTAOH						[735]
DDAB	[793]	[793,803]	[793,804]		[736]	
DDAPS	[795,805]	[795,805]		[795,805]		
DTAB		[796]			[736]	
Gemini		[806]			[736]	
C ₁₀ E ₅	[805,807]	[805]	[807]	[805]	[807]	
C ₁₀ E ₆	[807]		[807]		[807]	
C ₁₂ E ₃	[808]					
C ₁₂ E ₅	[808]	[809]	[807]		[807]	
	[807]					
C ₁₂ E ₈	[808]		[807]		[807]	
	[807]				[736]	
C ₁₂ E ₉	[808]					
C ₁₂ E ₁₀	[808]					
C ₁₂ E ₂₃	[808]					
C ₁₄ E ₆	[807]		[807]		[807]	
C ₁₆ E ₆	[807]		[807]		[807]	
<i>N</i> -Alkyl-malton-amides	[810]					

CPR: cetyl-pyridinium bromide; TTAB: tetradecyl trimethyl-ammonium bromide; CTAB, CTACl, CTAOH: hexadecyl trimethyl-ammonium bromide, chloride, hydroxide; DDAB: didodecyl dimethyl-ammonium bromide; DDAPS: 3-(*N,N*-dimethyl-do-decylammonia)-propane-sulfonate; Gemini: C_{*n*}H_{2*n*+1}N⁺(CH₃)₂(CH₂)₈N⁺(CH₃)₂(C_{*m*}H_{2*m*+1}); C_{*n*}E_{*m*}: poly(ethylene oxide) alkyl ethers (CH₃(CH₂)_{*n*-1}(OCH₂CH₂)_{*m*}OH).

information was obtained by imaging the surfactants in aqueous medium at very low force. A good understating of the interaction was a prerequisite for a successful imaging. Manne et al. studied the structure of surfactants adsorbed to solid surfaces. They imaged the cationic surfactant cetyl-trimethyl-ammonium-bromide (CTAB) adsorbed to a hydrophobic graphite surface [734]. When imaging with a very low force they observed parallel stripes spaced about 4.2 nm apart, i.e. about twice the length of the CTA⁺ ion. The adsorbed stripes were generally observed in three orientations. Based on observations like these Manne et al. [734,793] concluded that CTAB forms cylindrical hemimicelles on graphite (HOPG), full cylinders on mica and spherical micelles on silica. Meanwhile the structure of several surfactants on various surfaces has been revealed. Table 5 lists some publications on the structure of surfactants on solid surfaces. The surfactants were imaged with microfabricated silicon or silicon nitride tips. Anionic (SDS), neutral (C_{*n*}E_{*m*}, *N*-alkyl-maltonamides), zwiterionic (DDAPS, *N*-dodecyl-*N,N*-dimethyl-3-ammonio-1-propane-sulfonate), and cationic surfactants (CTAB, CTACl, CTAOH, DTAB, and Gemini) were studied.

Imaging surfactant aggregates is usually successful only at concentrations at or above the critical micellar concentration (CMC). At lower concentrations stable aggregates do not form. To get information about the adsorption of surfactants on solid surfaces even at low concentrations one relies on force

experiments. Different surfactants, such as C_nE_m [187], SDS [287,811], 1,2-diheptanoic-*sn*-glycero-3-phosphocholine [733], alkyl-trimethyl-ammonium cations [287,812–814], cetyl-pyridinium chloride, and dodecyl-pyridinium chloride [737,815] have been analyzed in force experiments with the AFM.

To analyze force curves obtained in surfactant solution and to relate measured quantities to other thermodynamic parameters Subramanian and Ducker [812] applied a formalism developed by Hall [816] and Ash et al. [817]. In their approach Ducker et al. relate the force-versus-distance of a sphere opposite to a flat plate of identical material to the amount of surfactant adsorbed. Therefore first the force F is related to the energy per unit area U_A using Derjaguin's approximation: $U_A = F/2\pi R$. This energy can be related to the change in surface excess:

$$\Gamma_i(x) - \Gamma_i(\infty) = -\frac{1}{2} \left(\frac{\partial U_A}{\partial \mu_i} \right)_{T,P,\mu_j,x}. \quad (8.10)$$

$\Gamma_i(x)$ is the surface excess of surfactant i when the two surfaces are at a distance x . For a free surface, that is when the two surfaces are at infinite distance, the surface excess assumes a value $\Gamma_i(\infty)$. The energy is differentiated with respect to the chemical potential of surfactant i at constant temperature T , pressure P , concentrations of possible other components j , and distance x . The chemical potential of surfactant i is related to its activity coefficient γ_i and the concentration c_i in the usual way:

$$\mu_i = \mu_i^0 + RT \ln(\gamma_i c_i). \quad (8.11)$$

Here, $R = 8.315 \text{ J K}^{-1} \text{ mol}^{-1}$ is the gas constant. Thus, by measuring force curves at different concentrations (and thus different chemical potentials) the change in the amount adsorbed per unit area can be calculated.

The approach has been successfully applied to analyze surface force experiments with the AFM [737,813,815]. It relies, however, on the fact that the system is all the time in full equilibrium. Small changes in adsorption can cause strong effects on the force. Problems relating to defining zero of separation and the reversibility of approach and retraction can sensitively change the results [818].

Most surfactants are studied in aqueous medium. Significantly less effort has been devoted to the analysis of surfactants in organic solvents. One exception is the work of Kanda et al. [819] on the interaction of mica and silicon oxide in cyclohexane in the presence of sodium bis(2-ethylhexyl)sulfosuccinate (AOT). Adsorption of AOT in the presence of trace amounts of water could clearly be monitored by observing the typical jumps through the adsorbed layer.

8.5. Steric forces

Chain molecules which are attached at some point to a surface and which dangle out into the solvent are thermally mobile. On approach of another surface the entropy of confining these dangling chains results in a repulsive entropic force which, for overlapping polymer molecules, is known as the "steric" or "overlap" repulsion. First direct quantitative measurements were made with the SFA (e.g. [820–823]). Reviews are given in Refs. [824,825].

The force between polymer coated surfaces immersed in a good solvent is mainly determined by two factors. The first one is the quality of the solvent. In good solvents the force tends to be repulsive, in bad solvents attractive. Moreover, in good solvents polymers tend to remain in solution rather than adsorbing

to surfaces. The second important factor is how and how much polymer is bound to the surface. If the polymer is physisorbed it can only reach a maximal adsorption density of the order of $1/R_g^2$. Here, R_g is the radius of gyration. To explain the meaning of R_g we have to realize that a linear polymer in a good solvent forms a random coil. This implies that the distance between the two ends fluctuates and will practically never be equal to the length of the stretched polymer (which is called the contour length). To characterize the size of such a randomly coiled chain we take the mean square of the end-to-end distance. The square root of this value, $\sqrt{\langle r_p^2 \rangle}$ is often called the size of a polymer. Polymer sizes are often determined by light scattering. In light scattering a hydrodynamic radius is measured which is given by $R_g = \sqrt{\langle r_p^2 \rangle}/6$. The adsorbed layer typically extends a distance $2R_g$ into the solution. Each polymer molecule might have several binding sites and might form loops. The adsorption time plays a crucial role since polymers at surface rearrange, a process which can take hours. Polymers can also be covalently bound to a surface (also called “grafted” or “tethered”) [825]. When the polymer is covalently bound to the surface the number of molecules on the surface – called “grafting density” Γ – can be much higher. For closely packed polymer chains ($\Gamma \gg 1/R_g^2$) we talk about a polymer brush. Polymer brushes can be made by binding a polymer to a surface (grafting to) or by synthesis of the polymer directly on the surface (grafting from). In this case the steric force acts over lengths, which are substantially larger than the radius of gyration; the equilibrium thickness is roughly [826] $L_0 = nl^{5/3}\Gamma^{1/3}$, where n is the number of segments (monomers) in a polymer chain and l is the length of one segment.

There is no simple, comprehensive theory to describe steric forces. Different components contribute to the force, and depending upon the situation, dominate the total force. The most important interaction is repulsive and of entropic origin. It is caused by the reduced configuration entropy of the polymer chains. If the thermal movement of a polymer chain at a surface is limited by the approach of another surface, then the entropy of the individual polymer chain decreases. In addition, the “concentration” of segments in the gap increases. This leads to an increased osmotic pressure. For brushes the steric repulsion between two similar parallel surfaces separated by a gap x was calculated by de Gennes [827]:

$$f(x) = k_B T \Gamma^{3/2} \left[\left(\frac{2L_0}{x} \right)^{9/4} - \left(\frac{x}{2L_0} \right)^{3/4} \right] \quad (8.12)$$

for $x < 2L_0$. Integration using Derjaguin’s approximation for a tip with a spherical end leads to

$$\begin{aligned} F(D) &= 2\pi R k_B T \Gamma^{3/2} \int_D^{2L_0} \left[\left(\frac{2L_0}{x} \right)^{9/4} - \left(\frac{x}{2L_0} \right)^{3/4} \right] dx \\ &= \frac{16\pi}{35} R k_B T L_0 \Gamma^{3/2} \left[12 - 7 \left(\frac{D}{2L_0} \right)^{-5/4} - 5 \left(\frac{D}{2L_0} \right)^{7/4} \right]. \end{aligned} \quad (8.13)$$

For the interaction of a sample with a polymer brush and a bare, non-adsorbing tip O’Shea et al. [828] replaced $2D$ by D and divided the pressure by 2.

To derive the above equation De Gennes assumed a step profile for the polymer volume fraction in the undisturbed brush, i.e., the polymer volume fraction is constant up to the thickness of the polymer brush and then it drops to zero. This is a rather severe assumption. Milner et al. [829,830] described more

realistically the polymer volume fraction by a second-order polynom (parabolic profile) leading to [831] (with a corrected minus sign in [832]):

$$f(x) = \frac{P_0}{L_0^*} \left[\ln\left(\frac{x}{2L_0^*}\right) + 2\left(\frac{x}{2L_0^*}\right) - \left(\frac{x}{2L_0^*}\right)^4 \right], \quad (8.14)$$

and after applying Derjaguin's approximation

$$F(D) = 4\pi R P_0 \left[\frac{2L_0^*}{D} + \left(\frac{D}{2L_0^*}\right)^2 - \frac{1}{5} \left(\frac{D}{2L_0^*}\right)^5 - \frac{9}{5} \right] \quad (8.15)$$

with

$$P_0 = \frac{k_B T n}{2} \left(\frac{\pi^2 l^4}{12} \right)^{1/3} \Gamma^{5/3}, \quad (8.16)$$

where n is again the number of monomers.

The thickness of the brush in the Milner–Witten–Cates is slightly larger than in the Alexander–de Gennes model: $L_0^* = (24/\pi^2)^{1/3} L_0 = 1.34L_0$.

The above two sets of equations were used by several authors to analyze force experiments on brushes [832] (see Fig. 38). In some cases brushes were made by grafting a polymer from the surface. Examples are monomethoxypolyethylene glycol on silicon nitride in aqueous solutions analyzed with a micro-fabricated tip [132], polystyrene (PS) grafted to silicon oxide and analyzed in toluene at different temperatures [833], and poly(4-vinylpyridine) (PVP) and poly(methacrylic acid) (PMAA) interacting with PS microspheres in aqueous medium [75]. More frequently used and industrially more relevant

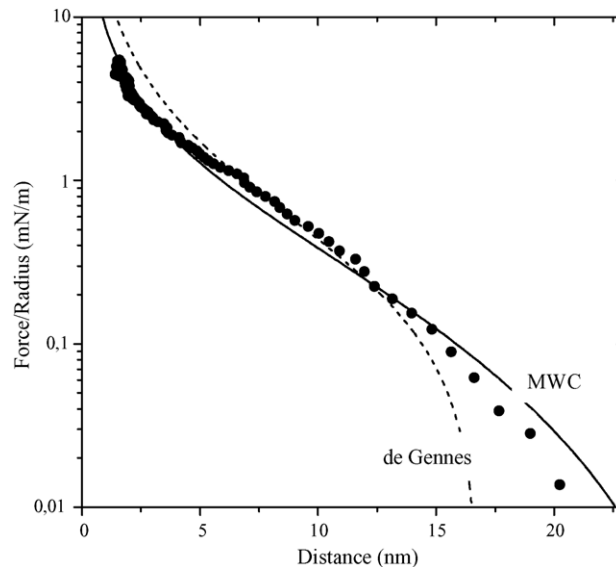


Fig. 38. Force curve between a silica sphere and a hydrophobized silicon surface with adsorbed triblock copolymer Pluronic F108 in aqueous medium. The experimental force profiles (filled circles) are fitted by the de Gennes model (dashed) and the Milner, Witten, and Cates model (solid line). Replotted from [832] with kind permission of Gee.

systems are physisorbed diblock copolymers. A diblock copolymer is a linear polymer where one part consists entirely of monomer A, while the other part is made of monomer B. In contrast to a random copolymer the monomers are not mixed, but arranged in two homogeneous blocks or sequences. One block strongly adsorbs to the surface and attaches the polymer to the surface. It is not well dissolved in the liquid. The liquid is, however, a good solvent for the other block. This well dissolved block is responsible for the steric repulsion. Several diblock copolymers have been analyzed with the AFM. Examples are PEO–PS in xylene, propanol, and dodecane on mica [828], PVP–PS and poly(4-*tert*-butylstyrene)–sodium poly(styrene-4-sulfonate) in aqueous medium [834], PEO–PMAA on aluminum oxide in aqueous medium [833], and PVP–PS on silicon analyzed in toluene and water [835]. In a similar way the triblock copolymers, PEO–PP–PEO (trade name “Pluronic”), were studied in aqueous medium adsorbed to hydrophobic surfaces [832,836].

For a low grafting density ($\Gamma < 1/R_g^2$), sometimes called the mushroom regime, the repulsive force per unit area in a good solvent and between two polymer coated surfaces is [837]

$$f(x) = \frac{k_B T \Gamma}{x} \left(\frac{2\pi^2 R_g^2}{x^2} - 1 \right) \quad \text{for } x \leq 3\sqrt{2}R_g, \quad (8.17)$$

and

$$f(x) = \frac{k_B T \Gamma x}{R_g^2} \exp \left[-\frac{x^2}{4R_g^2} \right] \quad \text{for } x > 3\sqrt{2}R_g. \quad (8.18)$$

All the above equations assume that the two interacting surfaces are smooth on the length scale of the grafting density ($R \gg 1/\sqrt{\Gamma}$) and the radius of gyration ($R \gg R_g$). For a microfabricated tip with its small radius of curvature this is often not fulfilled. Indeed, when comparing steric forces measured with microfabricated tips with results obtained with the SFA the AFM force curves are less steep indicating an apparently softer polymer layer [834,835]. Theory and simulations showed that the polymer chains partially avoid compression by escaping from underneath the AFM tip [838–841]. This escaping of chains is not only effective in the mushroom regime [842] but also in the brush regime [843].

Another contribution to the steric interaction is the intersegment force. The intersegment force is caused by the direct interaction between segments of polymers with each other. This interaction depends strongly on the solvent. When the interaction among the monomers is stronger than the interaction of the monomers with the solvent, this results in an attractive force.

Bridging forces, arising when a polymer binds to both surfaces, usually lead to an attraction at large separations. Bridging is only effective at low surface coverage. Only then do the polymer segments have a chance to find an adsorption site on the opposite surface. Bridging was for example observed by Biggs for PAA between two zirconia surfaces [166] and between mica and silicon nitride by Senden et al. [844]. Bridging forces have also been observed on the single molecule level with the AFM (see Section 11). They have also been observed in polymer melts [845].

Polymer brushes which are fixed to the surface at a well-defined density are ideal to study steric interaction. Many studies deal with a more practical situation encountered in flocculation, i.e., polymer induced aggregation of dispersed particles, or the opposite, i.e. steric stabilization of dispersions. In these cases mainly inexpensive homopolymers are used and one aim is to analyze the mechanism which leads to dispersion in a specific system [168]. In some cases the interaction between physisorbed layers can also be described by one of the above equations [188]. In many cases the adsorbed layers are not in

thermodynamic equilibrium and the interaction changes the structure of the adsorbed polymer [163,342,846]. In some studies the adsorption per se was studied. Examples are the adsorption of PEO to silica [847], of poly(sodium styrenesulfonate) (PSS) to silica and alumina [161,442], and modified polyisobutylene with surfactants to steel [848]. In some cases the study of steric interactions is applied to biological and medical issues, like in the case of Morra et al. [849] (collagen on titanium surfaces) and of Brown and Hoh [850] (neurofilaments).

9. Soft surfaces

9.1. Particle–bubble interaction

While the electric double layer on a solid surface is relatively well understood and theories are able to account for colloidal stability and coagulation kinetics quite well, there has been much less success in understanding the double-layer structure at liquid–liquid or liquid–gas interfaces. This is despite the fact that the stability of emulsions or dispersion of particles and gas bubbles play a central role in many industrial processes such as flotation or the deinking of paper. With the AFM or with AFM related setups the electric double-layers at such deformable interfaces can be analyzed. It is possible to measure the force between a solid microsphere and an oil drop (or another immiscible liquid) or a bubble in aqueous medium. These experiments are, however, more difficult to perform and to interpret. First, the tip or particle can even penetrate into the bubble or oil drop. In this case a three-phase contact line is formed and the capillary force completely dominates the interaction. Electrostatic double-layer forces can only be detected before a three-phase contact is formed. Second, since the interface is deformable it is difficult to determine zero distance, especially in the presence of surface forces. In principle the shape of the interface can be calculated using the Laplace equation [851,852]. This is, however, not trivial and in many cases practically impossible. Ducker et al. [337] attempted to plot separation against ‘actual’ separation by accounting for the bubble deformation with Hooke’s law and taking zero of separation as the point at which the linear compliance line reaches zero force. In performing such an analysis, one must be aware that comparisons are qualitative, as the deformation of the bubble (in particular at high loads) alters the interaction geometry as was originally noted [337,853]. In a previous review on different approaches Gillies et al. [854] suggested obtaining zero distance by fitting force curves in the presence of weak interaction forces and assuming rigid bodies. Such an approach is inappropriate, however, because bubbles with radii much greater than the colloid probe are likely to deform at forces not resolvable in typical AFM experiments [855]. Deformation of the bubble has been accounted for in two other analyses, i.e. Attard and Miklavcic [856–858] and Dagastine and co-workers [855,859]. Since a precise determination of zero distance is hard to achieve, an often used simplification (especially for determination of the contact angle, see below) is to take it as the point of snap-in during approach.

The earliest experimental insights into particle–bubble interactions were gained by pressing a captive bubble against a flat silica plate in aqueous solution [860–862]. These studies investigated the thickness of the separating films via interferometry as a function of applied pressure.

The colloid probe technique can be readily adapted to study particle–bubble interactions (for a recent review, see [863]). Therefore, a small bubble is attached to a hydrophobic surface at the bottom of the liquid cell of the AFM. The cantilever with the colloid probe is then placed above the crest of the bubble and force curves are recorded by approaching and retracting the colloid probe to and from the bubble.

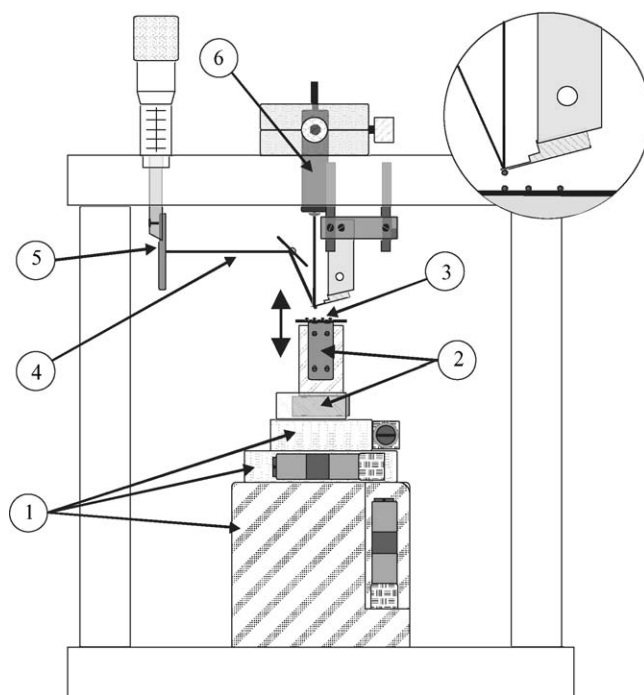


Fig. 39. Schematic of the particle interaction apparatus. (1) XYZ translation stage for coarse positioning of the sample. (2) Piezo transducers. (3) Sample. (4) Laser beam. (5) Position sensitive device. (6) Laser optics. The inset shows the colloidal probe with the laser beam in more detail (particles are not to scale).

First such experiments were done between differently treated silica particles and an air bubble [79]. As expected they showed that a hydrophilic particle is repelled by an air bubble while a hydrophobic particle jumps into the bubble. These early experiments were not very precise, i.e., the distance resolution was below 10 nm. The first precision experiments were done by Ducker et al. [337] who observed an electrostatic double-layer force that decayed exponentially with the expected Debye length. This observation was later confirmed with devices that were equipped with capacitively calibrated piezo translators (Fig. 39). Ducker et al. detected, however, an unexpected attractive force between a presumably hydrophilic silica particle and a bubble. Fielden et al. confirmed that between hydrophilic particles and air bubbles only repulsive forces are acting [853]. Their experiments can be considered as the first accurate measurements of the interaction between hydrophilic particles and a bubble. As expected from adsorption experiments a hydrophilic particle is repelled by an air bubble and a stable water film remains on the particle surface. The previously observed attraction was probably due to contamination. Furthermore, silica particles rendered hydrophobic by dehydroxylation or OTS treatment immediately snapped into the bubble, forming a three phase contact line. The electrostatic double-layer force observed before contact decayed with the expected Debye length.

Ducker et al. [337] and Fielden et al. [853] performed their experiments with commercial AFMs. For routine measurements this is not convenient because the liquid cells of commercial instruments are small and difficult to access manually. In addition, a thorough cleaning procedure is hampered by the fact that the cell consists of many different materials. Therefore Preuss et al. built their own device to measure the

force between particles and bubbles [31,864–866]. With this device the influence of different surfactants on the interaction of hydrophobic and hydrophilic particles with bubbles was studied.

As one example the force between a hydrophilic silica particle and an air bubble at different concentrations of dodecyltrimethylammonium bromide (DTAB) is shown in Fig. 40. Without surfactant the particle is repelled by the air bubble. At distances above 5 nm the electrostatic repulsion dominates. The reason are the negative surface charges on the silica surface and at the water–air interface [867–870]. Even at close distance a stable water film remains on the particle surface and no three phase contact is formed. Adding even small amounts of the cationic surfactant DTAB changes the interaction drastically. At concentrations between 0.1 mM and typically 5 mM DTAB (critical micellar concentration is ≈ 16 mM) no repulsion was observed. When the particle comes into contact with the air–water interface, it jumps into the bubble and a three phase contact is formed. Such a behavior can be explained with the strong adsorption of long-chain alkyl-trimethyl-ammonium ions to silica (e.g. [871]). At a concentration of 0.1 mM DTA⁺ ions form a monolayer on the silica surface. This reverses its surface charge from negative to positive and it makes the surface hydrophobic.

When increasing the DTAB concentration to 5.4 mM a small electrostatic repulsion was observed before the jump-in. The repulsion was at least partly due to electrostatic repulsion since it decayed exponentially with the Debye length. The reason is probably that at DTAB concentrations above 5 mM also the air–water interface becomes positively charged due to adsorbed DTAB. This leads to an electrostatic repulsion between the positively charged air/water interface and the positively charged silica surface. Above roughly 6 mM DTAB the jump-in disappeared and only repulsive forces were observed.

The interaction of a particle with an oil drop is relatively similar to that with an air bubble [872–874]. Both interfaces, the oil–water and the water–gas interface, are negatively charged at neutral pH. Therefore an electrostatic repulsion is observed when interacting with a silica particle. As expected from DLVO theory this repulsion decays roughly exponentially with a decay length equal to the Debye length [875].

The interaction between a sphere and the air–water interface can be used to deduce the contact angle between the liquid and the sphere. This so-called sphere tensiometry has been implemented much earlier for macroscopic bodies [876–879] and was subsequently extended to microsphere tensiometry using the colloid probe technique [865].

When the colloid probe approaches the bubble, the aqueous film separating the two will thin with time and/or applied load and finally rupture (except for very hydrophilic materials like silica), forming a three phase contact line. From this point on, capillary force will dominate the interaction and the particle will penetrate a certain distance into the bubble (Fig. 41c). The capillary force F_{cap} acting on the particle is given by [880]

$$F_{\text{cap}} = 2\pi R\gamma \sin \alpha \sin(\theta_r - \alpha), \quad (9.1)$$

where R is the particle radius, γ the surface tension of the liquid, α the immersion angle (see Fig. 42) and θ_r is the receding contact angle of the liquid on the sphere. For zero capillary force we immediately get $\alpha = \theta_r$. This allows the calculation of the receding contact angle for a spherical particle from the distance D_r the particle has to be moved into the bubble to obtain zero capillary force (Fig. 41d). Knowing the particle radius and having determined D_r from the force curve, we can calculate the contact angle [865]:

$$\cos \theta_r = \frac{R - D_r}{R}. \quad (9.2)$$

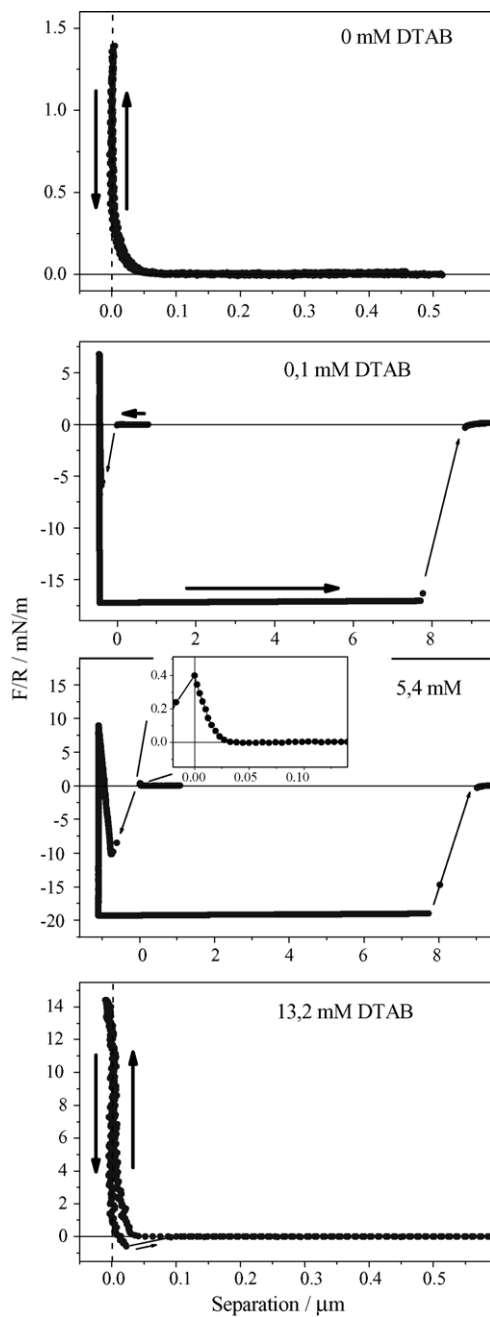


Fig. 40. Normalized force (F/R) vs. separation curve measured with a hydrophilic silica particle in aqueous electrolyte with no added dodecyltrimethylammonium bromide (DTAB), 0.1 mM DTAB, 5.4 mM DTAB, and 13.2 mM DTAB. The insert at 5.4 mM shows the electrostatic repulsion before the jump-in. For details see Ref. [31].

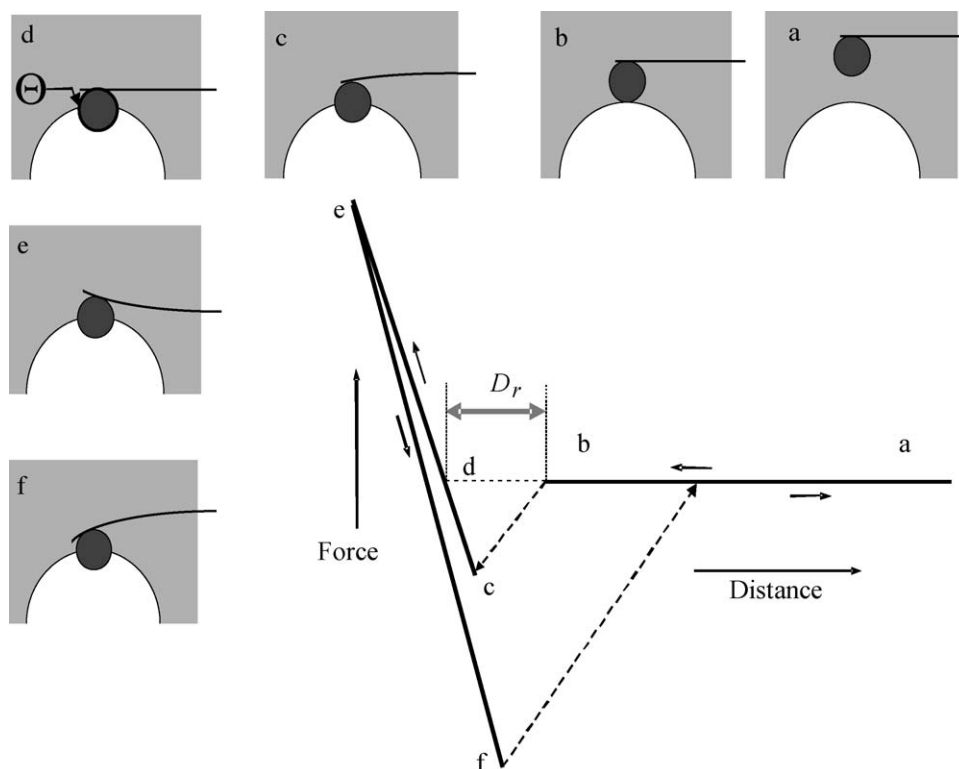


Fig. 41. Schematic of a force curve between a bubble and a hydrophobic colloid probe. D_r denotes the equilibrium immersion depth of the particle into the bubble and is equal to the difference of piezo position in (b) and (d).

By this method, contact angles in aqueous solution for silica [865,866], hydrophobized silica and polystyrene [874], polyethylene [881] and spheres with thiol-modified surfaces [865] were determined. In general, contact angles measured by microsphere tensionmetry were in good agreement with values obtained on corresponding planar substrates with some deviations found for thiol-modified surfaces [865] and silica spheres in the presence of surfactants [31].

Nguyen et al. [881] found a strong variation of contact angle for a 18 μm polyethylene particle for approach velocities greater than 10 $\mu\text{m/s}$. They assumed that the drag force on the particle and the deformation of the air–water interface lead to a decrease of the penetration depth of the particle and hence to a smaller (dynamic) contact angle.

As particles become smaller than 5 μm , line tension can become important [874]. Yakubov et al. proposed for this case a refined analysis, which accounted for the effects of line tension and the Laplace pressure resisting the particle's penetration into the bubble [874].

One obvious problem in microsphere tensionmetry is the occurrence of jump-in features. As soon as the gradient of attractive forces exceeds the value of the spring constant of the cantilever, the colloid probe will snap into the bubble. Additionally, the air–water interface may deform and jump into contact with the particle. Consequently, the jump-in may occur before the particle reaches the original position of the air–water interface. This will lead to an overestimation of D_r leading to an increased apparent contact angle. Typically, ranges of 5–100 nm are reported for the hydrophobic force. This

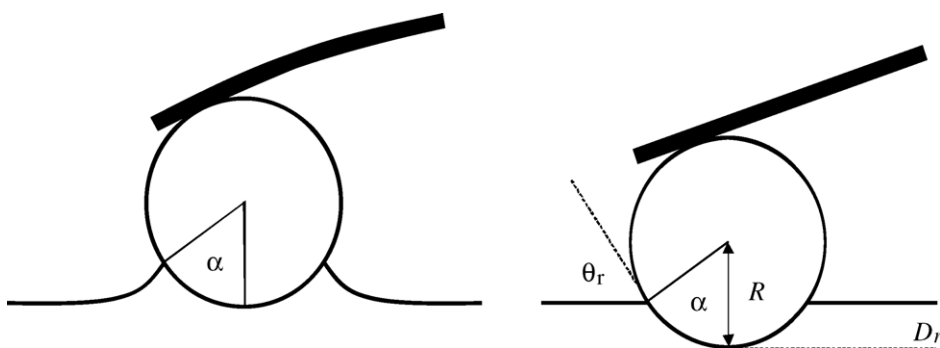


Fig. 42. Left: colloid probe with radius R at the air–water interface with immersion angle α . The deformed interface leads to a capillary force pulling on the cantilever. Right: equilibrium position of the particle at the interface. When the immersion angle equals the receding contact angle θ_r , no force is acting on the cantilever. The distance D_r corresponds to the equilibrium immersion depth of the particle into the bubble and can be obtained from the force curve as shown in Fig. 41.

means as long as the particles are much larger than this range, errors arising from this overestimation should not be serious.

When the colloid probe is forced further into the bubble (Fig. 41d and e), the interaction becomes repulsive and is generally reported to be linear, however in some cases non-linearity has been observed [864,865]. A linear repulsion can easily be explained by a spring-like resistance of the bubble against deformation; nonlinear behavior can result from movement of the three phase contact line over the particle surface.

Upon retraction of the particle from the bubble, forces again depend strongly on contact angle of the particle. For hydrophobic particles, the capillary force dominates, leading to a pronounced adhesion between particle and bubble. This leads to a snap-out when the restoring force of the cantilever exceeds the maximum capillary force (Fig. 41f). The detachment force is given by [876]

$$F_{det} = 2\pi R\gamma \sin^2 \frac{\theta_a}{2}, \quad (9.3)$$

where θ_a is the advancing contact angle of the liquid on the sphere. This dependence could be verified both for hydroxylated and hydrophobized silica spheres [853], but also values larger than expected were observed [865], probably because the movement of the three phase contact line was hindered by surface inhomogeneities. Wangsa-Wirawan et al. [882] studied the adhesion of protein inclusion bodies (protein-rich cell compartments produced in recombinant bacteria) immobilized on AFM tips to bubbles depending on pH and salt concentration to find optimum collection conditions for flotation.

For completely hydrophilic particles, forces are expected and found to be purely repulsive on retract as on approach [79,883]. However, Fielden et al. [853] observed a small adhesion between a silica sphere in spite of the fact that forces were purely repulsive on approach. Possible explanations could be a charge reversal of the surfaces during separation or impurities that lead to a small but significant contact angle. Preuss and Butt observed adhesion between silica spheres and a bubble in the presence of surfactants without prior snap-in, if surfactant concentrations and loading force were sufficiently high [31]. The origin for this adhesion is not yet understood, a possible explanation could be a restructuring of the surfactant layers at the surface. A promising approach to study interaction at the air–water interface in

the presence of surfactants or lipids has been introduced by Gillies et al. [884]. They combined a Langmuir–Blodgett trough with an AFM-related setup that allows bringing the colloidal probe in contact with the air–water interface from the aqueous phase whilst controlling the area per molecule within the monolayer of the surface active component at the air–water interface with the Langmuir–Blodgett trough. This allows selecting the phase state of the monolayer. Possible phase separations within the monolayer can be observed with an integrated fluorescence microscope.

9.2. Mechanical properties of microcapsules

Polyelectrolytes are polymers with a large number of groups that can dissociate in water and forming polyanions or polycations (multiply charged ions). They can be used to prepare ultrathin multilayer films adsorbed onto charged surfaces by consecutive layer-by-layer deposition of oppositely charged polyelectrolytes onto charged substrates [885]. The layer thickness can be controlled in the nanometer range by the number of adsorbed layers. Polyelectrolyte microcapsules (PMCs) can be prepared by this layer-by-layer deposition process on colloidal templates with subsequent dissolution of the particle core [886]. Hollow, spherical capsules with diameters of 20 nm–20 μm and shell thicknesses of 10–50 nm have been prepared by this technique. Polydispersity and size are determined by the templates and shell thickness by the number of polyelectrolyte layers. Usually, their shells are permeable only for low molecular species (<1 kDa) [887]. This makes PMCs promising candidates for drug targeting and release, and allows keeping enzymes in an active state inside the capsules where they cannot be reached by high molecular weight inhibitors from the outside [888]. For practical applications, understanding the shell permeability and mechanical properties of the PMCs is of importance. The latter can be studied by osmotically induced buckling [889], by osmotic swelling [890] or by direct probing with the AFM.

Probing the mechanical stiffness of PMCs with the AFM is done by compressing a single PMC between a colloid probe and a flat surface (usually a glass slide to allow simultaneous observation by optical microscopy) as indicated schematically in Fig. 43. The lower limit of the capsules is given by the requirement of optically aligning the capsule and the colloid probe, the upper limit by the maximum Z-range of the AFM piezo actuators. Thus, capsule radii of typically 1–7 μm are used in the AFM experiments. The best characterized pair of polyelectrolytes for layer by layer deposition is poly(allyl amine hydrochloride)/poly(sodium styrenesulfonate) (PAH/PSS) (for a review, see [891]). This pair has also been used for all AFM force experiments on PMCs except for [892], where also polyethyleneimine (PEI) and poly(diallyl-dimethyl-ammonium chloride) (PDADMAC) were used as polycations and [893], where DNA was used as polyanion. As template materials, melamine formaldehyde (MF), polylactic acid (PLA), weakly cross-linked polystyrene (PS), and MnCO_3 have been used. In principle the choice of template material should not influence the PMC properties, since the core particles are removed. This is, however, not true for two reasons: (1) MF and MnCO_3 can be dissolved by lowering the pH (1–2), for the other materials harsher conditions with organic solvents have to be used and this alters the state of the shell layer. (2) In the case of MF, a rest of positively charged oligomers may remain inside the capsules if they are filled by precipitation.

9.2.1. Theoretical models

Theoretical analysis of the compression of hollow PMCs by AFM has been done using two models that rely on different simplifications. In the first model, that assumes conservation of volume, drainage of water from the capsules is neglected on the time scale of the AFM experiment. Fig. 43 shows a schematic

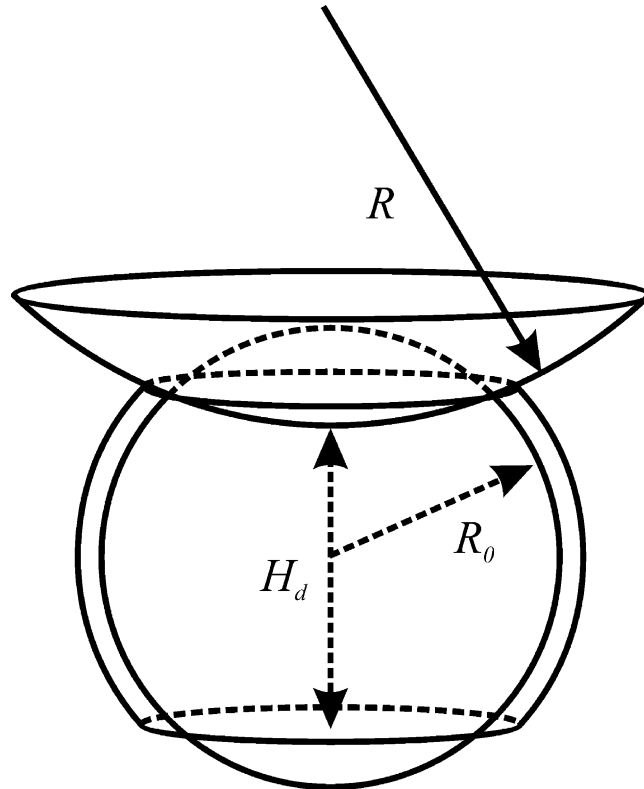


Fig. 43. Schematic of compression of a polyelectrolyte microcapsule between a plane and a colloid probe. R is the tip radius, R_0 the radius of the not deformed capsule, H_d is the height of the deformed capsule (redrawn after [894]).

for this situation. R_0 is the radius of the not deformed polyelectrolyte capsule and H_d the height of the deformed polyelectrolyte capsule. For small deformations, $R \gg R_0$ (approximately flat upper contact zone) and a value of the Poisson's ratio $\nu = 0.5$, the restoring force F can be approximated as [894]

$$F = \frac{\pi}{2\sqrt{2}} E t_s^2 \sqrt{\xi} + 4\pi E t_s R_0 \xi^3, \quad (9.4)$$

where E is the Young's modulus of the PMC shell material, t_s the shell thickness, and $\xi = 1 - H_d/2R_0$ is the relative deformation of the PMC. The first term on the right-hand side of Eq. (9.4) comes from the elastic energy of shell bending, the second term from the stretching of the shell during compression at constant volume. The relative contribution of bending effects becomes larger for decreasing ξ .

For typical experimental values ($t_s = 20$ nm, $R_0 = 2$ μ m), bending is negligibly small for $\xi \geq 0.15$ but dominating for $\xi \leq 0.04$ [895].

The second model describes the other extreme, where an infinite permeability of the PMC shell is assumed. In this case only the bending rigidity term contributes. Using a curvature of the buckling zone of $-1/R_0$, one obtains [895]:

$$F = \sqrt{2}\pi E t_s \sqrt{\xi}. \quad (9.5)$$

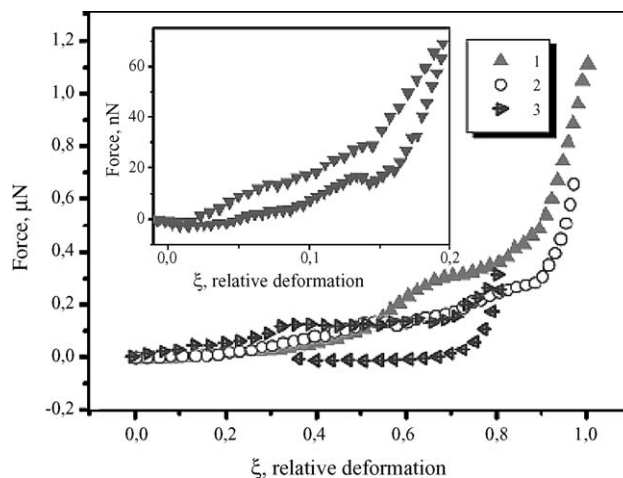


Fig. 44. Load–deformation curves for hollow PMCs. Curves 1 and 2 correspond to complete compression cycles that lead to destruction of the capsules (third regime). Curve 3 is a loading/unloading (upper/lower trace) cycle for a capsule being deformed up to the second regime. In the second regime drainage of the liquid from the capsule occurs and hysteresis in the force curve is observed. The inset shows a loading/unloading (upper/lower trace) cycle in the first regime, where the response of the capsule is elastic (reprinted from [896] with kind permission from Vinogradova).

9.2.2. Results for hollow capsules

Three different regimes within the deformation profiles for PMCs in water were found for hollow microcapsules [892,896,897] (see Fig. 44)

- for small loads ($\xi < 0.2\text{--}0.3$), PMCs showed an elastic response. Deformations were completely reversible. Only a small hysteresis was observed between approach and retract force–distance curves. No adhesion was observed. The force did not depend on approach speed;
- for intermediate loads ($0.2\text{--}0.3 < \xi < 0.7\text{--}0.8$), large hysteresis, speed dependence and only partial reversibility are observed, indicating drainage from the interior;
- for very high loads ($\xi > 0.7\text{--}0.8$) destruction of the capsules is induced, apparent from abrupt breaks in the load–deformation curve and irreversibility.

By combination of AFM with confocal microscopy, Lulevich and Vinogradova [897] were able to acquire force–distance curves and simultaneously to image the capsule deformation with high resolution from the side as well as from below. Confocal images obtained with this setup during force–distance measurements are shown in Fig. 45.

From the observation that deformations are reversible and independent of speed for small relative deformations, one can conclude that drainage from the PMCs is negligible under these conditions. Using relative deformations of 0.1–0.2 and assuming conservation of volume, values of Young’s modulus in the range 100–200 MPa were obtained for PAH/PSS PMCs based on MF [894,897], indicating that the polyelectrolyte shells behave similar to bulk elastomers. For PLA templated PMCs, Young’s modulus was 1–2 orders of magnitude smaller. This is caused by the treatment with organic solvents necessary to dissolve the template; Young’s modulus of PAH/PSS MnCO_3 based PMCs was found to decrease to comparably small values upon treatment with more aggressive acid media or organic solvents. PAH/PSS

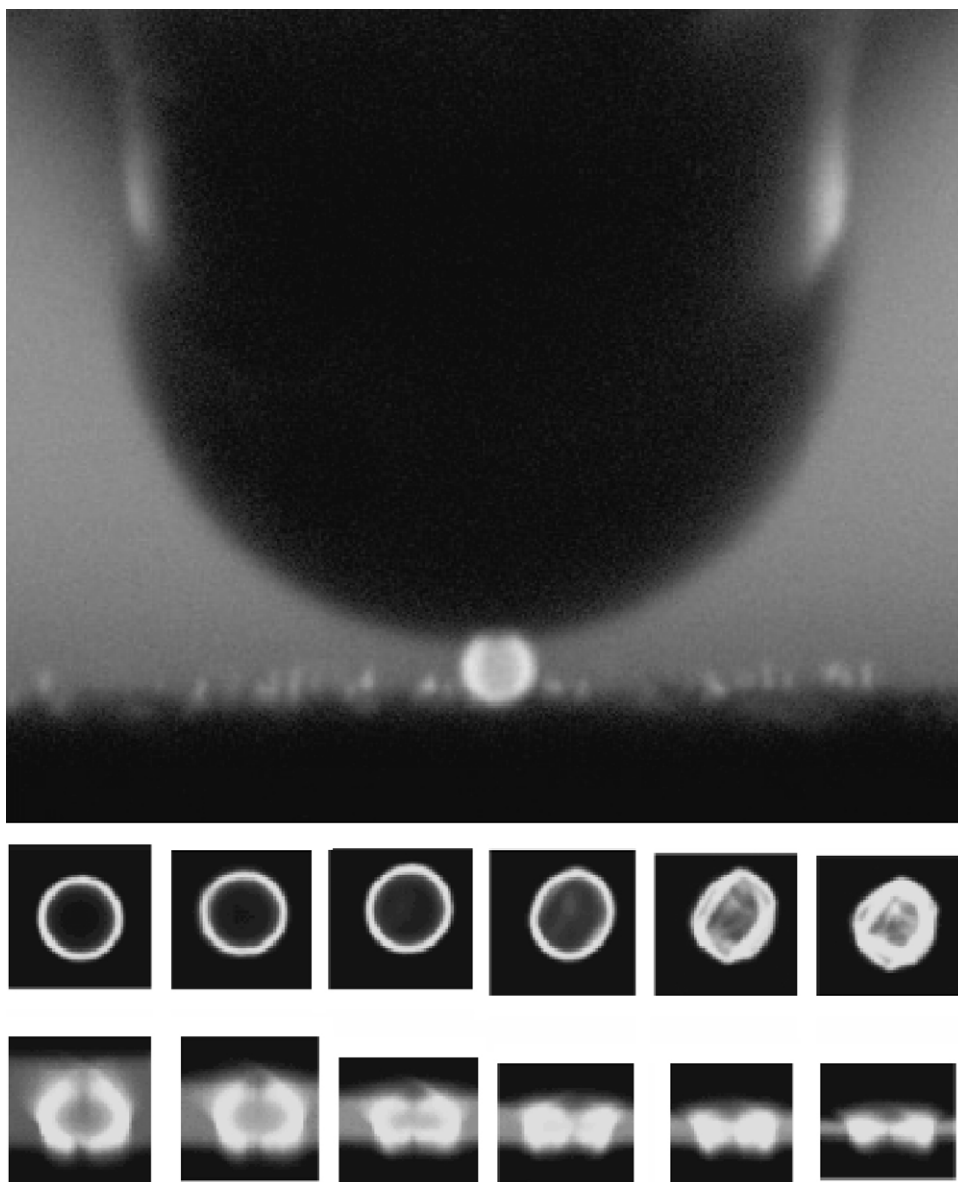


Fig. 45. Top: confocal image of a PMC confined between a colloid probe glass sphere and a glass plate. Bottom: confocal images of PMCs at different stages of deformation (upper row = bottom view, lower row = side view). From left to right $\xi = 0, 0.1, 0.25, 0.5, 0.75$ and 0.9 (reprinted from [897] with kind permission of Vinogradova).

PMCs based on MnCO_3 cores were found to have a stiffness comparable to those with MF templates [898]. Very high values of Young's modulus larger than 1 GPa for PAH/PSS PMCs templated with PS were found by Dubreuil et al. [892] from the buckling forces at very small deformations (Eq. (9.5)). This could be due to changes in the shell by the THF treatment necessary to remove PS. The stiffness of PAH/PSS (MnCO_3) microcapsules could be increased by a factor of 8 by precipitation of YF_3 nanoparticles onto the PMC

surface. The increase of PMC stiffness with shell layer thickness t_s was found to be proportional to t_s^2 at small deformations (bending rigidity dominates) [892,894], and linear in t_s for larger deformations [894]. PMC stiffness was found to be highest in pure water, decreasing slightly with increasing NaCl concentration up to 3 M [897,899]; between 3 and 5 M stiffness did not change any further [899]. Comparison with layer adsorbed electrolyte layer thickness measurements and SEM images led to the conclusion that the shells are in a tethered state for <3 M NaCl and in a melted state at higher concentrations [899]. Exposing PMCs to high or low pH values leads to softening [897]. At high pH, the charge density of the polycations will decrease, leading to less ionic cross-linking. At low pH, permeability of the capsules increases, leading to drainage during compression. No influence of molecular weight on mechanical properties was found [900]. Aging of PMCs for 6 months lead to softening due to a higher drainage rate.

9.2.3. Filled polyelectrolyte capsules

Filled PMCs can be produced in two ways. The first is the precipitation of metal complexes of polyanions as the first layer onto the template colloids. After dissolution of the core particles these polyanions will fill the PMC. Alternatively, the shell permeability can be reversibly increased by decreasing pH or addition of organic solvents to allow higher molecular substance to diffuse into the PMCs.

In general, filled PMCs are stiffer than hollow ones, as was shown for PAH/PSS capsules filled with PSS that was precipitated as PSS/Y³⁺ on MF [896,898] or MnCO₃ templates [898]. This is expected from the osmotic pressure acting across the shell. The distinct effect of filling on mechanical properties, however, depends again on how the capsules have to be treated chemically during preparation. Lulevich et al. [901] found a decrease of stiffness after filling of microcapsules with a neutral polymer (fluorescein isothiocyanate-dextran). This was attributed to an increased water permeability of the capsules after the treatment with acetone/water mixtures necessary to fill them. Lebedeva et al. [902] found that PAH/PSS (MF templated) filled by PSS using permeability increase with acetone were 1–2 times stiffer than the hollow ones, values were 10–100 times smaller than for those filled by precipitation [896,898]. For MF templated PMCs, filled with PSS with the precipitation method, an additional effect occurs that increases the stiffness and changes the shape of the load–deformation curve. Residuals of MF form a 3D network with PSS inside the capsule that contributes additionally to the mechanical stiffness, whereas for the MnO₃ templated ones only the osmotic pressure contributes.

AFM measurements on PMCs have resulted in valuable information on the mechanical properties of polyelectrolyte multilayers, mainly for the PAH/PSS system. Future studies could include improvements of the mechanical models including finite permeability of the shells or widen the range of polyelectrolytes. An example for the latter case is the recent paper by Vinogradova et al. [893] on PAH/DNA microcapsules. The inclusion of biomolecules as polyelectrolytes or polyampholytes could also lead to biological applications that mimic biocompartments.

9.3. Cells

9.3.1. Elastic properties of cells

AFM has become a standard tool of biological surface science due to its ability to image biological samples under physiological conditions at high resolution and probe molecular interactions of biomolecules. Another growing field in biological applications is the use of the AFM as a nanomechanical sensor that allows probing of the mechanical properties of cells. Reviews on this topic are given in [903,904].

Mechanical properties of single cells have been successfully probed with a variety of other techniques as cell poking [905], the micropipette aspiration technique [791,906,907], optical [908] and magnetic tweezers [909–911], and ultrasonic microscopy [912,913]. A first measurement of the mechanical properties of animal tissue by AFM force–distance curves was done by Tao et al. in 1992 [914] on a section of hydrated cow tibia. Strong variations of the mechanical properties over distances of 50 nm could be resolved. First single cells studies in 1993 of Weisenhorn et al. [915] gave values of 0.013–0.15 MPa for the elastic modulus of lung cancer cells.

Usually values of the Young's modulus are obtained by using a Hertzian contact model with different geometries (see Table 2 and Eq. (4.8)). Strictly, one cannot expect that living cells do actually meet the assumptions of the Hertz model, especially they will not be homogenous. Another problem is that the Poisson's ratio ν of the cell is not known and it varies over the cell surface. Typical values between 0.3 and 0.5 are assumed. A more sophisticated approach was to model the mechanical response of the cell membrane explicitly taking into account the mechanics of the cell membrane and that of the underlying cytoskeleton [916]. Alternatively, finite element modeling of the deformation of the cell surface was applied to interpret force–indentation curves [917]. A certain caveat is the approach speed of the cantilever towards the cell surface. At too high speeds ($>25 \mu\text{m/s}$), viscous contributions lead to a distortion of the elastic response.

The stiffness of a cell surface as observed by indentation with an AFM tip may originate from different sources. It can be caused by the cell wall itself or by underlying structures as the cytoskeleton or by a pressure difference between the cell interior and exterior. Arnoldi et al. [303] presented a theoretical model, taking into account the different contributions to measure cell stiffness by osmotic pressure inside the bacterium (turgor pressure), the bending elasticity of the cell wall, and the surface tension. Application of this model to indentation curves on the bacterium *Magnetospirillum gryphiswaldense* showed that measured cell response is dominated by the turgor pressure of $\sim 10^5$ Pa. Similar values of turgor pressure were found for *Pseudomonas aeruginosa* and *Enterococcus hirae* bacteria [918]. A complementary approach by Scheffer et al. [919] was to obtain the membrane bending stiffness from the shape of the force curve during detachment prior to jump-out using a model of axisymmetric bending of a thick annular plate [920]. The force necessary to penetrate the tensed cell membrane of an erythrocyte was determined to be in range of 10–30 nN [921] and to increase exponentially with approach speed of the AFM tip. Relative stiffness of Madine-Darby canine kidney (MDCK) cells was measured by Hoh and Schoenenberger [922] and A-Hassan et al. [923].

Approaching different strains of *E. coli* with a colloid probe, Li and Logan [924] found three distinct types of interaction: (1) steric repulsion by extracellular polymers that protruded from the cell surface (2) an elastic repulsion from the lipid bilayer that covers the cell wall and (3) a stiff repulsion caused by the cell wall itself.

Further measurements of the Young's modulus of cells have been performed with human platelet cells ($E = 1\text{--}50$ kPa) [925], human fibroblasts ($E \approx 5$ kPa) [926], mouse fibroblasts ($E = 1\text{--}60$ kPa) [927], smooth muscle cells (SMC) ($E = 5\text{--}8$ kPa) [301], guinea pig outer hair cells ($E = 2\text{--}4$ kPa) [928], cardiac cells ($E \approx 100$ kPa), skeletal muscle cells ($E = 25$ kPa), endothelial cells (1–7 kPa) [929,930], human bone cells [931], and fungal spores (*Phanerochaete chrysosporium* INA-12) and bacterial cells (*Lactococcus lactis* subspecies *lactis* bv. *diacetilactis* LMG 9452 and *Streptococcus salivarius* HB and HBC12) [369].

Comparison of the elastic properties of normal human epithelial cell lines (Hu609 and HCV29) and three cancerous ones (Hu456, T24, BC3726) showed that healthy cells have a Young's modulus of about

one order of magnitude higher than cancer cells [932]. Addition of chitosan lead to an increase of stiffness of the cancer cells, whilst the non-malignant cells were not influenced by chitosan. [933].

Cell fixation by glutaraldehyde is often used to simplify the study of cells and to improve imaging resolution [934]. Cell fixation is a process where cells are treated with different agents, e.g. glutaraldehyde, that cross-link proteins at the cell surface, thereby “freezing” the morphology of the cell. For liver endothelial cells typical values of the elastic modulus are around 2 kPa for the living cell and more than 100 kPa for the glutaraldehyde fixed cell [935] and for *E. coli* K12 strains a 4 fold increase of cell stiffness due to fixation was found [936].

Enzymatic digestion or chemical attack on components of the cytoskeleton is expected to lead to a softening of the cell and should reveal information on how much the cytoskeleton contributes to the observed stiffness of the cell. Rotsch et al. [937] observed a sevenfold decrease of elastic modulus for cultured rat liver macrophages (Kupffer cells) upon chemical attack of the cytoskeleton. Wu et al. [938] tested the influence of toxins acting on the cytoskeleton and fixing agents on fibroblast mouse (L929) cells.

The potential of the AFM for stable imaging and acquisition of force curves on living cells for extended time periods facilitates the study of dynamic processes due to external stimuli. Experiments concerned changes in cell stiffness upon increasing Ca^{2+} concentration [939,940] or the cellular contractility [941]. Also, the effect of cell differentiation [942], cell division [943], shear stress [917,944], culture time [307], and cell spreading [945] has been studied. Deformability of endothelial cell was found to increase after contact with monocytes (considered to play a major role in the early stage of atherosclerosis) [946]. Treatment of *E. coli* with an antimicrobial peptide (PGLa) led to the loss of cell stiffness and finally cell rupture [947].

9.3.2. Cell and animal adhesion

Adhesion of cells to surfaces is of critical importance in many medical, biological and industrial applications. Biocompatibility of implants and formation of biofilms on surfaces (films made up of cells, having in part different properties from isolated cells) [948] are closely related to this issue. In aqueous solutions, surface charges on cell and substrates surface are expected to contribute to the adhesion process, either promoting adhesion in the case of opposite charges or acting as a barrier due to electric double-layer repulsion (Section 6.1). Depending on ionic strength, this barrier may be reduced sufficiently to allow contact to surfaces. From this point on, other forces as the van der Waals or hydrophobic force may become dominant and promote adhesion. In fact in many studies bacterial adhesion is found to be strongly enhanced on hydrophobic substrates. The importance of hydrophobic forces may seem surprising at first sight, since cells usually exhibit a hydrophilic behavior, as can be seen from contact angle measurements [949]. However, local variations in hydrophobicity over the cell surface can lead to strong adhesion to hydrophobic surfaces. Vadillo-Rodriguez et al. probed the adhesion of hydrophobically or hydrophilically modified AFM tips to two different *Lactobazillus* strains. AFM force measurements as well as macroscopic contact angle measurements showed that the hydrophobicity of the bacteria changed with ionic strength [950].

In many cases, adhesion is mediated by the presence of proteins or lipopolysaccharides on the cell membrane, which can also give rise to steric forces upon approach. Dufrêne et al. measured forces on spores of *P. chryso sporium* using OH- and CH_3 -terminated AFM tips [951] or bare silicon tips [952] without detecting any adhesion. For germinating spores adhesive interactions were found due to binding of surface polysaccharides to the silicon nitride tips [953]. Considine et al. [954–956] used AFM measurements with silica AFM tips and a glass colloid probe to study the interaction of

oocysts of *Cryptosporidium parvum* with silica surfaces. Interactions upon approach showed a steric repulsion and upon retract adhesion due to formation of protein tethering (see Section 8.3.3 and Fig. 37) to the AFM tip was observed. Abu-Lail et al. [957] studied the influence of biopolymers at the cell surface on the interaction with silicon nitride AFM tips. For *E. coli*, removal of lipopolysaccharides reduced the range of steric repulsion on approach, increased the double-layer force, and reduced the adhesion. For *Pseudomonas putida* KT2442, they found a polymer brush-like behavior of the surface biopolymers [958]: Low salt concentration resulted in a long-range steric repulsion and low adhesion; high salt concentration led to brush collapse and higher adhesion.

In some cases cells may secrete substance to promote adhesion. The adhesive mucilage of diatoms (microalgae) was studied by Higgins et al. [959,960]. For *Craspedostauros australis*, the adhesive strands were found to be highly extensible and revealing a saw-tooth pattern in the force curve upon extension that could be fitted with the wormlike chain model (see Section 11.1), indicating stretching of single polymers on the cell membrane. No adhesion was observed for the *Pinnularia viridis* diatoms. For *Staphylococcus epidermidis* adhesion depended on strain type and surface coverage with slime produced by the bacteria [961].

Force–distance curves with the AFM can complement macroscopic cell adhesion assays as they allow obtaining laterally resolved information of adhesion [962–964].

Another mechanism for adhesion can be specific receptor–ligand interactions (see Section 11 and Ref. [965]). When present, these interactions often dominate the adhesion [966]. This type of interactions can be probed by functionalization of AFM tips or colloid probes with the corresponding biomolecules [967–969]. Adhesion of functionalized tips to cells surfaces may also be used to identify topographic structures. Pereira et al. [970] showed that AFM tips functionalized with a calcium channel blocker (nimodipine) adhered stronger to pores in the cell surface of *Saccharomyces cerevisiae* than to the rest of the cell surface, indicating that the pores might be calcium channels. [970].

Care should be taken, however, when trying to directly infer cell adhesion from interactions of AFM tips on cell surfaces. Vadillo-Rodriguez et al. [971] observed a strict correlation between hydrophobicity and adhesion in AFM experiments on *Lactobacillus* surfaces. This was not observed in flow chamber experiments. For interaction between different strands of *Streptococcus mitis* and a silicon nitride AFM tip, microscopic properties only partially correlated with macroscopic ones such as contact angle and surface charge density [972]. Interaction time and load may also be important. Vadillo-Rodriguez et al. [973] found an increase of adhesion on the 100 s timescale for *Streptococcus thermophilus* and Boonaert et al. [974] observed an increase in adhesion with load for *L. lactis* bacteria. Another complication can arise from physicochemical and mechanical changes of the cell surface by cell immobilization [975].

In the last few years, atomic force microscopy has also been applied to gain insight in the biomechanisms of animal locomotion. An example are Geckos—lizards that can run up walls and walk on the ceiling. Their feet are equipped with millions of small hairs (setae) that are responsible for adhesion of the feet to surfaces. Autumn et al. [976] measured the interaction of single setae with surfaces and found that adhesion forces were 10 times higher than estimated from experiments on whole animals. Furthermore, they could show that adhesion is mediated by van der Waals forces and not by capillary force. The feet of the jumping spider *Evarcha arcuata* attach to smooth surfaces by means of a claw tuft, the scopula, which is equipped with setae, these again being covered by numerous setules. It was found that a single setule can produce an adhesive force of 38 nN perpendicular to a surface [977]. Multiplying this with the number of setae and comparing it to the mean body weight, a safety factor of 160 is achieved.

For fly legs, attachment to smooth surfaces is also done by setae. Langer et al. [978] could show, that adhesive strength in this case comes not only from van der Waals forces but is strongly enhanced by the secretory footprint fluid. The bending stiffness of setae in attachment pads of the blowfly *Calliphora vicina* was determined by taking AFM force curves on these setae [979].

9.3.3. Cell probe measurements

To investigate the interaction forces between single cells and specific surfaces, the direct attachment of cells to an AFM cantilever in analogy to the colloid probe technique is an attractive approach. It allows the use of almost any substrate, but raises the issue of how to stably attach cells to an AFM cantilever. First attempts in this direction were made by Razatos et al. [980] who demonstrated that it is possible to coat silicon nitride AFM cantilevers including the tip with a layer of *E. coli* cells, if the cells were fixed by glutaraldehyde treatment. The authors took advantage of such functionalized tips to study the adhesion of *E. coli* [386,981] (see also Ref. [982]). The disadvantages of this approach are the need of glutaraldehyde fixation, which alters cell mechanical and surface properties, and the fact that cells may be displaced from the apex of the AFM tip during measurements.

The first true “cell probe” experiments were conducted by Bowen et al. in 1998 [983] by gluing single yeast cells (*S. cerevisiae*) onto tipless AFM cantilevers. They tested the adhesion of single yeast cells to different filtration membranes [643] (Fig. 46) and to mica surfaces [984]. For bacterial spores of *Aspergillus niger*, they conducted cell probe measurements of adhesion on mica in air [985] as well as in aqueous solution [986]. Further experiments involved *E. coli* [987] and *Navicula* species I diatoms [988].

The cell probe technique can be applied not only to bacterial cells but also to more complex cells. Luckham [320] measured the forces between red blood cells and fibroblasts and hydrophilic/hydrophobic

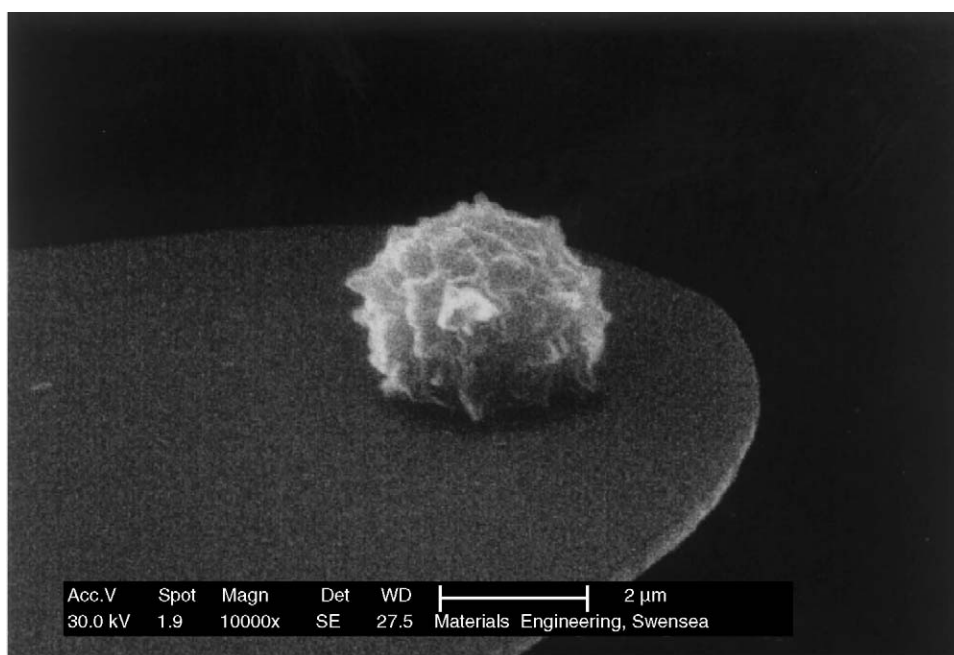


Fig. 46. Scanning electron micrograph of a single *Aspergillus niger* spore that has been attached to the end of an AFM cantilever to act as a “cell probe” (from [985] with kind permission from Bowen).

surfaces; adhesion was observed on the hydrophobic surfaces only. Doneva et al. [989] quantified the adhesion of human fibroblasts on biomaterials.

The use of the cell probe technique offers a new approach to probe cellular adhesion in a direct manner. There are, however, several issues that need further consideration. In a cell probe experiment, the cells are forced into contact with the surfaces and the contact times are usually short. This may be quite different to the typical situation in cell attachment under natural conditions. Bowen et al. [990] compared cell probe measurements of *Bacillus mycooides* adhesion with the spinning disk technique, where hydrodynamic shear is used to displace cells at a surface. The results were in qualitative agreement, but adhesive forces measured by AFM appeared up to 4000 times larger than by the spinning disk technique.

Another question is the impact of the mounting procedure on the physiological status of the cells. As an example, living *S. cerevisiae* cells showed different adhesion properties compared to cells fixed by glutaraldehyde [984].

The ability to mount single cells onto an AFM cantilever opens the field to cell–cell interaction to direct AFM force measurements. Due to the experimental difficulties involved, examples of such measurements are still rare [991–993]. These studies demonstrate the potential of the cell probe technique to directly access information on cell–cell interaction under physiological conditions. Due to the complexity of sample preparation, it will, however, hardly reach the status of a routine tool in this field.

10. Hydrodynamic force

10.1. Introduction

When doing experiments with the colloidal probe technique in liquids we have to take hydrodynamic effects into account. A microsphere approaching a planar surface or another sphere has to squeeze out the liquid to close the gap. This requires a force—the hydrodynamic force. Like Stokes friction, this force increases proportional to the velocity. In contrast to Stokes friction, however, it depends on distance. It depends on the distance because as the gap gets smaller and smaller it becomes more and more difficult to remove liquid from the remaining gap. Upon approach it is repulsive, upon retraction it is attractive.

Hydrodynamic forces between particles are important in many natural phenomena and industrial processes, either directly or indirectly. They directly influence the kinetics of coagulation since hydrodynamic forces hinder particles from getting into contact. This is particularly important when stirring a dispersion. Indirect relevance comes from the fact that hydrodynamic forces depend on the hydrodynamic boundary condition, or more generally on the mechanical properties of a liquid at a solid surface. As such, a measurement of hydrodynamic forces can provide information on the properties of liquids at solid surfaces. The mechanical properties of liquids at solid surfaces are important in lubrication, adhesion, wetting, colloidal hydrodynamics, and microfluidics.

In fluid mechanics one usually relies on the assumption that when liquid flows over a solid surface, the liquid molecules adjacent to the solid are stationary relative to the solid and that the viscosity is equal to the bulk viscosity. Though this might be a good assumption for macroscopic systems, it is questionable at molecular dimensions. Measurements with the SFA [994–997] and computer simulations [998–1000] showed that the viscosity of simple liquids can increase many orders of magnitude and liquids can even undergo a liquid-to-solid transition when being confined between solid walls separated only few molecular diameters; water seems to be an exception [1001,1002]. Several experiments also indicated that isolated

solid surfaces induce a layering in an adjacent liquid and that the mechanical properties of the first molecular layers are different from the bulk properties [78,724,725,1003]. An increase of the viscosity can be characterized by the position of the plane of shear. Simple liquids often show a shear plane which is typically three to six molecular diameters away from the solid–liquid interface [78,994,1004–1006].

A tenet of textbook continuum fluid dynamics is the “no-slip” boundary condition, which means that liquid molecules immediately at the surface of a solid move with exactly the same velocity as that solid. A possible slip was only discussed in the mainstream literature for polymer melts [1007,1008]. Recent experiments, however, indicated that fluids might slip past smooth surfaces [1009–1014]. The hydrodynamic boundary condition to describe slippage is [1015]

$$\frac{dv_x}{dz}(z=0) = \frac{v_x(z=0)}{b}. \quad (10.1)$$

Here, z is the direction normal to the planar surface, v_x the local velocity of the liquid in a direction parallel to the solid surface, and b is the so-called slip length. Specifically $v_x(z=0)$ is the fluid velocity directly at the surface, the so-called “slip velocity” and $dv_x/dz(z=0)$ is its gradient. The slip length is the distance behind the interface at which the liquid velocity extrapolates to zero.

An important parameter is the interaction between the liquid molecules and the solid wall. For “weak” liquid–wall interaction the liquid molecules interact more strongly with each other than with the solid wall. Experimentally, weak liquid–wall interaction implies that the contact angle Θ of the liquid on the solid surfaces is higher than 90° . For strong liquid–wall interaction the contact angle is low ($\Theta < 90^\circ$) or the liquid even wets the solid completely ($\Theta = 0$). Computer simulations [1016–1020] and experiments confirmed that for low fluid–wall interactions slippage occurs [1009,1021,1022].

Both interfacial effects discussed – slip and a change in viscosity – are experimentally related. The same effect as real surface slip, where the liquid molecules adjacent to the solid wall are actually moving along the wall, can be caused by a change in the viscosity close to the solid wall. If the viscosity of the near-to-wall layer is characterized by a viscosity η_s the effective slip is

$$b = h \left(\frac{\eta}{\eta_s} - 1 \right), \quad (10.2)$$

where η is the bulk viscosity and h is the thickness of the surface layer. For example, if we assume that the viscosity of a 1 nm thick layer is reduced by a factor of 2, the slip length is $b = 0.5$ nm. For most liquids, however, the viscosity at solid surfaces is increased rather than decreased.

In summary, it is not yet clear which boundary condition for which liquid and for which shear rate is correct. Most results indicate that slip is present on lyophobic surfaces, on which the liquid does not “like” to be in contact with the surface and the contact angle Θ is equal to or larger than 90° , and that the slip depends on the shear rate. It is not yet clear under which conditions slip occurs on lyophilic surfaces ($\Theta \ll 90^\circ$), in particular for water on hydrophilic surfaces.

10.2. Theory

When doing experiments with the colloidal probe technique in liquids we have to take hydrodynamic effects into account. We first consider the most simple case, that is a Newtonian liquid and no-slip boundary condition. A Newtonian liquid is a liquid where the viscosity is constant and does not depend on the shear rate. No-slip boundary condition is the usual boundary condition which requires that the

molecules directly in contact with the solid surfaces stick to the surface and do not slide laterally. For this case a sphere of radius R moving with a velocity v towards a planar surface has to overcome a repulsive force [78,1023,1024]

$$F = 6\pi\eta v \frac{R^2}{D}. \quad (10.3)$$

Eq. (10.3) is valid for small distances ($D \ll R$). The right side of Eq. (10.3) is equal to the expression of Stokes for the viscous drag on a sphere in bulk fluid multiplied with R/D . Since the hydrodynamic force scales with R^2 , it is only relevant for colloidal probe experiments and is negligible for experiments with microfabricated tips. In fact, in order to do quantitative experiments the probe should be relatively large ($R \geq 10 \mu\text{m}$). Otherwise the hydrodynamic force on the cantilever might contain a distance-dependent contribution [201]. Although the cantilever is at least a distance $2R$ away from the sample surface, due to its large cross-sectional area it might contribute to the whole force. Even in gaseous environment the compression of the gas in the gap between cantilever and surface needs to be considered [1025] and it can slightly change the resonance spectrum.

Benmouna and Johannsmann analyzed the hydrodynamic force in more detail [1026]. They point out that Eq. (10.3) is only valid if the microsphere is only weakly accelerated. For a typical force experiment this is no limitation. When analyzing thermal noise spectra, however, a frequency and distance-dependent damping coefficient has to be taken into account. Benmouna and Johannsmann also analyze the effect of cantilever tilt and lateral motions on the hydrodynamic force [107].

Experiments have shown that the assumptions of no-slip is generally not fulfilled. To take slip at the solid surfaces into account Vinogradova introduced a correction factor f^* and described the hydrodynamic force by [1027]

$$F = 6\pi\eta v \frac{R^2}{D} f^* \quad \text{with} \quad f^* = \frac{D}{3b} \left[\left(1 + \frac{D}{6b}\right) \ln \left(1 + \frac{6b}{D}\right) - 1 \right]. \quad (10.4)$$

As mentioned above, slip and a change of viscosity in a surface layer of the liquid can lead to the same phenomena. A first approach to take a change in viscosity into account was published by Feibelman, who calculated the hydrodynamic force assuming that tip and sample are coated with liquid layer of different viscosity [1028].

10.3. Experiments

We start by discussing hydrodynamic forces in Newtonian liquids. Here, the question is whether slip occurs or not (for a review see Refs. [1029,1030]). It is now generally accepted that slip occurs for liquids on lyophobic surfaces, for example for water on hydrophobic surfaces [1009]. This is a result of a number of experiments with the AFM and other techniques. Also simulations indicate that for weak liquid–wall interactions slip is expected. For strong liquid–wall interactions AFM results indicate that also slip occurs. Significant slip lengths of up to 20 nm were found by Craig et al. in aqueous sucrose solutions (viscosities of 0.01–0.08 Pa s) [1031]. They measured hydrodynamic forces between gold coated silica spheres and gold coated mica. The gold surfaces were coated with a self-assembled monolayer of alkanethiols leading to an advancing contact angle of 70° . In their case, slip lengths increased with increasing viscosity and shear rate.

Surface roughness can lead to an apparent slip length because in contact the liquid can still flow out of the gap beside the asperities. (In fact it was shown later that roughness has a much more drastic effect

[1032].) To exclude this Bonaccorso et al. [190] measured hydrodynamic effects between borosilicate glass particles and mica or silicon oxide in aqueous medium. The roughness of the particles was below 1 nm rms. Peak-to-valley distances of areas of $1 \mu\text{m}^2$ were below 2 nm. Mica was atomically flat. To verify that the surfaces were hydrophilic the receding contact angle of the glass particles were determined by microsphere tensiometry where the interaction of the particle with an air bubble in aqueous medium is measured [866]. Zero contact angle was obtained. Also mica is completely wetted by water ($\Theta < 5^\circ$). Slippage, characterized by a slip length of 8–9 nm was observed. The result, that slip occurs even for strong liquid–wall interaction was confirmed by experiments in propanol [1033]. At low approaching velocities oscillatory solvation forces indicate a layered structure of the confined propanol for at least three layers. Layering is only expected for strong liquid–wall interaction. In the same experiment, hydrodynamic forces were measured at high approaching velocity. Comparing measured force curves with calculations a significant effective slip was found, which could be described by a slip length of 10–14 nm. In contrast, in experiments with two particles glued to the cantilever to increase the distance of the cantilever, Vinogradova and Yakubov found no slip [1034].

Experiments [1035–1039], simulations [999,1017,1040,1041] and theory [1042,1043] indicate that the degree of slip depends on the shear rate. Slip seems to occur only from a certain critical shear rate on and it increases with the shear rate. This critical shear rate is correlated with the contact angle and thus surface wettability. Therefore it would be interesting to measure the hydrodynamic force for various shear rates. This is possible with the AFM, there are, however, limits. The problem is that the degree of shear depends on the exact position, the distance and the approaching velocity [78]. Considering a spherical tip of radius R at a distance D from a planar surface, we can write:

$$\frac{\partial v_r}{\partial z} = \frac{6vr}{(D + r^2/2R)^3} \left[z - \frac{1}{2}(D + r^2/2R) \right]. \quad (10.5)$$

Here, v_r is the velocity of a liquid element in radial direction at a given position z and r in the gap, v the approaching velocity ($v = dD/dt$), and $D + r^2/2R$ is the distance between the planar surface and the surface of the spherical particle at a given radial coordinate r . Shear is high at both solid–liquid interfaces (at $z = 0$ and $z = D + r^2/2R$). In radial direction it is zero at $r = 0$, increases with r up to $r = \sqrt{2DR/3}$ and then decreases to zero at $r \rightarrow \infty$. The absolute maximal shear rate is [78]

$$\left. \frac{\partial v_r}{\partial z} \right|_{\max} = \frac{9}{8} \sqrt{\frac{3R}{2D^3}} v. \quad (10.6)$$

For this reason it is difficult to quantify the shear rate. Nevertheless, semi-quantitative experiments are possible. Henry et al. [1044] for example showed that when surfaces are partially covered by adsorbed surfactants, slip ceases to depend directly on surface wettability.

Analyzing hydrodynamic force curves is not as simple as for usual force curves because they depend on the velocity, and the velocity decreases gradually from v_0 at large distances to zero at contact. Therefore hydrodynamic force curves have to be simulated by solving the equation of motion for a sphere moving towards a flat surface. Neglecting other surface forces, the hydrodynamic force is balanced by the restoring force of the cantilever $F_K = k_c(D - D_i + v_0 t)$. Here, D_i is the initial separation at $t = 0$. The expression $D - D_i + v_0 t$ is equal to the deflection of the cantilever. The effect of the hydrodynamic force is to retard the particle. As a consequence the velocity of the particle at a given time t is not equal to v_0 because the changing deflection of the cantilever has to be taken into account. This results in a

non-uniform velocity of the particle during approach and retraction. The equation of motion, $F_H = F_K$, was calculated separately for the approaching and retracting part:

$$-\frac{6\pi\eta R^2}{D} \frac{dD}{dt} f^* = \begin{cases} k_c(D - D_i + v_0 t) & \text{for approach} \\ k_c(D - D_r - v_0 t) & \text{for retraction} \end{cases} \quad (10.7)$$

The position of the piezo at the beginning of the retraction was D_r . Eq. (10.7) was solved numerically.

In an alternative approach Notley et al. used a dynamic mode to analyze hydrodynamic interactions [846]. A high frequency (≈ 400 Hz), low-amplitude (≈ 4 nm) oscillatory movement was superimposed to the piezoelectric scanner in addition to the slow up and down movement applied to take a force curve. The phase change and amplitude attenuation of the oscillatory cantilever deflection were measured as a function of the surface separation. From the ratio of the applied amplitude A_0 to the detected cantilever amplitude Z_0 they calculated the effective hydrodynamic thickness which is defined as D/η according to [1001,1045]

$$\frac{D}{\eta} = \frac{12\pi^2 R^2 \nu}{k_c \sqrt{(A_0/Z_0)^2 - 1}}. \quad (10.8)$$

Knowing D they determined the effective viscosity of the liquid layer between microsphere and sample. In this way they characterized polymers adsorbed to a solid surface [846]. Benmouna and Johannsmann analyzed thermal noise to determine the viscoelastic and hydrodynamic coupling between a microsphere and a swollen polymer layer [1026].

11. Single molecules

The unique capability of the AFM to acquire forces locally and with high sensitivity makes it possible to get information about the interactions of a single molecular pair. This kind of experiments is known as “force spectroscopy” (for reviews see Refs. [24,1046]). Two main fields of interest have emerged in recent years: Molecule stretching [1047–1049] and specific interactions between biological pairs [1050–1052]. Accordingly, two relevant classes of models have been developed: One to describe the stretching of a linear polymer, the other to describe rupture of a single bond.

11.1. Molecule stretching

In stretching experiments a macromolecule, bound with one part to the sample and with the other to the tip, is stretched until it detaches from one of the surfaces. The presence of an adhesion peak at a distance of up to the contour length of the polymer is indicative for a stretching phenomenon. One force–displacement curve may present several jumps, due to the presence of more than one bridging molecule. A typical example, the force curve of poly(vinyl acetate) in 3-heptanone, is shown in Fig. 47. As usual in this field of research attractive forces are shown as positive.

The basic cause of the attraction is the reduction of entropy of the linear polymer upon stretching, at least at low forces (below some 10 pN). Therefore we consider a linear flexible polymer chain held at both ends. As a result of thermal fluctuations, the molecule bends and curves locally and it changes its configuration all the time. It is a fact that the number of available configurations a linear polymer can

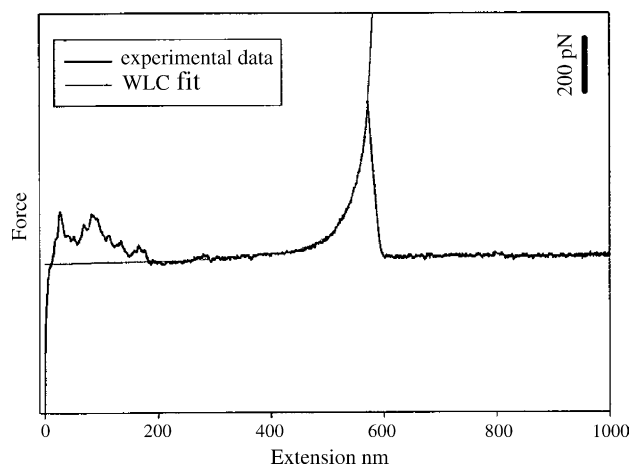


Fig. 47. Force–extension curve of a single poly(vinyl acetate) molecule in 3-heptanone, fitted with the worm-like-chain (WLC) model. Reprinted from [1069], with permission from the American Chemical Society.

assume is reduced when moving the ends away from each other. Thus, the entropy is reduced and in order to move the ends away from each other work has to be done and a force has to be applied.

This elastic behavior is described by two models: the freely jointed chain (FJC) [1053–1055] and the wormlike chain (WLC) [1049,1056–1058] model. In the FJC model the polymer is thought to consist of n chain links. Each link (or segment) has a length l_K , called the Kuhn length, whose orientation is completely independent of its neighbour's. The contour length is $l_0 = nl_K$. When a stretching force F is applied, the chain tries to regain a random configuration. For small forces ($F < k_B T/l_K$) the molecule still almost has a random coil configuration and the end-to-end extension is small. For large forces the molecule is nearly completely stretched. The relative extension $x = l/l_0$ versus force is given by the Langevin function [1053,1055]:

$$x = \coth\left(\frac{Fl_K}{k_B T}\right) - \frac{k_B T}{Fl_K}. \quad (11.1)$$

An extended FJC model (FJC+) [1059] includes also the elasticity of the single segments in the form:

$$x = \left[\coth\left(\frac{Fl_K}{k_B T}\right) - \frac{k_B T}{Fl_K} \right] \left(1 + \frac{F}{l_K k_{FJC}} \right), \quad (11.2)$$

where k_{FJC} is the elasticity of a segment in N/m.

In many cases a better description of the extension is given by the WLC model. In the WLC model the polymer is an elastic cylinder with a constant bending elasticity and of constant length [1056,1060]. The force required to stretch a WLC-modeled polymer is given by [1057,1058]

$$\frac{Fl_p}{k_B T} = x - \frac{1}{4} + \frac{1}{4(1-x)^2}, \quad (11.3)$$

where the persistence length l_p is the distance over which the orientational correlation is decreased by a factor e . For small extensions ($x < 0.5$) Eqs. (11.1) and (11.3) predict almost a similar behavior if the Kuhn and persistence lengths are related by $l_K \approx 2l_p$.

Although the standard WLC model already includes bending elasticity, a “stretching” elasticity can be included using a parameter K_{WLC} (in units of N) [1061]:

$$\frac{Fl_p}{k_B T} = x - \frac{1}{4} + \frac{1}{4(1-x)^2} - \frac{F}{K_{\text{WLC}}}. \quad (11.4)$$

Experiments about the stretching behavior of a molecule have been performed with polymers in different solvents [833,845,1062–1077], DNA [1078–1080], RNA [1081] and other macromolecules [1082–1086].

In the field of DNA research, the pioneering observations of Noy et al. [1087] have been confirmed by several experiments: the stretching of a DNA duplex (two coupled twisted strands) can be divided in three regions: a short elastic region, a pronounced flat region where the separation increases under almost constant force, indicative of a structural transformation, and a relatively stiff elastic region prior to the detachment.

In a fundamental experiment Al-Maawali et al. [1088] have calculated distributions of contour lengths of grafted PDMS chains from force–extension curves by means of Eq. (11.3). They have shown that the contour lengths distributions are correlated with the molecular weight distribution. For example, a surface grafted with PDMS of two different molecular weights (3 and 15–20 kDa) had a bimodal contour lengths distribution, with peaks corresponding to the two molecular weights. (See also [1089].) Later, also the effect of the polymer chains density on such a determination of the molecular weight has been studied [1090].

Lubensky and Nelson [1091,1092] have studied a class of micromanipulation experiments, exemplified by the pulling apart of the two strands of double-stranded DNA. When the pulling force is increased to a critical value, an “unzipping” or “unravelling” transition occurs. For random DNA sequences with short-ranged correlations, the authors obtain exact results for the number of monomers liberated and the specific heat, including the critical behavior at the transition. Unzipping experiments have been performed with an AFM also in the group of Gaub [1093]. The authors have acquired unzipping curves of DNA molecules with repeating blocks of 10 or 20 pure GC and 10 or 20 pure AT base pairs. Since the base-pairing energy of the AT pairs is higher than that of the GC pairs, the curves show a typical modulation with variation in force of 5–10 pN and with a period of 20–25 nm. The authors proved that unzipping curves are able to discriminate the DNA sequence with a resolution of 10 base pairs.

A special case of force–extension experiments is that of protein unfolding/refolding [1094–1101], whose typical fingerprint is a saw-tooth pattern in the force–displacement curve, corresponding to the successive stretching and unfolding of protein domains. Each stretching portion can be fitted with the FJC or the WLC model. Such experiments are particularly important in the case of proteins specifically designed to withstand forces, like titin [1102–1104] and spectrin [1105]. We cite a small part of the very wide existing literature. For a review see [1106].

Recently, Janovjak et al. [1107] have separated the elastic (conservative) and viscous (dissipative) contributions to the unfolding process by supplying small oscillation amplitudes to the vertical displacement of the cantilever at a frequency of 3 kHz. Similar force–extension curves have been revealed also for polymers [1108].

11.2. Rupture force of specific interactions

Using the AFM it has become possible to measure the rupture of single bonds depending on parameters such as the loading rate (increase in force per second), temperature, and other conditions.

This is possible for covalent bonds [1109] but most studies focus on the specific interaction between complementary biomolecules. In biology, specific bonds arise from the cooperation of several non-covalent bonds (e.g. hydrogen or ionic bonds) supported by the shape of the interacting molecules. In some cases the two molecules fit together by means of a “lock and key” mechanism. Specific bonds, like covalent bonds, have a precise stoichiometry.

The theory mostly used for describing rupture of a single bond due to an applied load goes back to Bell [1110], who studied the adhesion of cells to substrates. Single bond experiments also stimulated the development of an adequate theory to describe bond rupture (e.g. [1111–1115]). The idea is that an activation energy barrier U_0 has to be overcome before a bond ruptures. The applied force adds an energy term which effectively lowers the activation so that at some point thermal fluctuations can drive the system over the energy barrier and the bond breaks. An equation developed by Evans and Ritchie [1111] is often successfully applied to specific forces. The equation gives the mean rupture force F as a function of temperature and loading rate $k_c v_0$:

$$F_0 = \frac{k_B T}{x_\beta} \ln \left(\frac{\tau x_\beta v_0 k_c}{k_B T} e^{U_0/k_B T} \right). \quad (11.5)$$

Here, x_β is a distance, which characterizes the separation between the bound state and the transition state, and τ is the inverse of a vibration frequency. Please note that Eq. (11.5) is formally similar to Eq. (8.9) for the rupture of molecular layers; we only have to set $F_T = k_B T/x_\beta$. One important prediction of Eq. (11.5) is the logarithmic increase of the mean rupture with the loading rate. By measuring the rupture force versus the loading rate the activation barrier can be determined. Eq. (11.5) was also successfully used to analyze the adhesion for a Si_3N_4 tip on mica in water and for COOH-terminated tips and samples in ethanol [1116].

In order to measure specific forces with the AFM, it is necessary to functionalize the tips by covering them with one of the two molecules under study. The presence of a specific bond is revealed by one or more discontinuities in the withdrawal curve after jump-off-contact (due to aspecific adhesion). In principle, the jump-off-contact and the specific detachment may overlap, so that the specific force is hidden by the aspecific adhesion. In order to avoid this problem, one can perform the measurements in a particular liquid with small van der Waals force or attach one or both of the interacting molecules to the tip and/or to the sample via a spacer, i.e., a few nanometers long molecule which is stretched during the detachment and makes the rupture of the bond occur at distances greater than the jump-off-contact distance. Also, particular techniques of immobilization of the interacting molecules and the use of particular surfactants can reduce the non-specific interactions [1117].

Force–displacement curves with discontinuities due to specific forces contain information about (1) the force of a single binding event, (2) the rupture distance, depending on the length of the molecules and of the spacers, (3) the adhesion probability, i.e., the ratio between the number of force–displacement curves with specific detachment and the total number of force–displacement curves, depending on surface coverage and experimental conditions. The histograms of the force rupture values show a typical profile with peaks at multiple values of the force necessary for breaking one bond, corresponding to the number of bonds taking place in a contact.

In the last 5 years there has been a large number of works dealing with specific forces. As in the case of stretching experiments, the list of cited articles is limited to representative experiments. Host–guest complexes have played a predominant role in the study of specific forces. Several experiments have been performed with different complementary molecules in the last years [368,1118–1129]. It also has been

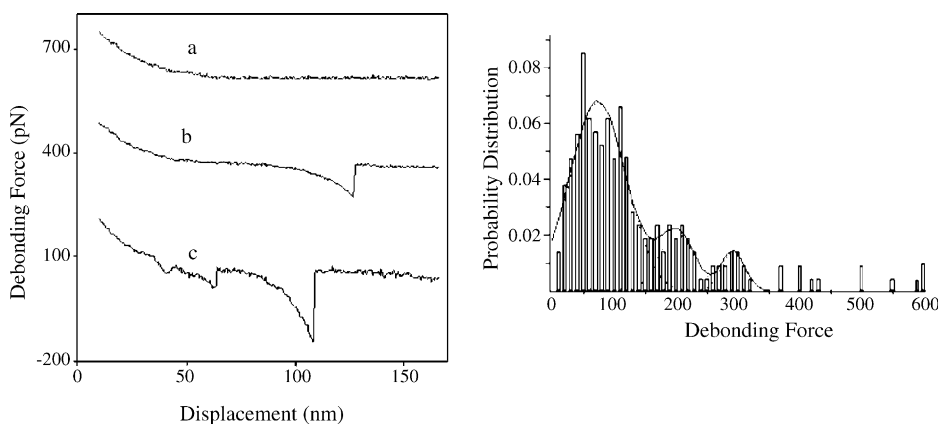


Fig. 48. Typical experimental force–distance curves obtained on a platelet surface in buffer. Curve (a) is acquired with an unmodified Si_3N_4 tip, and no specific adhesive peak can be seen. Curves (b) and (c), acquired with a tip functionalized with the peptide sequence arginine-glycine-aspartate, show several adhesive peaks. In curve (c) multiple jump-offs can be observed, suggesting multiple debonding events. In the right part, the related histogram is shown. Reprinted from [1127] with permission from Elsevier.

shown, that force–displacement curves with functionalized tips can be employed to distinguish molecules of different chirality [1130,1131].

Typical experimental force–distance curves showing several specific adhesive peaks, and the relative histogram, are shown in Fig. 48. The dependence of the bond-rupture force on the loading/unloading rate has been studied in a number of works [673,1132,1133]. Lo et al. [1134] have studied this dependence with biotin–streptavidin, taking advantage of the Poisson statistic method illustrated in Section 5, and have shown that the bond strength depends linearly on the logarithm of the loading rate (see Eq. (11.5)). The presence of more than one linear regime indicates the existence of several energy barriers. (See also [1135–1137].) The same dependence on the loading rate has been found also for DNA [1138].

Lo et al. [1139] have studied also the temperature dependence of the biotin–avidin specific force rupture. AFM force measurements have been performed at various temperatures (13–37 °C) with slow constant loading rates. The unbinding force at a fixed loading rate extracted with the Poisson's statistic is shown to decrease down to five-fold with increasing temperature. On the basis of a thermodynamic model similar to that of Eq. (11.5), the critical unbinding energy per biotin–avidin complex is estimated.

Bergkvist et al. [1140] have shown that specific forces can be exploited to study the orientation of proteins. Using ligands which bind to a defined region of the adsorbed protein, force–displacement curves are acquired, and the quantity of formed complexes gives an estimate of the amount of protein oriented in such a way as to allow ligand binding. (See also [1117,1141].)

Gutsmann et al. [1142] have used short cantilevers (length smaller than 20 μm) to improve the force resolution below 10 pN range. In this way they were able to detect two specific bond ruptures in force–displacement curves acquired with collagen fibers: one strong bond (jumps in force of several hundred pN) with a period of 78 nm and one weak bond (jumps in force smaller than 7 pN) with a period of 22 nm.

Several experiments also have been performed with DNA strands [1078,1143–1146], DNA-ligands [1147–1150], RNA [1151], RNA-ligands [1152], peptides [1153], and other complementary molecules [389,1154,1155]. In particular, Schumakovitch et al. [1156] have studied the temperature dependence of unbinding forces between complementary DNA strands. Sattin et al. [1146] determined the force

contribution of a single AT base pair. A challenging experiment was that of Afrin et al. [1157], who acquired force–displacement curves on the live cell surface with a tip functionalized with a covalent cross-linker, and have shown that only curves with the functionalized tip, and not the curves acquired with a normal, not functionalized tip, gave clear indication of prolonged adhesion which was terminated by a single step release.

12. Imaging based on force–distance curves

12.1. Force volume mode

Instead of taking forces–distance curves only on selected points of the sample, one can also acquire force–distance curves in every point corresponding to a pixel of the AFM image. Since the tip is scanned not only along the surface, but travels also in the *Z*-direction perpendicular to the surface, the term “force volume mode” has been coined for this mode of operation. From the array of force–distance curves the spatial variation of interactions throughout the sample surface can be obtained. This is usually done by post-processing of the force data, resulting in two-dimensional maps of physico-chemical sample properties, although real-time data analysis by special hardware is in principle possible [32,1158]. Since lateral movement of the AFM tip can be done in a retracted position in force volume mode, lateral forces on the sample during scanning can be avoided. Image resolutions comparable to tapping mode AFM can be achieved [1159]. A fundamental problem in force volume mode is the relatively long acquisition time that can easily amount to tens of minutes and can give rise to excessive drift. This and the memory usage for storing all data points limit the resolution of the force maps to usually 64×64 data points (in some cases also 128×128 force curves were acquired [1160,1161]) compared to the typical 512×512 pixels for standard AFM images. A promising approach to overcome the long acquisition time is the use of very small rectangular cantilevers that allow force-volume imaging at pixel frequencies of 25–65 Hz in liquid and enable imaging of single molecules in adhesion maps in real-time [1162]. Depending on the AFM used, also the maximum number of data points per force–distance curve is limited to smaller values compared to acquisition of single force–distance curves. This can, e.g., lead to the effect that specific ligand–receptor binding events that are visible in single force curves become unresolvable in the force volume mode [1163].

Earlier work in force volume imaging of biological surfaces has been summarized by Heinz and Hoh [1164]. More recently an article by Green et al. [1165] reviews force measurements on molecular interactions with a focus on two-dimensional mapping.

While the early realizations of the force volume mode [32,1158,1160,1166–1168] required development of special AFMs or supplementary hardware and software by these groups, this mode is now integrated into most commercial AFMs. A critical point that has hindered a widespread use of force volume is data evaluation, which is currently not part of standard AFM software of the commercial suppliers. Since some thousand force curves have to be evaluated for each data set, sophisticated software routines have to be developed by the users for automated analysis in order to make efficient use of force volume mode.

From adhesion or stiffness maps obtained by force volume mode, additional material contrast is available that may allow material identification. Examples are the identification of patterns in polystyrene generated by oxygen plasma treatment [1169], wear removal of a perfluoropolyether

lubricant from silicon surfaces [683], phase separation in polymer blends [1170], characterization of the hydrophilicity of $\text{TiO}_2\text{:OH}$ films before and after UV treatment [1171], the structure of collagen adsorbed on polystyrene [1172], hole formation by aging in Langmuir–Blodgett monolayer films of stearic acid [1173,1174], heat induced changes of ovalbumin (white egg protein) layers on mica in aqueous solution [1175]. Reynaud et al. [298] used single force curves on bulk samples reference materials for calibration and then measured in force volume mode the Young's modulus of a biphasic PMMA/polyacrylate polymer system. Schönherr et al. [124] used adhesion maps by OH-terminated AFM tips on oxyfluorinated films of isotactic polypropylene as a function of pH to get laterally resolved maps of force titration curves, resembling lateral variations in surface functional groups with a resolution of 20 nm.

Local variations in adhesion may also allow identification of surface contaminants [1176–1179], the study of the influence of surface topography [625,701,1180] and roughness [1179] on adhesion, or the monitoring of surface heterogeneity during production steps of PEO layer grafted to a glass surface [1181].

An interesting effect was observed by Kokkoli and Zukoski [1182] when mapping the interaction of a 20 μm colloid probe with a CH_3 terminated surface with striped pattern with COOH and CH_3 termination (width between 0.27 and 2.9 μm). For equal width of COOH and CH_3 stripes, adhesion contrast between hydrophilic and hydrophobic areas disappeared. In all other cases, the hydrophobic sphere could differentiate between the different surfaces.

Visualization of the local variations in elastic properties is ideal for characterization of composite materials and has been applied to commercial elastomers (RTV11TM and IntersleekTM) containing filler particles [273], carbon fiber/epoxy composites [1183], and a CaCO_3 filled silicone elastomer coating material [1184]. It has also been used to investigate the influence of film thickness on the apparent elastic modulus using a wedge shaped gelatin film sample [1185], to correlate distribution of elastic modulus over an agar gel surface to the network structure of agar fibers [1186], to measure the dependence of compressive modulus of poly(styrene-*co*-vinyl-benzyl-(trimethyl)-ammonium chloride) (VBTA) microspheres on the VBTA content [270], and to characterize the mechanical stiffness of the inner and outer layer of wool fibers [1187].

A considerable fraction of the studies using the force volume mode emanate from the field of biological applications. The ability to resolve specific interactions as antibody–antigen binding between AFM tip and sample surface with nanometer resolution by force distance curves [1188] makes the force volume mode an ideal tool for “affinity imaging”. It has been applied to biological model systems as biotin–streptavidin [1189], intercellular adhesion molecule-1 (ICAM-1) and anti-ICAM-1 [1159], ferritin–anti-ferritin [1190], fibrinogen–anti-fibrinogen [1191] and tyminine and adenine [1192,1193]. The obvious potential for mapping distributions of biomolecules on cell surfaces has been exploited to image distribution of mannan polymers on the yeast cells [1194], sugar chains on tissue sections of the rat vomeronasal epithelium [1195], receptor-associated protein binding proteins on 3T3 fibroblasts [1196], vitronectin receptors on a murine osteoblastic cell [1197], vascular endothelial growth factor (VEGF) receptor on bovine aortic endothelial cells [1198], tyrosine kinase A on PC 12 nerve cells [1199], calcitonin receptors on bone cells [1200]. AFM tips functionalized with *Helix pomatia* lectin that interacts specifically with a glycolipid on group A red blood cells allowed discrimination by adhesion maps between group A and group 0 red blood cells [1201] (see Fig. 49). As already explained in Section 11, non-specific interactions, like van der Waals and double-layer force, are always present. When detecting specific forces, non-specific interaction may be a problem, because they make the image quality

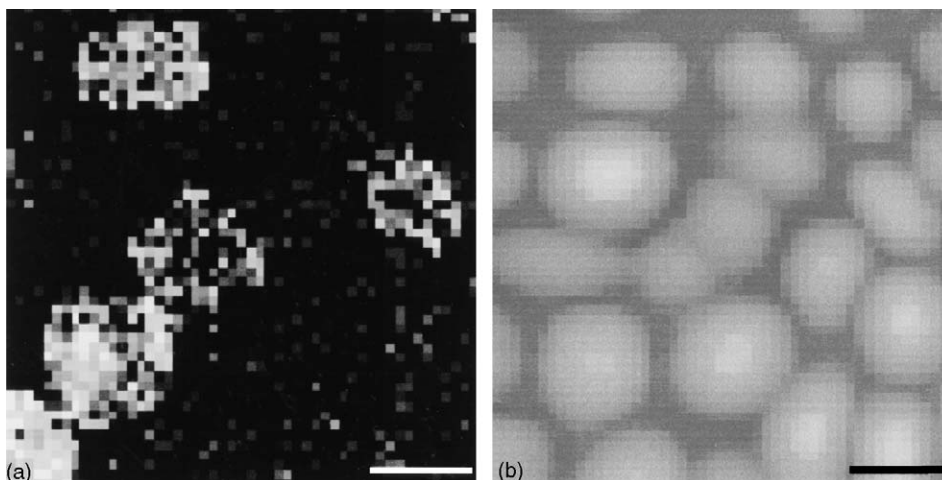


Fig. 49. (a) Adhesion image of a mixed layer of group A and group 0 red blood cells. Grayscale coding was calculated from the rupture forces between the cell layer and an AFM tip that was functionalized with *Helix pomatia* lectin. This lectin binds specifically to surface groups of group A red blood cells. (b) Topographic image of the same cell layer as in (a). Scale bars are 5 μm (from [1201] with kind permission of the authors).

worse and they may even hide the specific forces. To overcome this problem, Willemsen et al. [1202] tested imaging conditions in aqueous solution at low salt concentration, staying within the repulsive part of the DLVO forces and recording only adhesion events when discrete hopping of the tip over this barrier by thermal motion occurs.

On the other hand, non-specific interactions are expected to be important for the understanding of cell adhesion to surfaces. For biofilms of sulfate reducing bacteria on mica, adhesion forces to an AFM tip were found to be higher at cell–cell and cell–substratum interface than on the middle of cells [1203,1204]. In contrast, Auerbach et al. found lower adhesion at the cell–cell interface for biofilms of *P. putida* [1205].

From the approach part of the force curves, information about the local elastic properties of the cell surfaces can be extracted by evaluating the single force curves in the same way as described above in Section 9.3. This was applied to synaptic vesicles from *Torpedo californica* [1206], *M. gryphiswaldense* bacteria [1207] and oocysts of *C. parvum* [954].

By extracting pointwise the distance where the AFM tip just starts to touch the cell surface, “zero force” images of the undeformed cell surface can be obtained. From an analysis it was concluded that the stiff structures (commonly called “stress fibers”) observed in contact mode AFM images on cell surfaces arise from underlying cytoskeletal structures and become visible only by deformation of the cell membrane by the AFM tip [1208,1209].

If one is interested only in relative changes of elastic properties, the approach of “Force integration to equal limits”, developed by A-Hassan et al. [923] can be applied: The elasticity is calculated from the area $w = A_1 + A_2$ between the approach contact line and the axis $F = 0$ (see Fig. 17). The relative elasticity at two different points on the surface (points 1 and 2) is then given by

$$\frac{w_1}{w_2} = \left(\frac{k_1}{k_2} \right)^n, \quad (12.1)$$

where k_1 and k_2 are the local elastic constants as defined by Eq. (4.5). The value of the exponent n depends on the tip geometry, for a parabolic tip $n = 2/3$. This type of approach has been applied to obtain elasticity maps of Madine-Darby canine kidney (MDCK) cells [923] and to study the mechanical properties of several *Lactobacillus* strains with different characteristics of the cell wall [1210]. Results for the lactic acid bacteria could be explained on the basis of the different constituents of the cell surfaces (S-layer proteins, polysaccharides, lipoteichoic acids) present in the different strains.

For more detailed understanding of the mechanical properties of cells, force volume imaging has been combined with chemical modification of different components of the cytoskeleton, like actin [941,1208,1211,1212], vinculin [1161,1213], actomyosin [1214], and microtubules [941,1215].

The long acquisition time for force volume plots makes investigation of faster cellular processes by this method impossible. Sacrificing two-dimensional resolution by using single line scans can increase time resolution while still capturing spatial information in one direction. The group of Radmacher used this trick to study the dynamics of 3T3 fibroblasts [1216], MTLn3 cells [1217], and potorous triactylis kidney cells [1218].

12.2. Pulsed force mode atomic force microscopy

The pulsed force mode of AFM (PFM-AFM) was introduced by the group of Marti et al. [35,1219]. This mode can be added as an external module to any AFM that allows access to the feedback signal from the photo detector. XY scanning is done by the normal circuit of the AFM. A sinusoidal voltage is used to modulate the Z piezo of the AFM leading to oscillation amplitudes of typically 20–500 nm at a frequency of 100 Hz–2 kHz. The average distance between tip and sample is adjusted such that the tip is out of contact with the sample at the lowest point of the oscillation and reaches a defined maximum deflection at the highest point of the oscillation. In principle this allows recording force curves at this high frequency. To avoid the problems of high data acquisition rate, only selected points of the force curves are captured by sample-and-hold circuits and evaluated (Fig. 50). The maximal deflection (point B) is measured and

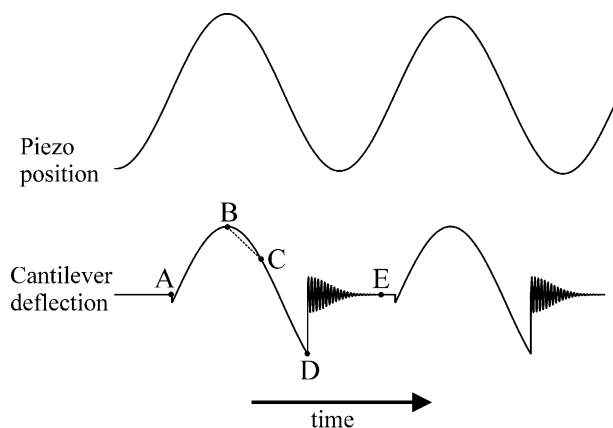


Fig. 50. Schematic of a pulsed force curve. The piezo position (upper trace) is varied in Z-direction by applying a sinusoidal voltage. During each cycle, the AFM tip gets in contact (A) with the sample surface, is deflected up to a fixed maximum value (B) and detaches from the surface again (D). Maximum applied force is given by the deflection value in (B), adhesion by the value in (D). The difference (B)–(C) is proportional to the slope of the force curve and is therefore related to the sample stiffness. The value in (E) will either correspond to zero force or to the magnitude of long-range forces if present.

used for the feedback control of the AFM instead of the standard deflection signal of the AFM, mimicking a continuous signal (setpoint) for the feedback loop during one oscillation. Thus, the maximum loading force on the sample is kept constant. The minimum value of the force curve (point D) is taken to be proportional to the adhesion force. A third point (point C) at a defined, user selectable distance from the maximum is taken to determine the sample stiffness. The difference of the values at B and C is proportional to the slope of the force curve and therefore to the sample stiffness. The zero force value of the force curve is recorded at a point far from the surface (point E). In the case of long-range electrostatic interactions, this value may also be used to map variations in surface charge density.

Since this analysis of the deflection signal is done in real-time, and the values can be feed into auxiliary channels of the AFM, high resolution images of adhesion or mechanical properties of the sample can be recorded in parallel with sample topography. Furthermore, the intermittent contact between tip and sample reduces shear forces, thereby allowing imaging of soft samples. Compared to the force volume mode, image acquisition is speeded up. Additionally data analysis is done online, avoiding tedious evaluation of the single force curves. On the other hand, the amount of information gained during the experiment is sacrificed. By reducing the whole force–distance curve to some significative points, information about the sample deformations and the elastic–plastic behavior of the sample, about additional peaks in the retraction curve, about the distance dependence of the attractive and repulsive forces prior to contact, etc., is lost. This limitation has been overcome by the development of the digital pulsed force mode, where the deflection signal is recorded with high time resolution, essentially recording full force curves [1220]. Data analysis can be either done in real-time to directly extract values, e.g., adhesion, stiffness as in the analog version of PFM-AFM, or can be done offline for a more detailed and sophisticated data analysis. As the oscillation amplitude is smaller than the full range of the Z piezo, usually stiffer cantilevers than in contact mode AFM are used to ensure detachment between tip and surface during each oscillation cycle. This leads to a reduced force resolution compared to single force curves or force volume mode.

PFM-AFM can also be used in liquids as shown by mapping the electric double-layer forces with a lateral resolution of 20 nm [34,1221]. However, one has to be careful with data interpretation under these conditions, since cantilever deflections due to liquid oscillation may become comparable to those by tip–sample interaction [1222] and depending on parameters such as driving frequency, amplitude and trigger settings, even contrast inversion of adhesion and stiffness images may occur [1223].

The high lateral resolution of PFM-AFM was exploited by Stifter et al. [1224] to compare model calculations for the adhesion between a sphere and a step or a spherical blister with the results of PFM measurements of the adhesion of an AFM tip on a HOPG surface with corresponding nano-sized surface defects. Adhesion force distributions of CH₃ modified tips on CH₃ terminated surfaces with different roughness in water showed strong influence of roughness on adhesion force and force distribution [1225].

The simultaneous acquisition of adhesion and stiffness images facilitates identification of different surface components. Sun et al. [1226] found that annealing of octyltriethoxysilane films on glass at elevated temperature lead to breakup of films and formation of islands but coverage of the glass surfaces was still observed between islands according to stiffness and adhesion data. Morton et al. [1227] found shallow depressions in the surface of caramel with 1–10 μm in diameter that exhibited higher adhesion to the silicon AFM probe and a lower stiffness than the surrounding sample. This is consistent with the view of caramel as fat droplets within a matrix of sugars. Characterization of lipid bilayers by PFM-AFM can be used to study their phase separation behavior [1228].

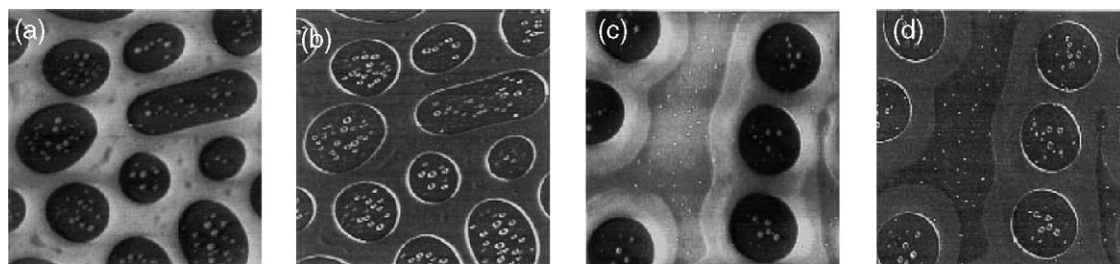


Fig. 51. PS/PMMA blends spin coated on a silicon substrate (scan size $10\ \mu\text{m}$). (a and c) Topography images (darker means lower), (b and d) adhesion images (darker means higher adhesion). PS and PMMA phase separate. PMMA, that has a higher interaction energy with silicon, forms the bottom layer (darkest in topography). PS stays at the surface and forms a second layer that tears up to form holes. For a composition of PS/PMMA of 58%:42% (a and b), holes in the PS layer are found that have PMMA at the bottom, covered with some PS droplets. PMMA appears darker in the adhesion image due to the higher interaction energy with the silicon tip. For a PS/PMMA composition of 61%:39% in (c and d), the PS layer is no longer continuous and a large lower area becomes visible. From the adhesion data (d), this area can be identified to consist of PMMA with small PS droplets just as the areas in the holes. (From [1219] with kind permission of the authors).

The reduction of shear force during scanning in the PFM-AFM makes it well suited for the investigation of soft surfaces. This was soon demonstrated for polymer surfaces [1219,1229] (see Fig. 51) and oil-like wetting agent layers on polypropylene [1230]. The distribution of fullerene (C_{60}) derivatives in poly(*p*-phenylene-vinylene) derivatives that are promising candidates for organic solar cells, could be imaged with high contrast in PFM-AFM due to the high stiffness of the fullerenes [1231]. Phase separation in a drug loaded polymeric system, cyclosporine A in hydroxypropyl methylcellulose, was detected by Hussain et al. [1232]. Ebner et al. [1233] used PFM-AFM to monitor topography and adhesion for each step in a multi-step process to obtain covalently grafted PEG layers on glass surfaces. Dickson and Berg [1234] monitored the increase in number and size of low adhesion sites on cellulose films that were hydrophobized by treatment with alkenyl succinic anhydride. In combination with a temperature stage, it was possible to follow the change in adhesion on a polystyrene surface during glass transition [1219] and to characterize the thermal behavior of microphases in polymer blends [1235]. Morphological and adhesive changes of polymer surfaces by ArF excimer laser illumination were studied for poly-carbonate [1236], Teflon [1237] and PMMA [1238]. Adhesion on pulsed laser deposited Teflon thin films was found to depend strongly on the annealing conditions [1239].

The usefulness of PFM for chemical force microscopy was shown using COOH and CH_3 terminated AFM tips to image the chemical composition of patterned COOH and CH_3 terminated SAMs [1240–1242]. Akimoto et al. [358] demonstrated that from the adhesive force between a gold-coated tip and a $\text{Au}(1\ 1\ 1)$ substrate covered with CH_3 terminated alkanethiols, one could discriminate between areas with different chain lengths of the alkanethiol. Berg and coworkers [1243,1244] characterized by PFM-AFM heterogeneous patterned films of silanes used as polymer adhesion promoters. Local variation in mechanical and adhesive properties of carbon-fiber bundles infiltrated with pyrolytic carbon were studied by Pfrang et al. [1245]. The significantly higher adhesive forces determined on the fibers compared with the carbon matrix was attributed to a higher concentration of polar groups on the fiber cross-sections due to the high degree of orientation of the graphene layers along the fiber axis. Münter et al. [1246] used PFM-AFM to differentiate different chemical species forming the so-called time-dependent haze on silicon wafers that arises from contaminations during storage and handling.

The high resolution of the pulsed force mode allows its application even on the single molecule level. Zhang et al. [1247,1248] probed the stiffness and adhesion properties of single polyphenylene dendrimer molecules. Zhu et al. [1249] were able to image single poly(sodium 4-styrenesulfonate) molecules even on a rough surface where single molecules are usually hard to detect by AFM by taking advantage of the adhesion contrast of the pulsed force mode. Single polyethyleneimine molecules in aqueous solution were imaged by adhesion and stiffness contrast using AFM probes modified with amino- and methyl-terminated groups that increased chemical sensitivity [1250]. Single DNA molecules stretched on organosilane surfaces were imaged by PFM using hydrophobized AFM tips [1251] and the influence of topography on adhesion at the single molecule level was studied [1252].

Due to its ease of operation PFM-AFM will continue to be a valuable addition to the wealth of operating modes of AFM, even though in most cases only relative values of adhesion and mechanical properties are acquired. An interesting extension of PFM-AFM called “CODY Mode” was introduced by Krottil et al. [1253]. They combined PFM-AFM with the so-called force modulation mode by additionally applying a second, smaller scale oscillation to the Z piezo during the contact between tip and sample. From the deflection signal during this phase, additional information about the viscoelastic properties of the material can be obtained.

13. Conclusions and perspectives

The field of force measurements with the AFM has reached a state of maturity. The basic mathematics to describe the cantilever and tip and the theory to describe forces acting on the tip have been developed for many applications. For example, the calibration of the elastic constant of the cantilever, playing a key role for quantitative force measurements, is nowadays a standard opportunity in commercial AFMs. Also the exact knowledge of tip shape and dimensions is necessary for quantitative and repeatable measurements, and the characterization of AFM tips is still a large problem in AFM force measurements. Such a problem has been overcome more and more frequently with the use of colloidal probes of known dimensions, often at expense of the resolution, since colloidal probes are usually larger than AFM tips. Headways are hence still necessary in the field of tip shape characterization.

Just by comparing this review with the previous review of Cappella and Dietler 6 years ago, it is evident that topics, that at that time were still questionable (e.g., elastic continuum theories), are now experimentally verified. Other issues, being at that time object of experimental verification, are nowadays almost a routine measurement (e.g., van der Waals, double-layer and solvation forces in liquids, or capillary forces). In such fields AFM experiments provide quantitative measurements that can be used for quantitative estimation of several material properties, e.g. Young’s modulus, Hamaker constant, Debye length, surface charges, etc.

The comparison of the two reviews shows also that the focus of research has moved on to other aspects of interface and colloid science. As examples can be cited the study of the hydrodynamic force, measurements of elasticity and adhesion of soft surfaces (like polymers and biological samples), capsules, and particles, the characterization of steric and hydrophobic forces, the study of double-layer forces at different pH, the application of DLVO forces measurements to the study of the adsorption of salts and polymers at liquid/solid or liquid/liquid interfaces, etc. All these fields of research present theoretical as well as experimental challenges.

We cannot identify a general trend where the field of force measurements with AFM is moving to. Rather we would like to mention some promising technical developments and open questions in interface and colloid science, where the AFM could be applied to and make a significant contribution.

- One such field of technical development is force mapping. Today, force mapping is limited by the long time required to take a whole image, the enormous amount of data, and a lack in a reliable automatic data analysis. To reduce the measuring time shorter cantilevers with a higher resonance frequency could be employed. The technique still has to be improved and made more user friendly but it is in principle available. The problem of moving and storing data is going to become less and less important with improved computer technology.
- A reliable automatic data analysis is available for “clean” force curves taken on homogeneous substrates and when looking only for simple parameters such as the adhesion force or the stiffness. There is certainly much room for improvement. Fast analysis methods and routines are also very important for force mapping, where enormous amounts of data must be processed in order to get images of some parameters.
- Another field of atomic force microscopy that is likely to become more reliable, more quantitative, and more user friendly in the next years is what is often called “chemical force microscopy”, eventually coupled with force mapping. More and more kinds of tip functionalization are nowadays available, making the range of detectable specific forces wider and wider. Also the experimental and theoretical know-how in this field is growing. The chemical selectivity of functionalized tips is becoming more and more important for the study of specific forces, single-bond forces, acid–base interactions and stretching of molecules. When coupled with force mapping, chemical force microscopy has now the realistic goal of “molecule recognition”, i.e., the capability not only to distinguish, but also to identify molecules on a surface.
- Many kinds of force curves cannot yet be interpreted. For example hydrophobic attraction is not fully understood. The penetration of the tip through a lipid or surfactant layer, and in general plastic deformations are not satisfactorily described. This is not an AFM specific problem, and further understanding of such phenomena needs most of all further work in colloid science in general.
- Currently it is difficult to measure attractive forces versus distance because often attractive forces cause a jump of the tip into contact. The whole range of the jump-in does not contain information on the force law. Dynamic and partially kinetic force experiments are a possible solution but still need to be developed further until they can be used reliably. Force feedback is another approach to the solution of this problem but most attempts so far have failed to build simple and reliable systems.
- An open question remains as to what happens at the molecular scale when a tip comes into contact with a solid surface. For the short time of contact the tip and the sample are exposed to extreme pressure and possibly temperature. Usually the surfaces can be scanned afterwards and often no damage is visible. On the other hand, computer simulations suggest that molecules are transferred between tip and sample. Pressure and pressure gradients underneath the tip are huge. Also the temperature caused by the pressure and possible friction might be high. Which effect does this have on solid surfaces? Does the fact that typically these extreme conditions are only applied for few microseconds prevent damage?
- It would be valuable to have additional information on the chemical composition or molecular structure of the sample or of the medium between tip and sample. This might be possible with already mentioned approaches (chemical force microscopy), but also by combining optical spectroscopic

techniques with atomic force microscopy. A metallized tip can, for example, be illuminated by a laser. Field enhancement at the very end of the tip increases the near-field contribution so that resolutions below the wavelength of the light are possible.

References

- [1] G. Binnig, H. Rohrer, C. Gerber, E. Weibel, *Phys. Rev. Lett.* 49 (1982) 57.
- [2] G. Binnig, H. Rohrer, C. Gerber, E. Weibel, *Phys. Rev. Lett.* 50 (1983) 120.
- [3] D.W. Pohl, W. Denk, M. Lanz, *Appl. Phys. Lett.* 44 (1984) 651.
- [4] A. Lewis, M. Isaacson, A. Harootunian, M. Muray, *Ultramicroscopy* 13 (1984) 227.
- [5] G. Binnig, C.F. Quate, C. Gerber, *Phys. Rev. Lett.* 56 (1986) 930.
- [6] A.L. Weisenhorn, P.K. Hansma, T.R. Albrecht, C.F. Quate, *Appl. Phys. Lett.* 54 (1989) 2651.
- [7] Y. Martin, H.K. Wickramasinghe, *Appl. Phys. Lett.* 50 (1987) 1455.
- [8] J.J. Sáenz, N. Garcia, P. Grütter, E. Meyer, H. Heinzelmann, R. Wiesendanger, L. Rosenthaler, H.R. Hidber, H.J. Güntherodt, *J. Appl. Phys.* 62 (1987) 4293.
- [9] S. Porthun, L. Abelmann, C. Lodder, *J. Magn. Mater.* 182 (1998) 238.
- [10] M.R. Koblischka, U. Hartmann, *Ultramicroscopy* 97 (2003) 103.
- [11] Y. Martin, C.C. Williams, H.K. Wickramasinghe, *J. Appl. Phys.* 61 (1987) 4723.
- [12] J.E. Stern, B.D. Terris, H.J. Mamin, D. Rugar, *Appl. Phys. Lett.* 53 (1988) 2717.
- [13] R. Erlandsson, G.M. McClelland, C.M. Mate, S. Chiang, *J. Vac. Sci. Technol. A* 6 (1988) 266.
- [14] M. Rohwerder, P. Leblanc, G.S. Frankel, M. Stratmann, in: P. Marcus (Ed.), *Analytical Methods for Corrosion Science and Engineering*, Dekker, New York, p. 605.
- [15] W.A. Ducker, T.J. Senden, R.M. Pashley, *Nature* 353 (1991) 239.
- [16] H.-J. Butt, *Biophys. J.* 60 (1991) 1438.
- [17] P.M. Claesson, T. Ederth, V. Bergeron, M.W. Rutland, *Adv. Colloid Interf. Sci.* 67 (1996) 119.
- [18] D. Tabor, R.H.S. Winterton, *Nature* 219 (1968) 1120.
- [19] J.N. Israelachvili, D. Tabor, *Proc. R. Soc. London A* 331 (1972) 19.
- [20] D.M. LeNeveu, R.P. Rand, V.A. Parsegian, *Nature* 259 (1976) 601.
- [21] V.A. Parsegian, R.P. Rand, N.L. Fuller, D.C. Rau, *Meth. Enzymol.* 127 (1986) 400.
- [22] V.A. Parsegian, N. Fuller, R.P. Rand, *Proc. Natl. Acad. Sci. U.S.A.* 76 (1979) 2750.
- [23] D.C. Prieve, *Adv. Colloid Interf. Sci.* 82 (1999) 93.
- [24] A. Janshoff, M. Neitzert, Y. Oberdörfer, H. Fuchs, *Angew. Chem. Int. Ed.* 39 (2000) 3212.
- [25] L. Meagher, R.M. Pashley, *Langmuir* 11 (1995) 4019.
- [26] H.-J. Butt, T. Müller, H. Gross, *J. Struct. Biol.* 110 (1993) 127.
- [27] M. Hegner, P. Wagner, G. Semenza, *Surf. Sci.* 291 (1993) 39.
- [28] G. Meyer, N.M. Amer, *Appl. Phys. Lett.* 53 (1988) 2400.
- [29] S. Alexander, L. Hellemans, O. Marti, J. Schneir, V. Elings, P.K. Hansma, M. Longmire, J. Gurley, *J. Appl. Phys.* 65 (1989) 164.
- [30] S.M. Hues, C.F. Draper, K.P. Lee, R.J. Colton, *Rev. Sci. Instrum.* 65 (1994) 1561.
- [31] M. Preuss, H.-J. Butt, *Langmuir* 14 (1998) 3164.
- [32] K.O. van der Werf, C.A.J. Putman, B.G. de Groth, J. Greve, *Appl. Phys. Lett.* 65 (1994) 1195.
- [33] A. Rosa, *Polym. Prepr. Am. Chem. Soc. Div. Polym. Chem.* 37 (1996) 616.
- [34] T. Miyatani, M. Horii, A. Rosa, M. Fujihira, O. Marti, *Appl. Phys. Lett.* 71 (1997) 2632.
- [35] A. Rosa-Zeiser, E. Weilandt, S. Hild, O. Marti, *Meas. Sci. Technol.* 8 (1997) 1333.
- [36] D. Sarid, *Scanning Force Microscopy*, Oxford University Press, New York, 1991.
- [37] G.Y. Chen, R.J. Warmack, T. Thundat, D.P. Allison, A. Huang, *Rev. Sci. Instrum.* 65 (1994) 2532.
- [38] T.R. Albrecht, S. Akamine, T.E. Carver, C.F. Quate, *J. Vac. Sci. Technol. A* 8 (1990) 3386.
- [39] H.-J. Butt, P. Siedle, K. Seifert, K. Fendler, T. Seeger, E. Bamberg, A.L. Weisenhorn, K. Goldie, A. Engel, *J. Microsc.* 169 (1993) 75.
- [40] T. Thundat, R.J. Warmack, G.Y. Chen, D.P. Allison, *Appl. Phys. Lett.* 64 (1994) 2894.

- [41] H.-J. Butt, *J. Colloid Interf. Sci.* 180 (1996) 251.
- [42] J.E. Sader, *Rev. Sci. Instrum.* 66 (1995) 4583.
- [43] D.A. Walters, J.P. Cleveland, N.H. Thomson, P.K. Hansma, M.A. Wendman, G. Gurley, V. Elings, *Rev. Sci. Instrum.* 67 (1996) 3583.
- [44] M.B. Viani, et al. *Rev. Sci. Instrum.* 70 (1999) 4300.
- [45] M.B. Viani, T.E. Schäffer, A. Chand, M. Rief, H.E. Gaub, P.K. Hansma, *J. Appl. Phys.* 86 (1999) 2258.
- [46] T. Schäffer, P.K. Hansma, *J. Appl. Phys.* 84 (1998) 4661.
- [47] M. Sasaki, K. Hane, S. Okuma, Y. Bessho, *Rev. Sci. Instrum.* 65 (1994) 1930.
- [48] J. Tamayo, R. Garcia, *Langmuir* 12 (1996) 4430.
- [49] R.G. Winkler, J.P. Spatz, S. Sheiko, M. Möller, P. Reineker, O. Marti, *Phys. Rev. B* 54 (1996) 8908.
- [50] R. Garcia, R. Pérez, *Surf. Sci. Rep.* 47 (2002) 197.
- [51] W.A. Ducker, R.F. Cook, *Appl. Phys. Lett.* 56 (1990) 2408.
- [52] J.E. Sader, *J. Appl. Phys.* 84 (1998) 64.
- [53] F.J. Elmer, M. Dreier, *J. Appl. Phys.* 81 (1997) 7709.
- [54] C. Bergaud, L. Nicu, *Rev. Sci. Instrum.* 71 (2000) 2487.
- [55] T.R. Albrecht, P. Grütter, D. Horne, D. Rugar, *J. Appl. Phys.* 69 (1991) 668.
- [56] H. Ueyama, Y. Sugawara, S. Morita, *Appl. Phys. A* 66 (1998) S295.
- [57] M.A. Lantz, S.J. O'Shea, M.E. Welland, *Appl. Phys. Lett.* 65 (1994) 409.
- [58] M.C. Friedenberg, C.M. Mate, *Langmuir* 12 (1996) 6138.
- [59] F. Giessibl, *Science* 267 (1995) 68.
- [60] Y. Sugawara, M. Ohta, H. Ueyama, S. Morita, F. Osaka, S. Ohkouchi, M. Suzuki, S. Mishima, *J. Vac. Sci. Technol. B* 14 (1996) 953.
- [61] R. Lüthi, E. Meyer, M. Bammerlin, A. Baratoff, T. Lehmann, L. Howald, C. Gerber, H.J. Güntherodt, *Z. Phys. B* 100 (1996) 165.
- [62] F.J. Giessibl, *Phys. Rev. B* 56 (1997) 16010.
- [63] N. Sasaki, M. Tsukuda, *Jpn. J. Appl. Phys.* 37 (1998) L533.
- [64] R. Boisgard, D. Michel, J.P. Aime, *Surf. Sci.* 401 (1998) 199.
- [65] B. Gotsmann, B. Seidel, B. Anczykowski, H. Fuchs, *Phys. Rev. B* 60 (1999) 11051.
- [66] U. Dürig, *Appl. Phys. Lett.* 75 (1999) 433.
- [67] H. Hölscher, B. Gotsmann, A. Schirmeisen, *Phys. Rev. B* 68 (2003) 153401.
- [68] T. Okajima, H. Sekiguchi, H. Arakawa, A. Ikai, *Appl. Surf. Sci.* 210 (2003) 68.
- [69] A. Roters, D. Johannsmann, *J. Phys.: Condens. Matter* 8 (1996) 7561.
- [70] P.R. Saulsen, *Phys. Rev. D* 42 (1990) 2437.
- [71] U. Dürig, J.K. Gimzewski, D.W. Pohl, R. Schlittler, *Force Sensing in Scanning Tunneling Microscopy*, IBM, Rüschlikon, 1986, p. 1.
- [72] J.P. Cleveland, T.E. Schäffer, P.K. Hansma, *Phys. Rev. B* 52 (1995) 8692.
- [73] A. Roters, M. Gelbert, M. Schimmel, J. Rühle, D. Johannsmann, *Phys. Rev. E* 56 (1997) 3256.
- [74] W.F. Heinz, M.D. Antonik, J.H. Hoh, *J. Phys. Chem.* 104 (2000) 622.
- [75] M. Gelbert, M. Biesalski, J. Rühle, D. Johannsmann, *Langmuir* 16 (2000) 5774.
- [76] H. Ma, J. Jimenez, R. Rajagopalan, *Langmuir* 16 (2000) 2254.
- [77] D.O. Koralek, W.F. Heinz, M.D. Antonik, A. Baik, J.H. Hoh, *Appl. Phys. Lett.* 76 (2000) 2952.
- [78] D.Y.C. Chan, R.G. Horn, *J. Chem. Phys.* 83 (1985) 5311.
- [79] H.-J. Butt, *J. Colloid Interf. Sci.* 166 (1994) 109.
- [80] B.A. Todd, S.J. Eppell, F.R. Zypman, *J. Appl. Phys.* 88 (2000) 7321.
- [81] B.A. Todd, S.J. Eppell, *J. Appl. Phys.* 94 (2003) 3563.
- [82] H.-J. Butt, M. Jaschke, *Nanotechnology* 6 (1995) 1.
- [83] U. Rabe, K. Janser, W. Arnold, *Rev. Sci. Instrum.* 67 (1996) 3281.
- [84] R.W. Stark, T. Drobek, W.M. Heckl, *Ultramicroscopy* 86 (2001) 207.
- [85] J.M. Neumeister, W.A. Ducker, *Rev. Sci. Instrum.* 65 (1994) 2527.
- [86] J.L. Hazel, V.V. Tsukruk, *Thin Solid Films* 339 (1999) 249.
- [87] J.E. Sader, I. Larson, P. Mulvaney, L.R. White, *Rev. Sci. Instrum.* 66 (1995) 3789.

- [88] A. Khan, J. Philip, P. Hess, *J. Appl. Phys.* 95 (2004) 1667.
- [89] T.A. Senden, W.A. Ducker, *Langmuir* 10 (1994) 1003.
- [90] N. Maeda, T.J. Senden, *Langmuir* 16 (2000) 9282.
- [91] S.M. Notley, S. Biggs, V.S.J. Craig, *Rev. Sci. Instrum.* 74 (2003) 4026.
- [92] F.L. Degertekin, B. Hadimioglu, T. Sulchek, C.F. Quate, *Appl. Phys. Lett.* 78 (2001) 1628.
- [93] J.D. Holbery, V.L. Eden, M. Sarikaya, R.M. Fisher, *Rev. Sci. Instrum.* 71 (2000) 3769.
- [94] J.P. Cleveland, S. Manne, D. Bocek, P.K. Hansma, *Rev. Sci. Instrum.* 64 (1993) 403.
- [95] E. Bonaccorso, H.-J. Butt, *J. Phys. Chem. B* 109 (2005) 253.
- [96] J.L. Hutter, J. Bechhoefer, *Rev. Sci. Instrum.* 64 (1993) 1868.
- [97] R. Proksch, T.E. Schäffer, J.P. Cleveland, R.C. Callahan, M.B. Viani, *Nanotechnology* 15 (2004) 1344.
- [98] R. Lévy, M. Maaloum, *Nanotechnology* 13 (2002) 33.
- [99] J.E. Sader, J.W.M. Chou, P. Mulvaney, *Rev. Sci. Instrum.* 70 (1999) 3967.
- [100] C.T. Gibson, G.S. Watson, S. Myhra, *Nanotechnology* 7 (1996) 259.
- [101] A. Torii, M. Sasaki, K. Hane, O. Shigeru, *Meas. Sci. Technol.* 7 (1996) 179.
- [102] Y.I. Rabinovich, R.H. Yoon, *Langmuir* 10 (1994) 1903.
- [103] P.J. Cumpson, P. Zhdan, J. Hedley, *Ultramicroscopy* 100 (2004) 241.
- [104] P. Attard, A. Carambassis, M.W. Rutland, *Langmuir* 15 (1999) 553.
- [105] L. Heim, M. Kappl, H.-J. Butt, *Langmuir* 20 (2004) 2760.
- [106] J.L. Hutter, *Langmuir* 21 (2005) 2630.
- [107] F. Benmouna, D. Johannsmann, *J. Phys.: Condens. Matter* 15 (2003) 3003.
- [108] E. Meyer, H. Heinzlmann, P. Grütter, T. Jung, T. Weisskopf, H.R. Hidber, R. Lapka, H. Rudin, H.J. Güntherodt, *J. Microsc.* 152 (1988) 269.
- [109] O. Wolter, T. Bayer, J. Greschner, *J. Vac. Sci. Technol. B* 9 (1991) 1353.
- [110] J. Itoh, Y. Tohma, T. Inoue, H. Yokoyama, K. Shimizu, *Jpn. J. Appl. Phys.* 33 (1994) 7167.
- [111] I.W. Rangelow, *Microelectron. Eng.* 23 (1995) 369.
- [112] A. Boisen, O. Hansen, S. Bouwstra, *J. Micromech. Microeng.* 6 (1996) 58.
- [113] D. Saya, K. Fukushima, H. Toshiyoshi, G. Hashiguchi, H. Fujita, H. Kawakatsu, *Sens. Actuators A* 95 (2002) 281.
- [114] J.B. Green, A. Idowu, S.S.F. Chan, *Mater. Today* 6 (2003) 22.
- [115] H.-J. Butt, K. Graf, M. Kappl, *Physics and Chemistry of Interfaces*, Wiley/VCH, Berlin, 2003.
- [116] A. Noy, D.V. Vezenov, C.M. Lieber, *Annu. Rev. Mater. Sci.* 27 (1997) 381.
- [117] D.A. Smith, S.D. Connell, C. Robinson, J. Kirkham, *Anal. Chim. Acta* 479 (2003) 39.
- [118] J.M. Kim, H. Muramatsu, *Nano Lett.* 5 (2005) 309.
- [119] L.H. Dubois, R.G. Nuzzo, *Annu. Rev. Phys. Chem.* 43 (1992) 437.
- [120] C.D. Frisbie, L.F. Rozsnyai, Y. Noy, M.S. Wrighton, C.M. Lieber, *Science* 265 (1994) 2071.
- [121] F.A. Ahimou, F.A. Denis, A. Touhami, Y.F. Dufrêne, *Langmuir* 18 (2002) 9937.
- [122] H.X. He, W. Huang, H. Zhang, Q.G. Li, S.F.Y. Li, Z.F. Liu, *Langmuir* 16 (2000) 517.
- [123] H. Schönherr, V. Chechik, C.J.M. Stirling, G.J. Vancso, *J. Am. Chem. Soc.* 122 (2000) 3679.
- [124] H. Schönherr, Z. Hruska, G.J. Vancso, *Macromolecules* 33 (2000) 4532.
- [125] E.W. van der Vegte, G. Hadziioannou, *Langmuir* 13 (1997) 4357.
- [126] D.V. Vezenov, A. Noy, L.F. Rozsnyai, C.M. Lieber, *J. Am. Chem. Soc.* 119 (1997) 2006.
- [127] M.L. Wallwork, D.A. Smith, J. Zhang, J. Kirkham, C. Robinson, *Langmuir* 17 (2001) 1126.
- [128] T. Nakagawa, K. Ogawa, T. Kurumizawa, S. Ozaki, *Jpn. J. Appl. Phys.* 32 (1993) L294.
- [129] R.L. Alley, K. Komvopoulos, R.T. Howe, *J. Appl. Phys.* 76 (1994) 5731.
- [130] T. Ito, M. Namba, P. Bühlmann, Y. Umezawa, *Langmuir* 13 (1997) 4323.
- [131] V.V. Tsukruk, V.N. Bliznyuk, *Langmuir* 14 (1998) 446.
- [132] A.S. Lea, J.D. Andrade, V. Hlady, *Colloids Surf. A* 93 (1994) 349.
- [133] M. Giesbers, J.M. Kleijn, M.A. Cohen Stuart, *J. Colloid Interf. Sci.* 252 (2002) 138.
- [134] T. Nakagawa, *Jpn. J. Appl. Phys.* 36 (1997) L162.
- [135] M.M. Sung, G.J. Kluth, R. Maboudian, *J. Vac. Sci. Technol. A* 17 (1999) 540.
- [136] J.E. Headrick, C.L. Berrie, *Langmuir* 20 (2004) 4124.
- [137] G.U. Lee, L.A. Chrisey, E. Ferrall, D.E. Pilloff, N.H. Turner, R.J. Colton, *Science* 36 (1996) 81.

- [138] M. Sano, J. Okamura, Y. Kanekiyo, S. Shinkai, *Colloids Surf. A* 169 (2000) 131.
- [139] J. Zhang, E. Uchida, Y. Uyama, Y. Ikada, *J. Colloid Interf. Sci.* 188 (1997) 431.
- [140] C. Jérôme, N. Willet, R. Jérôme, A.S. Duwez, *Chem. Phys. Chem.* 5 (2004) 147.
- [141] C.M. Chang, *Polymer Surface Modification and Characterization*, Carl Hanser Verlag, Munich, 1994.
- [142] H.F. Knapp, A. Stemmer, *Surf. Interf. Anal.* 27 (1999) 324.
- [143] M. Tomitori, T. Arai, *Appl. Surf. Sci.* 140 (1999) 432.
- [144] M. Ara, H. Tada, *Appl. Phys. Lett.* 83 (2003) 578.
- [145] C.M. Yam, Z.D. Xiao, J.H. Gu, S. Boutet, C.Z. Cai, *J. Am. Chem. Soc.* 125 (2003) 7498.
- [146] G. Hüttl, V. Klemm, R. Popp, F. Simon, E. Müller, *Surf. Interf. Anal.* 33 (2002) 50.
- [147] A.T. Woolley, C.L. Cheung, J.H. Hafner, C.M. Lieber, *Chem. Biol.* 7 (2000) R193.
- [148] A. Krishnan, E. Dujardin, T.W. Ebbesen, P.N. Yianilos, M.M.J. Treacy, *Phys. Rev. B* 58 (1998) 14013.
- [149] J.P. Lu, *Phys. Rev. Lett.* 79 (1997) 1297.
- [150] E.W. Wong, P.E. Sheehan, C.M. Lieber, *Science* 277 (1997) 1971.
- [151] S.S. Wong, A.T. Wooley, E. Joselevich, C.M. Lieber, *Chem. Phys. Lett.* 306 (1999) 219.
- [152] M.A. Lantz, S.J. O'Shea, M.E. Welland, *Rev. Sci. Instrum.* 69 (1998) 1757.
- [153] P. Siedle, H.-J. Butt, E. Bamberg, D.N. Wang, W. Kühlbrandt, J. Zach, M. Haider, *Inst. Phys. Conf. Ser.* 130 (1992) 361.
- [154] G. Hüttl, *Afm-untersuchungen der interpartikularen wechselwirkung keramischer materialien in flüssigkeiten: Beiträge zur methodenentwicklung*, Bergakademie Freiberg, Freiberg, Germany, 2001.
- [155] J.A. DeRose, J.P. Revel, *Microsc. Microanal.* 3 (1997) 203.
- [156] J.H. Hafner, *J. Phys. Chem. B* 105 (2001) 743.
- [157] K.H. Chung, Y.H. Lee, D.E. Kim, *Ultramicroscopy* 102 (2005) 161.
- [158] J. Vesenka, R. Müller, E. Henderson, *Rev. Sci. Instrum.* 65 (1994) 2249.
- [159] P. Markiewicz, M.C. Goh, *Rev. Sci. Instrum.* 66 (1995) 3186.
- [160] A.S. Foster, W.A. Hofer, A.L. Shluger, *Curr. Opin. Solid State Mater. Sci.* 5 (2001) 427.
- [161] L. Meagher, G. Maurdev, M.L. Gee, *Langmuir* 18 (2002) 2649.
- [162] W. Stöber, A. Fink, E. Bohn, *J. Colloid Interf. Sci.* 26 (1968) 62.
- [163] G.J.C. Braithwaite, A. Howe, P.F. Luckham, *Langmuir* 12 (1996) 4224.
- [164] E. Kokkoli, C.F. Zukoski, *J. Colloid Interf. Sci.* 230 (2000) 176.
- [165] H.G. Pedersen, L. Bergström, *J. Am. Ceram. Soc.* 82 (1999) 1137.
- [166] S. Biggs, *Langmuir* 11 (1995) 156.
- [167] J. Nalaskowski, M. Niewiadomski, V.K. Paruchuri, J.D. Miller, *Characterization of Spherical Alumina Particles Obtained by Melting in a Hydrogen–Oxygen Flame*, Society for Mining, Metallurgy, and Exploration, Littleton, 2003.
- [168] T. Kakui, T. Miyauchi, H. Kamiya, *J. Eur. Ceram. Soc.* 25 (2005) 655.
- [169] I. Larson, C.J. Drummond, D.Y.C. Chan, F. Grieser, *J. Am. Chem. Soc.* 115 (1993) 11885.
- [170] A. Kauppi, K.M. Andersson, L. Bergström, *Cement Concrete Res.* 35 (2005) 133.
- [171] G. Toikka, R.A. Hayes, J. Ralston, *Langmuir* 12 (1996) 3783.
- [172] D.T. Atkins, R.M. Pashley, *Langmuir* 9 (1993) 2232.
- [173] G. Gillies, M. Kappl, H.-J. Butt, *Langmuir* 21 (2005) 5882.
- [174] R. Raiteri, M. Preuss, M. Grattarola, H.-J. Butt, *Colloids Surf. A* 136 (1998) 191.
- [175] K.M. Anderson, L. Bergström, *J. Colloid Interf. Sci.* 246 (2002) 309.
- [176] E. Finot, E. Lesniewska, J.C. Mutin, J.P. Goudonnet, *J. Chem. Phys.* 111 (1999) 6590.
- [177] Y.Q. Li, N.J. Tao, J. Pan, A.A. Garcia, S.M. Lindsay, *Langmuir* 9 (1993) 637.
- [178] M.R. Yalamanchili, S. Veeramasoneni, M.A.D. Azevedo, J.D. Miller, *Colloids Surf. A* 133 (1998) 77.
- [179] C.K. Ober, M.L. Hair, *J. Polym. Sci., Polym. Phys. Ed.* 25 (1987) 1395.
- [180] G.E. Yakubov, H.-J. Butt, O.I. Vinogradova, *J. Phys. Chem. B* 104 (2000) 3407.
- [181] J. Nalaskowski, J. Drelich, J. Hupka, J.D. Miller, *J. Adhes. Sci. Technol.* 13 (1999) 1.
- [182] J. Drelich, J. Nalaskowski, J.D. Miller, *J. Colloid Interf. Sci.* 201 (1998) 253.
- [183] A. Carambassis, M.W. Rutland, *Langmuir* 15 (1999) 5584.
- [184] S. Zauscher, D.J. Klingenberg, *J. Colloid Interf. Sci.* 229 (2000) 497.
- [185] S.M. Notley, B. Pettersson, L. Wagberg, *J. Am. Chem. Soc.* 126 (2004) 13930.
- [186] R. Nigmatullin, R. Lovitt, C. Wright, M. Linder, T. Nakari-Setälä, M. Gama, *Colloids Surf. B* 35 (2004) 125.

- [187] M.W. Rutland, T.J. Senden, *Langmuir* 9 (1993) 412.
- [188] B.P. Frank, G. Belfort, *Langmuir* 13 (1997) 6234.
- [189] M.E. Karaman, L. Meagher, R.M. Pashley, *Langmuir* 9 (1993) 1220.
- [190] E. Bonaccorso, M. Kappl, H.-J. Butt, *Phys. Rev. Lett.* 88 (2002) 076103.
- [191] C.A.J. Putman, B.G. De Groot, N.F. Van Hulst, J. Greve, *J. Appl. Phys.* 72 (1992) 6.
- [192] M. Pierce, J. Stuart, A. Pungor, P. Dryden, V. Hlady, *Langmuir* 10 (1994) 3217.
- [193] T.E. Schäffer, *J. Appl. Phys.* 91 (2002) 4739.
- [194] N.P. D'Costa, J.H. Hoh, *Rev. Sci. Instrum.* 66 (1995) 5096.
- [195] R.W. Stark, *Rev. Sci. Instrum.* 75 (2004) 5053.
- [196] M. Jaschke, H.-J. Butt, *Rev. Sci. Instrum.* 66 (1995) 1258.
- [197] T.J. Senden, *Curr. Opin. Colloid Interf. Sci.* 6 (2001) 95.
- [198] J.B. Pethica, A.P. Sutton, *J. Vac. Sci. Technol. A* 6 (1988) 2490.
- [199] S.T. Huntington, P.G. Hartley, J. Katsifolis, *Ultramicroscopy* 94 (2003) 283.
- [200] S.C. Clark, J.Y. Walz, W.A. Ducker, *Langmuir* 20 (2004) 7616.
- [201] O.I. Vinogradova, H.-J. Butt, G.E. Yakubov, F. Feuillebois, *Rev. Sci. Instrum.* 72 (2001) 2330.
- [202] N.A. Burnham, R.J. Colton, H.M. Pollock, *J. Vac. Sci. Technol. A* 9 (1991) 2548.
- [203] G.L. Miller, J.E. Griffith, E.R. Wagner, *Rev. Sci. Instrum.* 62 (1991) 705.
- [204] P.J. Bryant, H.S. Kim, R.H. Decken, Y.C. Cheng, *J. Vac. Sci. Technol. A* 8 (1990) 2502.
- [205] D.A. Grigg, P.E. Russel, J.E. Griffith, *Ultramicroscopy* 42 (1992) 1504.
- [206] J. Mertz, O. Marti, J. Mlynek, *Appl. Phys. Lett.* 62 (1993) 2344.
- [207] S.P. Jarvis, A. Oral, T.P. Weihs, J.B. Pethica, *Rev. Sci. Instrum.* 64 (1993) 3515.
- [208] S.P. Jarvis, H. Yamada, S.I. Yamamoto, H. Tokumoto, J.B. Pethica, *Nature* 384 (1996) 247.
- [209] S.P. Jarvis, H. Tokumoto, *Probe Microsc.* 1 (1997) 65.
- [210] S.A. Joyce, J.E. Houston, *Rev. Sci. Instrum.* 62 (1991) 710.
- [211] H.I. Kim, J.G. Kushmerick, J.E. Houston, B.C. Bunker, *Langmuir* 19 (2003) 9271.
- [212] O.I. Vinogradova, R.G. Horn, *Langmuir* 17 (2001) 1604.
- [213] S.P. Jarvis, S.I. Yamamoto, H. Yamada, H. Tokumoto, J.B. Pethica, *Appl. Phys. Lett.* 70 (1997) 2238.
- [214] H.-J. Butt, A. Döppenschmidt, G. Hüttl, E. Müller, O.I. Vinogradova, *J. Chem. Phys.* 113 (2000) 1194.
- [215] J.H. Hoh, A. Engel, *Langmuir* 9 (1993) 3310.
- [216] B.V. Derjaguin, *Kolloid Zeitschrift* 69 (1934) 155.
- [217] B.A. Todd, S.J. Eppell, *Langmuir* 20 (2004) 4892.
- [218] S. Hudlet, M. Saint Jean, C. Guthmann, J. Berger, *Eur. Phys. J. B* 2 (1998) 5.
- [219] B.M. Law, F. Rieutord, *Phys. Rev. B* 66 (2002) 035402.
- [220] J. Colchero, A. Gil, A.M. Baró, *Phys. Rev. B* 64 (2001) 245403.
- [221] H.W. Hao, A.M. Baró, J.J. Sáenz, *J. Vac. Sci. Technol. B* 9 (1991) 1323.
- [222] G.M. Sacha, A. Verdaguer, J. Martínez, J.J. Sáenz, D.F. Ogletree, M. Salmeron, *Appl. Phys. Lett.* 86 (2005) 123101.
- [223] B.D. Terris, B.D. Stern, D. Rugar, H.J. Mamin, *Phys. Rev. Lett.* 63 (1989) 2669.
- [224] H. Yokoyama, T. Inoue, J. Itoh, *Appl. Phys. Lett.* 65 (1994) 3143.
- [225] S. Watanabe, K. Hane, T. Ohye, M. Ito, T. Goto, *J. Vac. Sci. Technol. B* 11 (1993) 1774.
- [226] C. Böhm, C. Roths, U. Müller, A. Beyer, E. Kubalek, *Mater. Sci. Eng. B* 24 (1994) 218.
- [227] S. Belaidi, P. Girard, G. Leveque, *J. Appl. Phys.* 81 (1997) 1023.
- [228] G. Koley, M.G. Spencer, H.R. Bhangale, *Appl. Phys. Lett.* 79 (2001) 545.
- [229] L. Boyer, F. Houzé, A. Tonck, J.L. Loubet, J.M. Georges, *J. Phys. D* 27 (1994) 1504.
- [230] B. Gady, R. Reifenberger, D.S. Rimai, L.P. DeMejo, *Langmuir* 13 (1997) 2533.
- [231] S. Gómez-Monivas, L.S. Froufe-Pérez, A.J. Caamano, J.J. Sáenz, *Appl. Phys. Lett.* 79 (2001) 4048.
- [232] S. Hudlet, M. Saint Jean, B. Roulet, J. Berger, C. Guthmann, *J. Appl. Phys.* 77 (1995) 3308.
- [233] X. de la Broise, M. Lannoo, C. Delerue, *J. Appl. Phys.* 82 (1997) 5589.
- [234] J. Hu, X.D. Xiao, M. Salmeron, *Appl. Phys. Lett.* 67 (1995) 476.
- [235] G.M. Sacha, J.J. Sáenz, *Appl. Phys. Lett.* 85 (2004) 2610.
- [236] C.M. Mate, R. Erlandsson, G.M. McClelland, S. Chiang, *Surf. Sci.* 208 (1989) 473.
- [237] N.A. Burnham, R.J. Colton, *J. Vac. Sci. Technol. A* 7 (1989) 2096.

- [238] C.M. Mate, M.R. Lorenz, V.J. Novotny, *J. Chem. Phys.* 90 (1989) 7550.
- [239] G.S. Blackman, C.M. Mate, M.R. Philpott, *Phys. Rev. Lett.* 65 (1990) 2270.
- [240] C.M. Mate, V.J. Novotny, *J. Chem. Phys.* 94 (1991) 8420.
- [241] Y.N. Moiseev, V.M. Mostepanenko, V.I. Panov, I.Y. Sokolov, *Sov. Phys. Tech. Phys.* 35 (1990) 84.
- [242] J.B. Pethica, W.C. Oliver, *Physica Scripta T19* (1987) 61.
- [243] O. Tabata, K. Kawahata, S. Sugiyama, I. Igarashi, *Sens. Actuators* 20 (1989) 135.
- [244] K.R. Virwani, A.P. Malshe, W.F. Schmidt, D.K. Sood, *Smart Mater. Struct.* 12 (2003) 1028.
- [245] H. Hertz, *J. Reine Angew. Math.* 92 (1882) 156.
- [246] K.L. Johnson, K. Kendall, A.D. Roberts, *Proc. R. Soc. London A* 324 (1971) 301.
- [247] B.V. Derjaguin, V.M. Muller, Y.P. Toporov, *J. Colloid Interf. Sci.* 53 (1975) 314.
- [248] V.M. Müller, V.S. Yushchenko, B.V. Derjaguin, *J. Colloid Interf. Sci.* 77 (1980) 91.
- [249] V.M. Müller, B.V. Derjaguin, Y.P. Toporov, *Colloids Surf.* 7 (1983) 251.
- [250] D. Maugis, *J. Colloid Interf. Sci.* 150 (1992) 243.
- [251] M.A. Lantz, S.J. O'Shea, M.E. Welland, K.L. Johnson, *Phys. Rev. B* 55 (1997) 10776.
- [252] I.N. Sneddon, *Int. J. Eng. Sci.* 3 (1965) 47.
- [253] E. Boschung, M. Heuberger, G. Dietler, *Appl. Phys. Lett.* 64 (1994) 1794.
- [254] W.C. Oliver, G.M. Pharr, *J. Mater. Res.* 7 (1992) 1564.
- [255] B.J. Briscoe, L. Fiori, E. Pelillo, *J. Phys. D* 31 (1998) 2395.
- [256] M.R. van Landingham, J.S. Villarrubia, W.F. Guthrie, G.F. Meyers, *Macromol. Symp.* 167 (2001) 15.
- [257] S. Watanabe, S. Miyake, M. Sutoh, M. Murakawa, *Surf. Coat. Technol.* 169/170 (2003) 295.
- [258] W. Hua, X. Wu, D. Shen, H. Lu, M. Polak, *Appl. Surf. Sci.* 189 (2002) 72.
- [259] J. Shieh, M.H. Hon, *Thin Solid Films* 391 (2001) 101.
- [260] M. Göken, R. Sakidja, W.D. Nix, J.H. Perepezko, *Mat. Sci. Eng. A* 312–319 (2001) 902.
- [261] D.L. Patrick, J.F. Flanagan, P. Kohl, R.M. Lynden-Bell, *J. Am. Chem. Soc.* 125 (2003) 6762.
- [262] C. Plassard, E. Lesniewska, I. Pochard, A. Nonat, *Ultramicroscopy* 100 (2004) 331.
- [263] H. Shulha, X. Zhai, V.V. Tsukruk, *Macromolecules* 36 (2003) 2825.
- [264] E.K. Dimitriadis, F. Horkay, J. Maresca, B. Kachar, R.S. Chadwick, *Biophys. J.* 82 (2002) 2798.
- [265] B. Mailhot, P.-O. Bussiere, A. Rivaton, S. Morlat-Therias, J.-L. Gardette, *Macromol. Rapid Commun.* 25 (2004) 436.
- [266] B. Cappella, H. Sturm, *J. Appl. Phys.* 91 (2002) 506.
- [267] B. Cappella, H. Sturm, E. Schulz, *J. Adhes. Sci. Technol.* 16 (2002) 921.
- [268] T.R. Matzelle, G. Geuskens, N. Kruse, *Macromolecules* 36 (2003) 2926.
- [269] O. Mermut, J. Lefebvre, D.G. Gray, C.J. Barrett, *Macromolecules* 36 (2003) 8819.
- [270] S. Tan, R.L. Sherman Jr., W.T. Ford, *Langmuir* 20 (2004) 7015.
- [271] M.D. Garrison, R. Luginbühl, R.M. Overney, B.D. Ratner, *Thin Solid Films* 352 (1999) 13.
- [272] A. Opdahl, G.A. Somorjai, *J. Pol. Sci. B* 39 (2001) 2263.
- [273] F.T. Arce, R. Avci, I.B. Beech, K.E. Cooksey, B. Wigglesworth-Cooksey, *J. Chem. Phys.* 119 (2003) 1671.
- [274] G.V. Lubarsky, M.R. Davidson, R.H. Bradley, *Surf. Sci.* 558 (2004) 135.
- [275] Y. Sun, B. Akhremitchev, G.C. Walker, *Langmuir* 20 (2004) 5837.
- [276] S.A. Chizhik, Z. Huang, V.V. Gorbunov, N.K. Myshkin, V.V. Tsukruk, *Langmuir* 14 (1998) 2606.
- [277] V.V. Tsukruk, Z. Huang, S.A. Chizhik, V.V. Gorbunov, *J. Mater. Sci.* 33 (1998) 4905.
- [278] I.U. Vakarelski, A. Toritani, M. Nakayama, K. Higashitani, *Langmuir* 17 (2001) 4739.
- [279] I.U. Vakarelski, K. Higashitani, *J. Colloid Interf. Sci.* 242 (2001) 110.
- [280] H. Shulha, A. Kovalev, N. Myshkin, V.V. Tsukruk, *Eur. Polym. J.* 40 (2004) 949.
- [281] B.B. Akhremitchev, G.C. Walker, *Langmuir* 15 (1999) 5630.
- [282] V.I. Uricanu, M.H.G. Duits, R.M.F. Nelissen, M.L. Bennink, J. Mellema, *Langmuir* 19 (2003) 8182.
- [283] L. Richert, A.J. Engler, D.E. Discher, C. Picart, *Biomacromolecules* 5 (2004) 1908.
- [284] K.R. Shull, D. Ahn, C.L. Mowery, *Langmuir* 13 (1997) 1799.
- [285] S.A. Chizhik, V.V. Gorbunov, I. Luzinov, N. Fuchigami, V.V. Tsukruk, *Macromol. Symp.* 167 (2001) 167.
- [286] V.V. Tsukruk, A. Sidorenko, V.V. Gorbunov, S.A. Chizhik, *Langmuir* 17 (2001) 6715.
- [287] Y.I. Rabinovich, I.U. Vakarelski, S.C. Brown, P.K. Singh, B.M. Moudgil, *J. Colloid Interf. Sci.* 270 (2004) 29.
- [288] D. Raghavan, X. Gu, T. Nguyen, M. van Landingham, A. Karim, *Macromolecules* 33 (2000) 2573.

- [289] V.V. Tsukruk, Z. Huang, *Polymer* 41 (2000) 5541.
- [290] M. Lemieux, S. Minko, D. Usov, M. Stamm, V.V. Tsukruk, *Langmuir* 19 (2003) 6126.
- [291] K.D. Yao, W.G. Liu, Z. Lin, X.H. Qiu, *Pol. Int.* 48 (1999) 794.
- [292] M. Hinz, A. Kleiner, S. Hild, O. Marti, U. Dürig, B. Gotsmann, U. Drechsler, T.R. Albrecht, P. Vettiger, *Eur. Polym. J.* 40 (2004) 957.
- [293] V.N. Bliznyuk, H.E. Assender, G.A.D. Briggs, *Macromolecules* 35 (2002) 6613.
- [294] O.K.C. Tsui, X.P. Wang, J.Y.L. Ho, T.K. Ng, X. Xiao, *Macromolecules* 33 (2000) 4198.
- [295] B. Cappella, S.K. Kaliappan, H. Sturm, *Macromolecules* 38 (2005) 1874.
- [296] G. Gillies, C.A. Prestidge, P. Attard, *Langmuir* 18 (2002) 1674.
- [297] M. Reitsma, V. Craig, S. Biggs, *Int. J. Adhes. Adhes.* 20 (2000) 445.
- [298] C. Reynaud, F. Sommer, C. Quet, N. El Bounia, T.M. Duc, *Surf. Interf. Anal.* 30 (2000) 185.
- [299] B. Du, J. Liu, Q. Zhang, T. He, *Polymer* 42 (2001) 5901.
- [300] P. Attard, *Langmuir* 17 (2001) 4322.
- [301] A.J. Engler, L. Richert, J.Y. Wong, C. Picart, D.E. Discher, *Surf. Sci.* 570 (2004) 142.
- [302] A. Touhami, B. Nysten, Y.F. Dufrêne, *Langmuir* 19 (2003) 4539.
- [303] M. Arnoldi, M. Fritz, E. Bauerlein, M. Radmacher, E. Sackmann, A. Boulbitch, *Phys. Rev. E* 62 (2000) 1034.
- [304] I. Lee, R.E. Marchant, *Colloids Surf. B* 19 (2000) 357.
- [305] J. Domke, S. Dannohl, W.J. Parak, O. Muller, W.K. Aicher, M. Radmacher, *Colloids Surf. B* 19 (2000) 367.
- [306] X.M. Liang, G.Z. Mao, K.Y.S. Ng, *J. Colloid Interf. Sci.* 278 (2004) 53.
- [307] H. Sato, N. Kataoka, F. Kajiya, M. Katano, T. Takigawa, T. Masuda, *Colloids Surf. B* 34 (2004) 141.
- [308] T. Yamada, H. Arakawa, T. Okajima, T. Shimada, A. Ikai, *Ultramicroscopy* 91 (2002) 261.
- [309] J.N. Israelachvili, *Intermolecular and Surface Forces*, Academic Press, London, 1992.
- [310] F. London, *Faraday Soc.* 33 (1937) 8.
- [311] A.D. McLachlan, *Proc. R. Soc. London A* 202 (1963) 224.
- [312] L.D. Landau, E.M. Lifshitz, *Electrodynamics of Continuous Media*, Pergamon Press, Oxford, 1963.
- [313] H.C. Hamaker, *Physica* 4 (1937) 1058.
- [314] E.M. Lifshitz, *Sov. Phys. JETP* 2 (1956) 73.
- [315] S. Eichenlaub, C. Chan, S.P. Beaudoin, *J. Colloid Interf. Sci.* 248 (2002) 389.
- [316] H. Skulason, C.D. Frisbie, *Langmuir* 16 (2000) 6294.
- [317] C.J. van Oss, M.K. Chaudhury, R.J. Good, *Chem. Rev.* 88 (1988) 927.
- [318] R.J. Good, L.A. Girifalco, *J. Phys. Chem.* 64 (1960) 561.
- [319] B. Cappella, G. Dietler, *Surf. Sci. Rep.* 34 (1999) 1–104.
- [320] P.F. Luckham, *Adv. Colloid Interf. Sci.* 111 (2004) 29.
- [321] S.W. Lee, W.M. Sigmund, *Colloids Surf. A* 204 (2002) 43.
- [322] I.U. Vakarelski, K. Ishimura, K. Higashitani, *J. Colloid Interf. Sci.* 227 (2000) 111.
- [323] C. Jacquot, J. Takadoum, *J. Adhes. Sci. Technol.* 15 (2001) 681.
- [324] S.W. Lee, W.M. Sigmund, *J. Colloid Interf. Sci.* 243 (2001) 365.
- [325] H.D. Ackler, R.H. French, Y.M. Chiang, *J. Colloid Interf. Sci.* 179 (1996) 460.
- [326] L. Bergström, *Adv. Colloid Interf. Sci.* 70 (1997) 125.
- [327] I. Larson, D.Y.C. Chan, C.J. Drummond, F. Grieser, *Langmuir* 13 (1997) 2429.
- [328] S. Biggs, P. Mulvaney, *J. Chem. Phys.* 100 (1994) 8501.
- [329] V. Kane, P. Mulvaney, *Langmuir* 14 (1998) 3303.
- [330] P.D. Ashby, L. Chen, C.M. Lieber, *J. Am. Chem. Soc.* 122 (2000) 9467.
- [331] C.J. Drummond, T.J. Senden, *Colloids Surf. A* 87 (1994) 217.
- [332] J.L. Hutter, J. Bechhoefer, *J. Appl. Phys.* 73 (1993) 4123.
- [333] D.B. Hough, L.R. White, *Adv. Colloid Interf. Sci.* 14 (1980) 3.
- [334] T.J. Senden, C.J. Drummond, *Colloids Surf. A* 94 (1995) 29.
- [335] S. Biggs, A.D. Proud, *Langmuir* 13 (1997) 7202.
- [336] P.G. Hartley, I. Larson, P.J. Scales, *Langmuir* 13 (1997) 2207.
- [337] W.A. Ducker, Z. Xu, J.N. Israelachvili, *Langmuir* 10 (1994) 3279.
- [338] A.C. Hillier, S. Kim, A.J. Bard, *J. Phys. Chem.* 100 (1996) 18808.

- [339] I. Larson, C.J. Drummond, D.Y.C. Chan, F. Grieser, *J. Phys. Chem.* 99 (1995) 2114.
- [340] K. Hu, F.R.F. Fan, A.J. Bard, A.C. Hillier, *J. Phys. Chem. B* 101 (1997) 8298.
- [341] S. Lee, W.M. Sigmund, *J. Colloid Interf. Sci.* 243 (2001) 365.
- [342] S. Biggs, *J. Chem. Soc., Faraday Trans.* 92 (1996) 2783.
- [343] M.E. Karaman, R.M. Pashley, T.D. Waite, S.J. Hatch, H. Bustamante, *Colloids Surf. A* 129 (1997) 239.
- [344] P. Kekicheff, S. Marcelja, T.J. Senden, V.E. Shubin, *J. Chem. Phys.* 99 (1999) 6098.
- [345] C.J. Drummond, G. Georgaklis, D.Y.C. Cahn, *Langmuir* 12 (1996) 2617.
- [346] G.U. Lee, D.A. Kidwell, R.J. Colton, *Langmuir* 10 (1994) 354.
- [347] T. Ederth, *Langmuir* 17 (2001) 3329.
- [348] J. Seog, D. Dean, A.H.K. Plaas, S. Wong-Palms, A.J. Grodzinsky, C. Ortiz, *Macromolecules* 35 (2002) 5601.
- [349] D.V. Vezenov, A.V. Zhuk, G.M. Whitesides, C.M. Lieber, *J. Am. Chem. Soc.* 124 (2002) 10578.
- [350] S.I. Zanette, A.O. Caride, V.B. Nunes, G.L. Klimchitskaya, F.L. Freire, R. Prioli, *Surf. Sci.* 453 (2000) 75.
- [351] K. Cooper, A. Gupta, S. Beaudoin, *J. Colloid Interf. Sci.* 234 (2001) 284.
- [352] E.R. Beach, G.W. Tormoen, J. Drelich, R. Han, *J. Colloid Interf. Sci.* 247 (2002) 84.
- [353] J. Drelich, G.W. Tormoen, E.R. Beach, *J. Colloid Interf. Sci.* 280 (2004) 484.
- [354] L.H.G.J. Segeren, B. Siebum, F.G. Karsenberg, J.W.A. Van den Berg, G.J. Vancso, *J. Adhes. Sci. Technol.* 16 (2002) 793.
- [355] A.M. Freitas, M.M. Sharma, *J. Colloid Interf. Sci.* 233 (2001) 73.
- [356] A.S. Duwez, C. Poulenis, P. Bertrand, B. Nysten, *Langmuir* 17 (2001) 6351.
- [357] J. Nalaskowski, J. Drelich, J. Hupka, J.D. Miller, *Langmuir* 19 (2003) 5311.
- [358] K. Akimoto, F. Sato, T. Morikawa, M. Fujihira, *Jpn. J. Appl. Phys.* 43 (2004) 4492.
- [359] R.M. Ralich, Y. Wu, R.D. Ramsier, P.N. Henriksen, *J. Vac. Sci. Technol. A* 18 (2000) 1345.
- [360] A. Noy, S. Zepeda, C.S. Orme, Y. Yeh, J.J. De Yoreo, *J. Am. Chem. Soc.* 125 (2003) 1356.
- [361] X. Jiang, C. Ortiz, P.T. Hammond, *Langmuir* 18 (2002) 1131.
- [362] S. Kidoaki, T. Matsuda, *Langmuir* 15 (1999) 7639.
- [363] G. Papastavrou, S. Akari, *Colloids Surf. A* 164 (2000) 175.
- [364] P. Warszynski, G. Papastavrou, K.D. Wandtke, H. Möhwald, *Colloids Surf. A* 214 (2003) 61.
- [365] H. Schonherr, M.T. van Os, R. Forch, R.B. Timmons, W. Knoll, G.J. Vancso, *Chem. Mater.* 12 (2000) 3689.
- [366] N.J. Brewer, G.J. Leggett, *Langmuir* 20 (2004) 4109.
- [367] R.S. Abandan, J.A. Swift, *Langmuir* 18 (2002) 4847.
- [368] M.S. Wang, L.B. Palmer, J.D. Schwartz, A. Razatos, *Langmuir* 20 (2004) 7753.
- [369] Y.F. Dufrêne, C.J.P. Boonaert, H.C. van der Mei, H.J. Busscher, P.G. Rouxhet, *Ultramicroscopy* 86 (2001) 113.
- [370] S.C. Clear, P.F. Nealey, *J. Colloid Interf. Sci.* 213 (1999) 238.
- [371] O. Noel, M. Brogly, G. Castelein, J. Schultz, *Langmuir* 20 (2004) 2707.
- [372] O. Noel, M. Brogly, G. Castelein, J. Schultz, *Eur. Polym. J.* 40 (2004) 965.
- [373] G.W. Tormoen, J. Drelich, E.R. Beach, *J. Adhes. Sci. Technol.* 18 (2004) 1.
- [374] J.H. Cho, D.H. Lee, J.A. Lim, K. Cho, *Langmuir* 20 (2004) 10174.
- [375] Y.P. Li, D.Y. Li, *J. Appl. Phys.* 95 (2004) 7961.
- [376] H.Y. Nie, M.J. Walzak, B. Berno, N.S. McIntyre, *Appl. Surf. Sci.* 145 (1999) 627.
- [377] H.Y. Nie, M.J. Walzak, B. Berno, N.S. McIntyre, *Langmuir* 15 (1999) 6484.
- [378] T. Nonogaki, S.H. Xu, S. Kugimiya, S. Sato, I. Miyata, M. Yonese, *Langmuir* 16 (2000) 4272.
- [379] P.E. Pullen, J.J. Pesek, M.T. Matyska, J. Frommer, *Anal. Chem.* 72 (2000) 2751.
- [380] G. Jänchen, M. Mertig, W. Pompe, *Surf. Interf. Anal.* 27 (1999) 444.
- [381] M. Schneider, H. Mohwald, S. Akari, *J. Adhes.* 79 (2003) 597.
- [382] A. Relini, S. Sottini, S. Zuccotti, M. Bolognesi, A. Gliozzi, R. Rolandi, *Langmuir* 19 (2003) 2908.
- [383] E.R. Beach, G.W. Tormoen, J. Drelich, *J. Adhes. Sci. Technol.* 16 (2002) 845.
- [384] B. Pignataro, G. Grasso, L. Renna, G. Marletta, *Surf. Interf. Anal.* 33 (2002) 54.
- [385] M.A. Rixman, D. Dean, C.E. Macias, C. Ortiz, *Langmuir* 19 (2003) 6202.
- [386] Y.L. Ong, A. Razatos, G. Georgiou, M.M. Sharma, *Langmuir* 15 (1999) 2719.
- [387] Y. Leng, S. Jiang, *J. Am. Chem. Soc.* 124 (2002) 11764.
- [388] H. Skulason, C.D. Frisbie, *J. Am. Chem. Soc.* 122 (2000) 9750.

- [389] H. Skulason, C.D. Frisbie, *J. Am. Chem. Soc.* 124 (2002) 15125.
- [390] H. Skulason, C.D. Frisbie, *Anal. Chem.* 74 (2002) 3096.
- [391] J.M. Williams, T. Han, T.P. Beebe, *Langmuir* 12 (1996) 1291.
- [392] Z.Q. Wei, C. Wang, C.F. Zhu, C.Q. Zhou, B. Xu, C.L. Bai, *Surf. Sci.* 459 (2000) 401.
- [393] G.A. Willing, R.D. Neuman, *Langmuir* 18 (2002) 8370.
- [394] B.V. Derjaguin, L. Landau, *Acta Physicochim. URSS* 14 (1941) 633.
- [395] E.J.W. Verwey, J.T.G. Overbeek, *Theory of the Stability of Lyophobic Colloids*, Elsevier Publishing Inc., New York, 1948.
- [396] D.Y.C. Chan, D.J. Mitchell, *J. Colloid Interf. Sci.* 95 (1983) 193.
- [397] M. Gouy, *J. Phys. (Paris)* 9 (1910) 457.
- [398] D.L. Chapman, *Phil. Mag. (London)* 25 (1913) 475.
- [399] P. Debye, E. Hückel, *Physikalische Zeitschrift* 24 (1923) 185.
- [400] R.J. Hunter, *Foundations of Colloid Science i and ii*, Clarendon Press, Oxford, 1995.
- [401] E. Barouch, E. Matijevic, *J. Chem. Soc., Faraday Trans. I* 81 (1985) 1797.
- [402] R. Hogg, T.W. Healy, D.W. Fuerstenau, *Trans. Faraday Soc.* 62 (1966) 1638.
- [403] H.-J. Butt, *Nanotechnology* 3 (1992) 60.
- [404] V.A. Parsegian, D. Gingell, *Biophys. J.* 12 (1972) 1192.
- [405] S.L. Carnie, D.Y.C. Chan, J.S. Gunning, *Langmuir* 10 (1994) 2993.
- [406] H. Ohshima, *J. Colloid Interf. Sci.* 162 (1994) 487.
- [407] J. Stankovich, S.L. Carnie, *Langmuir* 1996 (1996) 1453.
- [408] A.V. Nguyen, G.M. Evans, G.J. Jameson, *J. Colloid Interf. Sci.* 230 (2000) 205.
- [409] V.G. Levadny, M.L. Belaya, D.A. Pink, M.H. Jericho, *Biophys. J.* 70 (1996) 1745.
- [410] M. Prica, S. Biggs, F. Grieser, T.W. Healy, *Colloids Surf. A* 119 (1996) 205.
- [411] K. Hu, A.J. Bard, *Langmuir* 13 (1997) 5114.
- [412] D.E. Yates, S. Levine, T.W. Healy, *J. Chem. Soc., Faraday Trans. I* 70 (1974) 1807.
- [413] M. Grattarola, G. Massobrio, S. Martinoia, *IEEE Trans. Electron Devices* 39 (1992) 813.
- [414] D.L. Hareme, L.J. Bousse, J.D. Shott, J.D. Meindl, *IEEE Trans. Electron Devices* 34 (1987) 1700.
- [415] B.V. Zhmud, A. Meurk, L. Bergström, *J. Colloid Interf. Sci.* 207 (1998) 332.
- [416] R.M. Pashley, *J. Colloid Interf. Sci.* 83 (1981) 531.
- [417] P.M. Claesson, P. Herder, P. Stenius, J.C. Eriksson, R.M. Pashley, *J. Colloid Interf. Sci.* 109 (1986) 31.
- [418] P.J. Scales, F. Grieser, T.W. Healy, *Langmuir* 6 (1990) 582.
- [419] S. Nishimura, H. Tateyama, K. Tsunematsu, K. Jinnai, *J. Colloid Interf. Sci.* 152 (1992) 359.
- [420] G. Cevc, *Biochim. Biophys. Acta* 3 (1990) 311.
- [421] B.W. Ninham, V. Yaminsky, *Langmuir* 13 (1997) 2097.
- [422] K. Unno, T. Shibata, E. Makino, *Sens. Actuators A* 88 (2001) 247.
- [423] N. Iwata, T. Wakayama, S. Yamada, *Sens. Actuators A* 111 (2004) 26.
- [424] L.S. Cerovic, S.K. Milonjic, D. Bahloul-Hourlier, B. Doucey, *Colloids Surf. A* 197 (2002) 147.
- [425] B.V. Zhmud, J. Sonnefeld, L. Bergström, *Colloids Surf. A* 158 (1999) 327.
- [426] J. Lyklema, *Fundamentals of Interface and Colloid Science ii*, Academic Press, San Diego, 1995.
- [427] B.V. Zhmud, A. Meurk, L. Bergström, *Colloids Surf. A* 164 (2000) 3.
- [428] J.H. Hoh, J.P. Revel, P.K. Hansma, *Nanotechnology* 2 (1991) 119.
- [429] W.A. Ducker, T.J. Senden, R.M. Pashley, *Langmuir* 8 (1992) 1831.
- [430] A.L. Weisenhorn, P. Maivald, H.-J. Butt, P.K. Hansma, *Phys. Rev. B* 45 (1992) 11226.
- [431] X.Y. Lin, F. Creuzet, H. Arribart, *J. Phys. Chem.* 97 (1993) 7272.
- [432] L. Meagher, *J. Colloid Interf. Sci.* 152 (1992) 293.
- [433] G. Hüttel, D. Beyer, E. Müller, *Surf. Interf. Anal.* 25 (1997) 543.
- [434] G. Toikka, R.A. Hayes, *J. Colloid Interf. Sci.* 191 (1997) 102.
- [435] S. Biggs, P. Mulvaney, C.F. Zukoski, F. Grieser, *J. Am. Chem. Soc.* 116 (1994) 9150.
- [436] M. Giesbers, J.M. Kleijn, M.A. Cohen Stuart, *J. Colloid Interf. Sci.* 248 (2002) 88.
- [437] J. Gavaille, J. Takadoum, *J. Colloid Interf. Sci.* 250 (2002) 104.
- [438] G. Toikka, R.A. Hayes, J. Ralston, *J. Chem. Soc., Faraday Trans.* 93 (1997) 3523.

- [439] S. Sander, L.M. Mosley, K.A. Hunter, *Environ. Sci. Technol.* 38 (2004) 4791.
- [440] S. Veeramasuneni, M.R. Yalamanchili, J.D. Miller, *J. Colloid Interf. Sci.* 184 (1996) 594.
- [441] I. Larson, C.J. Drummond, D.Y.C. Chan, F. Grieser, *Langmuir* 13 (1997) 2109.
- [442] I. Muir, L. Meagher, M. Gee, *Langmuir* 17 (2001) 4932.
- [443] L. Meagher, R.M. Pashley, *J. Colloid Interf. Sci.* 185 (1997) 291.
- [444] J. Nalaskowski, S. Veeramasuneni, J.D. Miller, in: S. Atak, G. Önal, S. Celik (Eds.), *Innovations in Mineral and Coal Processing*, Balkema, Rotterdam, 1998, p. 159.
- [445] S. Nishimura, M. Kodama, H. Noma, H. Inoue, H. Tateyama, *Colloids Surf. A* 143 (1998) 1.
- [446] P. Weidenhammer, H.J. Jacobasch, *J. Colloid Interf. Sci.* 180 (1996) 232.
- [447] A. Drechsler, N. Petong, J. Zhang, D.Y. Kwok, K. Grundke, *Colloids Surf. A* 250 (2004) 357.
- [448] T. Ishino, H. Hieda, K. Tanaka, N. Gemma, *Jpn. J. Appl. Phys.* 33 (1994) 4718.
- [449] T. Arai, D. Aoki, Y. Okabe, M. Fujihira, *Thin Solid Films* 273 (1996) 322.
- [450] G.S. Watson, J.A. Blach, C. Cahill, D.V. Nicolau, D.K. Pham, J. Wright, S. Myhra, *Colloid Polym. Sci.* 282 (2003) 56.
- [451] G.S. Watson, J.A. Blach, C. Cahill, D.V. Nicolau, D.K. Pham, J. Wright, S. Myhra, *Biosens. Bioelectron.* 19 (2004) 1355.
- [452] J. Vandiver, D. Dean, N. Patel, W. Bonfield, C. Ortiz, *Biomaterials* 26 (2005) 271.
- [453] R.H. Yoon, S. Vivek, *J. Colloid Interf. Sci.* 204 (1998) 179.
- [454] S. Veeramasuneni, M.R. Yalamanchili, J.D. Miller, *Colloids Surf. A* 131 (1998) 77.
- [455] T. Ishino, H. Hieda, K. Tanaka, N. Gemma, *Jpn. J. Appl. Phys.* 33 (1994) L1552.
- [456] T. Arai, M. Fujihira, *J. Vac. Sci. Technol. B* 14 (1996) 1378.
- [457] R. Raiteri, M. Grattarola, H.-J. Butt, *J. Phys. Chem.* 100 (1996) 16700.
- [458] A. Döppenschmidt, H.-J. Butt, *Colloids Surf. A* 149 (1999) 145.
- [459] S.D. Campbell, A.C. Hillier, *Langmuir* 15 (1999) 891.
- [460] D. Barten, J.M. Kleijn, J. Duval, H.P. van Leeuwen, J. Lyklema, M.A. Cohen Stuart, *Langmuir* 19 (2003) 1133.
- [461] C. Dedeloudis, J. Fransaer, J.P. Celis, *J. Phys. Chem. B* 104 (2000) 2060.
- [462] J.M. Kleijn, D. Barten, M.A. Cohen Stuart, *Langmuir* 20 (2004) 9703.
- [463] T.J. Senden, C.J. Drummond, P. Kékicheff, *Langmuir* (1994) 358.
- [464] W.F. Heinz, J.H. Hoh, *Biophys. J.* 76 (1999) 528.
- [465] A.S. Johnson, C.L. Nehl, M.G. Mason, J.H. Hafner, *Langmuir* 19 (2003) 10007.
- [466] H.-J. Butt, *Biophys. J.* 63 (1992) 578.
- [467] C. Rotsch, M. Radmacher, *Langmuir* 13 (1997) 2825.
- [468] K. Estel, G. Kramer, F.J. Schmitt, *Colloids Surf. A* 161 (2000) 193.
- [469] C.E. McNamee, Y. Tsujii, M. Matsumoto, *Langmuir* 20 (2004) 1791.
- [470] G. Cevc, *J. Chem. Soc., Faraday Trans.* 87 (1991) 2733.
- [471] S. Leikin, V.A. Parsegian, D.C. Rau, R.P. Rand, *Annu. Rev. Phys. Chem.* 44 (1993) 369.
- [472] J.N. Israelachvili, H. Wennerström, *Nature* 379 (1996) 219.
- [473] I. Langmuir, *J. Chem. Phys.* 6 (1938) 873.
- [474] R.K. Schofield, *Trans. Faraday Soc.* 42 (1946) 219.
- [475] J.B. Hemwall, P.F. Low, *Soil Sci.* 82 (1956) 135.
- [476] J.N. Israelachvili, R.M. Pashley, *Nature* 306 (1983) 249.
- [477] V.N. Paunov, R.I. Dimova, P.A. Kralchevsky, G. Broze, A. Mehreteab, *J. Colloid Interf. Sci.* 182 (1996) 239.
- [478] N.A.M. Besseling, *Langmuir* 13 (1997) 2113.
- [479] A. Trokhymchuk, D. Henderson, D.T. Wasan, *J. Colloid Interf. Sci.* 210 (1999) 320.
- [480] S. Marcelja, N. Radic, *Chem. Phys. Lett.* 42 (1976) 129.
- [481] S. Marcelja, J.N. Israelachvili, H. Wennerström, *Nature* 385 (1997) 689.
- [482] R. Lipowsky, S. Grotehans, *Biophys. Chem.* 49 (1994) 27.
- [483] L. Perera, U. Essmann, M.L. Berkowitz, *Langmuir* 12 (1996) 2625.
- [484] J.N. Israelachvili, H. Wennerström, *J. Phys. Chem.* 96 (1992) 520.
- [485] G. Cevc, M. Hauser, A.A. Kornyshev, *Langmuir* 11 (1995) 3103.
- [486] S. Veeramasuneni, Y. Hu, M.R. Yalamanchili, J.D. Miller, *J. Colloid Interf. Sci.* 188 (1997) 473.
- [487] Y. Kanda, T. Nakamura, K. Higashitani, *Colloids Surf. A* 139 (1998) 55.

- [488] W.R. Bowen, N. Hilal, R.W. Lovitt, C.J. Wright, *J. Colloid Interf. Sci.* 197 (1998) 348.
- [489] S. Ohnishi, M. Murata, M. Hato, *Biophys. J.* 74 (1998) 455.
- [490] H. Mueller, H.-J. Butt, E. Bamberg, *Biophys. J.* 76 (1999) 1072.
- [491] L. Meagher, H.J. Griesser, *Colloids Surf. B* 23 (2002) 125.
- [492] D.J. Müller, A. Engel, *Biophys. J.* 73 (1997) 1633.
- [493] D.J. Müller, D. Fotiadis, S. Scheuring, S.A. Müller, A. Engel, *Biophys. J.* 76 (1999) 1101.
- [494] H.K. Christenson, P.M. Claesson, *Adv. Colloid Interf. Sci.* 91 (2001) 391.
- [495] P. Attard, *Adv. Colloid Interf. Sci.* 104 (2003) 75.
- [496] R.H. Yoon, D.H. Flinn, Y.I. Rabinovich, *J. Colloid Interf. Sci.* 185 (1997) 363.
- [497] J.N. Israelachvili, R. Pashley, *Nature* 300 (1982) 341.
- [498] J.N. Israelachvili, R. Pashley, *J. Colloid Interf. Sci.* 98 (1984) 500.
- [499] P.M. Claesson, C.E. Blom, P.C. Herder, B.W. Ninham, *J. Colloid Interf. Sci.* 114 (1986) 234.
- [500] K. Kurihara, T. Kunitake, *J. Am. Chem. Soc.* 114 (1992) 10927.
- [501] Y.I. Rabinovich, B.V. Derjaguin, N.V. Churaev, *Adv. Colloid Interf. Sci.* 16 (1982) 63.
- [502] Y.I. Rabinovich, B.V. Derjaguin, *Colloids Surf.* 30 (1988) 243.
- [503] T. Ederth, B. Liedberg, *Langmuir* 16 (2000) 2177.
- [504] Y.H. Tsao, D.F. Evans, H. Wennerström, *Science* 262 (1993) 547.
- [505] Y.I. Rabinovich, R.H. Yoon, *Colloids Surf. A* 93 (1994) 263.
- [506] J. Nalaskowski, S. Veeramasoneni, J. Hupka, J.D. Miller, *J. Adhes. Sci. Technol.* 13 (1999) 1519.
- [507] J. Mahnke, J. Stearnes, R.A. Hayes, D. Fornasiero, J. Ralston, *Phys. Chem. Chem. Phys.* 1 (1999) 2793.
- [508] J.W.G. Tyrrell, P. Attard, *Langmuir* 18 (2002) 160.
- [509] A. Carambassis, L.C. Jonker, P. Attard, M.W. Rutland, *Phys. Rev. Lett.* 80 (1998) 5357.
- [510] R.F. Considine, R.A. Hayes, R.G. Horn, *Langmuir* 15 (1999) 1657.
- [511] L. Meagher, V.S.J. Craig, *Langmuir* 10 (1994) 2736.
- [512] J. Nalaskowski, J. Hupka, J.D. Miller, *Physicochemical Problems in Mineral Processing*, 2000.
- [513] E. Kokkoli, C.F. Zukoski, *J. Colloid Interf. Sci.* 209 (1999) 60.
- [514] V.S.J. Craig, B.W. Ninham, R.M. Pashley, *Langmuir* 15 (1999) 1562.
- [515] O. Teschke, E.F. de Souza, *Chem. Phys. Lett.* 375 (2003) 540.
- [516] P.M. Claesson, H.K. Christenson, *J. Phys. Chem.* 92 (1988) 1650.
- [517] M. Hato, *J. Phys. Chem.* 100 (1996) 18530.
- [518] H.K. Christenson, V.V. Yaminski, *Colloids Surf. A* 129/130 (1997).
- [519] Q. Lin, E.E. Meyer, M. Tadmor, J.N. Israelachvili, T.L. Kuhl, *Langmuir* 21 (2005) 251.
- [520] J.C. Eriksson, S. Ljunggren, P.M. Claesson, *J. Chem. Soc., Faraday Trans. II* 85 (1989) 163.
- [521] A. Wallqvist, B. Berne, *J. Phys. Chem.* 99 (1995) 2893.
- [522] J. Forsman, B. Jönsson, C.E. Woodward, *J. Phys. Chem.* 100 (1996) 15005.
- [523] H.K. Christenson, P.M. Claesson, J.L. Parker, *J. Phys. Chem.* 96 (1992) 6725.
- [524] J. Wood, R. Sharma, *Langmuir* 11 (1995) 4797.
- [525] V.S.J. Craig, B.W. Ninham, R.M. Pashley, *Langmuir* 14 (1998) 5357.
- [526] R. Podgornik, V.A. Parsegian, *Chem. Phys.* 154 (1991) 477.
- [527] V.V. Yaminsky, B.W. Ninham, H.K. Christenson, R.M. Pashley, *Langmuir* 12 (1996) 1936.
- [528] V.V. Yaminsky, B.W. Ninham, *Langmuir* 9 (1993) 3618.
- [529] D. Andrienko, P. Patricio, O.I. Vinogradova, *J. Chem. Phys.* 121 (2004) 4414.
- [530] D.R. Berard, P. Attard, D.N. Patey, *J. Chem. Phys.* 98 (1993) 7236.
- [531] P. Attard, *Langmuir* 12 (1996) 1693.
- [532] V.V. Yaminsky, V.S. Yushchenko, E.A. Amelina, E.D. Shchukin, *J. Colloid Interf. Sci.* 96 (1983) 301.
- [533] R.M. Pashley, P.M. McGuiggan, B.W. Ninham, D.F. Evans, *Science* 229 (1985) 1088.
- [534] H.K. Christenson, P.M. Claesson, *Science* 235 (1988).
- [535] J.L. Parker, P.M. Claesson, P. Attard, *J. Phys. Chem.* 98 (1994) 8468.
- [536] P. Attard, *Langmuir* 16 (2000) 4455.
- [537] A.V. Nguyen, J. Nalaskowski, J.D. Miller, H.-J. Butt, *Int. J. Miner. Process.* 72 (2003) 215.

- [538] J. Nalaskowski, J. Hupka, J.D. Miller, Influence of Dissolved Gas on the Interaction Forces between Hydrophobic Surfaces in Water—Atomic Force Microscope Studies, Polonica-Zdoj, Poland, 1999.
- [539] R.F. Consideine, C.J. Drummond, *Langmuir* 16 (2000) 631.
- [540] E.E. Meyer, Q. Lin, J.N. Israelachvili, *Langmuir* 21 (2005) 256.
- [541] S.T. Lou, Z.Q. Quyang, Y. Zhang, X.J. Li, J. Hu, M.Q. Li, F.J. Yang, *J. Vac. Sci. Technol. B* 18 (2000) 2573.
- [542] N. Ishida, T. Inuoe, M. Miyahara, K. Higashitani, *Langmuir* 16 (2000) 6377.
- [543] J.W.G. Tyrrell, P. Attard, *Phys. Rev. Lett.* 87 (2001) 176104.
- [544] R. Steitz, T. Gutberlet, T. Hauss, B. Klösgen, R. Kratsev, S. Schemmel, A.C. Simonsen, G.H. Findenegg, *Langmuir* 19 (2003) 2409.
- [545] J. Yang, J. Duan, D. Fornasiero, J. Ralston, *J. Phys. Chem. B* 107 (2003) 6139.
- [546] A.C. Simonsen, P.L. Hansen, B. Klösgen, *J. Colloid Interf. Sci.* 273 (2004) 291.
- [547] D. Schwendel, T. Hayashi, R. Dahint, A. Pertsin, M. Grunze, R. Steitz, F. Schreiber, *Langmuir* 19 (2003) 2284.
- [548] T.R. Jensen, M.O. Jensen, N. Reitzel, K. Balashev, G.H. Peters, K. Kjaer, T. Bjornholm, *Phys. Rev. Lett.* 90 (2003) 086101.
- [549] M. Mao, J. Zhang, R.H. Yoon, W.A. Ducker, *Langmuir* 20 (2004) 1843.
- [550] D.R. Evans, V.S.J. Craig, T.J. Senden, *Physica A* 339 (2004) 101.
- [551] Y. Martin, D.W. Abraham, H.K. Wickramasinghe, *Appl. Phys. Lett.* 52 (1988) 1103.
- [552] R. Erlandsson, G. Hadziioannou, C.M. Mate, G.M. McClelland, S. Chaing, *J. Chem. Phys.* 89 (1988) 5190.
- [553] D.M. Schaefer, M. Carpenter, B. Gady, R. Reifengerger, L.P. DeMejo, D.S. Rimai, *J. Adhes. Sci. Technol.* 9 (1995) 1049.
- [554] D.M. Schaefer, M. Carpenter, R. Reifengerger, L.P. Demejo, D.S. Rimai, *J. Adhes. Sci. Technol.* 8 (1994) 197.
- [555] H. Rumpf, *Particle Technology*, Chapman & Hall, London, 1990.
- [556] Y.I. Rabinovich, J.J. Adler, A. Ata, R.K. Singh, B.M. Moudgil, *J. Colloid Interf. Sci.* 232 (2000) 10.
- [557] Y.I. Rabinovich, J.J. Adler, A. Ata, B.M. Moudgil, *J. Colloid Interf. Sci.* 232 (2000) 17.
- [558] K. Cooper, N. Ohler, A. Gupta, S. Beaudoin, *J. Colloid Interf. Sci.* 222 (2000) 63.
- [559] K. Cooper, A. Gupta, S. Beaudoin, *J. Colloid Interf. Sci.* 228 (2000) 213.
- [560] K. Cooper, A. Gupta, S. Beaudoin, *J. Electrochem. Soc.* 148 (2001) G662.
- [561] S. Eichenlaub, A. Gelb, S. Beaudoin, *J. Colloid Interf. Sci.* 280 (2004) 289.
- [562] H.B. Zhou, M. Gotzinger, W. Peukert, *Powder Technol.* 135 (2003) 82.
- [563] W.R. Bowen, R.W. Lovitt, C.J. Wright, *J. Mater. Sci.* 36 (2001) 623.
- [564] M.A.S. Quintanilla, A. Castellanos, J.M. Valverde, *Phys. Rev. E* 6403 (2001).
- [565] S. Jonat, S. Hasenzahl, A. Gray, P.C. Schmidt, *J. Pharm. Sci.* 93 (2004) 2635.
- [566] K. Meine, K. Kloss, T. Schneider, D. Spaltmann, *Surf. Interf. Anal.* 36 (2004) 694.
- [567] M. Götzinger, W. Peukert, *Langmuir* 20 (2004) 5298.
- [568] C. Creton, L. Leibler, *J. Polym. Sci. B* 34 (1996) 545.
- [569] H.C. Kim, T.P. Russell, *J. Polym. Sci. B* 39 (2001) 1848.
- [570] A. Mendez-Vilas, M.L. Gonzalez-Martin, L. Labajos-Broncano, M.J. Nuevo, *J. Adhes. Sci. Technol.* 16 (2002) 1737.
- [571] A. Mendez-Vilas, M.L. Gonzalez-Martin, M.J. Nuevo, *Appl. Surf. Sci.* 238 (2004) 9.
- [572] P. Richard, M. Nicodemi, R. Delannay, P. Ribiere, D. Bideau, *Nat. Mater.* 4 (2005) 121.
- [573] R.G. Cain, N.W. Page, S. Biggs, *Phys. Rev. E* 62 (2000) 8369.
- [574] R. Jones, *Granul. Matter* 4 (2003) 191.
- [575] R.I. Larsen, *Am. Ind. Hyg. Assoc. J.* 19 (1958) 265.
- [576] M.C. Kordecki, C. Orr, *Arch. Environ. Health* 1 (1960) 13.
- [577] G. Böhme, W. Kling, H. Krupp, H. Lange, G. Sandstede, *Zeitschr. Angew. Physik* 6 (1964) 486.
- [578] R. Polke, *Bull. Soc. Special Chim. France* A3241 (1969) 51.
- [579] D.K. Donald, *J. Appl. Phys.* 40 (1969) 3013.
- [580] D.F. St. John, D.J. Montgome, *J. Appl. Phys.* 42 (1971) 663.
- [581] D.K. Donald, *J. Adhes.* 4 (1972) 233.
- [582] F. Podczeczek, J.M. Newton, *J. Pharm. Sci.* 84 (1995) 1067.
- [583] J.M. Newton, K.K. Lam, *Powder Technol.* 73 (1992) 267.
- [584] J.M. Newton, K.K. Lam, *Powder Technol.* 73 (1992) 117.

- [585] J.M. Newton, K.K. Lam, *Powder Technol.* 76 (1993) 149.
- [586] F. Podczeck, J.M. Newton, M.B. James, *Int. J. Pharm.* 149 (1997) 151.
- [587] F. Podczeck, J.M. Newton, M.B. James, *J. Appl. Phys.* 79 (1996) 1458.
- [588] F. Podczeck, J.M. Newton, M.B. James, *J. Colloid Interf. Sci.* 187 (1997) 484.
- [589] F. Podczeck, J.M. Newton, M.B. James, *Powder Technol.* 83 (1995) 201.
- [590] P.R. Rennie, X.D. Chen, A.R. Mackereth, *Powder Technol.* 97 (1998) 191.
- [591] K. Hein, T. Hucke, M. Stintz, S. Ripperger, *Part. Part. Syst. Character.* 19 (2002) 269.
- [592] M. Kappl, H.-J. Butt, *Part. Part. Syst. Character.* 19 (2002) 129.
- [593] S. Biggs, G. Spinks, *J. Adhes. Sci. Technol.* 12 (1998) 461.
- [594] M. Reitsma, V.S.J. Craig, S. Biggs, *J. Adhes.* 74 (2000) 125.
- [595] B. Gady, R. Reifemberger, D.M. Schaefer, R.C. Bowen, D.S. Rimai, L.P. DeMejo, W. Vreeland, *J. Adhes.* 67 (1998) 19.
- [596] G. Toikka, G.M. Spinks, H.R. Brown, *J. Adhes.* 74 (2000) 317.
- [597] L.O. Heim, J. Blum, M. Preuss, H.-J. Butt, *Phys. Rev. Lett.* 83 (1999) 3328.
- [598] L. Heim, S. Ecke, M. Preuss, H.-J. Butt, *J. Adhes. Sci. Technol.* 16 (2002) 829.
- [599] D. Erts, A. Lohmus, R. Lohmus, H. Olin, A.V. Pokropivny, L. Ryen, K. Svensson, *Appl. Surf. Sci.* 188 (2002) 460.
- [600] M. Götzinger, W. Peukert, *Powder Technol.* 130 (2003) 102.
- [601] M. Götzinger, W. Peukert, *J. Adhes.* 80 (2004) 223.
- [602] J.Y. Park, D.F. Ogletree, M. Salmeron, C.J. Jenks, P.A. Thiel, *Tribol. Lett.* 17 (2004) 629.
- [603] J.D. Batteas, X.H. Quan, M.K. Weldon, *Tribol. Lett.* 7 (1999) 121.
- [604] Y.K. Hong, D.H. Eom, S.H. Lee, T.G. Kim, J.G. Park, A.A. Busnaina, *J. Electrochem. Soc.* 151 (2004) G756.
- [605] K. Cooper, S. Eichenlaub, A. Gupta, S. Beaudoin, *J. Electrochem. Soc.* 149 (2002) G239.
- [606] C. Dedeloudis, J. Fransaer, *Langmuir* 20 (2004) 11030.
- [607] T.H. Muster, I.S. Cole, *J. Electrochem. Soc.* 152 (2005) B125.
- [608] A. Meurk, J. Yanez, L. Bergstrom, *Powder Technol.* 119 (2001) 241.
- [609] E. Finot, E. Lesniewska, J.C. Mutin, J.P. Goudonnet, *Langmuir* 16 (2000) 4237.
- [610] E. Finot, E. Lesniewska, J.P. Goudonnet, J.C. Mutin, M. Domenech, A.A. Kadi, *Solid State Ionics* 141 (2001) 39.
- [611] S. Lesko, E. Lesniewska, A. Nonat, J.C. Mutin, J.P. Goudonnet, *Ultramicroscopy* 86 (2001) 11.
- [612] A. Paiva, N. Sheller, M.D. Foster, A.J. Crosby, K.R. Shull, *Macromolecules* 33 (2000) 1878.
- [613] B.H. Lee, H.J. Kim, *J. Appl. Polym. Sci.* 92 (2004) 625.
- [614] A.H. Barber, S.R. Cohen, S. Kenig, H.D. Wagner, *Compos. Sci. Technol.* 64 (2004) 2283.
- [615] S. Decossas, G. Cappello, G. Poignant, L. Patrone, A.M. Bonnot, F. Comin, J. Chevrier, *Europhys. Lett.* 53 (2001) 742.
- [616] T.H. Muster, G. Tiokka, R.A. Hayes, C.A. Prestidge, J. Ralston, *Colloids Surf. A* 106 (1996) 203.
- [617] Z.H. Xu, R. Chi, T. Difeo, J.A. Finch, *J. Adhes. Sci. Technol.* 14 (2000) 1813.
- [618] K.Q. Fa, J.A. Tao, J. Nalaskowski, J.D. Miller, *Langmuir* 19 (2003) 10523.
- [619] R. Chi, Z. Xu, T. DiFeo, J.A. Finch, J.L. Yordan, *J. Pulp. Pap. Sci.* 27 (2001) 152.
- [620] J. Nalaskowski, J. Drelich, J. Hupka, J.D. Miller, *Langmuir* 19 (2003) 5311.
- [621] A. Omoike, J.H. Horton, *Langmuir* 16 (2000) 1655.
- [622] M. Plaschke, J. Romer, R. Klenze, J.I. Kim, *Surf. Interf. Anal.* 30 (2000) 297.
- [623] T.L. Cail, M.F. Hochella, *Environ. Sci. Technol.* 39 (2005) 1011.
- [624] C.J. Roberts, *Eur. J. Pharm. Sci.* 24 (2005) 153.
- [625] U. Sindel, I. Zimmermann, *Powder Technol.* 117 (2001) 247.
- [626] T.H. Muster, C.A. Prestidge, *J. Pharm. Sci.* 91 (2002) 1432.
- [627] J.K. Eve, N. Patel, S.Y. Luk, S.J. Ebbens, C.J. Roberts, *Int. J. Pharm.* 238 (2002) 17.
- [628] V. Berard, E. Lesniewska, C. Andres, D. Pertuy, C. Laroche, Y. Pourcelot, *Int. J. Pharm.* 247 (2002) 127.
- [629] P. Begat, D.A.V. Morton, J.N. Staniforth, R. Price, *Pharm. Res.* 21 (2004) 1591.
- [630] M.D. Louey, P.J. Stewart, *Pharm. Res.* 19 (2002) 1524.
- [631] K.M. Ohta, M. Fuji, M. Chikazawa, *Pharm. Res.* 20 (2003) 804.
- [632] N. Islam, P. Stewart, I. Larson, P. Hartley, *Pharm. Res.* 21 (2004) 492.
- [633] M. Tsukada, R. Irie, Y. Yonemochi, R. Noda, H. Kamiya, W. Watanabe, E.I. Kauppinen, *Powder Technol.* 141 (2004) 262.
- [634] P.M. Young, R. Price, M.J. Tobyn, M. Buttrum, F. Dey, *J. Pharm. Sci.* 93 (2004) 753.

- [635] T.H. Ibrahim, T.R. Burk, F.M. Etzler, R.D. Neuman, J. Adhes. Sci. Technol. 14 (2000) 1225.
- [636] P.M. Young, R. Price, D. Lewis, S. Edge, D. Traini, J. Colloid Interf. Sci. 262 (2003) 298.
- [637] R. Ashayer, P.F. Luckham, S. Manimaaran, P. Rogueda, Eur. J. Pharm. Sci. 21 (2004) 533.
- [638] J.C. Hooton, C.S. German, S. Allen, M.C. Davies, C.J. Roberts, S.J.B. Tendler, P.M. Williams, Pharm. Res. 20 (2003) 508.
- [639] J.C. Hooton, C.S. German, S. Allen, M.C. Davies, C.J. Roberts, S.J.B. Tendler, P.M. Williams, Pharm. Res. 21 (2004) 953.
- [640] J.J. Wang, T.L. Li, S.D. Bateman, R. Erck, K.R. Morris, J. Pharm. Sci. 92 (2003) 798.
- [641] J. Lee, J. Pharm. Sci. 93 (2004) 2310.
- [642] N. Hilal, A.W. Mohammad, B. Atkin, N.A. Darwish, Desalination 157 (2003) 137.
- [643] W.R. Bowen, N. Hilal, R.W. Lovitt, C.J. Wright, J. Membr. Sci. 154 (1999) 205.
- [644] W.R. Bowen, T.A. Doneva, J. Colloid Interf. Sci. 229 (2000) 544.
- [645] W.R. Bowen, T.A. Doneva, Desalination 129 (2000) 163.
- [646] W.R. Bowen, T.A. Doneva, J.A.G. Stoton, Colloids Surf. A 201 (2002) 73.
- [647] W.R. Bowen, T.A. Doneva, H.B. Yin, Desalination 146 (2002) 97.
- [648] G. Wulff, Angew. Chem. Int. Ed. 34 (1995) 1812.
- [649] N. Hilal, V. Kochkodan, J. Membr. Sci. 213 (2003) 97.
- [650] N. Hilal, L. Al-Khatib, B.P. Atkin, V. Kochkodan, N. Potapchenko, Desalination 158 (2003) 65.
- [651] J.A. Brant, A.E. Childress, Environ. Eng. Sci. 19 (2002) 413.
- [652] J.A. Brant, A.E. Childress, J. Membr. Sci. 241 (2004) 235.
- [653] B.P. Frank, G. Belfort, J. Membr. Sci. 212 (2003) 205.
- [654] A. Gordano, V. Arcella, E. Drioli, Desalination 163 (2004) 127.
- [655] Q.L. Li, M. Elimelech, Environ. Sci. Technol. 38 (2004) 4683.
- [656] B. Bhushan, Proc. Inst. Mech. Eng. J. 215 (2001) 1.
- [657] Y.P. Zhao, L.S. Wang, T.X. Yu, J. Adhes. Sci. Technol. 17 (2003) 519.
- [658] B. Vogeli, H. von Kanel, Wear 238 (2000) 20.
- [659] H.W. Liu, B. Bhushan, Nanotechnology 15 (2004) 1246.
- [660] H.W. Liu, B. Bhushan, Ultramicroscopy 100 (2004) 391.
- [661] H.W. Liu, B. Bhushan, J. Vac. Sci. Technol. A 22 (2004) 1388.
- [662] B. Bhushan, H.W. Liu, Nanotechnology 15 (2004) 1785.
- [663] G.M.B.F. Snellings, S.O. Vansteenkiste, S.I. Corneillie, M.C. Davies, E.H. Schacht, Adv. Mater. 12 (2000) 1959.
- [664] C. Cassinelli, M. Morra, A. Pavesio, D. Renier, J. Biomater. Sci.-Polym. Ed. 11 (2000) 961.
- [665] M. Berry, T.J. McMaster, A.P. Corfield, M.J. Miles, Biomacromolecules 2 (2001) 498.
- [666] M.S. Schwarzenbach, P. Reimann, V. Thommen, M. Hegner, M. Mumenthaler, J. Schwob, H.J. Guntherodt, PDA J. Pharm. Sci. Technol. 56 (2002) 78.
- [667] A. Sethuraman, M. Han, R.S. Kane, G. Belfort, Langmuir 20 (2004) 7779.
- [668] E.M. Erb, X.Y. Chen, S. Allen, C.J. Roberts, S.J.B. Tendler, M.C. Davies, S. Forsen, Anal. Biochem. 280 (2000) 29.
- [669] C.C. Dupont-Gillain, C.M.J. Fauroux, D.C.J. Gardner, G.J. Leggett, J. Biomed. Mater. Res., Part A 67A (2003) 548.
- [670] D.S. Hwang, H.J. Yoo, J.H. Jun, W.K. Moon, H.J. Cha, Appl. Environ. Microbiol. 70 (2004) 3352–3359.
- [671] B.P. Frank, G. Belfort, Langmuir 17 (2001) 1905.
- [672] B.P. Frank, G. Belfort, Biotechnol. Prog. 18 (2002) 580.
- [673] S. Vengasandra, G. Sethumadhavan, F.N. Yan, R. Wang, Langmuir 19 (2003) 10940.
- [674] T.A. Kendall, M.F. Hochella, Geochim. Cosmochim. Acta 67 (2003) 3537.
- [675] J. Cleary, L. Bromberg, E. Magner, Langmuir 20 (2004) 9755.
- [676] W.G. Liu, F. Li, X.D. Zhao, K. De Yao, Q.G. Liu, Polym. Int. 51 (2002) 1459.
- [677] X.X. Sheng, T.S. Jung, J.A. Wesson, M.D. Ward, Proc. Natl. Acad. Sci. U.S.A. 102 (2005) 267.
- [678] W.J. O'Brien, J.J. Hermann, J. Adhes. 5 (1973) 91.
- [679] L.R. Fisher, J.N. Israelachvili, J. Colloid Interf. Sci. 80 (1981) 528.
- [680] H.K. Christenson, J. Colloid Interf. Sci. 121 (1988) 170.
- [681] Q. Ouyang, K. Ishida, K. Okada, Appl. Surf. Sci. 169 (2001) 644.
- [682] M. Fuji, K. Machida, T. Takei, T. Watanabe, M. Chikazawa, Langmuir 15 (1999) 4584.

- [683] B. Bhushan, C. Dandavate, *J. Appl. Phys.* 87 (2000) 1201.
- [684] X. Xiao, L. Qian, *Langmuir* 16 (2000) 8153.
- [685] N. Garoff, S. Zauscher, *Langmuir* 18 (2002) 6921.
- [686] R. Jones, H.M. Pollock, J.A.S. Cleaver, C.S. Hodges, *Langmuir* 18 (2002) 8045.
- [687] E.S. Yoon, S.H. Yang, H.G. Han, H. Kong, *Wear* 254 (2003) 974.
- [688] Y. Kaibara, K. Sugata, M. Tachiki, H. Umezawa, H. Kawarada, *Diam. Relat. Mater.* 12 (2003) 560.
- [689] L. Bocquet, J.L. Barrat, *Phys. Rev. Lett.* 70 (1993) 2726.
- [690] Y. Ando, *Wear* 238 (2000) 12.
- [691] M. Fuji, K. Machida, T. Takei, T. Watanabe, M. Chikazawa, *J. Phys. Chem. B* 102 (1998) 8782.
- [692] A. Ata, Y.I. Rabinovich, R.K. Singh, *J. Adhes. Sci. Technol.* 16 (2002) 337.
- [693] Y.I. Rabinovich, J.J. Adler, M.S. Esayanur, A. Ata, R.K. Singh, B.M. Moudgil, *Adv. Colloid Interf. Sci.* 96 (2002) 213.
- [694] S. Biggs, R.G. Cain, R.R. Dagastine, N.W. Page, *J. Adhes. Sci. Technol.* 16 (2002) 869.
- [695] Y.I. Rabinovich, M.S. Esayanur, K.D. Johanson, J.J. Adler, B.M. Moudgil, *J. Adhes. Sci. Technol.* 16 (2002) 887.
- [696] Z. Wei, Y.P. Zhao, *Chin. Phys. Lett.* 21 (2004) 616.
- [697] A. de Lazzer, M. Dreyer, H.J. Rath, *Langmuir* 15 (1999) 4551.
- [698] T. Stifter, O. Marti, B. Bhushan, *Phys. Rev. B* 62 (2000) 13667.
- [699] L. Sirghi, N. Nakagiri, K. Sugisaki, H. Sugimura, O. Takai, *Langmuir* 16 (2000) 7796.
- [700] D.L. Sedin, K.L. Rowlen, *Anal. Chem.* 72 (2000) 2183.
- [701] L. Sirghi, M. Nakamura, Y. Hatanaka, O. Takai, *Langmuir* 17 (2001) 8199.
- [702] R. Jones, H.M. Pollock, D. Geldart, A. Verlinden, *Powder Technol.* 132 (2003) 196.
- [703] R. Price, P.M. Young, S. Edge, J.N. Staniforth, *Int. J. Pharm.* 246 (2002) 47.
- [704] P.M. Young, R. Price, M.J. Tobby, M. Buttrum, F. Dey, *J. Pharm. Sci.* 92 (2003) 815.
- [705] N.H. Duong, E. Shen, T. Shinbrot, F. Muzzio, *Powder Technol.* 145 (2004) 69.
- [706] T. Thundat, X.Y. Zheng, G.Y. Chen, R.J. Warmack, *Surf. Sci.* 294 (1993) L939.
- [707] J. Hu, X.D. Xiao, D.F. Ogletree, M. Salmeron, *Science* 268 (1995) 267.
- [708] W. Gulbinski, D. Pailhery, T. Suszko, Y. Mathey, *Surf. Sci.* 475 (2001) 149.
- [709] H.K. Christenson, *J. Colloid Interf. Sci.* 104 (1985) 234.
- [710] H.K. Christenson, R.G. Horn, J.N. Israelachvili, *J. Colloid Interf. Sci.* 88 (1982) 79.
- [711] W. van Meegen, I. Snook, *J. Chem. Soc., Faraday Trans. II* 7 (1979) 1095.
- [712] L.A. Rowley, D. Nicholson, N.G. Parsonage, *Mol. Phys.* 31 (1976) 365.
- [713] F.F. Abraham, *J. Chem. Phys.* 68 (1978) 3713.
- [714] D.Y.C. Chan, D.J. Mitchell, B.W. Ninham, B.A. Pailthorpe, *Mol. Phys.* 35 (1978) 1669.
- [715] I.K. Snook, D. Henderson, *J. Chem. Phys.* 68 (1978) 2134.
- [716] J.E. Lane, T.H. Spurling, *Chem. Phys. Lett.* 67 (1979) 107.
- [717] P. Tarazona, L. Vicente, *Mol. Phys.* 56 (1985) 557.
- [718] M. Schoen, T. Gruhn, D.J. Diestler, *J. Chem. Phys.* 109 (1998) 301.
- [719] V.S. Mitlin, M.M. Sharma, *J. Colloid Interf. Sci.* 170 (1995) 407.
- [720] P. Padilla, S. Toxvaerd, *J. Chem. Phys.* 101 (1994) 1490.
- [721] R.K. Ballamudi, I.A. Bitsanis, *J. Chem. Phys.* 105 (1996) 7774.
- [722] M. Dijkstra, *Thin Solid Films* 330 (1998) 14.
- [723] M. Iwamatsu, *J. Colloid Interf. Sci.* 204 (1998) 374.
- [724] A.K. Doerr, M. Tolan, T. Seydel, W. Press, *Physica B* 248 (1998) 263.
- [725] C.J. Yu, A.G. Richter, J. Kmetko, A. Datta, P. Dutta, *Europhys. Lett.* 50 (2000) 487.
- [726] R.G. Horn, J.N. Israelachvili, *J. Chem. Phys.* 75 (1981) 1400.
- [727] H.K. Christenson, *J. Chem. Phys.* 78 (1983) 6906.
- [728] J. Schneider, Y.F. Dufrêne, W.R. Barger, G.U. Lee, *Biophys. J.* 79 (2000) 1107.
- [729] H. Mueller, H.-J. Butt, E. Bamberg, *J. Phys. Chem.* 104 (2000) 4552.
- [730] Y.F. Dufrêne, T. Boland, J.W. Schneider, W.R. Barger, G.U. Lee, *Faraday Discuss.* 111 (1998) 79.
- [731] J. Rädler, M. Radmacher, H.E. Gaub, *Langmuir* 10 (1994) 3111.
- [732] I. Burgess, C.A. Jeffrey, X. Cai, G. Szymanski, Z. Galus, J. Lipkowski, *Langmuir* 15 (1999) 2607.
- [733] W.A. Ducker, D.R. Clarke, *Colloids Surf. A* 94 (1994) 275.

- [734] S. Manne, J.P. Cleveland, H.E. Gaub, G.D. Stucky, P.K. Hansma, *Langmuir* 10 (1994) 4409.
- [735] M. Jaschke, H.-J. Butt, H.E. Gaub, S. Manne, *Langmuir* 13 (1997) 1381.
- [736] J.L. Wolgemuth, R.K. Workman, S. Manne, *Langmuir* 16 (2000) 3077.
- [737] W.J. Lokar, W.A. Ducker, *Langmuir* 20 (2004) 4553.
- [738] I. Pera, R. Stark, M. Kappl, H.-J. Butt, F. Benfenati, *Biophys. J.* 87 (2004) 2446.
- [739] P.G. de Gennes, *Langmuir* 6 (1990) 1448.
- [740] P. Richetti, L. Moreau, P. Barois, P. Kékicheff, *Phys. Rev. E* 54 (1996) 1749.
- [741] K. Kocevar, R. Blinc, I. Musevic, *Phys. Rev. E* 62 (2000) 3055.
- [742] S.J. O'Shea, M.E. Welland, T. Rayment, *Appl. Phys. Lett.* 60 (1992) 2356.
- [743] D.L. Klein, P.L. McEuen, *Appl. Phys. Lett.* 66 (1995) 2478.
- [744] S.J. O'Shea, M.E. Welland, *Langmuir* 14 (1998) 4186.
- [745] H. Shinto, M. Miyahara, K. Higashitani, *Langmuir* 16 (2000) 3361.
- [746] R. Lim, S.J. O'Shea, *Phys. Rev. Lett.* 88 (2002) 246101.
- [747] W. Han, S.M. Lindsay, *Appl. Phys. Lett.* 72 (1998) 1656.
- [748] R. Nishi, K. Kitano, I. Yi, Y. Sugawara, S. Morita, *Appl. Surf. Sci.* (2004) 654.
- [749] T. Nakada, S. Miyashita, G. Sazaki, H. Komatsu, A.A. Chernov, *Jpn. J. Appl. Phys.* 35 (1996) L52.
- [750] Y. Kanda, S. Iwasaki, K. Higashitani, *J. Colloid Interf. Sci.* 216 (1999) 394.
- [751] V. Franz, H.-J. Butt, *J. Phys. Chem. B* 106 (2002) 1703.
- [752] V. Mollica, A. Relini, R. Rolandi, M. Bolognesi, A. Gliozzi, *Eur. Phys. J. E* 3 (2000) 315.
- [753] H.-J. Butt, V. Franz, *Phys. Rev. E* 66 (2002) 031601.
- [754] V. Franz, S. Loi, H. Müller, E. Bamberg, H.-J. Butt, *Colloids Surf. B* 23 (2002) 191.
- [755] S. Loi, G.X. Sun, V. Franz, H.-J. Butt, *Phys. Rev. E* 66 (2002) 031602.
- [756] K.L. Johnson, *Contact Mechanics*, Cambridge University Press, Cambridge, 1985.
- [757] H.-J. Galla, W. Hartmann, U. Theilen, E. Sackmann, *J. Membr. Biol.* 48 (1979) 215.
- [758] L.K. Tamm, Z. Shao, in: P.I. Haris, D. Chapman (Eds.), *Biomembrane Structures*, IOS Press, Amsterdam, 1998, p. 169.
- [759] *Langmuir*, J. Franklin Inst. 218 (1934) 143.
- [760] K.B. Blodgett, *J. Am. Chem. Soc.* 57 (1935) 1007.
- [761] T.M. Bayerl, M. Bloom, *Biophys. J.* 58 (1990) 357.
- [762] G. Puu, I. Gustafson, *Biochim. Biophys. Acta* 1327 (1997) 149.
- [763] E. Reimhult, F. Höök, B. Kasemo, *Langmuir* 19 (2003) 1681.
- [764] S. Lingler, I. Rubinstein, W. Knoll, A. Offenhäuser, *Langmuir* 13 (1997) 7085.
- [765] A.T.A. Jenkins, T. Neumann, A. Offenhäuser, *Langmuir* 17 (2001) 265.
- [766] R.G. Horn, *Biochim. Biophys. Acta* 778 (1984) 224.
- [767] A.A. Brian, H.M. McConnell, *Proc. Natl. Acad. Sci. U.S.A.* 81 (1984) 6159.
- [768] L.K. Tamm, E. Kalb, in: S.G. Schulman (Ed.), *Molecular Luminescence Spectroscopy*, 1993, 253 pp.
- [769] J. Schneider, W. Barger, G.U. Lee, *Langmuir* 19 (2003) 1899.
- [770] R.P. Richter, A. Brisson, *Langmuir* 19 (2003) 1632.
- [771] L.M. Grant, F. Tiberg, *Biophys. J.* 82 (2002) 1373.
- [772] S. Künnecke, D. Krüger, A. Janshoff, *Biophys. J.* 86 (2004) 1545.
- [773] Z.V. Leonenko, E. Finot, H. Ma, T.E.S. Dahms, D.T. Cramb, *Biophys. J.* 86 (2004) 3783.
- [774] D.M. LeNeveu, R.P. Rand, V.A. Parsegian, D. Gingell, *Biophys. J.* 18 (1977) 209.
- [775] S. Nir, M. Andersen, *J. Membr. Biol.* 31 (1977) 1.
- [776] L.J. Lis, M. McAlister, N. Fuller, R.P. Rand, V.A. Parsegian, *Biophys. J.* 37 (1982) 657.
- [777] J. Marra, J.N. Israelachvili, *Biochemistry* 24 (1985) 4608.
- [778] P.K.T. Persson, B.A. Bergenstrahl, *Biophys. J.* 47 (1985) 743.
- [779] T.J. McIntosh, S.A. Simon, *Colloids Surf. A* 116 (1996) 251.
- [780] E.A.G. Aniansson, S.N. Wall, M. Almgren, H. Hoffman, I. Kielmann, W. Ulbricht, R. Zana, J. Lang, C. Tondre, *J. Phys. Chem.* 80 (1976) 905.
- [781] G.E.A. Aniansson, *J. Phys. Chem.* 82 (1978) 2805.
- [782] E. Evans, D. Needham, *J. Phys. Chem.* 91 (1987) 4219.
- [783] R.M. Servuss, W. Harbich, W. Helfrich, *Biochim. Biophys. Acta* 436 (1976) 900.

- [784] E. Sackmann, H.P. Duwe, H. Engelhardt, *Faraday Discuss. Chem. Soc.* 81 (1986) 281.
- [785] T.J. McIntosh, S. Advani, R.E. Burton, D.V. Zhelev, D. Needham, S.A. Simon, *Biochemistry* 34 (1995) 8520.
- [786] H.I. Petrache, N. Gouliaev, S. Tristram-Nagle, R. Zhang, R.M. Suter, J.F. Nagle, *Phys. Rev. E* 57 (1998) 7014.
- [787] J. Rädler, H. Strey, E. Sackmann, *Langmuir* 11 (1995) 4539.
- [788] N. Maeda, T.J. Senden, J.M. di Meglio, *Biochim. Biophys. Acta* 1564 (2002) 165.
- [789] R.M. Hochmuth, N. Mohandas, P.L. Blackshear, *Biophys. J.* 13 (1973) 747.
- [790] J. Dai, M.P. Sheetz, *Biophys. J.* 68 (1995) 988.
- [791] R.M. Hochmuth, E.A. Evans, *Biophys. J.* 39 (1982) 71.
- [792] X.M. Liang, G.Z. Mao, K.Y.S. Ng, *Colloids Surf. B* 34 (2004) 41.
- [793] S. Manne, H.E. Gaub, *Science* 270 (1995) 1480.
- [794] E.J. Wanless, W.A. Ducker, *J. Phys. Chem.* 100 (1996) 3207.
- [795] W.A. Ducker, L.M. Grant, *J. Phys. Chem.* 100 (1996) 11507.
- [796] W.A. Ducker, E.J. Wanless, *Langmuir* 12 (1996) 5915.
- [797] R.E. Lamont, W.A. Ducker, *J. Am. Chem. Soc.* 120 (1998) 7602.
- [798] W.A. Ducker, E.J. Wanless, *Langmuir* 15 (1999) 160.
- [799] O. Teschke, G. Ceotto, E.F. de Souza, *Appl. Phys. Lett.* 78 (2001) 3064.
- [800] C.H. See, J.H. O'Haver, *Colloids Surf. A* 243 (2004) 169.
- [801] J.F. Liu, G. Min, W.A. Ducker, *Langmuir* 17 (2001) 4895.
- [802] I.A. Aksay, M. Trau, S. Manne, I. Honma, N. Yao, L. Zhou, P. Fenter, P.M. Eisenberger, S.M. Gruner, *Science* 273 (1996) 892.
- [803] A. Blom, C. Drummond, E.J. Wanless, P. Richetti, G.G. Warr, *Langmuir* 21 (2005) 2779.
- [804] R. Atkin, V.S.J. Craig, S. Biggs, *Langmuir* 17 (2001) 6155.
- [805] L.M. Grant, W.A. Ducker, *J. Phys. Chem. B* 101 (1997) 5337.
- [806] S. Manne, T.E. Schäffer, Q. Huo, P.K. Hansma, D.E. Morse, G.D. Stucky, I.A. Aksay, *Langmuir* 13 (1997) 6382.
- [807] L.M. Grant, F. Tiberg, W.A. Ducker, *J. Phys. Chem. B* 102 (1998) 4288.
- [808] H.N. Patrick, G.G. Warr, S. Manne, I.A. Aksay, *Langmuir* 13 (1997) 4349.
- [809] J. Dong, G. Mao, *Langmuir* 16 (2000) 6641.
- [810] N.B. Holland, M. Ruegsegger, R.E. Marchant, *Langmuir* 14 (1998) 2790.
- [811] S. Veeramuneni, M.L. Free, J.D. Miller, J. Adhes. Sci. Technol. 12 (1998) 185.
- [812] V. Subramanian, W. Ducker, *J. Phys. Chem. B* 105 (2001) 1389.
- [813] W.J. Lokar, W.A. Ducker, *Langmuir* 18 (2002) 3167.
- [814] I.U. Vakarelski, S.C. Brown, Y.I. Rabinovich, B.M. Moudgil, *Langmuir* 20 (2004) 1724.
- [815] W.J. Lokar, W.A. Ducker, *Langmuir* 20 (2004) 378.
- [816] D.G. Hall, *J. Chem. Soc., Faraday Trans. II* 68 (1972) 2169.
- [817] S.G. Ash, D.H. Everett, C. Radke, *J. Chem. Soc., Faraday Trans. II* 68 (1973) 1256.
- [818] B.A. Pethica, *Colloids Surf. A* 105 (1995) 257.
- [819] Y. Kanda, T. Higuchi, K. Higashitani, *Adv. Powder Technol.* 12 (2001) 577.
- [820] J. Klein, P.F. Luckham, *Macromolecules* 17 (1984) 1041.
- [821] J.N. Israelachvili, M. Tirrell, J. Klein, Y. Almog, *Macromolecules* 17 (1984) 204.
- [822] J. Marra, H.K. Christenson, *J. Phys. Chem.* 93 (1989) 7180.
- [823] R.G. Horn, S.J. Hirz, G. Hadziioannou, C.W. Frank, J.M. Catala, *J. Chem. Phys.* 90 (1989) 6767.
- [824] V. Bergeron, P.M. Claesson, *Adv. Colloid Interf. Sci.* 96 (2002) 1.
- [825] E.P.K. Currie, W. Norde, M.A. Cohen Stuart, *Adv. Colloid Interf. Sci.* 100–102 (2003) 205.
- [826] S. Alexander, *J. Phys. (Paris)* 38 (1977) 983.
- [827] P.G. de Gennes, *Adv. Colloid Interf. Sci.* 27 (1987) 189.
- [828] S.J. O'Shea, M.E. Welland, T. Rayment, *Langmuir* 9 (1993) 1826.
- [829] S. Milner, T. Witten, M. Cates, *Europhys. Lett.* 5 (1988) 413.
- [830] S.T. Milner, T.A. Witten, M.E. Cates, *Macromolecules* 21 (1988) 2610.
- [831] N.V. Efremova, B. Bondurant, D.F. O'Brien, D.E. Leckband, *Biochemistry* 39 (2000) 3441.
- [832] S.C. McLean, H. Lioe, L. Meagher, V.S.J. Craig, M.L. Gee, *Langmuir* 21 (2005) 2199.
- [833] H.-J. Butt, M. Kappl, H. Müller, R. Raiteri, W. Meyer, J. Rühle, *Langmuir* 15 (1999).

- [834] T.W. Kelley, P.A. Schorr, K.D. Johnson, M. Tirrell, C.D. Frisbie, *Macromolecules* 31 (1998) 4297.
- [835] R.M. Overney, D.P. Leta, C.F. Pictroski, M.H. Rafailovich, Y. Liu, J. Quinn, J. Sokolov, A. Eisenberg, G. Overney, *Phys. Rev. Lett.* 76 (1996) 1272.
- [836] M. Musoke, P.F. Luckham, *J. Colloid Interf. Sci.* 277 (2004) 62.
- [837] A.K. Dolan, S.F. Edwards, *Proc. R. Soc. London A* 337 (1974) 509.
- [838] J. Jimenez, R. Rajagopalan, *Langmuir* 14 (1998) 2598.
- [839] M.C. Guffond, D.R.M. Williams, E.M. Sevick, *Langmuir* 13 (1997) 5691.
- [840] A. Milchev, V. Yamakov, K. Binder, *Europhys. Lett.* 47 (1999) 675.
- [841] A. Milchev, V. Yamakov, K. Binder, *Phys. Chem. Chem. Phys.* 1 (1999) 2083.
- [842] G. Subramanian, D.R.M. Williams, P.A. Pincus, *Europhys. Lett.* 29 (1995) 285.
- [843] M. Murat, G.S. Grest, *Macromolecules* 29 (1996) 8282.
- [844] T.J. Senden, J.M. Di Meglio, I. Silberzan, *CR Acad. Sci. Ser. IV: Phys. Astrophys.* 1 (2000) 1143.
- [845] G. Sun, H.-J. Butt, *Macromolecules* 37 (2004) 6086.
- [846] S.M. Notley, S. Biggs, V.S.J. Craig, *Macromolecules* 36 (2003) 2903.
- [847] M. Giesbers, J.M. Kleijn, G.J. Fleer, M.A. Cohen Stuart, *Colloids Surf. A* 142 (1998) 343.
- [848] S.D. Gurumayum Sharma, D. Moreton, B. Vincent, *J. Colloid Interf. Sci.* 263 (2003) 343.
- [849] M. Morra, C. Cassinelli, G. Cascardo, P. Cahalan, L. Cahalan, M. Fini, R. Giardino, *Biomaterials* 24 (2003) 4639.
- [850] H.G. Brown, J.H. Hoh, *Biochemistry* 36 (1997) 15035.
- [851] S.J. Miklavcic, R.G. Horn, D.J. Bachmann, *J. Phys. Chem.* 99 (1995) 16357.
- [852] D.J. Bachmann, S.J. Miklavcic, *Langmuir* 12 (1996) 4197.
- [853] M.L. Fielden, R.A. Hayes, J. Ralston, *Langmuir* 12 (1996) 3721.
- [854] G. Gillies, C.A. Prestidge, P. Attard, *Langmuir* 17 (2001) 7955.
- [855] R.R. Dagastine, D.C. Prieve, L.R. White, *J. Colloid Interf. Sci.* 269 (2004) 84.
- [856] P. Attard, S.J. Miklavcic, *Langmuir* 17 (2001) 8217.
- [857] P. Attard, S.J. Miklavcic, *J. Colloid Interf. Sci.* 247 (2002) 255.
- [858] P. Attard, S.J. Miklavcic, *Langmuir* 19 (2003) 2532.
- [859] D.Y.C. Chan, R.R. Dagastine, L.R. White, *J. Colloid Interf. Sci.* 236 (2001) 141.
- [860] T.D. Blake, J.A. Kitchene, *J. Chem. Soc., Faraday Trans. I* 68 (1972) 1435.
- [861] H.J. Schulze, *Colloid Polym. Sci.* 253 (1975) 730.
- [862] M.P. Aronson, H.M. Princen, *Colloid Polym. Sci.* 256 (1978) 140.
- [863] G. Gillies, M. Kappl, H.J. Butt, *Adv. Colloid Interf. Sci.*, in press.
- [864] M. Preuss, H.-J. Butt, *Int. J. Miner. Process.* 56 (1999) 99.
- [865] M. Preuss, H.-J. Butt, *J. Colloid Interf. Sci.* 208 (1998) 468.
- [866] S. Ecke, M. Preuss, H.-J. Butt, *J. Adhes. Sci. Technol.* 13 (1999) 1181.
- [867] S. Usui, H. Sasaki, H. Matsukawa, *J. Colloid Interf. Sci.* 81 (1981) 80.
- [868] R.H. Yoon, J.L. Yordan, *J. Colloid Interf. Sci.* 113 (1986) 430.
- [869] P. Saulnier, J. Lachaise, G. Morel, A. Graciaa, *J. Colloid Interf. Sci.* 182 (1996) 395.
- [870] H.J. Schulze, C. Cichos, *Z. Phys. Chem. Leipzig* 251 (1972) 252.
- [871] L.G.T. Eriksson, P.M. Claesson, J.C. Eriksson, V.V. Yaminsky, *J. Colloid Interf. Sci.* 181 (1996) 476.
- [872] P. Mulvaney, J.M. Perera, S. Biggs, F. Grieser, G.W. Stevens, *J. Colloid Interf. Sci.* 183 (1996) 614.
- [873] B.A. Snyder, D.E. Aston, J.C. Berg, *Langmuir* 13 (1997) 590.
- [874] G.E. Yakubov, O.I. Vinogradova, H.-J. Butt, *J. Adhes. Sci. Technol.* 14 (2000) 1783.
- [875] P.G. Hartley, F. Grieser, P. Mulvaney, G.W. Stevens, *Langmuir* 15 (1999) 7282.
- [876] A.D. Scheludko, A.D. Nikolov, *Colloid Polym. Sci.* 253 (1975) 396.
- [877] E. Bayramli, C. Huh, S.G. Mason, *Can. J. Chem.* 56 (1978) 818.
- [878] R. Gunde, S. Hartland, R. Mäder, *J. Colloid Interf. Sci.* 176 (1995) 17.
- [879] L. Zhang, L. Ren, S. Hartland, *J. Colloid Interf. Sci.* 180 (1996) 493.
- [880] A. Scheludko, B.V. Toshev, D.T. Bojadjev, *J. Chem. Soc., Faraday Trans. I* 72 (1976) 2815.
- [881] A.V. Nguyen, J. Nalaskowski, J.D. Miller, *J. Colloid Interf. Sci.* 262 (2003) 303.
- [882] N.D. Wangsa-Wirawan, A. Ikai, B.K. O'Neill, A.P.J. Middelberg, *Biotechnol. Prog.* 17 (2001) 963.
- [883] A.V. Nguyen, J. Nalaskowski, J.D. Miller, *Miner. Eng.* 16 (2003) 1173.

- [884] G. Gillies, K. Buscher, M. Preuss, M. Kappl, H.J. Butt, K. Graf, *J. Phys.: Condens. Matter* 17 (2005) S445.
- [885] G. Decher, *Science* 277 (1997) 1232.
- [886] E. Donath, G.B. Sukhorukov, F. Caruso, S.A. Davis, H. Mohwald, *Angew. Chem. Int. Ed.* 37 (1998) 2202.
- [887] G.B. Sukhorukov, E. Donath, H. Lichtenfeld, E. Knippel, M. Knippel, A. Budde, H. Mohwald, *Colloids Surf. A* 137 (1998) 253.
- [888] C.Y. Gao, E. Donath, H. Mohwald, J.C. Shen, *Angew. Chem. Int. Ed.* 41 (2002) 3789.
- [889] C. Gao, E. Donath, S. Moya, V. Dudnik, H. Mohwald, *Eur. Phys. J. E* 5 (2001) 21.
- [890] O.I. Vinogradova, D. Andrienko, V.V. Lulevich, S. Nordschild, G.B. Sukhorukov, *Macromolecules* 37 (2004) 1113.
- [891] X. Arys, A. Jonas, A. Laschewsky, R. Legras, in: A. Ciferri (Ed.), New York, 2000, 505 pp.
- [892] F. Dubreuil, N. Elsner, A. Fery, *Eur. Phys. J. E* 12 (2003) 215.
- [893] O.I. Vinogradova, O.V. Lebedeva, K. Vasilev, H.F. Gong, J. Garcia-Turiel, B.S. Kim, *Biomacromolecules* 6 (2005) 1495.
- [894] V.V. Lulevich, D. Andrienko, O.I. Vinogradova, *J. Chem. Phys.* 120 (2004) 3822.
- [895] O.I. Vinogradova, *J. Phys.: Condens. Matter* 16 (2004) R1105.
- [896] V.V. Lulevich, I.L. Radtchenko, G.B. Sukhorukov, O.I. Vinogradova, *J. Phys. Chem. B* 107 (2003) 2735.
- [897] V.V. Lulevich, O.I. Vinogradova, *Langmuir* 20 (2004) 2874.
- [898] G.B. Sukhorukov, D.G. Shchukin, W.F. Dong, H. Mohwald, V.V. Lulevich, O.I. Vinogradova, *Macromol. Chem. Phys.* 205 (2004) 530.
- [899] O.V. Lebedeva, B.S. Kim, K. Vasilev, O.I. Vinogradova, *J. Colloid Interf. Sci.* 284 (2005) 455.
- [900] V.V. Lulevich, S. Nordschild, O.I. Vinogradova, *Macromolecules* 37 (2004) 7736.
- [901] V.V. Lulevich, I.L. Radtchenko, G.B. Sukhorukov, O.I. Vinogradova, *Macromolecules* 36 (2003) 2832.
- [902] O.V. Lebedeva, L.S. Kim, O.I. Vinogradova, *Langmuir* 20 (2004) 10685.
- [903] K.D. Costa, *Disease Markers* 19 (2003) 139.
- [904] M. Radmacher, *Atomic Force Microscopy in Cell Biology*, 2002 67 pp.
- [905] N.O. Petersen, W.B. McConnaughey, E.L. Elson, *Proc. Natl. Acad. Sci. U.S.A.* 79 (1982) 5327.
- [906] M. Sato, M.J. Levesque, R.M. Nerem, *Arteriosclerosis* 7 (1987) 276.
- [907] E. Evans, A. Yeung, *Biophys. J.* 56 (1989) 151.
- [908] S.C. Kuo, M.P. Sheetz, *Trends Cell Biol.* 2 (1992) 116.
- [909] F.H.C. Crick, A.F.W. Hughes, *Exp. Cell Res.* 1 (1949) 37.
- [910] F. Amblard, B. Yurke, A. Pargellis, S. Leibler, *Rev. Sci. Instrum.* 67 (1996) 818.
- [911] A.R. Bausch, F. Ziemann, A.A. Boulbitch, K. Jacobson, E. Sackmann, *Biophys. J.* 75 (1998) 2038.
- [912] J. Bereiterhahn, *J. Microsc. (Oxford)* 146 (1987) 29.
- [913] T. Kundu, J. Bereiterhahn, K. Hillmann, *Biophys. J.* 59 (1991) 1194.
- [914] N.J. Tao, S.M. Lindsay, S. Lees, *Biophys. J.* 63 (1992) 1165.
- [915] A.L. Weisenhorn, M. Khorsandi, S. Kasas, V. Gotzos, H.-J. Butt, *Nanotechnology* 4 (1993) 106.
- [916] M. McElfresh, E. Baesu, R. Balhorn, J. Belak, M.J. Allen, R.E. Rudd, *Proc. Natl. Acad. Sci. U.S.A.* 99 (2002) 6493.
- [917] T. Ohashi, Y. Ishii, Y. Ishikawa, T. Matsumoto, M. Sato, *BioMed. Mater. Eng.* 12 (2002) 319.
- [918] X. Yao, J. Walter, S. Burke, S. Stewart, M.H. Jericho, D. Pink, R. Hunter, T.J. Beveridge, *Colloids Surf. B* 23 (2002) 213.
- [919] L. Scheffer, A. Bitler, E. Ben-Jacob, R. Korenstein, *Eur. Biophys. J. Biophys. Lett.* 30 (2001) 83.
- [920] W. Karunasena, C.M. Wang, S. Kitipornchai, Y. Xiang, *Comput. Struct.* 63 (1997) 455.
- [921] A. Hategan, R. Law, S. Kahn, D.E. Discher, *Biophys. J.* 85 (2003) 2746.
- [922] J.H. Hoh, C.A. Schoenenberger, *J. Cell Sci.* 107 (1994) 1105.
- [923] E. A-Hassan, W.F. Heinz, M.D. Antonik, N.P. D'Costa, S. Nageswaran, C.A. Schoenenberger, J.H. Hoh, *Biophys. J.* 74 (1998) 1564.
- [924] X. Li, B.E. Logan, *Langmuir* 20 (2004) 8817.
- [925] M. Radmacher, M. Fritz, C.M. Kacher, J.P. Cleveland, P.K. Hansma, *Biophys. J.* 70 (1996) 556.
- [926] G.R. Bushell, C. Cahill, F.M. Clarke, C.T. Gibson, S. Myhra, G.S. Watson, *Cytometry* 36 (1999) 254.
- [927] D. Ricci, M. Tedesco, M. Grattarola, *Microsc. Res. Technol.* 36 (1997) 165.
- [928] M. Sugawara, Y. Ishida, H. Wada, *Hearing Res.* 174 (2002) 222.
- [929] A.B. Mathur, A.M. Collinsworth, W.M. Reichert, W.E. Kraus, G.A. Truskey, *J. Biomech.* 34 (2001) 1545.
- [930] A.B. Mathur, G.A. Truskey, W.M. Reichert, *Biophys. J.* 78 (2000) 1725.

- [931] A. Simon, T. Cohen-Bouhacina, M.C. Porte, J.P. Aime, J. Amedee, R. Bareille, C. Baquey, *Cytometry, Part A* 54A (2003) 36.
- [932] M. Lekka, P. Laidler, D. Gil, J. Lekki, Z. Stachura, A.Z. Hryniewicz, *Eur. Biophys. J. Biophys. Lett.* 28 (1999) 312.
- [933] M. Lekka, P. Laidler, J. Ignacak, M. Labeledz, J. Lekki, H. Struszczyk, Z. Stachura, A.Z. Hryniewicz, *Biochim. Biophys. Acta Mol. Cell Res.* 1540 (2001) 127.
- [934] H.-J. Butt, E. Wolff, S.A.C. Gould, P.K. Hansma, *J. Struct. Biol.* 105 (1990) 54.
- [935] F. Braet, C. Rotsch, E. Wisse, M. Radmacher, *Appl. Phys. A* 66 (1998) S575.
- [936] S.B. Velegol, B.E. Logan, *Langmuir* 18 (2002) 5256.
- [937] C. Rotsch, F. Braet, E. Wisse, M. Radmacher, *Cell Biol. Int.* 21 (1997) 685.
- [938] H.W. Wu, T. Kuhn, V.T. Moy, *Scanning* 20 (1998) 389.
- [939] S.G. Shroff, D.R. Saner, R. Lal, *Am. J. Physiol. Cell Physiol.* 38 (1995) C286.
- [940] S.C. Lieber, N. Aubry, J. Pain, G. Diaz, S.J. Kim, S.F. Vatner, *Am. J. Physiol. Heart Circul. Physiol.* 287 (2004) H645.
- [941] M. Nagayama, H. Haga, M. Takahashi, T. Saitoh, K. Kawabata, *Exp. Cell Res.* 300 (2004) 396.
- [942] A.M. Collinsworth, S. Zhang, W.E. Kraus, G.A. Truskey, *Am. J. Physiol. Cell Physiol.* 283 (2002) C1219.
- [943] J.A. Dvorak, E. Nagao, *Exp. Cell Res.* 242 (1998) 69.
- [944] M. Sato, K. Nagayama, N. Kataoka, M. Sasaki, K. Hane, *J. Biomech.* 33 (2000) 127.
- [945] K. Bhadriraju, L.K. Hansen, *Exp. Cell Res.* 278 (2002) 92.
- [946] N. Kataoka, K. Iwaki, K. Hashimoto, S. Mochizuki, Y. Ogasawara, M. Sato, K. Tsujioka, F. Kajiya, *Proc. Natl. Acad. Sci. U.S.A.* 99 (2002) 15638.
- [947] A. da Silva, O. Teschke, *Biochim. Biophys. Acta Mol. Cell Res.* 1643 (2003) 95.
- [948] I.B. Beech, J.R. Smith, A.A. Steele, I. Penegar, S.A. Campbell, *Colloids Surf. B* 23 (2002) 231.
- [949] H.J. Busscher, A.H. Weerkamp, H.C. van der Mei, A.W.J. van Pelt, H.P. de Jong, J. Arends, *Appl. Environ. Microbiol.* 48 (1984) 980–983.
- [950] V. Vadillo-Rodriguez, H.J. Busscher, W. Norde, J. de Vries, H.C. van der Mei, *J. Bacteriol.* 186 (2004) 6647.
- [951] Y.F. Dufrêne, *Biophys. J.* 78 (2000) 3286.
- [952] C.J.P. Boonaert, P.G. Rouxhet, Y.F. Dufrêne, *Surf. Interf. Anal.* 30 (2000) 32.
- [953] Y.F. Dufrêne, C.J.P. Boonaert, P.A. Gerin, M. Asther, P.G. Rouxhet, *J. Bacteriol.* 181 (1999) 5350.
- [954] R.F. Considine, D.R. Dixon, C.J. Drummond, *Langmuir* 16 (2000) 1323.
- [955] R.F. Considine, D.R. Dixon, C.J. Drummond, *Water Res.* 36 (2002) 3421.
- [956] R.F. Considine, C.J. Drummond, D.R. Dixon, *Langmuir* 17 (2001) 6325.
- [957] N.I. Abu-Lail, T.A. Camesano, *Environ. Sci. Technol.* 37 (2003) 2173.
- [958] N.I. Abu-Lail, T.A. Camesano, *Biomacromolecules* 4 (2003) 1000.
- [959] M.J. Higgins, P. Molino, P. Mulvaney, R. Wetherbee, *J. Phycol.* 39 (2003) 1181.
- [960] M.J. Higgins, J.E. Sader, P. Mulvaney, R. Wetherbee, *J. Phycol.* 39 (2003) 722.
- [961] A. Mendez-Vilas, A.M. Gallardo-Moreno, M.L. Gonzalez-Martin, R. Calzado-Montero, M.J. Nuevo, J.M. Bruque, C. Perez-Giraldo, *Appl. Surf. Sci.* 238 (2004) 18.
- [962] A. Mendez-Vilas, A.M. Gallardo, C. Perez-Giraldo, M.L. Gonzalez-Martin, M.J. Nuevo, *Surf. Interf. Anal.* 31 (2001) 1027.
- [963] A. Mendez-Vilas, I. Corbacho, M.L. Gonzalez-Martin, M.J. Nuevo, *Appl. Surf. Sci.* 238 (2004) 51.
- [964] G.Y. Tang, H.K. Yip, L.P. Samaranyake, K.Y. Chan, G. Luo, H.H.P. Fang, *Arch. Oral Biol.* 49 (2004) 727.
- [965] D. Leckband, *Annu. Rev. Biophys. Biomol. Struct.* 29 (2000) 1.
- [966] C.E. Orsello, D.A. Lauffenburger, D.A. Hammer, *Trends Biotechnol.* 19 (2001) 310.
- [967] G.M.P. Prazeres, E. Batista, W. de Souza, P.M. Bisch, G. Weissmuller, *Exp. Parasitol.* 104 (2003) 40.
- [968] H. Kim, H. Arakawa, T. Osada, A. Ikai, *Appl. Surf. Sci.* 188 (2002) 493.
- [969] H. Kim, H. Arakawa, T. Osada, A. Ikai, *Colloids Surf. B* 25 (2002) 33.
- [970] R.D. Pereira, M.I.N. da Silva, M.A. Cotta, *FEBS Lett.* 552 (2003) 155.
- [971] V. Vadillo-Rodriguez, H.J. Busscher, H.C. van der Mei, J. de Vries, W. Norde, *Colloids Surf. B* 41 (2005) 33.
- [972] V. Vadillo-Rodriguez, H.J. Busscher, W. Norde, J. de Vries, H.C. van der Mei, *Langmuir* 19 (2003) 2372.
- [973] V. Vadillo-Rodriguez, H.J. Busscher, W. Norde, J. de Vries, H.C. van der Mei, *J. Colloid Interf. Sci.* 278 (2004) 251.
- [974] C.J.P. Boonaert, Y.F. Dufrêne, S.R. Derclaye, P.G. Rouxhet, *Colloids Surf. B* 22 (2001) 171.

- [975] V. Vadillo-Rodriguez, H.J. Busscher, W. Norde, J. de Vries, R.J.B. Dijkstra, I. Stokroos, H.C. van der Mei, *Appl. Environ. Microbiol.* 70 (2004) 5541.
- [976] K. Autumn, Y.A. Liang, S.T. Hsieh, W. Zesch, W.P. Chan, T.W. Kenny, R. Fearing, R.J. Full, *Nature* 405 (2000) 681.
- [977] A.B. Kesel, A. Martin, T. Seidl, *J. Exp. Biol.* 206 (2003) 2733.
- [978] M.G. Langer, J.P. Ruppertsberg, S. Gorb, *Proc. R. Soc. London B* 271 (2004) 2209.
- [979] S. Niederegger, S. Gorb, Y.K. Jiao, *J. Comp. Physiol. A: Neuroethol. Sens. Neural. Behav. Physiol.* 187 (2002) 961.
- [980] A. Razatos, Y.L. Ong, M.M. Sharma, G. Georgiou, *Proc. Natl. Acad. Sci. U.S.A.* 95 (1998) 11059–11064.
- [981] A. Razatos, Y.L. Ong, F. Boulay, D.L. Elbert, J.A. Hubbell, M.M. Sharma, G. Georgiou, *Langmuir* 16 (2000) 9155.
- [982] S.K. Lower, C.J. Tadanier, M.F. Hochella, *Geomicrobiol. J.* 18 (2001) 63.
- [983] W.R. Bowen, N. Hilal, R.W. Lovitt, C.J. Wright, *Colloids Surf. A* 136 (1998) 231.
- [984] W.R. Bowen, R.W. Lovitt, C.J. Wright, *J. Colloid Interf. Sci.* 237 (2001) 54.
- [985] W.R. Bowen, R.W. Lovitt, C.J. Wright, *Colloids Surf. A* 173 (2000) 205.
- [986] W.R. Bowen, R.W. Lovitt, C.J. Wright, *J. Colloid Interf. Sci.* 228 (2000) 428.
- [987] A. Hanna, M. Berg, V. Stout, A. Razatos, *Appl. Environ. Microbiol.* 69 (2003) 4474.
- [988] F.T. Arce, R. Avci, I.B. Beech, K.E. Cooksey, B. Wigglesworth-Cooksey, *Biophys. J.* 87 (2004) 4284.
- [989] T.A. Doneva, H.B. Yin, P. Stephens, W.R. Bowen, D.W. Thomas, *Spectr. Int. J.* 18 (2004) 587.
- [990] W.R. Bowen, A.S. Fenton, R.W. Lovitt, C.J. Wright, *Biotechnol. Bioeng.* 79 (2002) 170.
- [991] R.J. Emerson, T.A. Camesano, *Appl. Environ. Microbiol.* 70 (2004) 6012.
- [992] F. Ahimou, L.P. Mok, B. Bardot, C. Wesley, *J. Cell Biol.* 167 (2004) 1217.
- [993] X.H. Zhang, A. Chen, D. De Leon, H. Li, E. Noiri, V.T. Moy, M.S. Goligorsky, *Am. J. Physiol. Heart Circul. Physiol.* 286 (2004) H359.
- [994] J.N. Israelachvili, P.M. McGuiggan, H.M. Homola, *Science* 240 (1988) 189.
- [995] M.L. Gee, P.M. McGuiggan, J.N. Israelachvili, A.M. Homola, *J. Chem. Phys.* 93 (1990) 1895.
- [996] E. Kumacheva, J. Klein, *J. Chem. Phys.* 108 (1998) 7010.
- [997] A.L. Demirel, S. Granick, *J. Chem. Phys.* 115 (2001) 1498.
- [998] I. Bitsanis, T.K. Vanderlick, M. Tirrell, H.T. Davis, *J. Chem. Phys.* 89 (1988) 3152.
- [999] M. Schoen, C.L. Rhykerd, D.J. Diestler, J.H. Cushman, *Science* 245 (1989) 1223.
- [1000] P.A. Thompson, G.S. Grest, M.O. Robbins, *Phys. Rev. Lett.* 68 (1992) 3448.
- [1001] J.N. Israelachvili, *J. Colloid Interf. Sci.* 110 (1986) 263.
- [1002] U. Raviv, P. Laurat, J. Klein, *Nature* 413 (2001) 51.
- [1003] W.J. Huisman, J.F. Peters, M.J. Zwanenburg, S.A. de Vries, T.E. Derry, D. Abernathy, J.F. van der Veen, *Nature* 390 (1997) 379.
- [1004] J. van Alsten, S. Granick, *Phys. Rev. Lett.* 61 (1988) 2570.
- [1005] A.M. Homola, J.N. Israelachvili, P.M. McGuiggan, M.L. Gee, *Wear* 136 (1990) 65.
- [1006] J. Gao, W.D. Luedtke, U. Landman, *Phys. Rev. Lett.* 79 (1997) 705.
- [1007] J.J. Benbow, P. Lamb, *SPE Trans.* 3 (1963) 7.
- [1008] M.M. Denn, *Annu. Rev. Fluid Mech.* 22 (1990) 13.
- [1009] O.I. Vinogradova, *Int. J. Miner. Process.* 56 (1999) 31.
- [1010] R. Pit, H. Hervet, L. Léger, *Phys. Rev. Lett.* 85 (2000) 980.
- [1011] J. Baudry, E. Charlaix, A. Tonck, D. Mazuyer, *Langmuir* 17 (2001) 5232.
- [1012] D.C. Trethewey, C.D. Meinhart, *Phys. Fluids* 14 (2002) L9.
- [1013] R.G. Horn, O.I. Vinogradova, M.E. Mackay, N. Phan-Thien, *J. Chem. Phys.* 112 (2000) 6424.
- [1014] J.T. Cheng, N. Giordano, *Phys. Rev. E* 65 (2002) 031206.
- [1015] J.C. Maxwell, *Phil. Trans. R. Soc. London Ser. A* 170 (1867) 231.
- [1016] M. Sun, C. Ebner, *Phys. Rev. Lett.* 69 (1992) 3491.
- [1017] P.A. Thompson, S.M. Troian, *Nature* 389 (1997) 360.
- [1018] M.J. Stevens, M. Mondello, G.S. Grest, S.T. Cui, H.D. Cochran, P.T. Cummings, *J. Chem. Phys.* 106 (1997) 7303.
- [1019] J.L. Barrat, L. Bocquet, *Phys. Rev. Lett.* 82 (1999) 4671.
- [1020] J. Gao, W.D. Luedtke, U. Landman, *Tribol. Lett.* 9 (2000) 3.
- [1021] P.A. Durbin, *J. Fluid Mech.* 197 (1988) 157.
- [1022] C. Cottin-Bizonne, S. Jurine, J. Baudry, J. Crassous, F. Restagno, E. Charlaix, *Eur. Phys. J. E* 9 (2002) 47.

- [1023] H. Brenner, *Chem. Eng. Sci.* 16 (1961) 242.
- [1024] R.G. Cox, *Int. J. Multiphase Flow* 1 (1974) 343.
- [1025] P. Fontaine, P. Guenoun, J. Daillant, *Rev. Sci. Instrum.* 68 (1997) 4145–4151.
- [1026] F. Benmouna, D. Johannsmann, *Eur. Phys. J. E* 9 (2002) 435.
- [1027] O.I. Vinogradova, *Langmuir* 11 (1995) 2213.
- [1028] P.J. Feibelman, *Langmuir* 20 (2004) 1239.
- [1029] J.S. Ellis, M. Thompson, *Phys. Chem. Chem. Phys.* 6 (2004) 4928.
- [1030] C. Neto, D.R. Evans, V.S.J. Craig, H.-J. Butt, *Rev. Mod. Phys.* (2005).
- [1031] V.S.J. Craig, C. Neto, D.R.M. Williams, *Phys. Rev. Lett.* 87 (2001) 4504.
- [1032] E. Bonaccorso, H.-J. Butt, V. Craig, *Phys. Rev. Lett.* 90 (2003) 144501.
- [1033] G. Sun, E. Bonaccorso, V. Franz, H.-J. Butt, *J. Chem. Phys.* 117 (2002) 10311.
- [1034] O.I. Vinogradova, G.E. Yakubov, *Langmuir* 19 (2003) 1227.
- [1035] H.W. Hu, G.A. Carson, S. Granick, *Phys. Rev. Lett.* 66 (1991) 2758.
- [1036] G. Luengo, J.N. Israelachvili, S. Granick, *Wear* 200 (1996) 328.
- [1037] Y. Zhu, S. Granick, *Phys. Rev. Lett.* 87 (2001) 096105.
- [1038] C. Cheikh, G. Koper, *Phys. Rev. Lett.* 91 (2003) 156102.
- [1039] C.H. Choi, J.A. Westin, K.S. Breuer, *Phys. Fluids* 15 (2003) 2897.
- [1040] M.O. Robbins, P.A. Thompson, G.S. Grest, *MRS Bull.* (1993) 45.
- [1041] S.A. Gupta, H.D. Cochran, P.T. Cummings, *J. Chem. Phys.* 107 (1997) 10316.
- [1042] B.C. Eu, *Phys. Rev. A* 36 (1987) 400.
- [1043] Y. Rabin, I. Hersht, *Physica A* 200 (1993) 708.
- [1044] C.L. Henry, C. Neta, D.R. Evans, S. Biggs, V.S.J. Craig, *Physica A* 339 (2004) 60.
- [1045] J. Klein, *Annu. Rev. Mater. Sci.* 26 (1996) 581–612.
- [1046] W. Zhang, X. Zhang, *Prog. Polym. Sci.* 28 (2003) 1271.
- [1047] M. Rief, F. Oesterhelt, B. Heymann, H.E. Gaub, *Science* 275 (1997) 1295.
- [1048] J. Fritz, D. Anselmetti, J. Jarchow, X. Fernández-Busquets, *J. Struct. Biol.* 119 (1997) 165.
- [1049] H. Kikuchi, N. Yokoyama, T. Kajiyama, *Chem. Lett.* 11 (1997) 1107.
- [1050] E.L. Florin, V.T. Moy, H.E. Gaub, *Science* 264 (1994) 415.
- [1051] V.T. Moy, E.L. Florin, H.E. Gaub, *Science* 266 (1994) 257.
- [1052] G.U. Lee, L.A. Chrisey, R.J. Colton, *Science* 266 (1994) 771.
- [1053] W. Kuhn, F. Grün, *Kolloid Zeitschrift* 101 (1942) 248.
- [1054] E.F. Casassa, *Polym. Lett.* 5 (1967) 773.
- [1055] M. Fixman, J. Kovac, *J. Chem. Phys.* 58 (1973) 1564.
- [1056] O. Kratky, G. Porod, *Recl. Trav. Chim. Pays-Bas* 68 (1949) 1106.
- [1057] C. Bustamante, J.F. Marko, E.D. Siggia, S. Smith, *Science* 265 (1994) 1599.
- [1058] J.F. Marko, E.D. Siggia, *Macromolecules* 28 (1995) 8759.
- [1059] S.B. Smith, Y. Cui, C. Bustamante, *Science* 271 (1996) 795.
- [1060] T. Odijk, *Macromolecules* 28 (1995) 7016.
- [1061] M.D. Wang, H. Yin, R. Landick, J. Gelles, S.M. Block, *Biophys. J.* 72 (1997) 1335.
- [1062] T.J. Senden, J.M. de Meglio, P. Auroy, *Eur. Phys. J. B* 3 (1998) 211.
- [1063] D. Zhang, C. Ortiz, *Macromolecules* 37 (2004) 4271.
- [1064] J.E. Bemis, B.B. Akhremitchev, G.C. Walker, *Langmuir* 15 (1999) 2799.
- [1065] B.J. Haupt, T.J. Senden, E.M. Sevick, *Langmuir* 18 (2002) 2174.
- [1066] C. Ortiz, G. Hadziioannou, *Macromolecules* 32 (1999) 780.
- [1067] T. Hugel, M. Grosholz, H. Clausen-Schaumann, A. Pfau, H. Gaub, M. Seitz, *Macromolecules* 34 (2001) 1039.
- [1068] S. Zou, Y.J. Ma, M.A. Hempenius, H. Schonherr, G.J. Vancso, *Langmuir* 20 (2004) 6278.
- [1069] H.B. Li, W.K. Zhang, W.Q. Xu, X. Zhang, *Macromolecules* 33 (2000) 465.
- [1070] B.C. van der Aa, R.M. Michel, M. Asther, M.T. Zamora, P.G. Rouxhet, Y.F. Dufrière, *Langmuir* 17 (2001) 3116.
- [1071] N.I. Abu-Lail, T.A. Camesano, *Langmuir* 18 (2002) 4071.
- [1072] W. Zhang, S. Zou, C. Wang, X. Zhang, *J. Phys. Chem. B* 104 (2000) 10258.
- [1073] S. Yamamoto, Y. Tsujii, T. Fukuda, *Macromolecules* 33 (2000) 5995.

- [1074] H. Li, B. Liu, X. Zhang, C. Gao, J. Shen, G. Zou, *Langmuir* 15 (1999) 2120.
- [1075] W.Q. Shi, Z.Q. Wang, S.X. Cui, X. Zhang, Z.S. Bo, *Macromolecules* 38 (2005) 861.
- [1076] W.Q. Shi, S. Cui, C. Wang, L. Wang, X. Zhang, X.J. Wang, L. Wang, *Macromolecules* 37 (2004) 1839.
- [1077] H. Haschke, M.J. Miles, S. Sheppard, *Single Mol.* 2/3 (2002) 171.
- [1078] R. Eckel, R. Ros, A. Ros, S.D. Wilking, N. Sewald, D. Anselmetti, *Biophys. J.* 85 (2003) 1968.
- [1079] H. Clausen-Schaumann, M. Rief, C. Tolksdorf, H.E. Gaub, *Biophys. J.* 78 (2000) 1997.
- [1080] M. Sletmoen, G. Skjak-Braek, B.T. Stokke, *Biomacromolecules* 5 (2004) 1288.
- [1081] M. Bonin, R. Zhu, Y. Klaue, J. Oberstrass, E. Oesterschulze, W. Nellen, *Nucl. Acids Res.* 30 (2002) e81.
- [1082] I. Lee, K. Akiyoshi, *Biomaterials* 25 (2004) 2911.
- [1083] S. Zou, W.K. Zhang, X. Zhang, B.Z. Jiang, *Langmuir* 17 (2001) 4799.
- [1084] A. Ptak, S. Takeda, C. Nakamura, J. Miyake, M. Kageshima, S.P. Jarvis, H. Tokumoto, *J. Appl. Phys.* 90 (2001) 3095.
- [1085] W. Rong, A.E. Pelling, A. Ryan, J.K. Gimzewski, S.K. Friedlander, *Nano Lett.* 4 (2004) 2287.
- [1086] J.G. Forbes, A.J. Jin, K. Wang, *Langmuir* 17 (2001) 3067.
- [1087] A. Noy, D.V. Vezenov, J.F. Kayyem, T.J. Meade, C. Lieber, *Chem. Biol.* 4 (1997) 519.
- [1088] S. Al-Maawali, J.E. Bemis, B.B. Akhremitchev, R. Leecharoen, B. Janesko, G.C. Walker, *J. Phys. Chem. B* 105 (2001) 3965.
- [1089] D. Goodman, J.N. Kizhakkedathu, D.E. Brooks, *Langmuir* 20 (2004) 3297.
- [1090] D. Goodman, J.N. Kizhakkedathu, D.E. Brooks, *Langmuir* 20 (2004) 6238.
- [1091] D.K. Lubensky, D.R. Nelson, *Phys. Rev. Lett.* 85 (2000) 1572.
- [1092] D.K. Lubensky, D.R. Nelson, *Phys. Rev. Lett.* 65 (2002) 31917.
- [1093] R. Krautbauer, M. Rief, H.E. Gaub, *Nano Lett.* 3 (2003) 493.
- [1094] M. Rief, M. Gautel, F. Oesterhelt, J.M. Fernandez, H.E. Gaub, *Science* 276 (1997) 1109.
- [1095] F. Oesterhelt, D. Oesterhelt, M. Pfeiffer, A. Engel, H.E. Gaub, D.J. Müller, *Science* 286 (2000) 143.
- [1096] J.G. Forbes, K. Wang, *J. Vac. Sci. Technol. A* 22 (2004) 1439.
- [1097] A. Kedrov, C. Ziegler, H. Janovjak, W. Kuhlbrandt, D.J. Muller, *J. Mol. Biol.* 340 (2004) 1143.
- [1098] T. Okajima, H. Arakawa, M.T. Alam, H. Sekiguchi, A. Ikai, *Biophys. Chem.* 107 (2004) 51.
- [1099] C. Nemes, J.J. Ramsden, N. Rozlosnik, *Physica A* 313 (2002) 578.
- [1100] T. Wang, H. Arakawa, A. Ikai, *Ultramicroscopy* 91 (2002) 253.
- [1101] J.M. Fernandez, H.B. Li, *Science* 303 (2004) 1674.
- [1102] A.F. Oberhauser, P.K. Hansma, M. Carrion-Vazquez, J.M. Fernandez, *Proc. Natl. Acad. Sci. U.S.A.* 98 (2001) 468.
- [1103] H. Lu, K. Schulten, *Biophys. J.* 79 (2000) 51.
- [1104] M. Rief, M. Gautel, A. Schemmel, H.E. Gaub, *Biophys. J.* 75 (1998) 3008.
- [1105] M. Rief, J. Pascual, M. Saraste, H.E. Gaub, *J. Mol. Biol.* 286 (1999) 553.
- [1106] B. Samorì, G. Zuccheri, P. Baschieri, *Chem. Phys. Chem.* 6 (2005) 29.
- [1107] H. Janovjak, D.J. Muller, A.D.L. Humphris, *Biophys. J.* 88 (2005) 1423.
- [1108] D. Marenduzzo, A. Maritan, A. Rosa, F. Seno, *Eur. Phys. J. E* 15 (2004) 83.
- [1109] M. Grandbois, M. Beyer, M. Rief, H. Clausen-Schaumann, H. Gaub, *Science* 283 (1999) 1727.
- [1110] G.I. Bell, *Science* 200 (1978) 618.
- [1111] E. Evans, K. Ritchie, *Biophys. J.* 72 (1997) 1541.
- [1112] M. Rief, J.M. Fernandez, H.E. Gaub, *Phys. Rev. Lett.* 81 (1998) 4764.
- [1113] U. Seifert, *Phys. Rev. Lett.* 84 (2000) 2750.
- [1114] B. Heymann, H. Grubmüller, *Phys. Rev. Lett.* 84 (2000) 6126.
- [1115] D.F.J. Tees, R.E. Waugh, D.A. Hammer, *Biophys. J.* 80 (2001) 668.
- [1116] S. Zepeda, Y. Yeh, A. Noy, *Langmuir* 19 (2003) 1457.
- [1117] K.L. Brogan, J.H. Shin, M.H. Schoenfish, *Langmuir* 20 (2004) 9729.
- [1118] S. Zapotoczny, T. Auletta, M.R. de Jong, H. Schönherr, J. Huskens, F.C.J.M. van Veggel, D.N. Reinhoudt, G.J. Vancso, *Langmuir* 18 (2002) 6988.
- [1119] F. Schwesinger, R. Ros, T. Strunz, D. Anselmetti, H.J. Guntherodt, A. Honegger, L. Jermutus, L. Tiefenauer, A. Pluckthun, *Proc. Natl. Acad. Sci. U.S.A.* 97 (2000) 9972.
- [1120] Y. Harada, M. Kuroda, A. Ishida, *Langmuir* 16 (2000) 708.
- [1121] X.H. Zhang, D.F. Bogorin, V.T. Moy, *Chem. Phys. Chem.* 5 (2004) 175.

- [1122] X.H. Zhang, V.T. Moy, *Biophys. Chem.* 104 (2003) 271.
- [1123] H. Sekiguchi, H. Arakawa, H. Taguchi, T. Ito, R. Kokawa, A. Ikai, *Biophys. J.* 85 (2003) 484.
- [1124] I. Lee, R.E. Marchant, *Ultramicroscopy* 97 (2003) 341.
- [1125] X.H. Zhang, E. Wojcikiewicz, V.T. Moy, *Biophys. J.* 83 (2002) 2270.
- [1126] M. Micic, I. Benitez, M. Ruano, M. Mavers, M. Jeremic, K. Radotic, V. Moy, R.M. Leblanc, *Chem. Phys. Lett.* 347 (2001) 41.
- [1127] I. Lee, R.E. Marchant, *Surf. Sci.* 491 (2001) 433.
- [1128] T. Auletta, M.R. de Jong, A. Mulder, F.C.J.M. van Veggel, J. Huskens, D.N. Reinhoudt, S. Zou, S. Zapotoczny, H. Schonherr, G.J. Vancso, L. Kuipers, *J. Am. Chem. Soc.* 126 (2004) 1577.
- [1129] S. Wielert-Badt, P. Hinterdorfer, H.J. Gruber, J.T. Lin, D. Badt, B. Wimmer, H. Schindler, R.K.H. Kinne, *Biophys. J.* 82 (2002) 2767.
- [1130] R. McKendry, M.-E. Theoclitou, T. Rayment, C. Abell, *Nature* 391 (1988) 566.
- [1131] M. Mahapatro, C. Gibson, C. Abell, T. Rayment, *Ultramicroscopy* 97 (2003) 297.
- [1132] C. Gergely, J.C. Voegel, P. Schaaf, B. Senger, M. Maaloum, J.K.H. Horber, J. Hemmerle, *Proc. Natl. Acad. Sci. U.S.A.* 97 (2000) 10802.
- [1133] H. Schonherr, M.W.J. Beulen, J. Bugler, J. Huskens, F.C.J.M. van Veggel, D.N. Reinhoudt, G.J. Vancso, *J. Am. Chem. Soc.* 122 (2000) 4963.
- [1134] Y.S. Lo, Y.J. Zhu, T.P. Beebe Jr., *Langmuir* 17 (2001) 3741.
- [1135] P.Y. Meadows, J.E. Bemis, G.C. Walker, *Langmuir* 19 (2003) 9566.
- [1136] G.L.B. Kada, L.H. Jeyakumar, F. Kienberger, V.P. Pastushenko, S. Fleischer, H. Schindler, F.A. Lai, P. Hinterdorfer, *Ultramicroscopy* 86 (2001) 129.
- [1137] C.B. Yuan, A. Chen, P. Kolb, V.T. Moy, *Biochemistry* 39 (2000) 10219.
- [1138] T. Strunz, K. Oroszlan, R. Schafer, H.J. Guntherodt, *Proc. Natl. Acad. Sci. U.S.A.* 96 (1999) 11277.
- [1139] Y.S. Lo, J. Simons, T.P. Beebe, *J. Phys. Chem. B* 106 (2002) 9847.
- [1140] M. Bergkvist, J. Carlsson, S. Oscarsson, *J. Phys. Chem. B* 105 (2001) 2062.
- [1141] R. Gamsjaeger, B. Wimmer, H. Kahr, A. Tinazli, S. Picuric, S. Lata, R. Tampe, Y. Maulet, H.J. Gruber, P. Hinterdorfer, C. Romanin, *Langmuir* 20 (2004) 5885.
- [1142] T. Gutschmann, G.E. Fantner, J.H. Kindt, M. Venturoni, S. Danielsen, P.K. Hansma, *Biophys. J.* 86 (2004) 3186.
- [1143] O. Lioubashevski, F. Patolsky, I. Willner, *Langmuir* 17 (2001) 5134.
- [1144] L. Ling, H.-J. Butt, R. Berger, *J. Am. Chem. Soc.* 126 (2004) 13992.
- [1145] M.P. Schotanus, K.S. Aumann, K. Sinniah, *Langmuir* 18 (2002) 5333.
- [1146] B.D. Sattin, A.E. Pelling, M.C. Goh, *Nucl. Acids Res.* 32 (2004) 4876.
- [1147] F. Kuhner, T. Costa, P.M. Bisch, S. Thalhammer, W.M. Heckl, H.E. Gaub, *Biophys. J.* 87 (2004) 2683.
- [1148] Y. Jin, K.M. Wang, W.H. Tan, P. Wu, Q. Wang, H.M. Huang, S.S. Huang, Z.W. Tang, Q.P. Guo, *Anal. Chem.* 76 (2004) 5721.
- [1149] Y.X. Jiang, F. Qin, Y.Q. Li, X.H. Fang, C.L. Bai, *Nucl. Acids Res.* 32 (2004) e101.
- [1150] Y.X. Jiang, C.F. Zhu, L.S. Ling, L.J. Wan, X.H. Fang, C. Bai, *Anal. Chem.* 75 (2003) 2112.
- [1151] N.H. Green, P.M. Williams, O. Wahab, M.C. Davies, C.J. Roberts, S.J.B. Tendler, S. Allen, *Biophys. J.* 86 (2004) 3811.
- [1152] I.A. Andreev, S.H. Kim, N.O. Kalinina, D.V. Rakitina, A.G. Fitzgerald, P. Palukaitis, M.E. Taliany, *J. Mol. Biol.* 339 (2004) 1041.
- [1153] C. Nakamura, S. Takeda, M. Kageshima, M. Ito, N. Sugimoto, K. Sekizawa, J. Miyake, *Biopolymers* 76 (2004) 48.
- [1154] A. Touhami, B. Hoffmann, A. Vasella, F.A. Denis, Y.F. Dufre ne, *Langmuir* 19 (2003) 1745.
- [1155] S. Kado, K. Yamada, K. Kimura, *Langmuir* 20 (2004) 3259.
- [1156] I. Schumakovitch, W. Grange, T. Strunz, P. Bertoncini, H.J. Guntherodt, M. Hegner, *Biophys. J.* 82 (2002) 517.
- [1157] R. Afrin, T. Yamada, A. Ikai, *Ultramicroscopy* 100 (2004) 187.
- [1158] B. Cappella, P. Baschieri, C. Frediani, P. Miccoli, C. Ascoli, *Nanotechnology* 8 (1997) 82.
- [1159] O.H. Willemssen, M.M.E. Snel, K.O. van der Werf, B.G. de Grooth, J. Greve, P. Hinterdorfer, H.J. Gruber, H. Schindler, Y. van Kooyk, C.G. Figdor, *Biophys. J.* 75 (1998) 2220.
- [1160] D.D. Koleske, G.U. Lee, B.I. Gans, K.P. Lee, D.P. Dilella, K.J. Wahl, W.R. Barger, L.J. Whitman, R.J. Colton, *Rev. Sci. Instrum.* 66 (1995) 4566.
- [1161] W.H. Goldmann, R. Galneder, M. Ludwig, A. Kromm, R.M. Ezzell, *FEBS Lett.* 424 (1998) 139.

- [1162] O.H. Willemsen, M.M.E. Snel, S.J.T. van Noort, K.O. van der Werf, B.G. de Grooth, C.G. Figdor, J. Greve, *Ultramicroscopy* 80 (1999) 133.
- [1163] N.B. Holland, C.A. Siedlecki, R.E. Marchant, *J. Biomed. Mater. Res.* 45 (1999) 167.
- [1164] W.F. Heinz, J.H. Hoh, *Nanotechnology* 17 (1999) 143.
- [1165] N.H. Green, S. Allen, M.C. Davies, C.J. Roberts, S.J.B. Tendler, P.M. Williams, *Trac-Trends Anal. Chem.* 21 (2002) 64.
- [1166] M. Radmacher, M. Fritz, J.P. Cleveland, D.A. Walters, P.K. Hansma, *Langmuir* 10 (1994) 3809.
- [1167] D.R. Baselt, J.D. Baldeschwieler, *J. Appl. Phys.* 76 (1994) 33.
- [1168] M. Heuberger, G. Dietler, L. Schlapbach, *Nanotechnology* 6 (1995) 12.
- [1169] C.C. Dupont-Gillain, B. Nysten, V. Hlady, P.G. Rouxhet, *J. Colloid Interf. Sci.* 220 (1999) 163.
- [1170] P.J. Eaton, P. Graham, J.R. Smith, J.D. Smart, T.G. Nevell, J. Tsibouklis, *Langmuir* 16 (2000) 7887.
- [1171] M. Nakamura, L. Sirghi, T. Aoki, Y. Hatanaka, *Surf. Sci.* 507 (2002) 778.
- [1172] C.C. Dupont-Gillain, I. Jacquemart, *Surf. Sci.* 539 (2003) 145.
- [1173] B. Pignataro, C. Consalvo, G. Compagnini, A. Licciardello, *Chem. Phys. Lett.* 299 (1999) 430.
- [1174] B. Pignataro, S. Panebianco, C. Consalvo, A. Licciardello, *Surf. Interf. Anal.* 27 (1999) 396.
- [1175] L.V. Najbar, R.F. Considine, C.J. Drummond, *Langmuir* 19 (2003) 2880.
- [1176] G.A. Willing, T.R. Burk, F.M. Etzler, R.D. Neuman, *Colloids Surf. A* 193 (2001) 117.
- [1177] G.A. Willing, T.H. Ibrahim, F.M. Etzler, R.D. Neuman, *J. Colloid Interf. Sci.* 226 (2000) 185.
- [1178] S. Allen, S.D.A. Connell, X. Chen, J. Davies, M.C. Davies, A.C. Dawkes, C.J. Roberts, S.J.B. Tendler, P.M. Williams, *J. Colloid Interf. Sci.* 242 (2001) 470.
- [1179] F.L. Leite, A. Riul, P.S.P. Herrmann, *J. Adhes. Sci. Technol.* 17 (2003) 2141.
- [1180] H.A. Mizes, *J. Adhes.* 51 (1995) 155.
- [1181] G. Jogikalmath, J.K. Stuart, A. Pungor, V. Hlady, *Colloids Surf. A* 154 (1999) 53.
- [1182] E. Kokkoli, C.F. Zukoski, *Langmuir* 17 (2001) 369.
- [1183] S.L. Gao, E. Mader, S.F. Zhandarov, *Carbon* 42 (2004) 515.
- [1184] P. Eaton, F.F. Estarlich, R.J. Ewen, T.G. Nevell, J.R. Smith, J. Tsibouklis, *Langmuir* 18 (2002) 10011.
- [1185] J. Domke, M. Radmacher, *Langmuir* 14 (1998) 3320.
- [1186] T. Nitta, H. Haga, K. Kawabata, K. Abe, T. Sambongi, *Ultramicroscopy* 82 (2000) 223.
- [1187] A.N. Parbhu, W.G. Bryson, R. Lal, *Biochemistry* 38 (1999) 11755.
- [1188] P. Hinterdorfer, W. Baumgartner, H.J. Gruber, K. Schilcher, H. Schindler, *Proc. Natl. Acad. Sci. U.S.A.* 93 (1996) 3477.
- [1189] M. Ludwig, W. Dettmann, H.E. Gaub, *Biophys. J.* 72 (1997) 445.
- [1190] S. Allen, X. Chen, J. Davies, M.C. Davies, J.C. Edwards, S.J.B. Tendler, P.M. Williams, *Appl. Phys. A* 66 (1999) S255.
- [1191] A. Agnihotri, C.A. Siedlecki, *Ultramicroscopy* 102 (2005) 257.
- [1192] Ijiro, *Colloids Surf. A* 198–200 (2002) 677.
- [1193] H. Sunami, K. Ijiro, O. Karthaus, S. Kraemer, S. Mittler, W. Knoll, M. Simomura, *Mol. Cryst. Liquid Cryst.* 371 (2001) 151.
- [1194] M. Gad, A. Itoh, A. Ikai, *Cell Biol. Int.* 21 (1997) 697.
- [1195] T. Osada, S. Takezawa, A. Itoh, H. Arakawa, M. Ichikawa, A. Ikai, *Chem. Senses* 24 (1999) 1.
- [1196] T. Osada, A. Itoh, A. Ikai, *Ultramicroscopy* 97 (2003) 353.
- [1197] H. Kim, H. Arakawa, T. Osada, A. Ikai, *Ultramicroscopy* 97 (2003) 359.
- [1198] N. Almqvist, R. Bhatia, G. Primbs, N. Desai, S. Banerjee, R. Lal, *Biophys. J.* 86 (2004) 1753.
- [1199] C.V.G. Reddy, K. Malinowska, N. Menhart, R. Wang, *Biochim. Biophys. Acta Biomembr.* 1667 (2004) 15.
- [1200] P.P. Lehenkari, G.T. Charras, A. Nykanen, M.A. Horton, *Ultramicroscopy* 82 (2000) 289.
- [1201] M. Grandbois, W. Dettmann, M. Benoit, H.E. Gaub, *J. Histochem. Cytochem.* 48 (2000) 719.
- [1202] O.H. Willemsen, M.M. Snel, L. Kuipers, C.G. Figdor, J. Greve, B.G.D. Grooth, *Biophys. J.* 76 (1999).
- [1203] H.H.P. Fang, K.Y. Chan, L.C. Xu, *J. Microbiol. Meth.* 40 (2000) 89.
- [1204] L.C. Xu, K.Y. Chan, H.H.P. Fang, *Mater. Charact.* 48 (2002) 195.
- [1205] I.D. Auerbach, C. Sorensen, H.G. Hansma, P.A. Holden, *J. Bacteriol.* 182 (2000) 3809.
- [1206] D.E. Laney, R.A. Garcia, S.M. Parsons, H.G. Hansma, *Biophys. J.* 72 (1997) 806.
- [1207] M. Arnoldi, C.M. Kacher, E. Bauerlein, M. Radmacher, M. Fritz, *Appl. Phys. A* 66 (1998) S613.
- [1208] C. Rotsch, M. Radmacher, *Biophys. J.* 78 (2000) 520.
- [1209] Y. Yamane, H. Shiga, H. Haga, K. Kawabata, K. Abe, E. Ito, *J. Electron Microsc.* 49 (2000) 463.

- [1210] P. Schär-Zammaretti, J. Ubbink, *Ultramicroscopy* 97 (2003) 199.
- [1211] U.G. Hofmann, C. Rotsch, W.J. Parak, M. Radmacher, *J. Struct. Biol.* 119 (1997) 84.
- [1212] M. Walch, U. Ziegler, P. Groscurth, *Ultramicroscopy* 82 (2000) 259.
- [1213] W.H. Goldmann, D.E. Ingber, *Biochem. Biophys. Res. Commun.* 290 (2002) 749.
- [1214] B.A. Smith, B. Tolloczko, J.G. Martin, P. Grutter, *Biophys. J.* 88 (2005) 2994.
- [1215] H. Haga, S. Sasaki, K. Kawabata, E. Ito, T. Ushiki, T. Sambongi, *Ultramicroscopy* 82 (2000) 253.
- [1216] C. Rotsch, K. Jacobson, M. Radmacher, *Proc. Natl. Acad. Sci. U.S.A.* 96 (1999) 921.
- [1217] C. Rotsch, K. Jacobson, J. Condeelis, M. Radmacher, *Ultramicroscopy* 86 (2001) 97.
- [1218] R. Matzke, K. Jacobson, M. Radmacher, *Nat. Cell Biol.* 3 (2001) 607.
- [1219] H.U. Krottil, T. Stifter, H. Waschipky, K. Weishaupt, S. Hild, O. Marti, *Surf. Interf. Anal.* 27 (1999) 336.
- [1220] P.M. Spizig, *Dynamische rasterkraftmikroskopie*, University of Ulm, Ulm, 2002.
- [1221] T. Miyatani, S. Okamoto, A. Rosa, O. Marti, M. Fujihira, *Appl. Phys. A* 66 (1998) S349.
- [1222] X. Chen, M.C. Davies, C.J. Roberts, S.J.B. Tandler, P.M. Williams, *Appl. Phys. Lett.* 77 (2000) 3462.
- [1223] S. Krüger, D. Krüger, A. Janshoff, *Chem. Phys. Chem.* 5 (2004) 989.
- [1224] T. Stifter, E. Weilandt, O. Marti, S. Hild, *Appl. Phys. A* 66 (1998) S597.
- [1225] F. Sato, H. Okui, U. Akiba, K. Suga, M. Fujihira, *Ultramicroscopy* 97 (2003) 303.
- [1226] C.H. Sun, D.E. Aston, J.C. Berg, *J. Colloid Interf. Sci.* 248 (2002) 96.
- [1227] D.N. Morton, C.J. Roberts, M.J. Hey, J.R. Mitchell, J. Hipkiss, J. Vercauteren, *J. Food Sci.* 68 (2003) 1411.
- [1228] M. Menke, S. Kunneke, A. Janshoff, *Eur. Biophys. J. Biophys. Lett.* 31 (2002) 317.
- [1229] O. Marti, T. Stifter, H. Waschipky, M. Quintus, S. Hild, *Colloids Surf. A* 154 (1999) 65.
- [1230] A. Leijala, J. Hautajarvi, *Text. Res. J.* 68 (1998) 193.
- [1231] T. Röder, H.S. Kitzerow, J.C. Hummelen, *Synth. Met.* 141 (2004) 271.
- [1232] S. Hussain, D.B. Grandy, M. Reading, D.Q.M. Craig, *J. Pharm. Sci.* 93 (2004) 1672.
- [1233] A. Ebner, F. Kienberger, C.M. Stroh, H.J. Gruber, P. Hinterdorfer, *Microsc. Res. Technol.* 65 (2004) 246.
- [1234] L.E. Dickson, J.C. Berg, *J. Adhes. Sci. Technol.* 15 (2001) 171.
- [1235] D.B. Grandy, D.J. Hourston, D.M. Price, M. Reading, G.G. Silva, M. Song, P.A. Sykes, *Macromolecules* 33 (2000) 9348.
- [1236] M. Csete, J. Kokavecz, Z. Bor, O. Marti, *Mater. Sci. Eng. C: Biomimetic Supramol. Syst.* 23 (2003) 939.
- [1237] B. Hopp, N. Kresz, J. Kokavecz, T. Smausz, H. Schieferdecker, A. Doring, O. Marti, Z. Bor, *Appl. Surf. Sci.* 221 (2004) 437.
- [1238] B. Hopp, T. Smausz, J. Kokavecz, N. Kresz, Z. Bor, S. Hild, O. Marti, *J. Appl. Phys.* 96 (2004) 5548.
- [1239] N. Kresz, J. Kokavecz, T. Smausz, B. Hopp, A. Csete, S. Hild, O. Marti, *Thin Solid Films* 453/454 (2004) 239.
- [1240] Y. Okabe, M. Furugori, Y. Tani, U. Akiba, M. Fujihira, *Ultramicroscopy* 82 (2000) 203.
- [1241] Y. Okabe, U. Akiba, M. Fujihira, *Appl. Surf. Sci.* 157 (2000) 398.
- [1242] K.M. Balss, G.A. Fried, P.W. Bohn, *J. Electrochem. Soc.* 149 (2002) C450.
- [1243] D.A. Ramrus, J.C. Berg, *J. Adhes. Sci. Technol.* 18 (2004) 1395.
- [1244] J. Buseman-Williams, J.C. Berg, *Langmuir* 20 (2004) 2026.
- [1245] A. Pfrang, K.J. Huttinger, T. Schimmel, *Surf. Interf. Anal.* 33 (2002) 96.
- [1246] N. Münter, B.O. Kolbesen, W. Storm, T. Müller, *J. Electrochem. Soc.* 150 (2003) G192.
- [1247] H. Zhang, P.C.M. Grim, P. Foubert, T. Vosch, P. Vanoppen, U.M. Wiesler, A.J. Berresheim, K. Müllen, F.C. de Schryver, *Langmuir* 16 (2000) 9009.
- [1248] H. Zhang, P.C.M. Grim, T. Vosch, U.M. Wiesler, A.J. Berresheim, K. Müllen, F.C. de Schryver, *Langmuir* 16 (2000) 9294.
- [1249] M. Zhu, S. Akari, H. Mohwald, *Nano Lett.* 1 (2001) 569.
- [1250] M. Schneider, M. Zhu, G. Papastavrou, S. Akari, H. Mohwald, *Langmuir* 18 (2002) 602.
- [1251] K.J. Kwak, H. Kudo, M. Fujihira, *Ultramicroscopy* 97 (2003) 249.
- [1252] K.J. Kwak, F. Sato, H. Kudo, S. Yoda, M. Fujihira, *Ultramicroscopy* 100 (2004) 179.
- [1253] H.U. Krottil, T. Stifter, O. Marti, *Rev. Sci. Instrum.* 71 (2000) 2765.